

Remote Sensing of Soil

Guest Editors: Mehrez Zribi, Nicolas Baghdadi, Michel Nolin, and Inge Sandholt





Remote Sensing of Soil

Applied and Environmental Soil Science

Remote Sensing of Soil

Guest Editors: Mehrez Zribi, Nicolas Baghdadi,
Michel Nolin, and Inge Sandholt



Copyright © 2011 Hindawi Publishing Corporation. All rights reserved.

This is a special issue published in volume 2011 of "Applied and Environmental Soil Science." All articles are open access articles distributed under the Creative Commons Attribution License, which permits unrestricted use, distribution, and reproduction in any medium, provided the original work is properly cited.

Editorial Board

Lynette K. Abbott, Australia
Joselito M. Arocena, Canada
Nanthi Bolan, Australia
Robert L. Bradley, Canada
Artemi Cerda, Spain
Hong J. Di, New Zealand
Oliver Dilly, Germany
Michael A. Fullen, UK
Ryusuke Hatano, Japan
William R. Horwath, USA

D. L. Jones, UK
Matthias Kaestner, Germany
Anastasios D. Karathanasis, USA
Heike Knicker, Spain
Takashi Kosaki, Japan
R. Lal, USA
Yongchao Liang, China
Mallavarapu Megharaj, Australia
A. J. Melfi, Brazil
Teodoro M. Miano, Italy

Jean Charles Munch, Germany
Amaresh K. Nayak, India
Alessandro Piccolo, Italy
Peter Shouse, USA
B. Singh, Australia
Keith Smettem, Australia
Marco Trevisan, Italy
Antonio Violante, Italy
Paul Voroney, Canada
Jianming Xu, China

Contents

Remote Sensing of Soil, Mehrez Zribi, Nicolas Baghdadi, Michel Nolin, and Inge Sandholt
Volume 2011, Article ID 904561, 2 pages

Use of Airborne Hyperspectral Imagery to Map Soil Properties in Tilled Agricultural Fields,
W. Dean Hively, Gregory W. McCarty, James B. Reeves III, Megan W. Lang, Robert A. Oesterling,
and Stephen R. Delwiche
Volume 2011, Article ID 358193, 13 pages

**Relationships between GPP, Satellite Measures of Greenness and Canopy Water Content with Soil
Moisture in Mediterranean-Climate Grassland and Oak Savanna**, Shishi Liu, Oliver A. Chadwick,
Dar A. Roberts, and Chris J. Still
Volume 2011, Article ID 839028, 14 pages

Mapping Agricultural Frozen Soil on the Watershed Scale Using Remote Sensing Data, Jalal Khaldoune,
Eric Van Bochove, Monique Bernier, and Michel C. Nolin
Volume 2011, Article ID 193237, 16 pages

**Comparisons of Brightness Temperatures of Landsat-7/ETM+ and Terra/MODIS around Hotien Oasis in
the Taklimakan Desert**, Yoshinari Oguro, Seiji Ito, and Kiyoshi Tsuchiya
Volume 2011, Article ID 948135, 11 pages

**Use of Imaging Spectroscopy for Mapping and Quantifying the Weathering Degree of Tropical Soils in
Central Brazil**, Gustavo M. M. Baptista, Rodrigo S. Corrêa, Perseu F. dos Santos, José S. Madeira Netto,
and Paulo R. Meneses
Volume 2011, Article ID 641328, 7 pages

**Digital Soil Mapping in the Absence of Field Training Data: A Case Study Using Terrain Attributes and
Semiautomated Soil Signature Derivation to Distinguish Ecological Potential**, Dawn M. Browning and
Michael C. Duniway
Volume 2011, Article ID 421904, 12 pages

Estimation of Soil Moisture in an Alpine Catchment with RADARSAT2 Images, L. Pasolli, C. Notarnicola,
L. Bruzzone, G. Bertoldi, S. Della Chiesa, V. Hell, G. Niedrist, U. Tappeiner, M. Zebisch, F. Del Frate,
and G. Vaglio Laurin
Volume 2011, Article ID 175473, 12 pages

Editorial

Remote Sensing of Soil

Mehrez Zribi,¹ Nicolas Baghdadi,² and Michel Nolin³

¹ CESBIO (CNRS/IRD/UPS/CNES), 18 Avenue Edouard Belin, 31401 Toulouse, Cedex 9, France

² TETIS/CEMAGREF, 500 Rue Jean-François Breton, 34093 Montpellier, Cedex 5, France

³ Agriculture et Agroalimentaire Canada, 979 Avenue de Bourgogne, Québec, QC, Canada G1W 2L4

Correspondence should be addressed to Mehrez Zribi, mehrez.zribi@ird.fr

Received 21 November 2011; Accepted 21 November 2011

Copyright © 2011 Mehrez Zribi et al. This is an open access article distributed under the Creative Commons Attribution License, which permits unrestricted use, distribution, and reproduction in any medium, provided the original work is properly cited.

Over the past few decades, the Earth's surface has witnessed major changes in land use. These changes are likely to continue, driven by demographic pressure or by climate change. In this context, monitoring tools are needed for maintaining a sustainable ecological status, improving soil conservation and water resource management. Floods, excess runoff, soil erosion, and related contamination and disequilibrium of the water and carbon cycles are, among others, key issues that are controlled and influenced by soil surface characteristics. The implementation of sustainable agricultural, hydrological, and environmental management requires an improved understanding of the soil, at increasingly finer scales. Conventional soil sampling and laboratory analyses cannot efficiently provide this information, because they are slow, expensive, and could not retrieve all temporal and spatial variabilities.

In this context, remote sensing has shown a high potential in soil characteristics retrieving in the last three decades. Different methodologies have been proposed for the estimation of soil parameters, based on different remote sensing sensors and techniques (passive and active). For passive remote sensing, we can consider four principal types of sensors:

- (i) optical remote sensing with limited number of bands (e.g., SPOT, ASTER, LANDSAT..., etc.) particularly adapted for vegetation cover description, land use analysis,
- (ii) optical remote sensing based on hyperspectral sensors, particularly adapted for soil texture description,
- (iii) optical remote sensing with thermal infrared band, adapted for soil temperature estimation,

- (iv) passive microwave remote sensing adapted to soil moisture and vegetation estimation.

For active remote sensing, different studies have shown a considerable potential for the characterization of different soil parameters: moisture, roughness, and texture. Active remote sensing is particularly based on two types of sensors: synthetic aperture radar (SAR) with high spatial resolution adapted to local and regional studies and scatterometer sensor more adapted to global estimations of soil parameters.

Three types of methodologies are generally used for soil parameters estimation: empirical models based only on satellite and ground databases, semiempirical models based on a mixture between physical modelling and real data, and finally physical models based only on the description of radiative transfert physics to analyze relationship between remote sensing signals and soil parameters.

These remote sensing studies concern particularly four soil parameters (moisture, roughness, temperature, and texture).

- (i) Soil moisture is a key parameter, influencing the manner in which rainwater is shared between the phenomena of evapotranspiration, infiltration, and runoff.
- (ii) Soil surface roughness is involved in the separation of water flow into infiltration and runoff. Moreover, monitoring the evolution of surface roughness is a way to estimate erosion risk particularly in agricultural areas.
- (iii) Soil texture is one of the most important soil properties influencing most physical, chemical, and biological soil processes. Hence, it is a key property for soil management.

- (iv) Soil temperature is a key parameter in the description of evapotranspiration and surface-atmosphere interface processes.

Based on this high potential of remote sensing to retrieve surface parameters, a high number of sensors have been launched in the last years to improve different methodologies proposed to retrieve operationally surface parameters.

In this context, our principal objective of this special issue is to present different studies illustrating quantitative analyses based on these different new sensors.

Pasolli et al. propose a technique for estimating soil moisture based on the support vector regression algorithm and the integration of ancillary data, using active remote sensing (RADARSAT 2 SAR data).

Liu et al. investigated the impact of soil moisture on gross primary production (GPP), chlorophyll content, and canopy water content represented by remotely sensed vegetation indices (VIs) in an open grassland and an oak savanna in California.

Using SAR (RADARSAT-1) remote sensing, Khaldoune et al. provide a classification of frozen/unfrozen soils in the entire Bras d'Henri River watershed near Quebec City (Quebec, Canada). It was developed to produce frozen soil maps under snow cover.

Browning and Duniway present a method to map soils with Landsat ETM+ imagery and high-resolution (5 m) terrain (IFSAR) data. They then characterize soil classes mapped using this semiautomated technique. The method distinguished spectrally distinct soil classes that differed in subsurface rather than surface properties.

Baptista et al. study tested the feasibility of applying AVIRIS sensor (Airborne Visible/InfraRed Imaging Spectrometer) for mapping and quantifying mineralogical components of three Brazilian soils. They showed to be possible mapping and quantifying the weathering degree of the studied soils.

Hively et al. propose the use of airborne hyperspectral imagery to map tilled agricultural fields properties. Soil hyperspectral reflectance imagery was obtained using an airborne imaging spectrometer (400–2450 nm, ~10 nm resolution, 2.5 m spatial resolution). The resulting raster maps showed variation associated with topographic factors, indicating the effect of soil redistribution and moisture regime on in-field spatial variability.

Finally, Oguro et al. discuss brightness temperature (BT) measurements and statistics over Taklimakan Desert. They are retrieved from the data of Landsat-7/ETM+ band 6 and Terra/MODIS band 31 and 32.

In spite the limited number of scientific papers and the difficulty to cover all techniques of remote sensing of soil, we hope that the readers will find this as a useful source of information.

Applied and Environmental Soil Science (AESS), who had faith in us and cooperated at all stages of compilation.

*Mehrez Zribi
Nicolas Baghdadi
Michel Nolin*

Acknowledgments

We would like to thank the reviewers who helped us in reviewing the articles and timely recommendations. We also would like to thank the staff of the Editorial Section of

Research Article

Use of Airborne Hyperspectral Imagery to Map Soil Properties in Tilled Agricultural Fields

W. Dean Hively,¹ Gregory W. McCarty,² James B. Reeves III,³ Megan W. Lang,⁴ Robert A. Oosterling,⁵ and Stephen R. Delwiche⁶

¹ U.S. Geological Survey, Eastern Geographic Science Center, Reston, VA, USA

² U.S. Department of Agriculture (USDA), Agricultural Research Service (ARS), Hydrology and Remote Sensing Laboratory, Beltsville, MD, USA

³ USDA-ARS Environmental Management and Byproducts Utilization Laboratory, Beltsville, MD, USA

⁴ USDA Forest Service, Northern Research Station, Beltsville, MD, USA

⁵ University of Maryland, Department of Geography, College Park, MD, USA

⁶ USDA-ARS Food Quality Laboratory, Beltsville, MD, USA

Correspondence should be addressed to W. Dean Hively, whively@usgs.gov

Received 10 January 2011; Revised 27 March 2011; Accepted 3 May 2011

Academic Editor: Mehrez Zribi

Copyright © 2011 W. Dean Hively et al. This is an open access article distributed under the Creative Commons Attribution License, which permits unrestricted use, distribution, and reproduction in any medium, provided the original work is properly cited.

Soil hyperspectral reflectance imagery was obtained for six tilled (soil) agricultural fields using an airborne imaging spectrometer (400–2450 nm, ~10 nm resolution, 2.5 m spatial resolution). Surface soil samples ($n = 315$) were analyzed for carbon content, particle size distribution, and 15 agronomically important elements (Mehlich-III extraction). When partial least squares (PLS) regression of imagery-derived reflectance spectra was used to predict analyte concentrations, 13 of the 19 analytes were predicted with $R^2 > 0.50$, including carbon (0.65), aluminum (0.76), iron (0.75), and silt content (0.79). Comparison of 15 spectral math preprocessing treatments showed that a simple first derivative worked well for nearly all analytes. The resulting PLS factors were exported as a vector of coefficients and used to calculate predicted maps of soil properties for each field. Image smoothing with a 3×3 low-pass filter prior to spectral data extraction improved prediction accuracy. The resulting raster maps showed variation associated with topographic factors, indicating the effect of soil redistribution and moisture regime on in-field spatial variability. High-resolution maps of soil analyte concentrations can be used to improve precision environmental management of farmlands.

1. Introduction

Spatial assessment of soil properties is important for understanding the dynamics of agricultural ecosystems. Site specific data can provide information that is critical to maintaining healthy soils and adequate nutrient supply for crop production, preventing losses of nutrients and sediments to the environment, and evaluating the transfer of elements such as carbon between land and atmosphere. Research has demonstrated that soil properties such as carbon content are correlated with field topography, soil texture, electrical conductivity, and soil reflectance [1–4]. A study by Venter et al. [5] documented accumulation of carbon in low areas of fields following soil translocation from higher areas, with

resulting carbon loss and soil degradation in elevated areas, and Thompson et al. [6] used soil-landscape modeling techniques to evaluate topographic distribution of soil texture and carbon content. These geographic approaches accounted for 28% to 68% of variation in measured carbon and demonstrated the complexity of environmental and management practices that affect soil characteristics. Recent research into soil health and sustainable cropping systems has demonstrated the potential of improved systems management based on knowledge of distributed soil properties [7]. Contemporary farm management relies on moderate resolution soil maps derived from photo and topographic interpretation. Accurate mapping of soil properties is made difficult due to high spatial variability observed within agricultural fields,

errors in spatial assessment of soil properties can result from inadequate or biased sampling of the landscape, and the high cost associated with collecting and analyzing soil samples often limits the amount of information available to farmers and land managers. However, advances in remote sensing technology are now providing tools to support geospatial mapping of soil properties, with applications in agricultural and environmental management.

Diffuse reflectance spectroscopy offers a rapid and non-destructive means for measurement of soil properties based on the reflectance spectra of illuminated soil [8–10]. A growing body of literature supports the use of spectral reflectance to determine soil properties, mostly using laboratory instrumentation to measure soil reflectance in the visible (400–700 nm) near infrared (700–2500 nm) and mid-infrared (2500–25,000 nm) wavelengths. Partial least squares (PLS) regression has emerged as a successful chemometric method for extracting predictive information from spectral reflectance datasets [10–12]. The PLS method characterizes high leverage orthogonal factors within observed spectral variance and matches them to similar factors that describe observed variance within measurements of a corresponding dependant variable. It has been successfully used to predict the results of soil laboratory analysis for carbon content [13, 14], particle size distribution [13, 15, 16] and elemental nutrient content [14, 17, 18], with results sometimes approaching the analytical accuracy of laboratory tests [12, 19]. A review of 44 studies [20] documented R^2 associated with prediction of soil carbon that ranged from 0.45 to 0.98, with a median of 0.86. Prediction accuracy depends on the signal:noise associated with the spectral data, and, like most analytical calibrations, is also highly influenced by the distribution of values in the measured dataset. The PLS-derived predictive equations, like most analytical calibrations, are most effective when the unknowns fall within the range of observations used to create the predictive equation, and the best success is obtained when an adequate number of locally obtained samples are included in the calibration data set [12, 21].

Advances in sensor technology have enabled satellite and airborne collection of hyperspectral imagery, allowing the acquisition of spectrally detailed geospatial reflectance data at field and landscape scales. By combining PLS regression of soil properties with reflectance data derived from airborne imagery, high-resolution maps of soil properties can be developed, thus overcoming the inaccuracies associated with geospatial interpolation of soil test data. Reports in the literature, for example, [16, 19, 22], indicate great potential for remote sensing approaches to map surface soil properties. However, additional research is needed to optimize data analysis procedures and improve prediction ability [19]. Separation of signal from noise is an important part of spectral data processing. Geometric and atmospheric adjustments are first required to derive a geospatially representative map of soil reflectance spectra. The imagery can then be smoothed spatially by averaging adjacent pixels, for example using a 3×3 low-pass filter. This can reduce the noise that results from random signal variability within the detector array while increasing the signal associated with number of

observations. It is also common to smooth the spectra in various ways, often by averaging adjacent wavebands or by calculation of first and second derivatives. Numerous math pretreatments have been evaluated for application of PLS to spectral reflectance data obtained from agricultural soils [8, 14, 23, 24].

In this paper, we have three objectives: (1) to evaluate 30 combinations of spectral math pretreatments and imagery smoothing techniques to identify most effective methods of preparing remote sensing data for partial least squares (PLS) analysis of soil properties (2) to develop and validate PLS predictions of soil concentrations for 19 laboratory analytes based on data extracted from airborne hyperspectral imagery and (3) to export resulting PLS vectors to geospatial imagery processing software and calculate high-resolution raster maps of predicted soil characteristics. Six recently tilled agricultural fields were intensively sampled to provide the calibration data set.

2. Materials and Methods

2.1. Field Sampling. On 10 April, 2007, we collected 315 soil samples from six fields (Figure 1) located on working grain farms on the Eastern Shore of the Chesapeake Bay (Delmarva Peninsula, near Easton, MD). Each of the fields (Temple 1S, 7.3 ha; Temple 1N, 7.1 ha; Temple 2, 8.9 ha; Temple 3, 18.1 ha; Mason, 14.6 ha; Schrader 9.8 ha) was chosen to provide uniform, smooth, bare-soil conditions, had been recently tilled (moldboard plow, field cultivator, and disk), and had little to no vegetation or plant residue. Soil conditions were moderately dry at the time of sampling, with six days of warm spring weather since the previous substantial rainfall (25 mm on 04 April, 2007). All fields were relatively flat (0% to 5% slope). Soil types included moderately well-drained silt loams (Pineyneck PiA, Mattapex-Butlertown MtA), poorly drained silt loams (Othello Ot), and well-drained sandy loams (Indleside IgB). Although the majority of Eastern Shore farms are managed using no-till practices, the tilled fields were otherwise typical of regional cash grain crop management strategies.

Sampling locations (315 total) were established at approximately 40 m intervals in transects across each field. Transects were established by using a tractor to pull a chisel plow shank through the soil at 20 cm depth. All sampling occurred on 10 April, 2007, during one long day of fieldwork with a large sampling crew. The soil was already well mixed from moldboard plowing, and this fresh tillage created an area of lightly disturbed soil behind the chisel plow shank from which surface soil samples (~400 g) were collected at each location. Because the chisel plow shank did not invert the soil, this sampling method approximated conditions at the bare soil surface that were observed by the imaging spectrophotometer. Number of samples ranged from 30 to 86 per field. Global positioning system (GPS) points were established for each sampling location using a handheld Trimble Geo-XT unit with submeter accuracy, calculated as the average of >20 sequential coordinate readings.

Soil samples were air dried (>48 hr) and ground to pass through a 2 mm sieve. Sand, silt, and clay content were



FIGURE 1: Field sites with soil sampling locations (black points) and SSURGO soil boundaries. See Materials and Methods for soil type designations.

determined using the hydrometer method of particle size analysis [25]. Standard soil nutrient analysis was performed at the University of Delaware Soil Testing Laboratory (http://ag.udel.edu/other_websites/DSTP/), using Mehlich III analysis [26] for potassium (K), calcium (Ca), magnesium (Mg), manganese (Mn), zinc (Zn), iron (Fe), nitrogen (N), phosphorus (P), copper (Cu), boron (B), sulfur (S), and aluminum (Al). Percent phosphorus saturation was calculated as a ratio of phosphorus to iron and aluminum content. Organic matter content (OM) was determined by loss on ignition. Subsamples were roller-milled for 12 hours prior to elemental analysis for carbon (C) and nitrogen (N) content by dry combustion using a TruSpec CN analyzer (Leco Corp, St. Joseph Mich, USA). None of the samples contained significant inorganic carbon. On the same day as field sampling for soils, airborne spectral imagery was acquired.

2.2. Imagery Collection. The airborne hyperspectral imaging spectrometer (HyperSpecTIR) used in this study was a push broom sensor developed by the SpecTIR Corporation (Reno Nevada, USA). It measured irradiance in 178 spectral

channels between 400 and 2450 nm with approximately 10-nm resolution [27]. Orthorectification was established to within one pixel (<2.5 m) tolerance. An upward facing radiation sensor measured incoming solar radiation which was used to calibrate imagery to ground reflectance and limit atmospheric effects to the space beneath the aircraft.

The plane was flown at 1800 m altitude with a ground speed of 210 km hr^{-1} , between 10:00 and 14:00 hrs, on 10 April, 2007. At this altitude, the imagery covered a swath 800 m wide (320 adjacent 2.5 m pixels). Flight paths were flown parallel to the principle plane of the sun. A correction for cross-track illumination was tested but did not improve results and was therefore not adopted. A number of sensor errors were identified where faulty detector elements produced erroneous results within particular wavebands, resulting in along-track striping in the field maps of predicted analyte concentrations. The 15 most obvious of these errors were corrected with spatial smoothing by replacing each faulty reflectance value with the average value of the two neighboring detector elements within the particular faulty waveband. While it was clear from visual inspection of the

predicted imagery that bad detector elements remained, only the 15 most obvious errors were corrected.

Soil spectra associated with each sampling location were extracted from the imagery by overlaying GPS point shapefiles (<1 m geopositioning error) of sampling locations and selecting the data associated with each underlying pixel. This was done for both the original imagery (1-pixel extraction) and spatially smoothed imagery to which a 3×3 low-pass filter had been applied (9-pixel extraction). Imagery processing was conducted using ENVI 4.7. Elevation data for each pixel were derived from a 3-m LIDAR digital elevation map that was resampled at 2.5 m resolution, with a vertical accuracy of 0.20 m. A 2.5 m resolution wetness index was also calculated from the LIDAR data, using SAGA software to apply two consecutive iterations of an enhanced lee 3×3 filter. This measure approximates the cumulative influence of upslope contributing area. Near infrared reflectance spectra for each of the 315 dried, ground soil samples were also obtained in the laboratory using a bench spectrometer and controlled light source, with methods and PLS results reported in McCarty et al. [28].

2.3. Spectral Data Processing. Fifteen spectral math pretreatments were evaluated using a SAS Ver. 9.12 program modified for hyperspectral data processing [23]. These included untransformed spectra, first derivatives with gap ranging from 1 to 64, and second derivatives with gap ranging from 1 to 64. Each of these math pretreatments was applied separately to the smoothed and unsmoothed spectra, resulting in a total of 30 data combinations that were used independently to calculate PLS predictions for each laboratory analyte using all 315 samples. Both the spectral data and the analyte values were mean centered prior to PLS analysis. The number of factors used in each PLS regression was chosen by the PRESS algorithm [24] within SAS Proc PLS and ranged from four to ten. Testing for outliers was not performed, and all observed values were included in the analysis. Goodness of fit was determined using repeated leave-one-out cross validation, with results presented as coefficient of determination (R^2). Ranking analysis was employed to test for significant differences among math treatments, for all analytes predicted with $R^2 > 0.50$.

Once the best math treatment was chosen, PLS Toolbox Ver. 4.0 (Eigenvector Research, Wenatchee, Wash, USA), operating within the Matlab (Ver. 7.0) environment, was used to perform PLS analysis using mean-centered spectral and analyte data from five of the six fields (269 samples). Goodness of fit was determined using repeated leave-one-out cross validation, with results presented as coefficient of determination (R^2) and residual mean square error (RMSE). Data from the remaining field (Temple 1S, 46 samples) were treated as unknown samples and predicted from PLS coefficients, with prediction accuracy reported as bias (mean of predicted values minus mean of observed values) divided by the mean of predicted values (bias/mean(pred)) as well as standard deviation of validation [24, Section 18.8] divided by standard error of prediction (sd/se pred).

The use of Matlab allowed the mathematical flattening of the PLS factors into a 178 band vector of coefficients, and

the scalar product of this vector with each pixel's imagery-derived spectrum was used to calculate predicted analyte concentrations. This calculation was made for each pixel of the hyperspectral imagery by using IDL code run within the ENVI 4.7 programming environment to calculate the appropriate band math. In this manner, geospatial field maps of predicted analyte concentrations were produced.

3. Results and Discussion

3.1. Soil Test Results. Observed analyte concentrations for the six sampled fields are described in Table 1. Soils were dry at the time of sampling, with moisture content ranging from 10% to 23% for the majority (91%) of samples (Table 1). Overall, the distribution of observed carbon content values was not large, ranging from 0.6 to 2.0% (Table 1). The Mason site, which had recently transitioned from long term conventional grain production to organic grain production, exhibited low soil carbon (mean 0.7%) content relative to the other fields (means of 1.2 to 1.4%). The Schrader site had received long-term applications of dairy manure and exhibited somewhat increased soil C (mean 1.4%) relative to the other fields. The remaining four fields (Table 1: Temple 1S, Temple 1N, Temple 2, and Temple 3) were managed by one farmer, and were under similar management (conventional corn-wheat/soybean rotation). Overall, carbon content was low, as is typical of Maryland Eastern Shore farmland. Concentrations of the remaining analytes were within the normal range for agricultural soils, although variability among sites was not great.

3.2. Choice of Math Treatment. A SAS "shotgun approach" for hyperspectral data processing has previously been used to provide a factorial comparison of the effects of various math pretreatments on PLS analysis of soil spectra [23]. This method was used to compare a total of 15 different spectral pretreatments including 1st and 2nd derivatives with various gap widths (Table 2). Results showed that there were no statistical differences among the majority of the treatments, with the simplest treatments (no derivative, first derivative gap 2) often resulting in the best fit. This led to the conclusion that the PLS data mining techniques are capable of extracting the majority of signal information from the untransformed spectral data, without the need for math pretreatment.

There is some argument to be made that different math treatments are more appropriate for particular analytes, due to the physical interaction of light with those particular constituents. Some evidence for this was shown for potassium, for which a first derivative gap 8 increased R^2 from 0.514 (first derivative gap 2) to 0.578 (Table 2). However, caution must be taken to prevent overfitting of datasets, and further study is needed to justify the selection of a diversity of math treatments for use with particular analytes. Ultimately, the first derivative gap 2 was selected as the best math overall treatment even though it was slightly, but not significantly, outperformed in several cases (Table 2).

3.3. Partial Least Squares Regression: Calibration Dataset. Once the best math treatment was decided upon, PLS regression

TABLE 1: Observed laboratory analyte concentrations for the six bare soil fields that were sampled on 10 April, 2007, with number of samples collected (n). See Section 2 for analyte descriptions.

Field		C%	Sand%	Silt%	Clay%	pH	OM%	K mg/kg	Ca mg/kg	Mg mg/kg	Mn mg/kg	Zn mg/kg	Fe mg/kg	Al mg/kg	N mg/kg	P mg/kg	Cu mg/kg	B mg/kg	S mg/kg	Al mg/kg	Moisture%	Elevation m	Wetness
Temple 1S (n = 46) 7.3 ha	min	1.07	36.5	28.9	3.3	4.6	1.70	94	378	55	8	1.1	97	327	0.03	23	1.8	0.21	20.5	348	5	-5.0	7.2
	max	1.63	65.4	51.8	12.5	6.4	2.70	974	1214	242	111	6.9	409	798	0.12	585	6.0	0.79	82.0	798	35	2.7	12.7
	Mean	1.32	48.6	42.4	9.0	5.7	2.22	247	817	142	34	2.5	205	501	0.07	95	3.3	0.40	41.4	503	15	0.0	10.2
	sd	0.15	7.3	6.3	2.0	0.4	0.25	154	171	39	31	1.1	75	121	0.02	110	0.8	0.14	12.5	119	4	1.5	1.1
Temple 1N (n = 52) 7.1 ha	min	0.89	32.3	24.6	5.8	4.7	1.30	83	501	69	9	1.3	115	299	0.02	22	1.9	0.19	27.7	299	11	-4.8	7.1
	max	1.75	66.9	55.7	16.6	6.3	3.00	493	1252	257	115	3.9	360	960	0.12	175	5.0	0.74	75.0	960	20	2.7	13.3
	mean	1.21	49.5	40.9	9.6	5.3	2.12	226	785	137	32	2.5	207	559	0.06	67	3.3	0.37	46.3	557	16	0.0	10.4
	sd	0.17	7.6	6.7	2.2	0.4	0.33	89	192	46	29	0.7	71	146	0.02	29	0.6	0.14	13.9	148	2	1.5	1.2
Temple 2 (n = 55) 8.9 ha	min	0.88	34.1	24.7	3.9	5.4	1.40	43	482	107	4	0.8	129	306	0.03	11	1.9	0.17	26.6	306	11	-5.0	6.8
	max	1.91	68.2	55.4	17.3	7.0	3.10	571	1423	420	22	4.4	403	648	0.11	265	5.9	0.67	108.8	648	42	1.5	12.7
	mean	1.29	47.6	42.5	9.8	6.3	2.17	164	953	256	10	1.9	231	463	0.07	49	3.3	0.41	48.2	463	17	0.0	9.8
	sd	0.22	7.6	6.2	2.4	0.4	0.35	103	185	63	3	0.7	74	68	0.02	39	0.9	0.13	19.2	70	5	1.2	1.0
Temple 3 (n = 86) 18.1 ha	min	1.00	19.0	31.4	6.3	5.6	1.50	71	615	134	8	1.4	91	352	0.03	22	2.0	0.35	23.8	352	8	-5.9	5.7
	max	2.04	59.5	67.9	19.7	7.2	3.40	445	1857	488	112	8.7	380	1049	0.11	243	9.1	4.42	147.3	1049	34	1.0	12.4
	mean	1.32	32.9	54.9	12.2	6.3	2.50	210	992	226	34	3.0	183	652	0.07	95	4.0	0.93	37.1	652	14	0.0	10.4
	sd	0.18	8.0	7.1	2.9	0.3	0.37	70	271	64	23	1.2	77	188	0.01	51	1.1	0.77	14.5	188	4	0.5	1.0
Mason (n = 30) 14.6 ha	min	0.55	47.6	9.5	1.3	5.7	0.50	43	357	75	20	2.5	71	567	0.02	34	2.2	0.29	17.1	567	6	-2.7	6.4
	max	1.40	87.7	43.4	10.9	6.8	2.20	213	775	223	94	12.2	131	1033	0.07	320	21.2	0.61	29.8	1033	18	2.9	13.4
	mean	0.75	69.4	23.7	6.9	6.3	0.97	111	540	133	51	5.7	102	803	0.03	148	4.4	0.42	21.7	803	10	0.0	10.5
	sd	0.19	9.7	7.9	2.5	0.3	0.39	42	111	34	20	1.9	17	125	0.01	71	3.4	0.08	3.4	125	3	1.0	1.3
Schrader (n = 46) 9.8 ha	min	1.09	37.2	18.0	6.0	4.9	2.10	253	478	99	22	4.1	120	541	0.04	86	3.5	0.44	28.1	541	6	-2.7	7.9
	max	1.88	73.9	45.9	18.7	6.8	3.50	600	1066	212	111	8.6	410	822	0.09	232	12.9	0.85	44.1	822	23	2.9	11.9
	mean	1.41	51.9	37.7	10.4	6.1	2.65	449	801	160	52	6.0	177	669	0.07	133	6.6	0.62	35.6	669	15	0.0	10.6
	sd	0.18	8.6	6.7	2.7	0.4	0.34	89	113	27	19	1.0	62	66	0.01	35	1.8	0.10	3.4	66	3	1.0	0.5
Overall (n = 315) 65.8 ha	min	0.55	19.0	9.5	1.3	4.6	0.50	43	357	55	4	0.8	71	299	0.02	11	1.8	0.17	17.1	299	5	-5.9	5.7
	max	2.04	87.7	67.9	19.7	7.2	3.50	974	1857	488	115	12.2	410	1049	0.12	585	21.2	4.42	147.3	1049	42	2.9	13.4
	mean	1.26	46.8	43.1	10.1	6.0	2.21	236	855	186	34	3.4	190	598	0.06	93	4.1	0.57	39.5	598	15	0.0	10.3
	sd	0.25	13.1	11.2	2.9	0.5	0.56	136	238	70	26	1.8	77	168	0.01	53	1.3	0.30	12.3	127	4	1.1	1.0

TABLE 2: Partial least squares (PLS) prediction model goodness of fit (R^2) associated with each of 15 math treatments, for the 13 analytes that predicted with $R^2 > 0.5$, calculated using data from all 315 soil sampling locations¹. The first derivative gap two (1Dg2, depicted in bold) was selected as the overall most successful model although it was occasionally outperformed (italic). See Section 2 for analyte descriptions.

Derivative	Gap	C	Sand	Silt	Clay	pH	OM	K	Ca	Mg	Mn	Zn	Fe	Al	average
		R^2	R^2	R^2	R^2	R^2	R^2	R^2	R^2	R^2	R^2	R^2	R^2	R^2	R^2
NON	0	0.578	0.762	0.763	0.585	0.442	0.685	0.555	0.669	0.692	0.642	0.670	0.754	0.777	0.659
1ST	1	0.555	0.770	0.761	0.565	0.517	0.706	0.522	0.654	0.719	0.624	0.606	0.707	0.799	0.654
1ST	2	0.591	0.763	0.763	0.617	0.549	0.717	0.514	0.676	0.708	0.638	0.647	0.740	0.782	0.670
1ST	4	0.595	0.754	0.740	0.596	0.451	0.692	0.513	0.630	0.616	0.565	0.675	0.703	0.773	0.639
1ST	8	0.584	0.748	0.739	0.600	0.413	0.668	0.578	0.635	0.642	0.580	0.636	0.637	0.727	0.630
1ST	16	0.588	0.740	0.744	0.550	0.442	0.672	0.547	0.610	0.619	0.567	0.591	0.666	0.725	0.620
1ST	32	0.525	0.730	0.722	0.554	0.381	0.640	0.520	0.648	0.619	0.542	0.580	0.669	0.765	0.607
1ST	64	0.338	0.623	0.619	0.470	0.317	0.537	0.413	0.519	0.580	0.488	0.568	0.636	0.669	0.521
2ND	1	0.542	0.585	0.597	0.424	0.361	0.526	0.484	0.708	0.705	0.529	0.599	0.665	0.729	0.573
2ND	2	0.507	0.681	0.682	0.372	0.499	0.566	0.493	0.665	0.664	0.566	0.591	0.673	0.769	0.595
2ND	4	0.576	0.714	0.724	0.409	0.449	0.660	0.484	0.672	0.669	0.606	0.613	0.749	0.752	0.621
2ND	8	0.536	0.698	0.689	0.533	0.472	0.602	0.528	0.595	0.631	0.542	0.638	0.743	0.753	0.612
2ND	16	0.580	0.729	0.725	0.573	0.487	0.661	0.498	0.590	0.640	0.598	0.617	0.680	0.712	0.622
2ND	32	0.564	0.715	0.698	0.609	0.432	0.631	0.548	0.622	0.592	0.548	0.606	0.639	0.688	0.607
2ND	64	0.525	0.596	0.589	0.421	0.156	0.599	0.511	0.556	0.464	0.501	0.538	0.602	0.614	0.513

¹ Analytes that predicted poorly ($R^2 < 0.5$) included: N (< 0.303), P (< 0.355), Cu (< 0.358), B (< 0.169), S (< 0.282), and P saturation (< 0.127).

was performed in Matlab using a calibration dataset of 269 samples (all sampling locations from five of the six fields), with results reported in Table 3. It should be noted that spectral data for the 315 samples used to calculate the SAS PLS in Table 2 were extracted from an earlier version of image processing output in which the 15 band errors had not yet been corrected and to which cross-track illumination had been applied. This discrepancy resulted in slightly lower R^2 being used in Table 2 than in Table 3, but was not thought to have affected the relative performance of math treatments. Using Matlab PLS on 269 samples, 13 of the 19 analytes were predicted with $R^2 > 0.50$ (Table 3(a)), and the remaining seven were predicted with $R^2 < 0.40$: N (< 0.30), P (< 0.36), Cu (< 0.36), B (< 0.17), S (< 0.28), and P saturation (< 0.13). A comparison of observed and predicted values for a selection of analytes (carbon, silt, aluminum, and iron) is shown in Figure 2.

Prediction accuracy for carbon ($R^2 = 0.65$) fell well within the range of results (0.45 to 0.98) found in a survey of 44 studies [20] but was somewhat poor in comparison with results found in some other studies for example, [11, 14, 15]. The somewhat poor R^2 for carbon might lead to the conclusion that the sensor did not capture a good reflectance signal due to the increased noise often associated with airborne sensors that derives from atmospheric effects and variations in sensor-soil-sun geometry across the imagery. Indeed, a number of studies have found remote sensing spectroscopy to have reduced signal: noise relative to laboratory-based measurements [24]. However, the carbon PLS results reported in McCarty et al. [28], calculated for all 315 soil samples in this data set, using repeated leave-

one-out correlation to determine goodness of fit, showed that spectra from the airborne sensor were as effective ($R^2 = 0.67$) as spectra from a near-infrared benchtop laboratory spectrophotometer ($R^2 = 0.64$) in predicting soil carbon concentrations. For the remaining 12 analytes under consideration, the airborne sensor exhibited decreased accuracy relative to the laboratory spectrophotometer in three cases (change in R^2 of -0.03 to -0.08) and exhibited increased accuracy in nine cases (change in R^2 of 0.01 to 0.20).

These observations led to the conclusion that the airborne sensor provides a viable option for mapping soil properties and that the somewhat poor prediction accuracies observed in this experiment apparently stemmed from features associated with the local soil environment or the calibration dataset, rather than the effectiveness of the airborne sensor. The distribution and range of observed analyte concentrations within a calibration dataset can have a substantial impact on prediction accuracy, and the somewhat low prediction accuracy for carbon content observed in this study ($R^2 = 0.65$) is likely associated with the limited range and low values of soil carbon contents found within the calibration dataset (0.6% to 2.0%).

For the other analytes, prediction accuracies (Table 3(a)) were comparable with those found in other studies [8, 15, 17, 18]. Using principal components regression, Chang et al. [18] predicted Melich III analyte concentrations, and, similarly to this study, found Cu and P to have poor predictions, silt and clay content to predict with $R^2 \sim 0.8$, and a number of other analytes, including Fe, Mg, Mn, K, and pH, predicting with $R^2 > 0.6$. It is not always known whether successful predictions are the direct action of the

TABLE 3: Partial least squares (PLS) model accuracy in predicting soil analyte concentrations¹ for (a) the 269 calibration samples using repeated leave-one-out cross validation and (b) 46 validation samples from the field (Temple 1S) that had been left apart from the calibration. Results were derived using a first derivative gap 2 math pretreatment, using spectra derived from unsmoothed imagery (2.5 m² pixel size) or from spatially smoothed imagery to which a 3 × 3 low pass filter had been applied. See Section 2 for analyte descriptions. Units refer to analyte residual mean squared error (RMSE) values. Bold indicates sd/sepred > 1.20.

Factors no.	C%	Sand%	Silt%	Clay%	pH	OM%	K mg/kg	Ca mg/kg	Mg mg/kg	Mn mg/kg	Zn mg/kg	Fe mg/kg	Al mg/kg
	8	9	10	9	10	10	4	8	9	10	8	10	10
(a) 269 calibration samples collected from five agricultural fields													
using unsmoothed imagery													
R^2	0.65	0.79	0.79	0.66	0.51	0.75	0.59	0.69	0.69	0.62	0.64	0.75	0.76
RMSE	0.19	7.9	6.9	2.2	0.4	0.4	89.5	166.1	50.3	19.6	1.4	49.3	104.7
using smoothed imagery													
R^2	0.64	0.80	0.80	0.68	0.58	0.77	0.61	0.71	0.71	0.67	0.67	0.78	0.81
RMSE	0.18	7.2	6.2	2.0	0.4	0.3	86.1	151.8	45.5	17.8	1.2	43.8	89.0
(b) 46 validation samples collected from the remaining agricultural field (Temple 1S)													
using unsmoothed imagery													
² se pred	0.20	9.0	7.3	2.4	0.5	0.4	147.1	178.1	51.4	27.5	1.2	52.9	123.9
³ bias	0.10	−2.88	1.42	1.00	0.03	0.34	24.92	40.45	31.84	3.23	0.45	2.12	107.33
bias/mean (pred)	0.08	−0.06	0.03	0.11	0.01	0.15	0.10	0.05	0.22	0.09	0.18	0.01	0.21
⁴ sd/se pred	0.74	0.81	0.86	0.84	0.89	0.63	1.05	0.96	0.76	1.15	0.92	1.41	0.98
using smoothed imagery													
se pred	0.15	9.5	7.9	2.9	0.4	0.3	154.9	233.6	58.5	38.3	1.3	98.0	170.4
bias	−0.10	−0.87	−0.66	0.95	−0.25	−0.13	−23.06	−2.46	−2.07	−0.38	0.10	−5.26	77.66
bias/mean (pred)	−0.08	−0.02	−0.02	0.10	−0.05	−0.06	−0.10	0.00	−0.02	−0.01	0.04	−0.03	0.14
sd/se pred	0.86	1.29	1.26	1.07	0.97	0.74	1.04	1.34	1.41	1.25	0.98	1.91	1.29

¹ Analytes that predicted poorly ($R^2 < 0.5$) in the set of 315 samples (N, P, Cu, B, S, and P saturation) are not included here

²se pred: sd(observed-predicted)

³bias: mean(pred)−mean(obs)

⁴sd: standard deviation.

analyte upon the reflectance signal or instead the covariation of analyte concentrations with other factors which are influencing the spectral response [29]. Phosphorus, for example, has no expected reflectance resonance and is generally poorly predicted (e.g., 0.36 in this study, 0.40 in [18], and as low as 0.10 in other studies [8, 29]), and yet occasionally will be predicted with considerable accuracy [8, 29], likely due to covariation with spectrally responsive factors associated with labile organic matter.

3.4. Validation. Chemometric predictions of soil properties are typically validated by predicting analyte concentrations for samples that were not included in the calibration data set, and comparing the predicted results to observed values. This can be achieved by calculating repeated leave-one-out or leave-ten-out predictions, or by selecting a distinct set of samples either randomly, spatially, or based on even sample distribution within the range of observed values [24, Section 18]. We chose to adopt a rigorous validation by removing an entire agricultural field comprising 46 samples (Temple 1S) from the data set, leaving 269 samples for calibration. This field was one of four Temple fields that received similar crop management (corn-soy/wheat rotation with full tillage and no use of cover crops) and

it exhibited analyte concentrations in the mid-range of the six fields (Table 1, Figure 2). When predicted values were calculated for the 46 validation samples and compared to observed values, bias ranged from 1% to 22% of observed analyte concentrations (Table 3(b)). Seven of the analytes exhibited sd/se pred > 1.20 (bold text in Table 3(b)) using the spectra extracted from smoothed imagery, indicating that the prediction was useful for those elements (sand, silt, Ca, Mg, Mn, Fe, and Al), while only one analyte (Fe) exhibited sd/se pred > 1.20 using the spectra extracted from unsmoothed imagery, indicating that spatial smoothing helped to increase signal: noise in the spectral data set.

3.5. Prediction Maps. For each analyte, a PLS regression vector of 178 coefficients was exported from Matlab and applied to the mean-centered first derivative reflectance spectra associated with each pixel of the hyperspectral imagery to calculate a 2.5-m raster map of predicted analyte concentrations. Prediction maps for a selection of analytes (carbon, silt, iron, and aluminum) were derived in this manner using both unsmoothed and smoothed imagery (Figure 3). Bend-Dor et al. [19] have discussed the need for attention to imagery processing methods to extract maximum information from spectroscopic imagery. In this study, smoothing

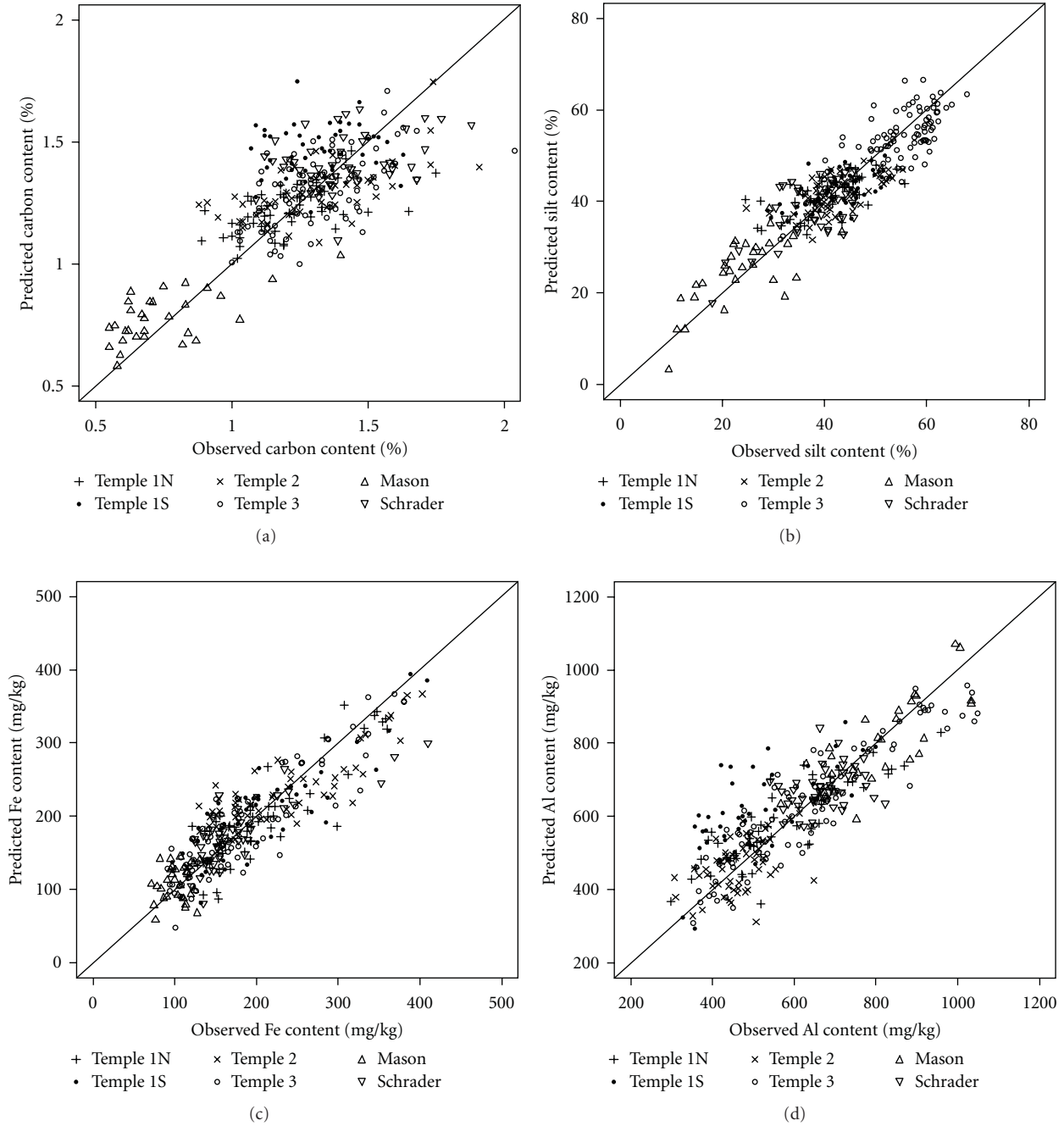


FIGURE 2: Comparison of observed analyte concentrations with values predicted using partial least squares (PLS) regression on reflectance spectra extracted from smoothed imagery to which a 3×3 low-pass filter had been applied, for (a) soil carbon, (b) silt, (c) iron, and (d) aluminum content. The field containing 41 sampling points that were left out for validation (Temple 1S) is depicted with solid circles.

the hyperspectral imagery with a 3×3 low band filter prior to spectral data extraction resulted in somewhat improved prediction accuracies in comparison to unsmoothed imagery (Table 3(a)). While this result implies that the smoothed extent of nine adjacent pixels (56.2 m^2) provided a better average representation of soil characteristics at each sampling point than did individual 6.25 m^2 pixels, it is more likely that the increased accuracy associated with the smoothed imagery is attributable to improvement of signal and reduction in

sensor detector element variability (noise) that results from coaddition of the nine adjacent spectra. Smoothing also generally improved the range and distribution of predicted analyte values found within each field image (Table 4), likely due to the correction of aberrations within the detector elements. However, it should be noted that discontinuities (striping) along the plant's flight path were evident in both smoothed and unsmoothed predicted imagery (Figure 3), indicating the effects of variable detector element sensitivity

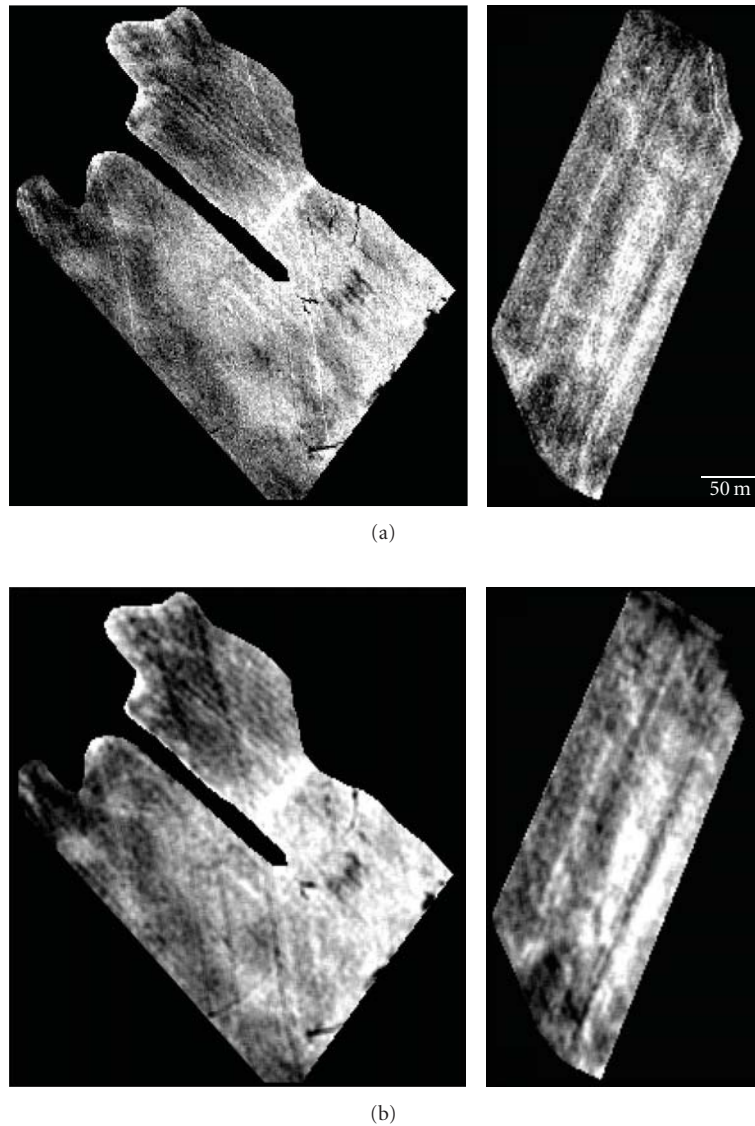


FIGURE 3: Maps of predicted soil carbon content calculated from (a) unsmoothed imagery (1-pixel data extraction) and (b) spatially smoothed imagery (9-pixel data extraction). Two of the six sampled fields are depicted here, with Temple 3 on the left and Schrader on the right. Predicted values ranged from 0.4% (black) to 2.5% (white).

along the sensor array and the need for continued improvement in sensor technology. Several additional imagery adjustments were considered, including cross-track illumination, transformation from reflectance (R) to $\log(1/R)$, and also spectral smoothing (not shown). However, none of these operations improved results and they were therefore avoided.

3.6. Topographic Analysis. Visual interpretation of field topographic features relative to the predicted analyte maps revealed accumulation of carbon, silt, iron, and aluminum in low areas (Figure 4). This result is in agreement with previous studies in Iowa that have linked increased soil C carbon contents in low areas with soil redistribution processes [3], and with a study by Terra et al. [1] who detected a correlation of soil properties with topographic indices and electrical conductivity that explained 50% of observed variability in car-

bon content. Other studies have evaluated the links between topography and soil constituents such as organic carbon at the landscape scale, showing accumulation at the bottom of slopes and in valley bottoms [30]. This study's work was conducted at the field scale, reflecting microtopographic soil distribution processes within a relatively flat elevation gradient (0%–5% slope), as well as the formative effects of soil moisture distribution and spatially variable biological processes resulting from soil heterogeneity and the balance of redoxomorphic status between oxic and anoxic conditions. Understanding distribution patterns of soil analytes, and the influence of hydrogeomorphic controls on these patterns, can provide greater certainty about the influence of soil erosion and soil ecology on the fate of carbon and nutrients.

To investigate potential causes of spatial distribution in predicted analyte values, a 2.5 m elevation map (re-sampled

TABLE 4: Predicted concentrations of select analytes (C, Silt, Al, Fe) derived from n pixels of near infrared hyperspectral imagery for each of the six bare soil fields using either unsmoothed (1-pixel) imagery with 2.5 m resolution, or spatially smoothed (9-pixel) imagery to which a 3×3 low pass filter had been applied¹. See Section 2 for analyte descriptions.

Field		C		Silt		Al		Fe	
		1-pixel%	9-pixel%	1-pixel%	9-pixel%	1-pixel mg/kg	9-pixel mg/kg	1-pixel mg/kg	9-pixel mg/kg
Temple 1S $n = 11731$	min	0.97	1.13	14.6	14.4	34	245	40	56
	max	1.86	1.94	80.1	58.7	1017	947	474	394
	mean	1.41	1.48	42.1	41.1	633	631	194	192
	sd	0.10	0.10	5.9	5.0	98	92	46	44
Temple 1N $n = 11436$	min	0.85	0.96	1.0	5.6	-31	147	37	64
	max	1.95	2.04	68.9	59.1	1304	897	452	429
	mean	1.23	1.25	43.6	42.1	589	555	200	210
	sd	0.11	0.11	5.8	4.9	115	112	60	65
Temple 2 $n = 14221$	min	-0.48	0.81	14.6	8.7	34	-389	40	54
	max	2.07	2.92	80.1	75.7	1017	1013	474	529
	mean	1.27	1.28	42.1	38.2	633	512	194	226
	sd	0.25	0.18	5.9	7.1	98	146	46	63
Temple 3 $n = 28955$	min	0.39	0.60	0.2	1.2	-137	0	-288	-6
	max	2.29	2.48	80.8	74.9	1173	1031	465	474
	mean	1.27	1.27	52.3	51.7	632	639	173	170
	sd	0.17	0.16	7.9	7.5	154	145	71	63
Mason $n = 23351$	min	0.41	0.44	-7.6	-7.5	-198	290	0	0
	max	2.27	1.94	64.9	48.5	1231	1180	391	391
	mean	0.81	0.81	27.7	28.7	755	776	111	108
	sd	0.11	0.10	6.4	7.1	96	100	32	27
Schrader $n = 15684$	min	0.91	0.98	12.3	13.4	255	296	58	66
	max	2.08	2.05	61.6	56.9	996	971	346	315
	mean	1.45	1.48	38.6	38.3	669	681	177	172
	sd	0.13	0.15	6.0	5.8	87	81	35	34
Overall $n = 105378$	min	0.97	1.13	14.6	14.4	255	296	58	66
	max	1.86	1.94	61.6	48.5	996	897	346	315
	mean	1.20	1.22	41.3	40.5	660	648	168	171

¹ See Table 3 for the accuracy (R^2) associated with each analyte prediction model.

TABLE 5: Correlation between predicted analyte concentrations and topographic indices including (a) relative elevation data derived from 3 m LIDAR DEM, and (b) wetness index calculated from 3 m LIDAR DEM, for one of the six sampled fields (Mason). Predicted values were calculated for unsmoothed imagery (2.5 m pixel size) and for smoothed imagery to which a 3×3 low band filter had been applied. See Section 2 for analyte descriptions.

	C R^2	Silt R^2	Al R^2	Fe R^2
(a) correlation with normalized elevation				
unsmoothed	0.100	0.000	0.232	0.013
smoothed	0.051	0.007	0.386	0.000
(b) correlation with wetness index				
unsmoothed	0.183	0.008	0.161	0.091
smoothed	0.178	0.021	0.317	0.037

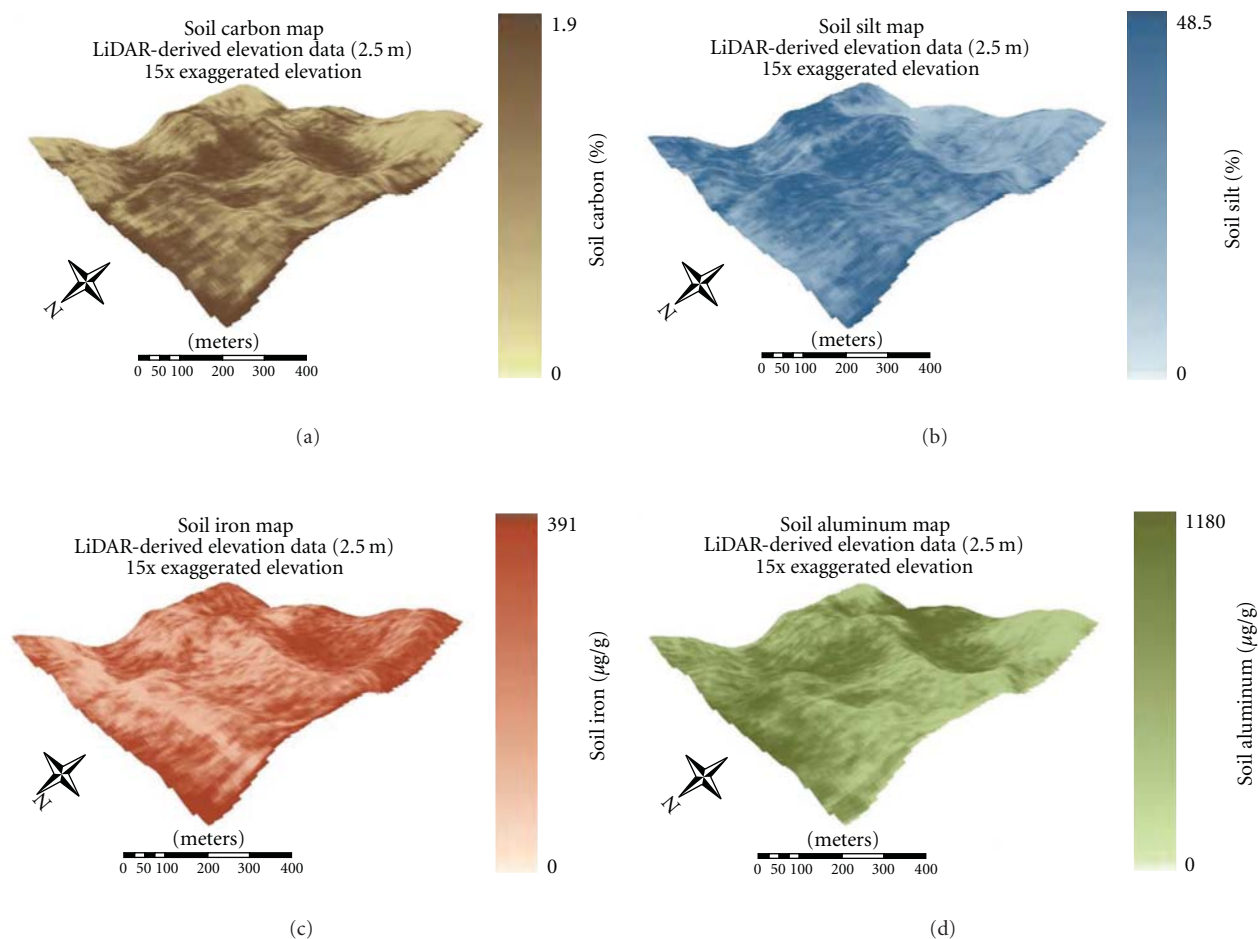


FIGURE 4: Map of predicted values for select analytes (C, Silt, Fe, Al), overlaid on a high-resolution digital elevation map, for one of the six sampled fields (Mason). Predicted values were derived from imagery that had been smoothed with a 3×3 low pass filter.

from 3-m LIDAR DEM) was used to calculate a normalized elevation value (observed—field mean elevation) and a soil wetness index (two consecutive iterations of a SAGA enhanced lee 3×3 filter) for each pixel of the predicted analyte maps. The normalized elevation variable was somewhat correlated (Table 5(a)) with predicted concentrations of aluminum ($R^2 = 0.23, 0.39$ for unsmoothed and spatially smoothed imagery, respectively) and was not well correlated with predicted concentrations of silt, iron, and carbon. The wetness index was similarly correlated with predicted aluminum concentration ($R^2 = 0.16, 0.32$) and was a better predictor for soil carbon, explaining 17% of observed variability (Table 5(b)). In all cases, the topographic variables were better correlated with spatially smoothed predictions than those made from unsmoothed imagery. The comparatively poor correlation with topographic indices observed in this study might indicate that soil carbon and elemental nutrient content is more related to variability in field management and manure application than to elevation and soil redistribution, or that a more complex set of topography-influenced ecological and physical processes than was measured is at play. On low relief ($<2\%$ slope), ditch drained, Coastal Plain

soils such as were sampled in this study, soil redistribution due to erosion is likely limited to short distances ($<1\text{--}10\text{ m}$), and prior converted wetland areas within fields can exhibit retained capacity for redoxomorphic activities that affect iron and aluminum transformations and increase denitrification and carbon accumulation. In this landscape, spatial distribution of soil carbon and nutrient content is likely influenced by a complex interaction of drainage status and land use history that is not easily characterized [5], and ultimately it may be more feasible to map surficial soil parameters using remote sensing technology than to predict them based on measurement and understanding of site specific processes.

Soil moisture can become an interfering variable in remote sensing chemometric analyses, as it mutes the soil's reflectance signal in a number of specific wavebands that are associated with water absorption bands [31]. Soil moisture for the 315 samples included in this study ranged between 5% and 42%, with most samples falling near the mean of 15% moisture. When observed moisture content was incorporated with the first derivative spectra of soil samples as a 177th predictor variable (following appropriate mean centering and variation normalization), the prediction

accuracies associated with PLS models for C, silt, Al, and Fe did not improve (change in R^2 of <0.02). Similarly, when silt was included as an additional predictor variable, to possibly account for interferences between soil particle size distribution and spectral reflectance, the prediction accuracies associated with PLS models for C, silt, Al, and Fe did not improve. These results verify that PLS analysis is a robust method that can successfully extract predictive information from remotely sensed imagery of *in situ* agricultural soils.

4. Conclusions

Aircraft-based acquisition of hyperspectral reflectance imagery can currently provide the necessary data to map soil properties in an efficient and rapid manner, and future improvements in sensor technology are expected to improve the signal:noise and spatial resolution associated with remote sensing imagery. Results of this remote sensing study, conducted on relatively flat, moderately well drained, Coastal Plain silt loam soils, showed that the PLS framework is robust, and spectral math pretreatments can be kept simple, with a first derivative gap 2 providing good results for all analytes. Spatial smoothing of reflectance imagery using a 3×3 low-band filter improved results, likely by reducing noise inherent to variability within the spectrophotometer's detector array. Fifteen of the 19 tested analytes predicted with $R^2 > 0.50$ (with R^2 from 0.51 to 0.79 for C, sand, silt, clay, pH, OM, K, Ca, Mg, Mn, Zn, Fe, and Al content; Table 3). Prediction accuracy for carbon was not particularly good ($R^2 = 0.64$) for this selection of sampled fields, perhaps owing to the low concentrations and limited range of observed variability (0.5% to 2%) in the calibration data set, but prediction accuracies for other analytes were on par with those found in other studies [8, 15, 18]. Predicted map values of select analytes, particularly aluminum, were correlated to field topography, indicating the influence of environmental processes on soil properties. Further research is needed to understand the interplay of measurable topographic and hydrological variation inherent in this relatively flat agricultural landscape with management variables such as tillage, crop rotation, and additions of manures and fertilizers that also affect soil chemical and physical properties.

Remote sensing approaches that use multispectral or hyperspectral imagery to predict soil properties are necessarily limited to analysis of plowed fields with very little crop residue or vegetation cover (bare soil). As a result, techniques that extrapolate soil properties data based on correlations derived from more easily measured parameters, such as topography, wetness, and cropping pattern may provide. The fields used in this study were carefully selected to have negligible amounts of surface residue, green vegetation, or hydrologically active areas. If this technique were put in practice on a larger scale, band filtering could be employed to remove such non-soil areas from analysis based on thresholding of spectral indices that correlate well with biomass (e.g., normalized difference vegetation index [32]), crop residue (e.g., cellulose adsorption index [33]), or soil moisture (e.g., water adsorption [13, 31]).

As hyperspectral imagery becomes more readily available and at lower cost, the application of partial least squares (PLS) regression to soil spectral reflectance data can provide an effective method for calculating high-resolution raster maps of important soil properties including texture, pH, and carbon and nutrient content. This information can then be used to inform farmer decision making, support precision environmental management of agricultural fields, increase sustainable crop production, and help to reduce nutrient, sediment, and carbon losses from agricultural systems.

Acknowledgments

This paper has benefitted greatly from the comments of two anonymous reviewers, and the project is also indebted to input from known scientific colleagues, with thanks going out to Drs. Craig Daughtry, Terry Slonecker, Guy Serbin, and the late Paul Doraiswamy. Technical assistance was provided by Kusuma Prabhakara and Dr. Beth Gardner, and laboratory and field work by Alex White and Antonio Pereira. Thanks to the University of Delaware Soil Test Laboratory for efficient sample processing. Thanks to Oliver Weatherbee and the SpecTIR corporation for airborne imagery acquisition. Support for this project was provided by the USDA Choptank River Conservation Effects Assessment Project. Any use of trade, firm, or product names is for descriptive purposes only and does not imply endorsement by the U.S. Government.

References

- [1] J. A. Terra, J. N. Shaw, D. W. Reeves, R. L. Raper, E. Van Santen, and P. L. Mask, "Soil carbon relationships with terrain attributes, electrical conductivity, and a soil survey in a coastal plain landscape," *Soil Science*, vol. 169, no. 12, pp. 819–831, 2004.
- [2] G. C. Simbahan and A. Dobermann, "Sampling optimization based on secondary information and its utilization in soil carbon mapping," *Geoderma*, vol. 133, no. 3–4, pp. 345–362, 2006.
- [3] J. C. Ritchie, G. W. McCarty, E. R. Venteris, and T. C. Kaspar, "Soil and soil organic carbon redistribution on the landscape," *Geomorphology*, vol. 89, no. 1–2, pp. 163–171, 2007.
- [4] U. W. A. Vitharana, M. Van Meirvenne, D. Simpson, L. Cockx, and J. De Baerdemaeker, "Key soil and topographic properties to delineate potential management classes for precision agriculture in the European loess area," *Geoderma*, vol. 143, no. 1–2, pp. 206–215, 2008.
- [5] E. R. Venteris, G. W. McCarty, J. C. Ritchie, and T. Gish, "Influence of management history and landscape variables on soil organic carbon and soil redistribution," *Soil Science*, vol. 169, no. 11, pp. 787–795, 2004.
- [6] J. A. Thompson, E. M. Pena-Yewtukhiw, and J. H. Grove, "Soil-landscape modeling across a physiographic region: topographic patterns and model transportability," *Geoderma*, vol. 133, no. 1–2, pp. 57–70, 2006.
- [7] O. J. Idowu, H. M. Van Es, G. S. Abawi et al., "Use of an integrative soil health test for evaluation of soil management impacts," *Renewable Agriculture and Food Systems*, vol. 24, no. 3, pp. 214–224, 2009.
- [8] R. A. Viscarra Rossel, D. J. J. Walvoort, A. B. McBratney, L. J. Janik, and J. O. Skjemstad, "Visible, near infrared, mid infrared or combined diffuse reflectance spectroscopy for simultaneous

- assessment of various soil properties,” *Geoderma*, vol. 131, no. 1-2, pp. 59–75, 2006.
- [9] J. B. Reeves III, G. W. McCarty, and W. D. Hively, “Mid-versus near-infrared spectroscopy for on-site analysis of soils,” in *Proximal Soil Sensing*, R. A. Viscarra Rossel, A. McBratney, and B. Minasny, Eds., chapter 11, pp. 133–142, Springer, New York, USA, 2010.
 - [10] D. J. Brown, K. D. Shepherd, M. G. Walsh, M. D. Mays, and T. G. Reinsch, “Global soil characterization with VNIR diffuse reflectance spectroscopy,” *Geoderma*, vol. 132, no. 3-4, pp. 273–290, 2006.
 - [11] H. M. Bartholomeus, M. E. Schaepman, L. Kooistra, A. Stevens, W. B. Hoogmoed, and O. S. P. Spaargaren, “Spectral reflectance based indices for soil organic carbon quantification,” *Geoderma*, vol. 145, no. 1-2, pp. 28–36, 2008.
 - [12] D. J. Brown, R. S. Brickley, and P. R. Miller, “Validation requirements for diffuse reflectance soil characterization models with a case study of VNIR soil C prediction in Montana,” *Geoderma*, vol. 129, no. 3-4, pp. 251–267, 2005.
 - [13] C. W. Chang, D. A. Laird, and C. R. Hurburgh, “Influence of soil moisture on near-infrared reflectance spectroscopic measurement of soil properties,” *Soil Science*, vol. 170, no. 4, pp. 244–255, 2005.
 - [14] G. W. McCarty, J. B. Reeves, V. B. Reeves, R. F. Follett, and J. M. Kimble, “Mid-infrared and near-infrared diffuse reflectance spectroscopy for soil carbon measurement,” *Soil Science Society of America Journal*, vol. 66, no. 2, pp. 640–646, 2002.
 - [15] G. W. McCarty and J. B. Reeves, “Comparison of near infrared and mid infrared diffuse reflectance spectroscopy for field-scale measurement of soil fertility parameters,” *Soil Science*, vol. 171, no. 2, pp. 94–102, 2006.
 - [16] T. Selige, J. Böhner, and U. Schmidhalter, “High resolution topsoil mapping using hyperspectral image and field data in multivariate regression modeling procedures,” *Geoderma*, vol. 136, no. 1-2, pp. 235–244, 2006.
 - [17] J. Wetterlind, B. Stenberg, and M. Söderström, “Increased sample point density in farm soil mapping by local calibration of visible and near infrared prediction models,” *Geoderma*, vol. 156, no. 3-4, pp. 152–160, 2010.
 - [18] C. W. Chang, D. A. Laird, M. J. Mausbach, and C. R. Hurburgh, “Near-infrared reflectance spectroscopy—principal components regression analyses of soil properties,” *Soil Science Society of America Journal*, vol. 65, no. 2, pp. 480–490, 2001.
 - [19] E. Ben-Dor, S. Chabrilat, J. A. M. Demattè et al., “Using imaging spectroscopy to study soil properties,” *Remote Sensing of Environment*, vol. 113, no. 1, pp. 538–555, 2009.
 - [20] G. M. Vasques, S. Grunwald, and J. O. Sickman, “Comparison of multivariate methods for inferential modeling of soil carbon using visible/near-infrared spectra,” *Geoderma*, vol. 146, no. 1-2, pp. 14–25, 2008.
 - [21] C. Guerrero, R. Zornoza, I. Gómez, and J. Mataix-Beneyto, “Spiking of NIR regional models using samples from target sites: effect of model size on prediction accuracy,” *Geoderma*, vol. 158, no. 1-2, pp. 66–77, 2010.
 - [22] C. Gomez, R. A. Viscarra, and A. B. McBratney, “Soil organic carbon prediction by hyperspectral remote sensing and field vis-NIR spectroscopy: an Australian case study,” *Geoderma*, vol. 146, pp. 403–411, 2008.
 - [23] J. B. Reeves and S. R. Delwiche, “SAS partial least squares regression for analysis of spectroscopic data,” *Journal of Near Infrared Spectroscopy*, vol. 11, no. 6, pp. 415–431, 2003.
 - [24] “ASTM International. Standard practices for infrared multivariate quantitative analysis,” E 1655-05, ASTM International, West Conshohocken, Pa, USA, 2005.
 - [25] G. W. Gee and J. W. Bauder, “Particle Size Analysis,” in *Methods of Soil Analysis, Part 1: Physical and Mineralogical Methods*, A. Klute, Ed., pp. 404–408, American Society of Agronomy, Madison, Wisconsin, USA, 2nd edition, 1986.
 - [26] A. Mehlich, “Mehlich 3 soil test extractant: a modification of Mehlich 2 extractant,” *Communications in Soil Science and Plant Analysis*, vol. 15, no. 12, pp. 1409–1416, 1984.
 - [27] C. M. Jengo and J. LaVeigne, “Sensor performance comparison of hyperspecTIR instruments 1 and 2,” in *Proceedings of IEEE Aerospace Conference*, pp. 1799–1805, March 2004.
 - [28] G. W. McCarty, W. D. Hively, J. B. Reeves, M. Lang, E. Lund, and O. Weatherbee, “Infrared sensors to map soil carbon in agricultural ecosystems,” in *Proximal Soil Sensing*, R. A. Viscarra Rossel, Ed., vol. 1 of *Progress in Soil Science*, pp. 165–176, Springer, 2010.
 - [29] B. Stenberg and R. A. Viscarra Rossel, “Diffuse reflectance spectroscopy for high-resolution soil sensing,” in *Proximal Soil Sensing*, R. A. Viscarra Rossel, A. M. McBratney, and B. Minasny, Eds., *Progress in Soil Science Book Series*, Chapter 3, Springer, New York, NY, USA, 2010.
 - [30] W. Schwanghart and T. Jarmer, “Linking spatial patterns of soil organic carbon to topography—a case study from south-eastern Spain,” *Geomorphology*, vol. 126, pp. 252–263, 2011.
 - [31] C. Y. Wu, A. R. Jacobson, M. Laba, and P. Baveye, “Alleviating moisture content effects on the visible near-infrared diffuse-reflectance sensing of soils,” *Soil Science*, vol. 174, no. 8, pp. 456–465, 2009.
 - [32] C. Tucker, “Red and photographic infrared linear combinations for monitoring vegetation,” *Remote Sensing of Environment*, vol. 8, no. 2, pp. 127–150, 1979.
 - [33] G. Serbin, C. S. T. Daughtry, E. R. Hunt, J. B. Reeves, and D. J. Brown, “Effects of soil composition and mineralogy on remote sensing of crop residue cover,” *Remote Sensing of Environment*, vol. 113, no. 1, pp. 224–238, 2009.

Research Article

Relationships between GPP, Satellite Measures of Greenness and Canopy Water Content with Soil Moisture in Mediterranean-Climate Grassland and Oak Savanna

Shishi Liu, Oliver A. Chadwick, Dar A. Roberts, and Chris J. Still

Department of Geography, University of California, Santa Barbara 93106, USA

Correspondence should be addressed to Shishi Liu, shishi@umail.ucsb.edu

Received 11 November 2010; Revised 7 March 2011; Accepted 5 April 2011

Academic Editor: Mehrez Zribi

Copyright © 2011 Shishi Liu et al. This is an open access article distributed under the Creative Commons Attribution License, which permits unrestricted use, distribution, and reproduction in any medium, provided the original work is properly cited.

We investigated the impact of soil moisture on gross primary production (GPP), chlorophyll content, and canopy water content represented by remotely sensed vegetation indices (VIs) in an open grassland and an oak savanna in California. We found for the annual grassland that GPP late in the growing season was controlled by the declining soil moisture, but there was a 10–20-day lag in the response of GPP to soil moisture. However, during the early and middle part of the growing season, solar radiation accounted for most of the variation in GPP. In the oak savanna, the grass understory exhibited a similar response, but oak trees were not sensitive to soil moisture in the upper 50 cm of the soil profile. Furthermore, while we found most VIs to be more or less related to soil moisture, the Visible Atmospherically Resistance Index (VARI) was the most sensitive to the change of soil moisture.

1. Introduction

Plant-available soil moisture is a key element in ecosystem functioning, since it links energy balance and hydrological cycles, contributes to vegetation composition and richness, and impacts productivity. California's Mediterranean climate is characterized by highly variable winter precipitation and prolonged summer drought, and its vegetation communities are strongly affected by the availability of water, resulting in pronounced annual cycles of growth and senescence [1]. For example, the growing season of annual grasslands typically begins in the wet and cool winter after major rain events and extends to the late spring supported by a declining supply of soil moisture. Given the nature of the hydroclimate regime in California, understanding the response of different plant functional types to soil water availability should be a primary objective of any advanced natural resource management system.

Semiarid savanna in California, which is composed of widely spaced trees, understory grasses, and forbs, is a common land cover type in California. It has been hypothesized that trees and grasses are able to coexist because of either their differences in resource-acquisition potentials or

differences in demographic mechanisms, under such disturbances as fires and grazing [2–4]. In general, spatial niche separation in root distributions appears to be more prevalent in arid systems [5], and plant-available moisture, rather than nutrients, may be the main resource limiting plant growth in savannas [6, 7]. Regardless of the ultimate controls on savanna structure, trees and grasses compete for available soil water, and although grasses are typically superior competitors for water in the upper horizons owing to their relatively shallow and dense root systems, trees are thought to persist because of exclusive access to deeper water [2]. The exchange of carbon dioxide (CO₂) and water vapor between the atmosphere and plants is controlled in most plants through the opening of stomata, which is driven by a number of environmental factors including the amount of water in soil [8]. The photosynthetic rate will decrease as plants receive the signal of water stress through osmotic adjustment [9]. Deficiencies of water have also been shown to adversely affect chlorophyll production and canopy water content in some plants [10], but not adversely impact chlorophyll production in others [11, 12]. The correlation between photosynthesis, chlorophyll content and canopy water content with soil moisture therefore varies among

different types of vegetation. In this study, we investigated the responses of different plant functional types to soil moisture dynamics within California's semiarid oak savanna. Vegetation responses may include many aspects, but here we focused on: (1) CO₂ assimilation, as measured by leaf CO₂ exchanges, and (2) greenness and canopy water content, as represented by remote sensing vegetation indices (VIs).

There have been many studies of the controls of environmental variables, particularly precipitation, on CO₂ exchanges in forests, savannas, and grasslands [13–19]. Many long-term carbon flux studies have concluded that precipitation has a great impact on the interannual variability of primary production, but have often ignored the fact that precipitation is not equal to water available to vegetation. Plant-available soil moisture depends not only on the amount and the timing of precipitation, but also on the hydrological and physical properties of soil. However, few studies have concentrated on analyzing the impact of soil moisture on productivity of vegetation, mainly due to the scarcity of soil moisture data. Knapp et al. [20] evaluated landscape variability in soil-water-plant relations and net primary production (NPP) in tall grass prairie and found that NPP was linearly related with soil water content along two transects ($R^2 = 0.66$). Reynolds et al. [21] studied the relationship between rainfall, soil moisture and plant responses, and their results suggested that productivity in deserts did not respond to rainfall events directly but to available soil moisture. Although Xu and Baldocchi's [17] study stated that leaf area index (LAI) explained over 84% of the variance in gross primary production (GPP) in the Mediterranean annual grassland and the remaining 16% was attributed to some combinations of vapor pressure deficit (VPD), temperature, radiation, and soil moisture, the direct impact of soil moisture on GPP was not explored. Therefore, it is essential to investigate the relationship between GPP and soil moisture for arid and semiarid ecosystems dominated by different plant functional types on both seasonal and interannual timescales.

Soil moisture dynamics not only affect a plant's carbon assimilation, but also impact canopy properties (such as leaf area, leaf water content, and greenness) through stomatal control and biochemical control [22, 23], resulting in variability in vegetation spectral signatures. Although microwave remote sensing has demonstrated the capability for measuring soil moisture [24–26], it is difficult to evaluate how vegetation responds to the change of soil moisture using microwave remote sensing techniques, because vegetation is semitransparent in the spectral region. VIs, derived from optical remote sensing reflectance data, have proven to qualitatively and quantitatively respond to vegetation properties, including chlorophyll content [26–28] and canopy water content [29, 30]. Because of their sensitivity to changes in vegetation properties, VIs have been related with soil moisture either to estimate soil moisture or to evaluate the extent of water stress. For example, Farrar et al. [31] showed that the Normalized Difference Vegetation Index (NDVI) varied with soil moisture in a concurrent month in southern African savannas. Dennison et al. [32] found a significant nonlinear relationship between soil water availability and

equivalent water thickness (EWT) derived from Airborne Visible/Infrared Imaging Spectrometer (AVIRIS) for different vegetation types. While EWT is not a vegetation index, it is highly responsive to changes in leaf area [33]. Studies in the US Corn Belt have also shown a linear relationship between NDVI and soil moisture [34, 35]. In particular, Adegoke and Carleton [34] found that vegetation indices lagged up to 8 weeks behind soil moisture. In addition, remotely sensed vegetation indices together with surface radiant temperature have also been used to estimate surface soil moisture [36–38]. These results provide evidence that vegetation indices are responsive to soil moisture variations in arid and semiarid areas, but the relationship between vegetation indices and soil moisture is modified by temperature and soil properties. As Rodriguez-Iturbe [39] stated in the vision of the future water resources research “satellite measurements provide us with a wealth of information about the spatiotemporal evolution of vegetation at different scales and under different climatic conditions. Much research needs to be carried out in the development of models which effectively represent the space-time dynamic interaction between climate, soil, and vegetation, especially in water-controlled ecosystem.”

In this study, to explore vegetation responses to changes in soil moisture, we evaluated the relationship between soil moisture and GPP, and remotely sensed measures of greenness and canopy water content in a Mediterranean-climate annual grassland and an oak savanna. Specifically, we addressed the following questions.

- (1) How does GPP respond to seasonal soil moisture fluctuations in annual grassland and oak savanna in California? Is soil moisture the major factor determining seasonal variability of GPP for these grassland and oak savanna?
- (2) What is the relationship between MODIS-derived VIs and field-measured soil moisture in Mediterranean-climate grassland and oak savanna? Which index is the most sensitive to the change of soil moisture?

2. Data and Methods

2.1. Site Information. We used data from two AmeriFlux sites located in the foothills of the Sierra Nevada in California. One site (Vaira Ranch) is located in an annual open grassland ecosystem, and the other site (Tonzi Ranch) is an oak/grass savanna, 3 km away from the open grassland in Vaira Ranch. Deciduous blue oaks (*Quercus douglasii*) dominate the savanna site, and oak trees cover about 40% of the landscape within a square kilometer of the flux tower. The vegetation under the oak trees and in the open grassland is comprised of cool-season C3 annual nonnative species, including *Brachypodium distachyon* L., *Hypochaeris glabra* L., *Trifolium dubium* Sibth., *Trifolium hirtum* All., *Dichelostemma volubile* A., and *Erodium botrys* Cav [40]. The climate is Mediterranean with high temperatures, low relative humidity, and no rain in summer, but cool and wet winters. Precipitation is concentrated between October and May, with the mean monthly precipitation ranging from 30 mm to 100 mm and the mean annual precipitation about

559 mm. Detailed descriptions about these two sites have been presented in Xu et al. [41], Baldocchi et al. [42], and Ma et al. [40]. The soil in the open grassland site is an Exchequer very rocky silt loam (Lithic Xerorthents), with 30% sand, 57% silt, and 13% clay [39]. At the oak savanna site, the soil is classified as Auburn very rock silt loam (Lithic Haploxerepts). It contains 43% sand, 43% silt, and 13% clay [38].

2.2. Data. CO₂ and water vapor fluxes were measured at a 30 min interval using eddy covariance systems. At the savanna site, the CO₂ flux was measured both in the understory (2 m above the ground) and overstory (23 m above the ground). It is assumed that the overstory tower collected CO₂ flux from both oak trees and grasses, while the understory tower primarily measured flux from grassland. GPP was computed by subtracting ecosystem respiration from net carbon exchange, in which ecosystem respiration was derived from nighttime measurements of net ecosystem carbon exchange using flux partitioning methods described by Xu and Baldocchi [17].

Standard meteorological and soil parameters were measured continuously with an array of sensors. Volumetric soil water content was measured with frequency domain reflectometry sensors, which were placed vertically at depths of 5, 10, and 20 cm for the open grassland site and 5, 20, and 50 cm for the oak savanna site. LAI of the herbaceous vegetation was measured periodically using destructive sampling methods at intervals of 2–4 weeks [17]. Meteorological data used in this study included precipitation, photosynthetically active radiation (PAR), air temperature, and VPD. At the oak savanna site, PAR, air temperature, and VPD were measured in both the understory and overstory. Phenological dates of the beginning and the end of growing season were based on the data provided by Ma et al. [40]. Details about the experiment, instruments, data processing, and data quality have been presented by Flanagan et al. [16] and Baldocchi et al. [42].

A composite MODIS time series at 500 m spatial resolution developed at UC Santa Barbara [43] was analyzed from 2002 to 2006. These data have a 16-day compositing period and preserve the original seven MODIS 500 m resolution bands while selecting for the pixel within each compositing period that is the most stable for spectral shape and brightness, thereby minimizing the adverse impacts of clouds, aerosols, and the changing viewing geometry on MODIS spectra. Four vegetation indices that are sensitive to chlorophyll content and canopy water content were calculated based on reflectance data, including the Normalized Difference Vegetation Index (NDVI: [44]), the Visible Atmospherically Resistance Index (VARI: [45]), the Normalized Difference Water Index (NDWI: [46]), and the Shortwave Angle Slope Index (SASI: [47]).

2.3. Methods. In our analyses, half hourly measured air temperature, volumetric soil water content, and VPD were averaged during the daytime when PAR exceeded 10 $\mu\text{mol}/\text{m}^2/\text{s}$, and the measurements of PAR, GPP, and precipitation were

accumulated by day for both sites. Soil water content at 10 cm and 20 cm was utilized in the analyses of grassland, and soil water content at 20 cm and 50 cm was used for the oak tree analyses. We chose soil moisture at a certain depth instead of the average of soil water content at three depths because the difference, in terms of comparing the values, between these two approaches was minimal.

For analyzing relationships between vegetation indices and soil moisture, soil moisture was extracted on the same day as the selected MODIS pixel and it was also averaged within the 16-day period. Vegetation indices were calculated based on the reflectance of the day when the image was taken; detailed information about NDVI, VARI, NDWI, and SASI are presented below.

NDVI is calculated as

$$\text{NDVI} = \frac{(R_{\text{NIR}} - R_{\text{red}})}{(R_{\text{NIR}} + R_{\text{red}})}, \quad (1)$$

where R_{NIR} and R_{red} represent the reflectance of near infrared and red wavelengths, respectively. NDVI is the most extensively used VI, a good indicator of canopy structure, green biomass, green LAI, and chlorophyll content [48]. However, it is well documented that NDVI saturates at high LAI values and it is also affected by other factors such as soil background, canopy shadows, illumination, and atmospheric conditions [48, 49]. Unlike NDVI, VARI utilizes the difference between green reflectance and red reflectance in response to changes in chlorophyll, and therefore VARI is sensitive to variations of green vegetation fraction, with correction of atmosphere effect. VARI is calculated as

$$\text{VARI} = \frac{(R_{\text{green}} - R_{\text{red}})}{(R_{\text{green}} + R_{\text{red}} - R_{\text{blue}})}. \quad (2)$$

NDWI replaces the red band in the NDVI with the 1240 nm shortwave infrared (SWIR) band, in order to maximize the spectral expression of water in leaves and to take advantage of high near-infrared reflectance of vegetations and soils. Thus NDWI responds to changes in the water content of a vegetation canopy. It is calculated as

$$\text{NDWI} = \frac{(R_{\text{NIR}} - R_{\text{SWIR}})}{(R_{\text{NIR}} + R_{\text{SWIR}})}, \quad (3)$$

where R_{NIR} and R_{SWIR} represent reflectance of near infrared and SWIR, respectively.

Whiting et al. [50] demonstrated that the SWIR region could be fitted by an inverted Gaussian function that is highly correlated to moisture content in soils. SASI simulates the general shape of this part of the spectrum, calculated as product of the angle at the SWIR1 (at 1240 nm) of MODIS data and the difference of the reflectance at NIR and the SWIR2 (at 1640 nm):

$$\beta = \cos^{-1} \left(\frac{a^2 + b^2 - c^2}{2 * a * b} \right) \quad \text{radians}, \quad (4)$$

$$\text{Slope} = \text{SWIR2} - \text{NIR},$$

$$\text{SASI} = \beta * \text{Slope},$$

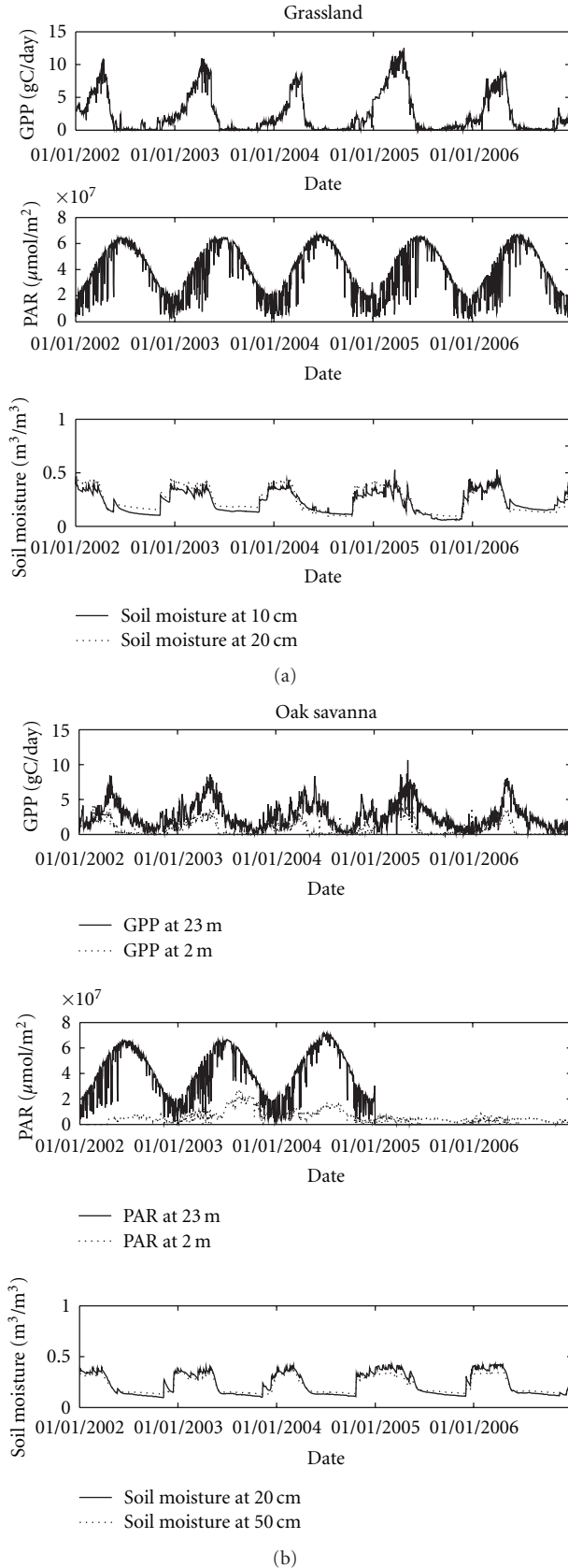


FIGURE 1: Time series of GPP (gC/day), PAR ($\mu\text{mol}/\text{m}^2$), and daily soil moisture (m^3/m^3) at two different depths in the open grassland (a) and the oak savanna (b).

where a , b , and c are the Euclidian distances between NIR and SWIR1, SWIR1 and SWIR2, and SWIR2 and NIR. Since SASI is based on the SWIR region, it is sensitive to moisture and not photosynthetic activity, revealing different dynamics from NDVI. High positive values characterize dry soils, and high negative values characterize healthy vegetation, while, for the case of plant dry matter, SASI approaches zero [51].

We performed all statistical calculations with MATLAB 7.1. For regression analysis, we used the least-square method, and the probability of significance (P value) was determined at the significance level of .01. The significance of the correlation between two variables was evaluated using the Pearson correlation coefficient (r) and the coefficient of determination of linear regressions (R^2).

3. Results

3.1. GPP and Soil Moisture in the Grassland and Oak Savanna

3.1.1. In the Open Grassland. To understand the environmental conditions and the impact of soil moisture on GPP in the open grassland, time series of daily GPP, PAR, and volumetric soil moisture from 2002 to 2006 are shown in Figure 1(a). The invasive grasses at this site typically germinate a week after an autumn rainstorm with total precipitation of at least 15 mm [17]. At the beginning of the growing season, soil-water resources were sufficient, but the temperature was low and PAR was limited, so the grasses grew slowly, leading to a slow, steady increase in GPP. In the spring, warmer temperature, longer day length, and ample soil moisture contributed to the fast growth of grasses and GPP reached its peak in March or April. Grasses usually maintained peak GPP for a short time of one to two weeks, and then following the rapid decline in soil moisture and an increase in air temperature after peak, GPP declined to zero within two months.

Although grasses respond to increased soil moisture, our analysis shows that, at the beginning of the winter growing season, well before GPP reached its peak, grass growth was not controlled by soil water availability. The relationship between GPP and soil moisture at both depths was negative and weak. This is because the frequent winter precipitation and low evapotranspiration rate at this time led to sufficient soil water, but the low PAR and low air temperature limited photosynthesis, resulting in slow growth and low water demand. However, the soil dry-down curve did coincide with declining grass GPP (Figure 2). Both soil moisture and GPP decreased to a steady state within two months, but the decrease of soil moisture occurred earlier than GPP. Therefore, we assessed the correlation between GPP and lagged soil moisture for each year when they were decreasing. Interestingly, there was a significant linear relationship between GPP and soil moisture lagged by 10 to 20 days in the open grassland site. And the relationship was stronger for soil moisture at 10 cm than for soil moisture at 20 cm. The lag time was determined based on the maximum correlation coefficients between GPP and lagged soil moisture. Table 1(a) shows the lag between

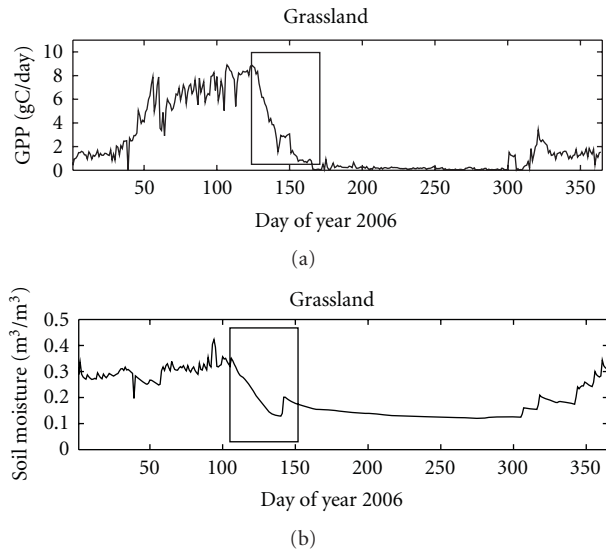


FIGURE 2: An example of decreasing GPP in agreement with declining soil moisture. Seasonal variation in GPP and soil moisture at 10 cm in 2006, the highlighted part showing the declines in GPP and soil moisture.

GPP and soil moisture at 10 cm, the regression models, and statistics for the open grassland site.

Autumn rainfall determined the timing of grassland greenup, and frequent rainfall in the spring maintained ample moisture in the soil, ensuring the steady growth of grasses. Years 2002, 2003, and 2006 had moderate amounts of precipitation. We found a significant linear relationship between GPP and a roughly 20-day lagged soil moisture in these three years in the open grassland, indicating the declining rate of grassland productivity was controlled by the dry-down rate of the soil. The small slope of the linear relationship in 2003 was caused by the abrupt drop of GPP on day 136, from 8.89 gC/day to 3.67 gC/day, and GPP stayed below 4 gC/day after the drop. This decrease in GPP was probably caused by an increase in the daytime mean air temperature from 17.7°C on day 135 to 19.5°C on day 136, which led to an increase in VPD. Year 2004 experienced much less precipitation and a longer drought period. The early decrease of soil moisture resulted in a shortened growing season and low annual GPP. Year 2005 was very wet, and the soil maintained high soil water content until the end of May, resulting in a lengthy period of elevated GPP. In 2006, daily GPP in the growing season was less than the other years, with a maximum of 8.9 gC/day, while in the other years, except in 2004, daily GPP was as high as 10.5 gC/day in April. Continuous hot and dry weather following the day when GPP reached its peak of 8.9 gC/day was the main reason that caused the quick decrease of soil moisture as well as GPP. Smaller magnitudes of GPP during the growing season resulted in the smaller slope values in the linear relationship for 2006.

3.1.2. In the Oak Savanna. Environmental conditions in the grassland under the canopy of oak trees are different from

the open grassland, primarily because the canopy modifies PAR, air temperature, and VPD (Figure 1). For example, the average annual cumulative PAR beneath the canopy was only 10%–30% of the values in the open grassland. The comparison between soil moisture in open grassland and soil moisture measured under oak trees at the same depth suggests that soil in oak savanna had higher water holding capacity and higher wilting point. The lower GPP in grasses under oak canopies was mainly caused by reduced PAR due to shading, which in turn reduced the photosynthetic rates of grasses. The reduced PAR under the oak canopy substantially limited the extension of leaves as well as photosynthetic activities.

The relationship between declining GPP and lagged soil moisture at the end of spring was still observed in grasses under the oak canopy, but it was less pronounced (Table 1(b)). The lag with the highest correlation between GPP and soil moisture ranged from 5 days in 2003 to 22 days in 2002, differing slightly from the open grassland. This difference was likely caused by the modified radiation and air temperature environment under the tree canopy. It is also likely that the oak trees impacted soil water in ways that affected below-canopy grasses, such as by hydraulic redistribution [52].

The comparison of seasonal variations in oak tree canopy GPP against 50 cm soil moisture suggests that oak GPP is not controlled by soil water availability in the upper soil horizons. Oak trees in the savanna started to develop leaves in March when soil moisture and light were ample and air temperature was increasing. The leaf expansion stage overlapped with vigorous growth of grasses. Peak oak canopy GPP was achieved in May while the moisture in shallow soil was depleted and the understory grasses were senescing. A substantial portion of the growing season lacked any precipitation and the trees retained leaves for several months until winter arrived. The weak relationship between oak GPP and soil water content in the upper horizons is supported by the findings of others that trees are able to store water and nutrients and to tap water from deeper soil horizons [53, 54]. The cumulative GPP in the growing season of oak trees for each year did not change much even in the very dry year, indicating that the growth of oak trees is not prone to the short-term environmental changes, presumably due to its very deep root system and possibly some internal storage capability.

3.2. Vegetation Indices and Soil Moisture. In this section, we investigate the impact of soil-moisture fluctuations on the canopy chlorophyll content and water content as represented by different vegetation indices derived from MODIS data. Figure 3 shows the time series of indices and soil moisture at 20 cm at both sites. NDVI, VARI, and NDWI showed similar responses to the changing soil moisture over the five-year period, while SASI responded in an opposite way. However, changes in the indices were not in phase with the change of soil moisture, similar to the GPP response to the declining soil moisture. At the beginning and the middle part of the growing season (before GPP and VIs decreased), NDVI, VARI, and NDWI were low (SASI was high) and started

TABLE 1: Regression models and statistics of relationships between GPP and lagged volumetric soil moisture at 10 cm in open grassland (θ_{10}) and at 20 cm in oak savanna (θ_{20}). All the relationships are significant at the 99% level.

(a) Open grassland				
Year	Lag (day)	Period	Regression models	R^2
2002	18	84–125	$GPP = -4.293 + 44.217 * \theta_{10}$	0.94
2003	15	121–150	$GPP = -1.0791 + 17.161 * \theta_{10}$	0.92
2004	24	63–101	$GPP = -5.303 + 42.952 * \theta_{10}$	0.73
2005	25	92–129	$GPP = -4.663 + 47.295 * \theta_{10}$	0.78
2006	20	96–136	$GPP = -3.070 + 35.811 * \theta_{10}$	0.92

(b) Oak savanna				
Year	Lag (day)	Period	Regression models	R^2
2002	22	84–125	$GPP = -2.16 + 0.14 * \theta_{20}$	0.79
2003	5	131–151	$GPP = -1.14 + 0.11 * \theta_{20}$	0.60
2004	20	69–92	$GPP = -1.98 + 0.12 * \theta_{20}$	0.52
2005	22	128–156	$GPP = -0.56 + 0.1 * \theta_{20}$	0.34
2006	20	126–150	$GPP = -1.47 + 0.1822 * \theta_{20}$	0.87

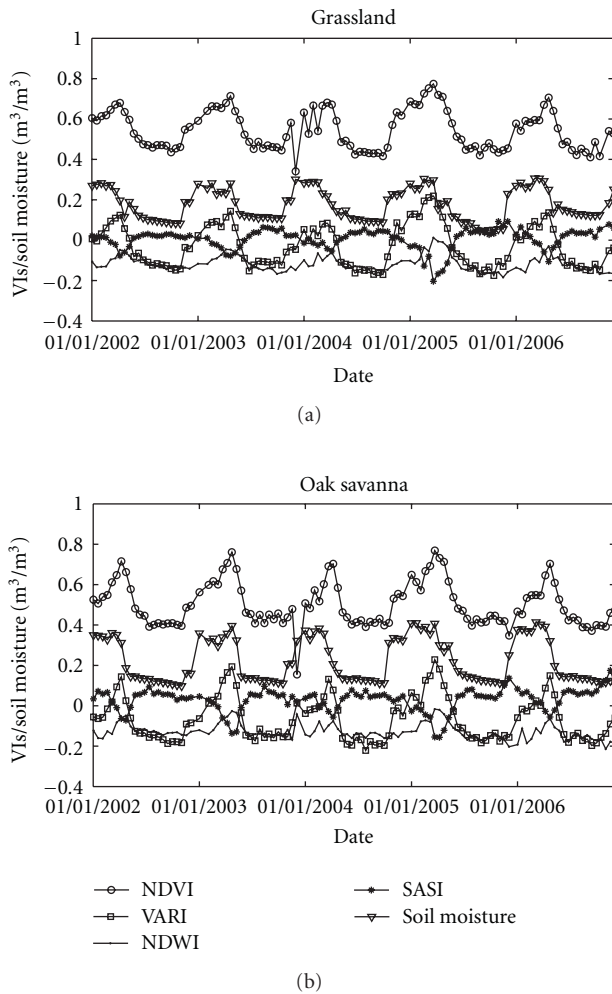


FIGURE 3: Time series of NDVI, VARI, NDWI, SASI, and soil moisture at 10 cm in the open grassland (a) and at 20 cm in the oak savanna (b).

to increase (SASI started to decrease) when soil moisture became sufficient. NDVI, VARI, and NDWI began to decline (SASI began to increase) after soil moisture started to drop in the spring. To analyze relationships between four vegetation indices and soil moisture, we evaluated Pearson correlation coefficients (r) between these indices and soil moisture at different depths extracted on the exact day selected for the composite and averaged over the 16-day compositing period (Table 2). The results demonstrate that the four indices are more or less related to soil moisture. Overall, VARI had the strongest relationship at both sites, and VARI increased as soil moisture increased during the five-year study period. The weaker relationships between NDWI/SASI and soil moisture were surprising as one would expect NDWI and SASI to be more responsive to the change of soil moisture because of their sensitivity to the leaf water content. In the open grassland, the relationship was marginally stronger with averaged soil moisture at 10 cm compared to 20 cm; in the oak savanna, the relationship was slightly stronger with soil moisture at 20 cm.

Interestingly, the curve of the relationship between VARI and 16-day average soil moisture was slightly different in the open grassland and oak savanna site, although at both sites, the relationship can be fitted with a quadratic polynomial statistical function (Figure 4). The relationship in the open grassland was clear and nearly linear, but in the oak savanna, the relationship is more scattered and VARI tends to drop at high soil water content. VARI in the oak savanna site was more variable (variance is 0.21) than it was in the open grassland (variance is 0.14). VARI changed dramatically in the middle of the growing season of grasses. This is probably because the growing season of Blue Oaks starts later than the grasses in the oak savanna, which may cause the abrupt increase in vegetation indices during the period when trees were greening up and grasses were in the middle of the growing season. In addition, VARI was lower in the oak savanna at the beginning of the growing season when soil

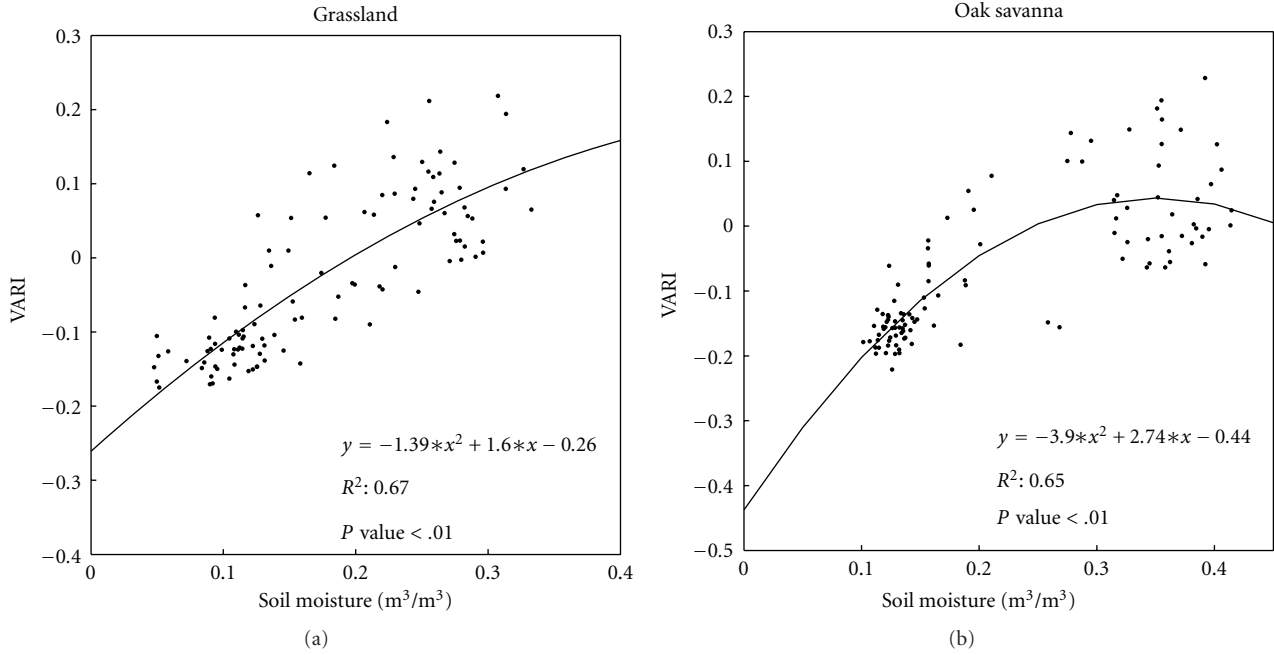


FIGURE 4: The relationship between VARI and averaged soil moisture at 10 cm in open grassland and averaged soil moisture at 20 cm in oak savanna during the same five-year measurement period.

TABLE 2: Correlation coefficients (r) between NDVI, VARI, NDWI, SASI, and instantaneous volumetric soil moisture (θ_{10} and θ_{20}) and 16-day average soil moisture ($\theta_{avg,10}$ and $\theta_{avg,20}$) in the open grassland (a) and oak savanna (b).

(a) Open grassland				
	NDVI	VARI	NDWI	SASI
θ_{10}	0.71	0.81	0.43	-0.45
θ_{20}	0.69	0.79	0.41	-0.43
$\theta_{avg,10}$	0.74	0.82	0.46	-0.48
$\theta_{avg,20}$	0.72	0.80	0.44	-0.46
(b) Oak savanna				
	NDVI	VARI	NDWI	SASI
θ_{20}	0.65	0.79	0.45	-0.50
θ_{50}	0.61	0.74	0.40	-0.44
$\theta_{avg,20}$	0.69	0.78	0.41	-0.49
$\theta_{avg,50}$	0.67	0.74	0.38	-0.45

moisture was sufficient, resulting in a cluster of low VARI at high soil water content. However, further studies about the background effect and the reflectance signature of the oak savanna are needed to explain the variations of vegetation indices in the oak savanna site.

Furthermore, we analyzed the relationships between the indices and soil moisture during the beginning and middle part of the growing season before GPP and VIs began to decrease. We also analyzed the relationships separately during the dry-down and senescence season when soil moisture began to decline and finally became depleted. We

did not find significant relationships between any of the indices and soil moisture during the beginning and middle part of the growing season, which explained the scattered pattern shown in Figure 4 as well as the weak relationship for NDWI and SASI. The analysis during dry-down and senescence period revealed a stronger linear relationship between VARI and averaged soil moisture (Figure 5(a)), suggesting that VARI can quantify the change of soil moisture via the change in chlorophyll content when plants are subject to water stress.

Since GPP was linearly related with lagged soil moisture during the dry-down season in the grassland, we evaluated the relationship between the vegetation indices and soil moisture lagged by 0 to 30 days during the dry-down season. A stronger linear relationship between VARI and 17–22-day lagged soil moisture was observed in the open grassland (Figure 6(a)). This result is in agreement with the finding of the strong relationship between GPP and lagged soil moisture from year 2002 to year 2006 during the dry-down season in the open grassland. We also examined the relationship between VIs and soil moisture in the oak savanna during the same dry-down period (Figure 6(b)). Relationships are slightly stronger with 11-day lagged soil moisture. Using lagged soil moisture improved the significance of the relationship between soil moisture and VARI (Figure 5(b)), implying that canopy chlorophyll content is affected by the antecedent soil water status.

The comparison between VARI and NDWI at both sites suggests that the change of NDWI at the beginning of the growing season was slower than the change of VARI. VARI began to increase after the first major autumn rainstorm, which coincided with the phenology data provided by

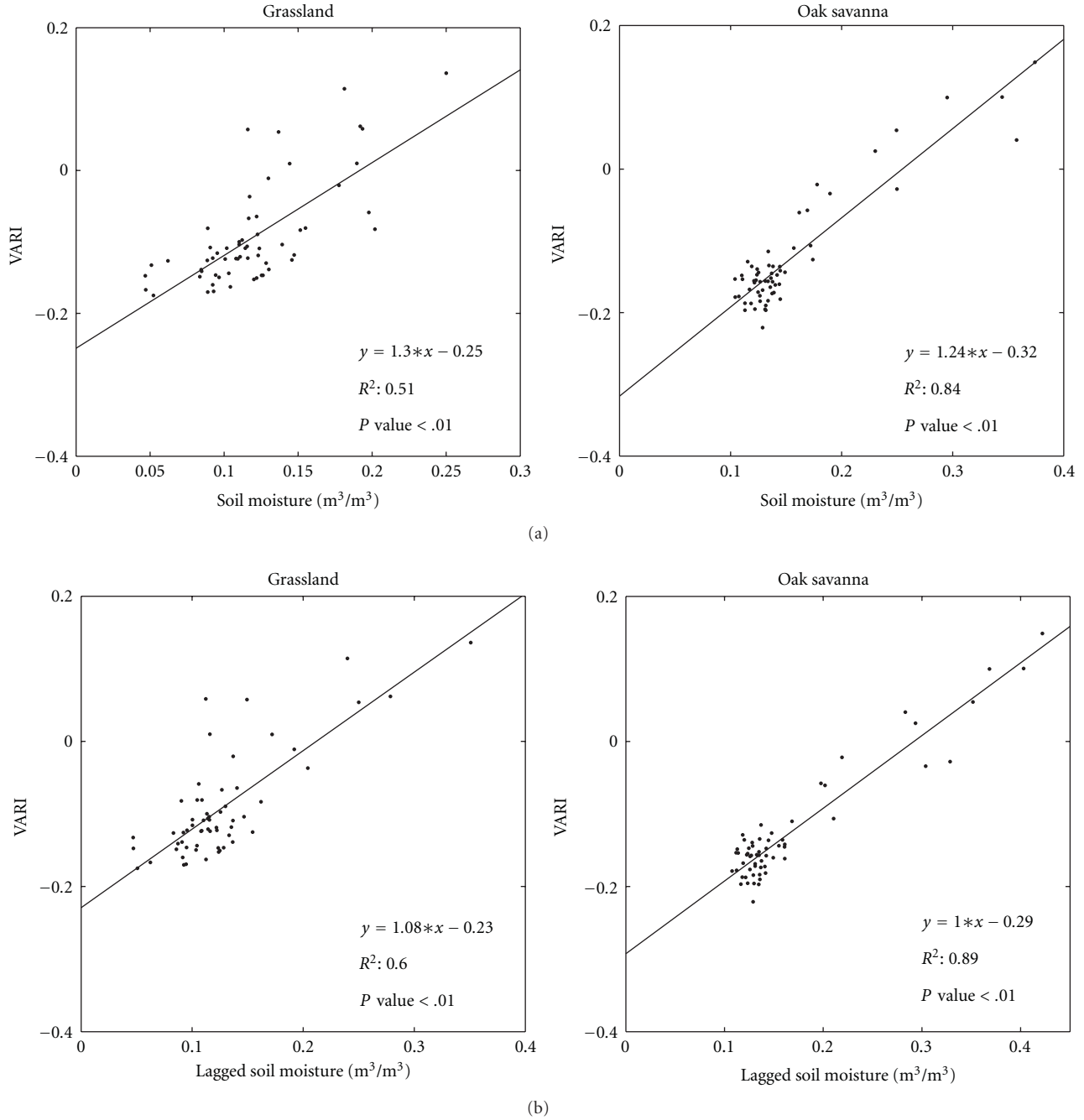


FIGURE 5: The relationships between VARI and averaged soil moisture (a), lagged soil moisture (b) at 10 cm in the open grassland and at 20 cm in the oak savanna during the dry-down and senescence season.

Ma et al. [40], while NDWI did not respond to the change of canopy until January. This explained the significant relationship, particularly in the open grassland, between NDWI and soil moisture during the five-year period.

4. Discussion

4.1. Environmental Controls on GPP. GPP was weakly correlated with soil moisture during the beginning and middle part of the growing season, but was strongly correlated with

soil moisture lagged up to 25 days during the dry-down period. To investigate factors other than soil moisture that controlled GPP, we evaluated the relationships among GPP and PAR, air temperature, precipitation, and VPD by calculating the correlation coefficients (r) in the open grassland and in the grassland under oak canopy. At both sites, PAR and air temperature were strongly correlated with GPP during the beginning and middle part of the growing season before GPP began to decline. However, the regression model between air temperature and GPP was less

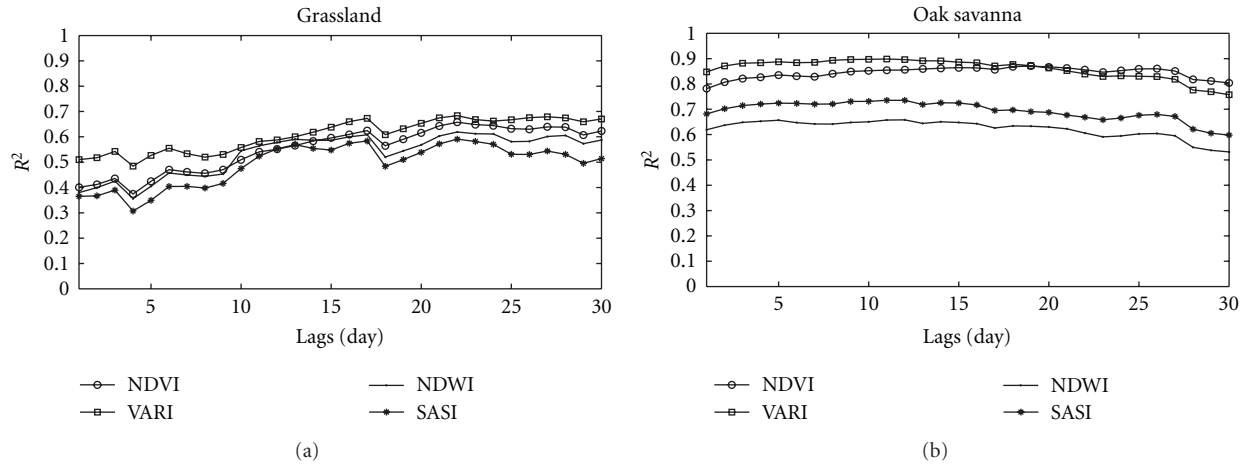


FIGURE 6: The correlation coefficients between VIs and soil moisture lagged up to 30 days at 10 cm in open grassland (a) and at 20 cm in oak savanna (b) during the dry-down and senescence season.

significant in comparison to the correlation between PAR and GPP, indicating the stronger control of PAR on GPP. Figure 7 shows the linear relationship between GPP and PAR during the beginning and middle part of the growing season. Outliers highlighted in Figure 7 revealed the pulses of GPP in response to specific rainfall events when GPP increased abruptly on the sunny day right after the rainfall in the open grassland site.

Grasses responded slowly to the change of soil moisture, in comparison to their responses to VPD. During the late growing season, after GPP reached its peak, VPD was negatively correlated with GPP, explaining from 20% (in 2002) to 57% (in 2004) of the variability in GPP. However, GPP was also observed to decrease because of cool weather, with low temperature and low PAR, even though the precipitation events had occurred several days before and supplied sufficient water.

The impact of environmental variables on the GPP of oak trees was not significant. PAR accounted for only 20% of the variability in GPP in the growing season. At the beginning of the growing season, pulses of GPP in response to specific rainfall events were observed. After the rain stopped, the GPP of oak trees was negatively correlated with air temperature in the dry season, which accounted for 60% of the variability in GPP of oak trees. The impact of VPD on stomatal conductance and thus leaf photosynthesis and GPP was more obvious in the middle of the growing season (between April and July), when water in the soil was becoming limited. During this period, VPD was negatively correlated with GPP, explaining about 40% to 48% percent of the variability of GPP. GPP usually decreased as soon as VPD reached above 2.0 kPa and when air temperature exceeded 19°C.

4.2. The Soil Effect on the Relationships between Vegetation Indices and Soil Moisture. Based on the previous analyses, VIs derived from MODIS data respond to the change in soil moisture, particularly in the open grassland, because a change in soil moisture may induce a change in leaf water

content as well as a change in chlorophyll concentration and leaf internal structure [55]. Factors that may confound the relationship between soil moisture and a change in a VI are the combined impacts of the amount of exposed soil and green vegetation density within the pixel. In an early stage of vegetation development, green LAI is low and exposed soil or senesced plant material may be high. In this case, the change in substrate albedo associated with a change in soil moisture may significantly modify pixel reflectance [56, 57]. At maximum LAI, the amount of exposed soil is low, and VIs would be expected to be the least sensitive to changes in substrate albedo and most sensitive to a change in leaf water content or chlorophyll content. To evaluate a potential impact of exposed soil- and soil-moisture-related changes in substrate albedo, the VI-soil-moisture correlation was analyzed at low LAI (0.4–0.5 for the open grassland and 0.1–0.2 for the grassland under oak canopy at the beginning and the end of the growing season) and at the high LAI (2.0–2.5 for the open grassland and 1.0–1.5 for the grassland under oak canopy). At low LAI, the relationships between VIs and soil moisture were weak, suggesting that soil-moisture-related changes in albedo were minimal on normalized vegetation indices as shown by [57, 58]. In contrast, strong linear relationships between NDVI/VARI and soil moisture were observed at both sites when LAI was high (Figure 8). This result implies that when leaves are fully developed, the chlorophyll content and leaf area are highly sensitive to the change of soil moisture. The linear relationships are more pronounced in open grassland than in oak savanna, where oak trees are not developing in phase with grasses and confounding the reflectance signal.

5. Conclusions

In this paper, we explored the responses of a grassland and an oak savanna to changing soil moisture based on five years of flux tower and meteorological data, along with MODIS imagery for the same period. Analysis of the relationship

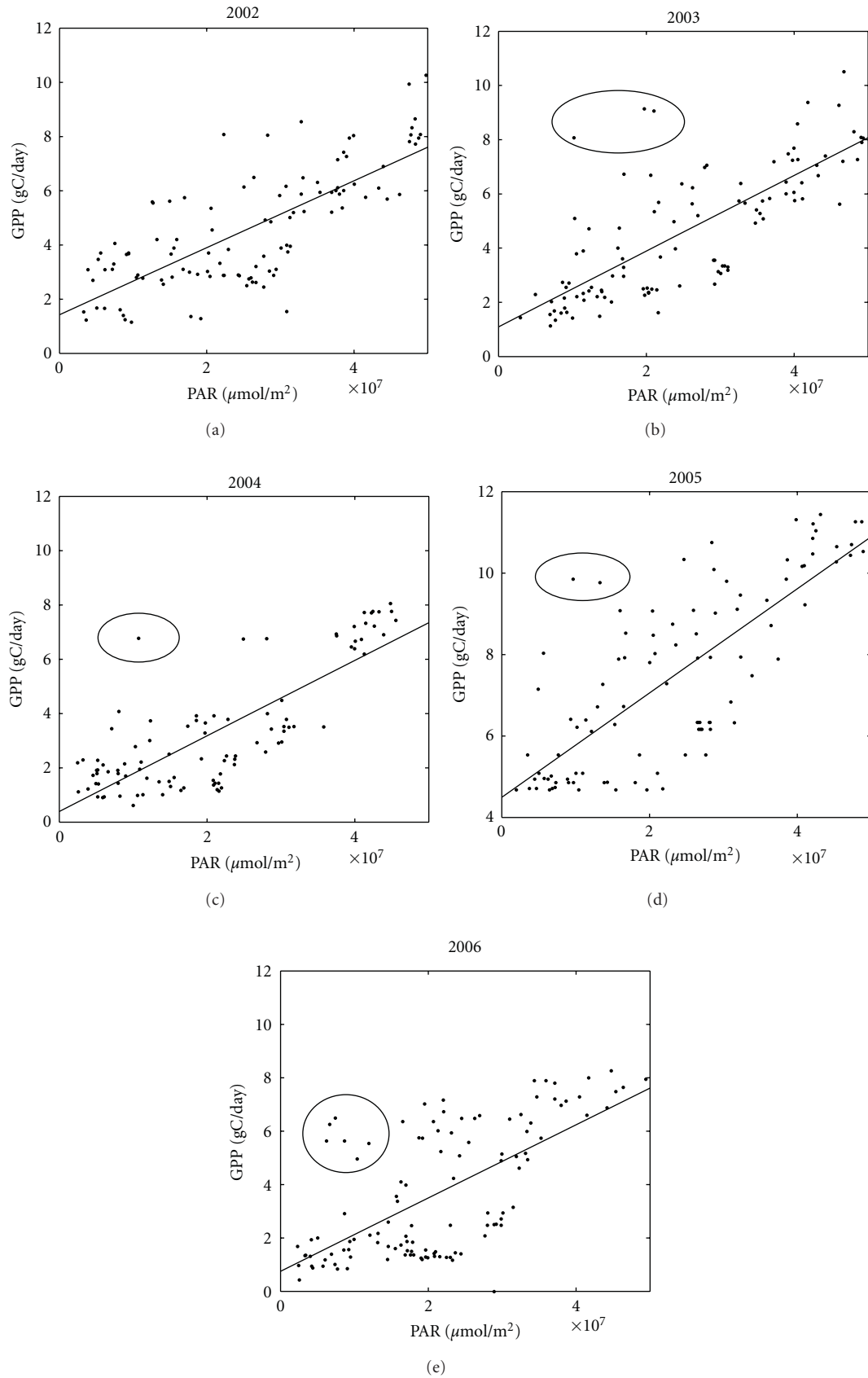


FIGURE 7: The relationship between daily PAR and GPP in the growing season of the open grassland before GPP declined. Pulses due to rain events are highlighted by circles.

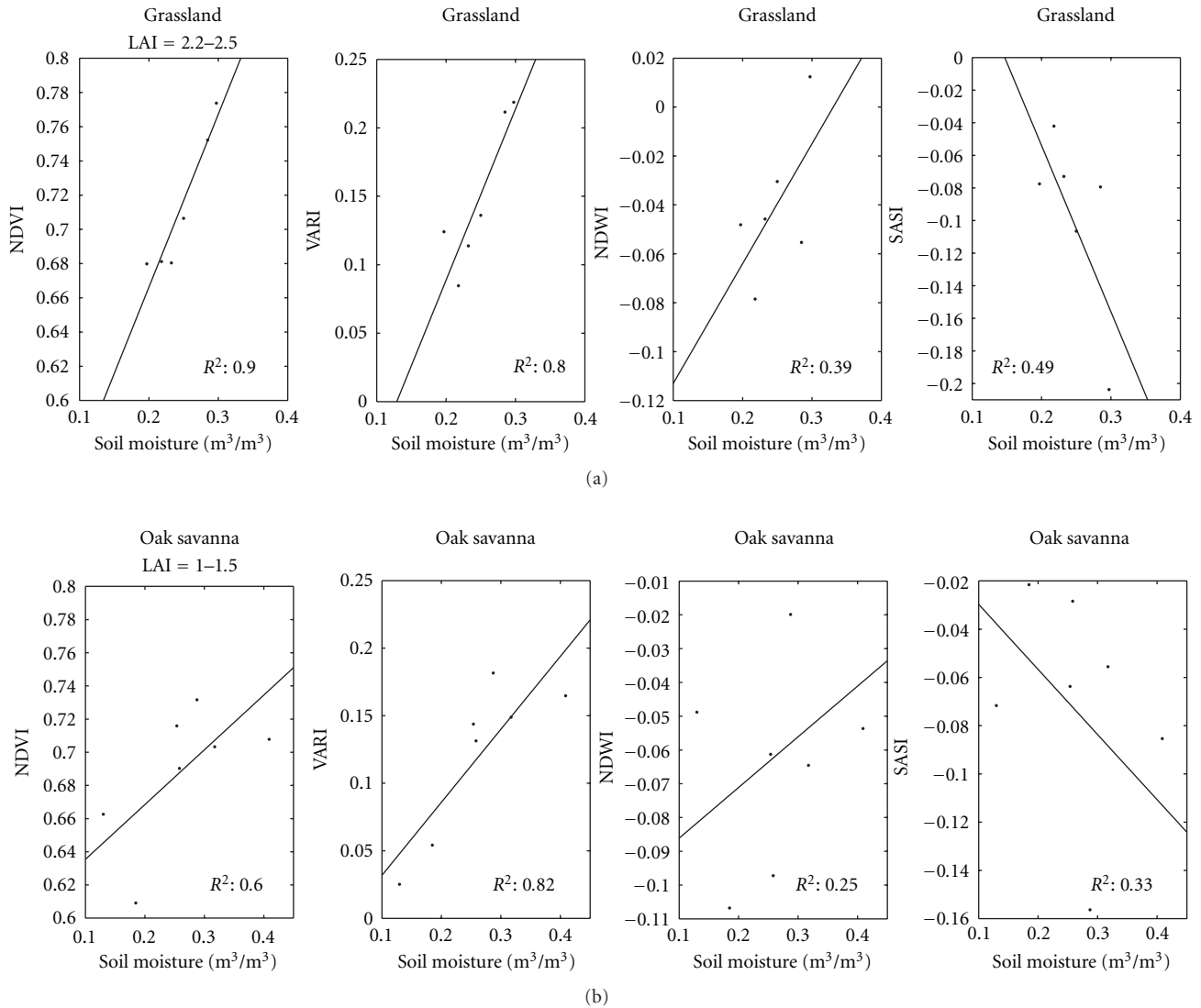


FIGURE 8: Relationships between vegetation indices and averaged soil moisture at 10 cm in the open grassland (a), and at 20 cm in the oak savanna (b) when LAI reached its maximum at each site.

between soil moisture and GPP in open grassland and oak savanna showed that in annual grasslands, the senescence rate of grasses was controlled by the declining rate of soil moisture, but with a 10–20-day lag between GPP and soil moisture. This result implies that GPP during the late growing season is affected by antecedent soil water availability. However, during the beginning and middle part of the growing season, the build-up toward maximum GPP was largely controlled by PAR, which drives photosynthesis, surface sensible and latent heating, and air temperature. Although GPP during the late growing season in understory grasses was still linearly correlated with antecedent soil moisture, the relationship was weaker than in the open grassland. The phenology of the Blue oak canopy is somewhat divorced from the rainfall cycle; this species leafs out in March and senesces in October or November, and thus missing the initial stages of the annual soil moisture recharge while remaining photosynthetically active after the soil dry-down

period. The annual GPP of oak trees did not vary across years, and even in the extreme dry year 2004, the annual oak GPP only decreased 2.1% in comparison to the GPP in prior, normal rainfall year (2003).

To investigate the impact of soil moisture on canopy chlorophyll content and water content, we assessed the relationships between soil moisture and four VIs derived from MODIS imagery. Overall, grass NDVI and VARI had a stronger relationship with soil moisture during the dry-down and senescence season, when the leaf water content and greenness were the most sensitive to changes in soil moisture. Furthermore, as expected, VIs were linearly correlated with lagged soil moisture during the dry-down period. The analysis of the relationship between VIs and soil moisture at low grass LAI value demonstrated that normalized reflectance reduced the soil background effect which resulted from the change of soil water content. However, at the highest LAI value, when grasses are fully developed, chlorophyll

content was highly responsive to the change of soil moisture, leading to strong relationships between NDVI/VARI and soil moisture.

Although this study was based in California, the results should be applicable to other semiarid and arid regions in the world, including warm desert and semidesert, and other Mediterranean-climate areas. These regions are important because of their high plant diversity and, in Mediterranean-climate regions, their high human population density. As climate change may aggravate water stress in these areas, studies focusing on the response of ecosystems to the change of soil water availability are essential for conservation studies and for natural resource management. The combination of flux tower data and remotely sensed data provides a novel strategy for examining the response of vegetation to soil-moisture fluctuations. The clear relationship between MODIS-derived VIs and soil moisture in the open grassland during the dry-down period indicates that remotely sensed data can detect soil water availability in shallowly rooted vegetation during the water-limited period. However, it is difficult to effectively use remotely sensed data to assess the response to soil water availability in ecosystems that are dominated by deeply rooted plants, because deeply rooted plants are less responsive to the short-term change of environmental variables. Within these limitations, it seems clear that incorporation of remotely sensed data in studies of vegetation response to declining soil water availability will expand the range of spatial scales and advance prediction of plant water stress in climate change scenarios.

Acknowledgments

This study was funded by Kearney Foundation of Soil Science, Award no. 2007.037, Modeling Soil Moisture in California at Multiple Scales. The authors are grateful to Dr. Baldocchi and his group for sharing measurements and providing comments on this paper and the VIPER Lab in the Department of Geography at University of California, Santa Barbara for providing MODIS composite images. Finally, they wish to thank two anonymous reviewers for their comments which greatly improved the paper.

References

- [1] J. Major, "California Climate in relation to vegetation," in *Terrestrial Vegetation of California*, M. G. Barbour and J. Major, Eds., pp. 11–74, California Native Plant Society Special Publication 9, 1988.
- [2] H. Walter, *Ecology of Tropical and Subtropical Vegetation*, Oliver and Boyd, Edinburgh, UK, 1971.
- [3] R. J. Scholes and S. R. Archer, "Tree-grass interactions in Savannas," *Annual Review of Ecology and Systematics*, vol. 28, pp. 517–544, 1997.
- [4] A. Kulmatiski, R. J. T. Verweij, K. H. Beard, and E. C. February, "A depth-controlled tracer technique measures vertical, horizontal and temporal patterns of water use by trees and grasses in a subtropical savanna," *New Phytologist*, vol. 188, no. 1, pp. 199–209, 2010.
- [5] H. J. Schenk and R. B. Jackson, "Rooting depths, lateral root spreads and below-ground/above-ground allometries of plants in water-limited ecosystems," *Journal of Ecology*, vol. 90, no. 3, pp. 480–494, 2002.
- [6] B. H. Walker, D. Ludwig, and S. Holling, "Stability of semi-arid savanna grazing systems," *Journal of Ecology*, vol. 69, no. 2, pp. 473–498, 1981.
- [7] F. Van Langevelde, C. A. D. M. Van De Vijver, and L. Kumar, "Effects of fire and herbivory on the stability of savanna ecosystems," *Ecology*, vol. 84, no. 2, pp. 337–350, 2003.
- [8] N. B. Thomas, "The control of stomata by water balance," *New Phytologist*, vol. 168, pp. 275–292, 2005.
- [9] T. C. Hsiao, "Plant responses to water stress," *Annual Review of Plant Physiology*, vol. 24, pp. 519–570, 1973.
- [10] H. K. Lichtenthaler, "Vegetation stress: an introduction to the stress concept in plants," *Plant Physiology*, vol. 148, pp. 4–14, 1996.
- [11] O. E. Sala, W. J. Parton, L. A. Joyce, and W. K. Lauenroth, "Primary production of the central grassland region of the United States," *Ecology*, vol. 69, no. 1, pp. 40–45, 1988.
- [12] C. Körner, *Alpine Plant Life. In Functional Plant Ecology of High Mountain Ecosystems*, Springer, Berlin, Germany, 1999.
- [13] G. Maracci, G. Schmuck, B. Hosgood, and G. Andreoli, "Interpretation of reflectance spectra by plant physiological parameters," in *Proceedings of the International Geoscience and Remote Sensing Symposium (IGARSS '91) Remote Sensing: Global Monitoring for Earth Management*, pp. 2303–2306, Helsinki University of Technology, Espoo, Finland, June 1991.
- [14] J. M. Briggs and A. K. Knapp, "Interannual variability in primary production in tallgrass prairie: climate, soil moisture, topographic position, and fire as determinants of above-ground biomass," *American Journal of Botany*, vol. 82, no. 8, pp. 1024–1030, 1995.
- [15] A. K. Knapp and M. D. Smith, "Variation among biomes in temporal dynamics of aboveground primary production," *Science*, vol. 291, no. 5503, pp. 481–484, 2001.
- [16] L. B. Flanagan, L. A. Wever, and P. J. Carlson, "Seasonal and interannual variation in carbon dioxide exchange and carbon balance in a northern temperate grassland," *Global Change Biology*, vol. 8, no. 7, pp. 599–615, 2002.
- [17] L. Xu and D. D. Baldocchi, "Seasonal variation in carbon dioxide exchange over a Mediterranean annual grassland in California," *Agricultural and Forest Meteorology*, vol. 123, no. 1–2, pp. 79–96, 2004.
- [18] A. C. Risch and D. A. Frank, "Carbon dioxide fluxes in a spatially and temporally heterogeneous temperate grassland," *Oecologia*, vol. 147, no. 2, pp. 291–302, 2006.
- [19] D. D. Baldocchi, "Assessing the eddy covariance technique for evaluating carbon dioxide exchange rates of ecosystems: past, present and future," *Global Change Biology*, vol. 9, no. 4, pp. 479–492, 2003.
- [20] A. K. Knapp, J. T. Fahnestock, S. P. Hamburg, L. B. Statland, T. R. Seastedt, and D. S. Schimel, "Landscape patterns in soil-plant water relations and primary production in tallgrass prairie," *Ecology*, vol. 74, no. 2, pp. 549–560, 1993.
- [21] J. F. Reynolds, P. R. Kemp, K. Ogle, and R. J. Fernández, "Modifying the 'pulse-reserve' paradigm for deserts of North America: precipitation pulses, soil water, and plant responses," *Oecologia*, vol. 141, no. 2, pp. 194–210, 2004.
- [22] A. Porporato, F. Laio, L. Ridolfi, and I. Rodriguez-Iturbe, "Plants in water-controlled ecosystems: active role in hydrologic processes and response to water stress I. Scope and general outline," *Advances in Water Resources*, vol. 24, no. 7, pp. 695–705, 2001.

- [23] M. M. Chaves, J. S. Pereira, J. Maroco et al., "How plants cope with water stress in the field? Photosynthesis and growth," *Annals of Botany*, vol. 89, pp. 907–916, 2002.
- [24] E. T. Engman and N. Chauhan, "Status of microwave soil moisture measurements with remote sensing," *Remote Sensing of Environment*, vol. 51, no. 1, pp. 189–198, 1995.
- [25] M. C. Dobson and F. T. Ulaby, "Active microwave soil moisture research," *IEEE Transactions on Geoscience and Remote Sensing*, vol. 24, no. 1, pp. 23–36, 2007.
- [26] T. Schmugge, P. E. O'Neill, and J. R. Wang, "Passive microwave soil moisture research," *IEEE Transactions on Geoscience and Remote Sensing*, vol. 24, no. 1, pp. 12–22, 2007.
- [27] J. A. Gamon, B. Field, M. L. Goulden et al., "Relationships between NDVI, canopy structure, and photosynthesis in three Californian vegetation types," *Ecological Applications*, vol. 5, no. 1, pp. 28–41, 1995.
- [28] A. A. Gitelson and M. N. Merzlyak, "Signature analysis of leaf reflectance spectra: algorithm development for remote sensing of chlorophyll," *Journal of Plant Physiology*, vol. 148, no. 3–4, pp. 494–500, 1996.
- [29] E. R. Hunt and B. N. Rock, "Detection of changes in leaf water content using Near- and Middle-Infrared reflectances," *Remote Sensing of Environment*, vol. 30, no. 1, pp. 43–54, 1989.
- [30] T. J. Jackson, D. Chen, M. Cosh et al., "Vegetation water content mapping using landsat data derived normalized difference water index for corn and soybeans," *Remote Sensing of Environment*, vol. 92, no. 4, pp. 475–482, 2004.
- [31] T. J. Farrar, S. E. Nicholson, and A. R. Lare, "The influence of soil type on the relationships between NDVI, rainfall, and soil moisture in semiarid Botswana. II. NDVI response to soil moisture," *Remote Sensing of Environment*, vol. 50, no. 2, pp. 121–133, 1994.
- [32] P. E. Dennison, D. A. Roberts, S. R. Thorgusen, J. C. Regelbrugge, D. Weise, and C. Lee, "Modeling seasonal changes in live fuel moisture and equivalent water thickness using a cumulative water balance index," *Remote Sensing of Environment*, vol. 88, no. 4, pp. 442–452, 2003.
- [33] D. A. Roberts, S. L. Ustin, S. Ogunjemiyo et al., "Spectral and structural measures of northwest forest vegetation at leaf to landscape scales," *Ecosystems*, vol. 7, no. 5, pp. 545–562, 2004.
- [34] J. O. Adegoke and A. M. Carleton, "Relations between soil moisture and satellite vegetation indices in the U.S. Corn Belt," *American Meteorology Society*, vol. 3, no. 4, pp. 395–405, 2001.
- [35] Y. Gu, E. Hunt, B. Wardlow, J. B. Basara, J. F. Brown, and J. P. Verdin, "Evaluation of MODIS NDVI and NDWI for vegetation drought monitoring using Oklahoma Mesonet soil moisture data," *Geophysical Research Letters*, vol. 35, no. 22, Article ID L22401, 2008.
- [36] R. R. Gillies, T. N. Carlson, J. Cui, W. P. Kustas, and K. S. Humes, "A verification of the 'triangle' method for obtaining surface soil water content and energy fluxes from remote measurements of NDVI and surface radiant temperature," *International Journal of Remote Sensing*, vol. 18, no. 15, pp. 3145–3166, 1997.
- [37] I. Sandholt, K. Rasmussen, and J. Andersen, "A simple interpretation of the surface temperature/vegetation index space for assessment of surface moisture status," *Remote Sensing of Environment*, vol. 79, no. 2–3, pp. 213–224, 2002.
- [38] K. Mallick, B. K. Bhattacharya, and N. K. Patel, "Estimating volumetric surface moisture content for cropped soils using a soil wetness index based on surface temperature and NDVI," *Agricultural and Forest Meteorology*, vol. 149, no. 8, pp. 1327–1342, 2009.
- [39] I. Rodriguez-Iturbe, "Ecohydrology: a hydrologic perspective of climate-soil-vegetation dynamics," *Water Resources Research*, vol. 36, no. 1, pp. 3–9, 2000.
- [40] S. Ma, D. D. Baldocchi, L. Xu, and T. Hehn, "Inter-annual variability in carbon dioxide exchange of an oak/grass savanna and open grassland in California," *Agricultural and Forest Meteorology*, vol. 147, no. 3–4, pp. 157–171, 2007.
- [41] L. Xu, D. D. Baldocchi, and J. Tang, "How soil moisture, rain pulses, and growth alter the response of ecosystem respiration to temperature," *Global Biogeochemical Cycles*, vol. 18, pp. 4002–4012, 2004.
- [42] D. D. Baldocchi, L. Xu, and N. Kiang, "How plant functional-type, weather, seasonal drought, and soil physical properties alter water and energy fluxes of an oak-grass savanna and an annual grassland," *Agricultural and Forest Meteorology*, vol. 123, no. 1–2, pp. 13–39, 2004.
- [43] P. E. Dennison, D. A. Roberts, and S. H. Peterson, "Spectral shape-based temporal compositing algorithms for MODIS surface reflectance data," *Remote Sensing of Environment*, vol. 109, pp. 510–522, 2007.
- [44] J. W. Rouse, R. H. Haas, J. A. Schell, and D. W. Deering, "Monitoring vegetation system in the great plains with ERTS," in *Proceedings of the 3rd ERTS Symposium*, vol. 1 of NASA SP-351, pp. 309–317, NASA, Washington, DC, USA, 1973.
- [45] A. A. Gitelson, Y. J. Kaufman, R. Stark, and D. Rundquist, "Novel algorithms for remote estimation of vegetation fraction," *Remote Sensing of Environment*, vol. 80, no. 1, pp. 76–87, 2002.
- [46] B. C. Gao, "NDWI—A normalized difference water index for remote sensing of vegetation liquid water from space," *Remote Sensing of Environment*, vol. 58, no. 3, pp. 257–266, 1996.
- [47] A. Palacios-Orueta, S. Khanna, J. Litago, M. L. Whiting, and S. L. Ustin, "Assessment of NDVI and NDWI spectral indices using MODIS time series analysis and development of a new spectral index based on MODIS shortwave infrared bands," in *Proceedings of the 1st International Conference of Remote Sensing and Geoinformation Processing*, pp. 207–209, Trier, Germany, 2006.
- [48] J. A. Gamon, C. B. Field, M. L. Goulden et al., "Relationships between NDVI, canopy structure, and photosynthesis in three Californian vegetation types," *Ecological Applications*, vol. 5, no. 1, pp. 28–41, 1995.
- [49] J. M. Paruelo, H. E. Epstein, W. K. Lauenroth, and I. C. Burke, "ANPP estimates from NDVI for the central grassland region of the United States," *Ecology*, vol. 78, no. 3, pp. 953–958, 1997.
- [50] M. L. Whiting, L. Li, and S. L. Ustin, "Predicting water content using Gaussian model on soil spectra," *Remote Sensing of Environment*, vol. 89, no. 4, pp. 535–552, 2004.
- [51] S. Khanna, A. Palacios-Orueta, M. L. Whiting, S. L. Ustin, D. Riaño, and J. Litago, "Development of angle indexes for soil moisture estimation, dry matter detection and land-cover discrimination," *Remote Sensing of Environment*, vol. 109, no. 2, pp. 154–165, 2007.
- [52] M. M. Caldwell, T. E. Dawson, and J. H. Richards, "Hydraulic lift: consequences of water efflux from the roots of plants," *Oecologia*, vol. 113, no. 2, pp. 151–161, 1998.
- [53] M. A. Davis, K. J. Wrage, and P. B. Reich, "Competition between tree seedlings and herbaceous vegetation: support for a theory of resource supply and demand," *Journal of Ecology*, vol. 86, no. 4, pp. 652–661, 1998.
- [54] R. S. Oliveira, L. Bezerra, E. A. Davidson et al., "Deep root function in soil water dynamics in cerrado savannas of central Brazil," *Functional Ecology*, vol. 19, no. 4, pp. 574–581, 2005.

- [55] S. Jacquemoud, "Inversion of the PROSPECT + SAIL canopy reflectance model from AVIRIS equivalent spectra: theoretical study," *Remote Sensing of Environment*, vol. 44, no. 2-3, pp. 281–292, 1993.
- [56] H. Bach and W. Verhoef, "Sensitivity studies on the effect of surface soil moisture on canopy reflectance using the radiative transfer model GeoSAIL," in *Proceedings IEEE International Geoscience and Remote Sensing Symposium (IGARSS '03)*, pp. 1679–1681, Toulouse, France, July 2003.
- [57] L. Wang, J. J. Qu, X. Hao, and Q. Zhu, "Sensitivity studies of the moisture effects on MODIS SWIR reflectance and vegetation water indices," *International Journal of Remote Sensing*, vol. 29, no. 24, pp. 7065–7075, 2008.
- [58] G. Rondeaux, M. Steven, and F. Baret, "Optimization of soil-adjusted vegetation indices," *Remote Sensing of Environment*, vol. 55, no. 2, pp. 95–107, 1996.

Research Article

Mapping Agricultural Frozen Soil on the Watershed Scale Using Remote Sensing Data

Jalal Khaldoune,¹ Eric Van Bochove,² Monique Bernier,¹ and Michel C. Nolin²

¹ *Institut National de la Recherche Scientifique—Eau, Terre et Environnement (INRS-ETE), 490 rue de la Couronne, QC, Canada G1K 9A9*

² *Agriculture and Agri-Food Canada, Soils and Crops Research and Development Centre, 2560 Hochelaga Boulevard, QC, Canada G1V 2J3*

Correspondence should be addressed to Jalal Khaldoune, khaldoune@yahoo.com

Received 6 December 2010; Revised 21 February 2011; Accepted 20 March 2011

Academic Editor: Mehrez Zribi

Copyright © 2011 Jalal Khaldoune et al. This is an open access article distributed under the Creative Commons Attribution License, which permits unrestricted use, distribution, and reproduction in any medium, provided the original work is properly cited.

This paper presents an empirical model for classifying frozen/unfrozen soils in the entire Bras d'Henri River watershed (167 km²) near Quebec City (Quebec, Canada). It was developed to produce frozen soil maps under snow cover using RADARSAT-1 fine mode images and in situ data during three winters. Twelve RADARSAT-1 images were analyzed from fall 2003 to spring 2006 to discern the intra- and interannual variability of frozen soil characteristics. Regression models were developed for each soil group (parent material-drainage-soil type) and land cover to establish a threshold for frozen soil from the backscattering coefficients (HH polarization). Tilled fields showed higher backscattering signal (+3 dB) than the untilled fields. The overall classification accuracy was 87% for frozen soils and 94% for unfrozen soils. With respect to land use, that is, tilled versus untilled fields, an overall accuracy of 89% was obtained for the tilled fields and 92% for the untilled fields. Results show that this new mapping approach using RADARSAT-1 images can provide estimates of surface soil status (frozen/unfrozen) at the watershed scale in agricultural areas.

1. Introduction

Soil freezing is a critical attribute for sustaining agricultural production. It has a major impact on soil water erosion at snowmelt [1, 2] and causes winterkill of perennial crops [3]. Soil water erosion and surface runoff are major sources for transporting water from agricultural land to streams. Soil sediments adversely affect surface water quality and often carry phosphorus, ammonia, pathogens, trace elements, and other contaminants from agricultural sources [4]. In Eastern Canada, the extent of this diffuse pollution is exacerbated when significant snowmelt runoff occurs on bare and erodible frozen agricultural soils located on sloping fields [5]. Environmental conditions in spring can significantly affect water transport. Early snow accumulation on wet soils may result in more unfrozen soils [6], or shallowly frozen soils, that allow higher infiltration of water at spring melt which consequently decreases runoff [7, 8]. Late snow accumulation on relatively dry soils with cold air temperatures will allow frost to penetrate deeper below the soil surface. Soils

frozen below a 15-cm depth can impede water infiltration [9] and generate a greater risk of erosion and snowmelt runoff at spring thaw. Despite the environmental impacts of frozen soils, soil temperature is poorly documented in Canada; agricultural lands are not systematically monitored by meteorological stations. Clearly, soil temperature is a critical attribute needed in meteorological databases to predict frozen soil status, to analyze environmental impacts of agricultural production, and to develop best management practices.

Remote sensing offers promising techniques for monitoring near-surface frozen and unfrozen soil status on broad geographical scales [10]. In the past, passive microwave remote sensing was explored. [11] used special sensor microwave/imager (SSM/I) data to detect soil freeze and thaw states over snow-free land. Using data from the Nimbus 7 scanning multichannel microwave radiometer (SMMR) for brightness temperature, [12] shows that frozen ground can be discerned from unfrozen ground for pasture soils. Both sensors provide poor spatial resolution (10–50 km), however, which restricts their use to only very large areas.

Satellite measurements of thermal radiation (3–14 μm) have been widely used to determine soil surface temperature [13–15], but these thermal sensors cannot provide data under cloudy conditions. In addition, since much of the frozen soil in Eastern Canada is covered by snow, the need to determine frozen and unfrozen status under snow cover conditions is obvious. Unlike the thermal infrared or passive microwave sensors, synthetic aperture radar (SAR) systems can potentially provide information concerning soil freezing dynamics under snow cover at high resolution regardless of cloud cover and time of day and night. The radar signal predominantly depends on the dielectric constant of soil which itself is directly related to the water and ice content, respectively [16]. RADARSAT-1 is a high SAR spatial resolution (9 m) sensor operating in the C-band (5.3 GHz) which also covers the watershed level when the soil is dry and the snow cover is virtually transparent [17]. According to [18], only 5% of the transmitted signal is diffused into the snow cover to a 30-cm depth, which corresponds to a decrease of approximately 0.2 dB in the backscattered signal. Some specific studies on radar conclude that results obtained using SAR sensors may provide useful information on ground moisture and near-surface frozen and unfrozen bare soil status [17, 19–21]. However, imaging frozen soil on the watershed scale using RADARSAT-1 remains unexplored.

Active sensors discern frozen soil by detecting variations in liquid soil water content. These variations are related to soil dielectric constant values [22–26]. The average dielectric constant value of dry soil is about 2–3, while that of liquid water is 80 [27]. The dielectric contrast between soil and air is low when the soil is dry (~ 3), because less energy is diffused at its surface [23]. The soil dielectric constant increases proportionally with volumetric liquid water content, which allows the radar sensor to discern dry soil from wet soil. Under critical winter conditions, a greater proportion of soil water freezes which leads to a significant decrease of the average soil dielectric constant; frozen water has a dielectric constant of ice (3.2) which is similar to that of dry soil [28–30]. The opposite phenomenon occurs during spring thaw when the ice within soil melts, which results in the radar cross-section increasing by several dB [31–34]. Reflections occur at interfaces that are related to abrupt changes in dielectric permittivity, for example, at the frozen/unfrozen ground interface. Hence, radar can be employed to spatially distinguish between dry and wet areas as well as between frozen and unfrozen soil.

Soil properties (i.e., structure, texture, and drainage) influence the soil water content and consequently its freezing dynamics. Each soil has its specific latent heat flux that increases with water content and which requires more heat loss to freeze [35, 36]. Mineral soils freeze more quickly and more deeply than organic soils because of their lesser capacity to store water [37]. The same relation exists between sandy and clay soils.

Soil moisture is not the only attribute that affects the radar backscattering signal; vegetative cover and soil surface roughness also have an effect [38, 39]. Many studies have evaluated the effects of surface roughness on the radar signal [23, 40–43]. For example [44] report that surface roughness

effects are more important with greater soil moisture content and [45] suggest that the effect of roughness may be considered as being constant within an agricultural area for some cases. Although surface roughness indices are affected by many factors, such as crop, soil management, crop residues, and field orientation, winter conditions preceding the spring melt in eastern Canada present more stable indices due to the lack of agricultural activity compared with other seasons. Consequently, these more stable surface conditions are favourable to successive radar image acquisitions during winter.

The objective of this study was to classify the near-surface agricultural soils as being frozen or unfrozen relative to changes in the RADARSAT-1 backscattering signal under dry snow cover. A linear regression model between the soil surface temperature and the radar backscattering signal was developed to predict surface temperatures, to classify RADARSAT-1 images, and to derive frozen soil maps on the watershed scale. The regression model was assessed from interactions between in situ ground measurements and remote sensing data acquired from 12 representative agricultural fields within the Bras d'Henri watershed (167 km^2) during winters from 2003 to 2006.

2. Material and Methods

2.1. Study Area. The Bras d'Henri study site (167 km^2) is a subwatershed of the Beaurivage and Chaudière basins, located south of Quebec City and the Saint-Lawrence River (Figure 1). Soil classification and attributes of the studied area are described in Table 1; they belong mainly to the podzol (47.6%), gleysol (30.5%), organic (11.1%), and brunisol (5.7%) order. The drainage classes for the mineral and organic soils ranged from being well (21.9%), moderately (16.6%), imperfectly (17.2%), poorly (26.5%), and very poorly drained (15.2%). The surface texture ranged from sandy loam to loam, while the family particle-size classes include soils with sandy, coarse-loamy, fine-silty, and sandy-skeletal attributes (Table 1). The organic soils identified in the watershed consist of highly decomposed humic layers [46]. Soils were generally developed over fluvial and fluviolacustrine deposits [47].

The cold temperate climate is characterized by a severe winter with a moderate and subhumid summer. Mean annual temperature is 4.5°C–6.6°C with an average annual precipitation of 1126 mm and a normal snowfall of 320 cm. Early snow accumulation may insulate the soil from freezing depending on local conditions. The freezing period starts around mid-November and lasts until mid-April. The studied area has the most intensive livestock production of the watershed, which generates a surplus of nutrients. Slope of the fields in the studied area ranges from 0% to 9%, which increases the risk of surface runoff, soil water erosion, and the transport of sediments, phosphorus, and other contaminants (pathogens, herbicides, and trace elements) from agricultural land to streams [6].

2.2. In Situ Data Measurements. Field observations, including soil temperature, soil moisture content, and snowpack

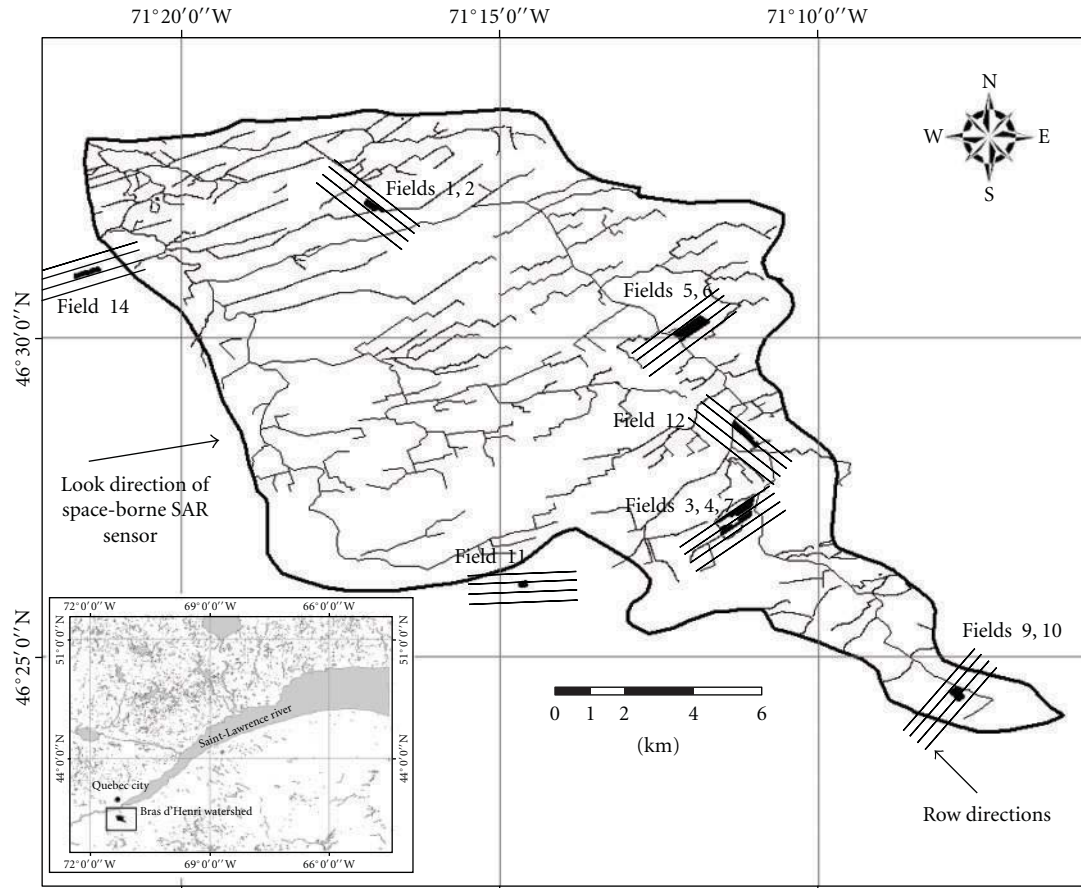


FIGURE 1: Location of the 12 study fields within the Bras d'Henri watershed.

characteristics, were measured in 12 fields and are described in Tables 1 and 2. Field data for analysis were collected simultaneously with satellite acquisitions. All soil attributes repeatedly measured on the same field were averaged. Because the influence of soil moisture on radar signals under dense vegetation (forest) is weak, these areas were eliminated from the radar image analysis. Therefore, soil moisture measurements were considered for only bare soil and sparsely dispersed vegetation (Figure 2).

The soil temperature was measured at six different depths (5, 10, 15, 35, and 50 cm below the soil surface) using copper-constantan thermocouples (Type T, Omega, Stamford, Connecticut). Thermocouples were installed during the fall and their locations were georeferenced. Air temperature was measured with a portable thermometer. Each field was sampled over five temperature profiles, with the minimum distance between profiles being 45 m. A digital elevation model (DEM) and detailed soil maps were used to determine five representative locations within each field.

A time domain reflectometer (TDR) probe was also installed at 5 cm below the soil surface for dielectric constant measurement [48]. Soil moisture was measured using TDR technology. An automatic meteorological station was mounted on a representative field within the monitoring network. Hourly average air temperature, snow height, and

wind direction were recorded. The snow was considered to be dry when the air temperature was below 0°C on the night preceding a SAR image acquisition.

The effect of soil type and land use (tilled versus untilled) on the radar signal was evaluated relative to the soil series classification according to [49]. The resultant soil classification was based on soil properties, with emphasis on various soil drainage indicators. The Beaurivage sandy loam soils belong to the moderate-to-rapid soil permeability class ($5\text{--}15\text{ cm hr}^{-1}$), whereas the other soils have moderate-to-slow permeability ($0.5\text{--}1.5\text{ cm hr}^{-1}$). Since the measurements taken by synthetic aperture radar (SAR) instruments are sensitive to soil moisture, it is hypothesized that the drainage class of each soil type studied within the watershed has an impact on the radar backscattering signal. Moreover, the soil classification at the series level is principally based on soil drainage and soil water holding capacity, two attributes highly related to soil moisture content and soil dielectric constant.

2.3. SAR Data Acquisitions. Twelve RADARSAT-1 SAR images were acquired during three winter seasons, from fall 2003 to spring 2006. Images were centered on 46° 29' N and 71° 14' W. RADARSAT-1 was scheduled to acquire C band (frequency 5.3 GHz corresponding to a wavelength of

TABLE 1: Soil classification and attributes of the 12 fields selected as training/validation sites.

Field no.	Soil series	Parent material	Soil drainage class	Surface texture	Land use	Number of pixels	Incidence angle (°)	Row direction (°) ^(a)
1	Mawcook	Till	Poorly drained	Sandy loam	Untilled field	264	38.12	—
2	Mawcook	Till	Poorly drained	Sandy loam	Tilled field	272	38.12	45
3	Le Bras	Fluviolacustrine	Poorly drained	Loam	Untilled field	227	38.51	—
4	Le Bras	Fluviolacustrine	Poorly drained	Loam	Tilled field	230	38.51	155
5	Neubois	Fluviolacustrine	Moderate to imperfect	Loam	Untilled field	265	38.47	—
6	Neubois	Fluviolacustrine	Moderate to imperfect	Loam	Tilled field	264	38.47	155
7	Beaurivage	Fluvial	Moderate	Sandy loam	Untilled field	228	38.51	—
9	Woodbridge	Till	Moderate to imperfect	Loam	Untilled field	241	38.74	—
10	Woodbridge	Till	Moderate to imperfect	Loam	Tilled field	257	38.74	155
11	Organic soil	Organic	Very poorly drained	Organic	Tilled field	235	38.27	10
12	Beaurivage	Fluvial	Moderate	Sandy loam	Tilled field	228	38.52	52
14	Beaurivage	Fluvial	Well drained	Loamy sand	Untilled field	112	37.79	—

^(a)The direction of space-borne SAR sensor is considered equal to 0° of the compass dial.

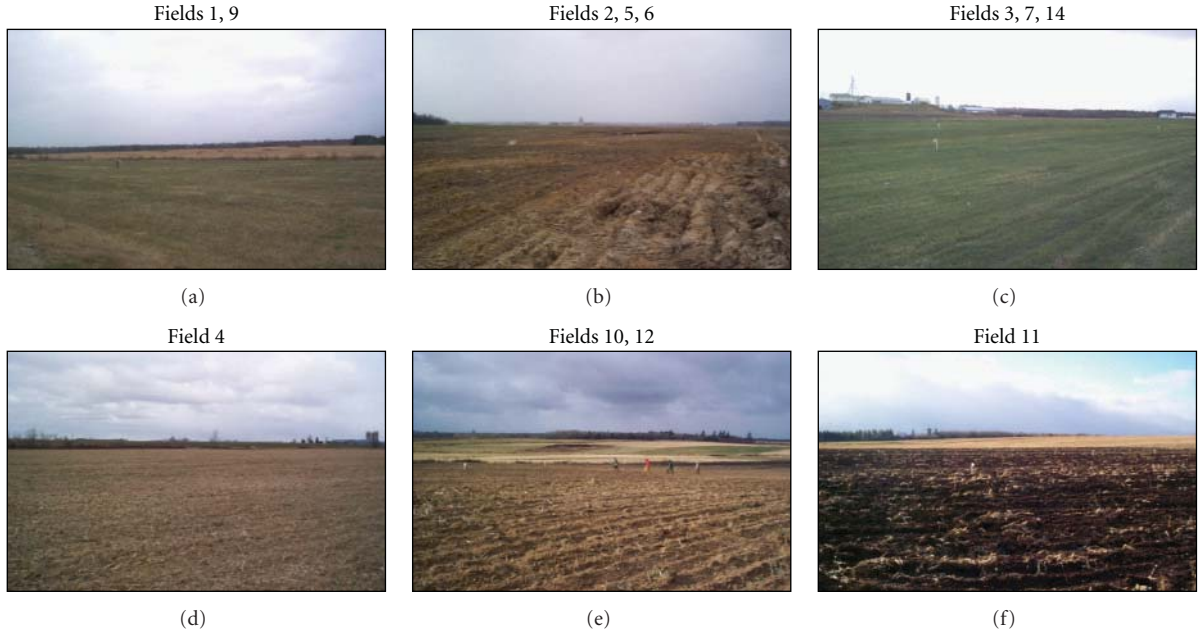


FIGURE 2: Photographs showing the types of land cover considered in this study: untilled fields (1, 3, 7, 9, and 14), tilled fields (2, 4, 5, 6, 10, 11, and 12).

TABLE 2: Soil textures and attributes of the 12 fields selected as training/validation sites.

Field no.	Organic (%)	Sand (%)	Silt (%)	Clay (%)	Texture	Altitude (m)
1	4.31	56.7	30.5	12.8	Sandy loam	139.36
2	3.50	55.0	31.6	13.5	Sandy loam	140.03
3	3.35	47.9	38.7	13.4	Loam	180.37
4	5.11	52.3	34.2	13.5	Sandy loam	178.46
5	4.25	47.4	42.0	10.7	Loam	158.06
6	2.68	44.2	43.2	12.5	Loam	157.31
7	3.75	47.6	45.0	7.4	Loam	184.38
9	3.05	52.8	39.7	7.4	Sandy loam	282.81
10	3.75	41.2	45.4	13.3	Loam	292.37
11	42.06	—	—	—	Organic	173.19
12	3.40	69.4	25.4	5.3	Sandy loam	173.67
14	1.82	79.5	17.1	3.4	Loamy sand	131.88

5.6 cm) polarization HH SAR images on ascending orbit in fine mode (F1F), which corresponded to incidence angles varying from 36.9° to 40.1°. It has been shown that low incidence angles (20°–30°) reduce the influence of soil surface roughness [23, 43, 50–52]. However, for this study, despite its high incidence angle, the fine beam mode of RADARSAT-1 was selected for its fine spatial resolution (9 m × 9 m) that offers an advantage for mapping frozen soils at the field scale. Moreover, the roughness has to remain unchanged during the acquisition of all images.

The OrthoEngine program of PCI Geomatica (V9.1.5) was used to geometrically correct each RADARSAT-1 image registered with intensity (power) backscatter values in 32-bit real channel. The mathematical modelling was based on a photogrammetry method [53], and the output images

were resampled to a pixel spacing of 9 m using the bilinear technique.

A mask was applied to all fields allowing the extraction of the mean, the minimum, the maximum, and the standard deviation from image intensity values. Radar data intensity values were converted to backscattering coefficients (dB) using (1) and (2) to allow a quantitative comparison of frozen and unfrozen soil values within the scene

$$\text{dB} = 10 \times \log_{10}(\text{Intensity}), \quad (1)$$

where the intensity (power) is given by

$$\text{Intensity} = \sigma_{ij} = \frac{DN * DN + A_0}{A_j} * \sin(I_{ij}), \quad (2)$$

TABLE 3: Description of the RADARSAT-1 images acquired over the Bras d'Henri watershed during the three winter seasons (2003-2004 to 2005-2006) and the reasons for the use of only 12 radar images in this study.

Winter season	Dates of RADARSAT-1 image acquisitions	Use (yes/no)	Reason
First	08 November 2003	Yes	Dry snow
	02 December 2003	Yes	Dry snow
	26 December 2003	No	Wet snow surface coinciding with the RADARSAT-1 overpass
	19 January 2004	Yes	Dry snow
	25 January 2004	No	Wet snow surface coinciding with the RADARSAT-1 overpass
	29 February 2004	Yes	Dry snow
Second	02 November 2004	Yes	Dry snow
	06 December 2004	No	Acquisition failures due to the conflicts with other users.
	10 January 2005	No	Acquisition failures due to the conflicts with other users.
	13 January 2005	Yes	Dry snow
	06 February 2005	No	Wet snow surface coinciding with the RADARSAT-1 overpass
	14 February 2005	No	Acquisition failures due to the conflicts with other users.
Third	08 January 2006	Yes	Dry snow
	01 February 2006	Yes	Dry snow
	25 February 2006	Yes	Dry snow
	21 March 2006	Yes	Dry snow
	14 April 2006	Yes	Dry snow
	08 May 2006	Yes	Dry snow

where σ_{ij} is the output backscattering coefficient for line i , pixel j , DN is the input image value for line i , pixel j , A_0 is the gain offset from the first member of SAR scaling offset segment (A_0 SEG), A_j is the expanded gain scaling tabular value for pixel j , and I_{ij} is the local incidence angle.

In order to map frozen soils on the watershed scale, only images that presented dry snow cover conditions were retained (Table 3). Images taken wherever air temperature was above the freezing point were discarded due to a wet snow cover. The backscattering behavior changes for a wet snow cover, resulting in low values of the backscattering coefficient for incident angle $\theta > 20^\circ$. The lower values under wet snow conditions are due to increased attenuation by the snow cover when its surface is relatively smooth [54, 55]. The RADARSAT-1 images were filtered to smooth and wipe off the noise, reducing the speckle effect. To achieve this task, a 5×5 Gaussian filter was applied to all 12 RADARSAT-1 images [56].

The three assumptions underlying the linear regression model were verified prior to using the data: (1) residuals were normally distributed, (2) the residual mean was equal to zero, and (3) residuals were not autocorrelated

3. Results and Discussion

The effects of land use, air temperature, and snow cover thickness on frost depth were studied for the 12 fields selected for monitoring and validation. In the following sections, the backscattering coefficients of the images are related to ground data measurements (snow cover thickness, soil moisture, and frozen soil depth) taking soil type into account. These relationships were developed for untilled and tilled fields (Figure 2), during two winters (November 2003 to April 2004 and November 2004 to April 2005) and then applied to a third winter (January to April 2006).

3.1. Snow Cover and Soil Temperature. The weather records for the 2004, 2005, and 2006 winter seasons are presented in Figure 3. In general, the average daily temperature drops below 0°C on November and the snowpack initiates on December. However, the average air temperature does not stay continuously below 0°C during the winter Figure 3(a). The minimum recorded air temperature was -27.5°C on January 25, 2004, -27°C on January 13, 2005, and -17°C on February 26, 2006. The daily average snow accumulation

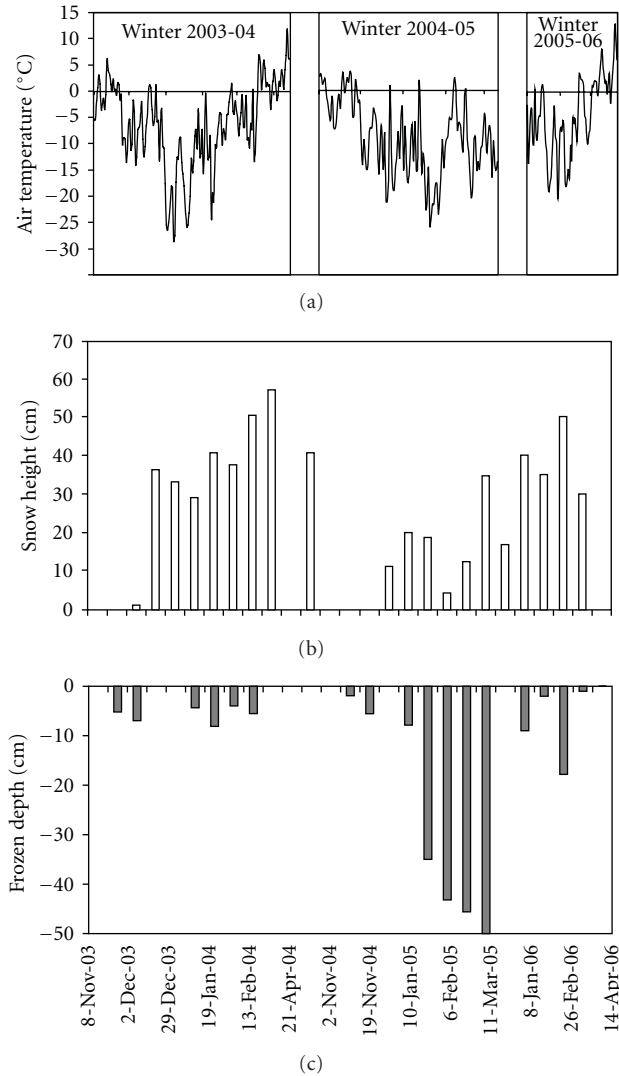


FIGURE 3: Temporal variation for: (a) air temperature, (b) snow height, and (c) frozen depth (0–50 cm depth).

reached its maximum in different months from year to year (Figure 3(b)).

During the winter of 2004, it was observed that when the air temperature dropped below -10°C , the near-surface soil layers froze. The first soil type to freeze was the Neuboiss loam (fields 5 and 6), while the organic soil (field 11) was the last (results not shown). Snow accumulation began on December 22 with a snow-cover thickness of about 38 cm. The period of freezing was preceded by snow accumulation which reached a maximum of 66 cm in field 2 on February 29, 2004. Because field 2 was tilled, the frost penetrated deeper in the soil (30 cm) than in the untilled field 1 (11 cm), which was covered with hay. The winter of 2005 had less precipitation and less snow cover (20 cm), while the air temperature was similar to the winter of 2004. This condition accelerated the frost penetration into the ground, which reached a depth of up to 50 cm. The variation in the snow cover (10 to 66 cm) was compared with the variation of soil surface temperature. Soil surface temperature was maintained near 0°C during

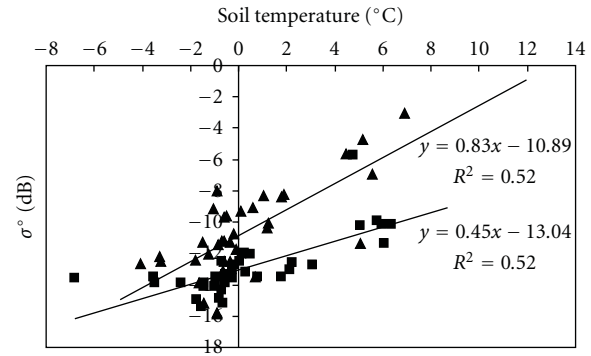


FIGURE 4: Linear regression models between backscattering coefficient, σ° , with ground measured soil temperature (0–5 cm depth) for tilled fields (triangle) and untilled fields (square).

long periods. Generally, snow cover played an important role by maintaining heat on the soil surface, even when the air temperature dropped below -10°C . Thaw started in mid-March (Figure 3(c)).

The winter of 2006 was warmer. In March, with the onset of snowmelt, the shallow unfrozen ground quickly became saturated up to the surface. Flow occurred overland because the ground had limited storage capacity (Figure 3(c)).

3.2. Backscattering Coefficients and Ground Soil Measurements. Figure 4 illustrates the relationship between backscattering coefficients (σ°) and the soil temperature for data acquired during 2004, 2005, and 2006. Since the spatial resolution of the developed model is approximately 9 m, the radar signal mean values were compared with the mean values of the ground soil temperature and the soil moisture (Figure 5) taken from the same sampling cells. It is assumed that surface roughness was homogenous for each considered class (tilled and untilled). Thus, a regression line was fitted to all points belonging to each class (tilled and untilled) (Figure 4). For both the tilled and untilled class, the coefficient of determination (R^2) was 0.52, which is considered satisfactory. There is a comparable correlation between σ° and soil temperature for surface soil temperatures below 0°C , which progressively becomes weaker with increasing surface soil temperature. When the soil temperature is below 0°C , there is no significant difference in the σ° and the soil temperature relationship for the tilled and the untilled fields. However, when the soil temperature is above 0°C , one can distinguish two relationships wherein the σ° for the tilled fields is higher than that of the untilled fields. This can be explained by the high sensitivity of the backscattered signal to soil roughness when soil moisture increased. Given that the range of observations from this study is -7°C to 7°C , soil moisture would have decreased when the soil was frozen, and thus the soil would have been dry [23, 33]. Consequently, the radar signal would penetrate the soil with minimal effect on soil roughness. However, when soil temperature increases, soil moisture content also increases, and consequently, the backscattered signal increases and can

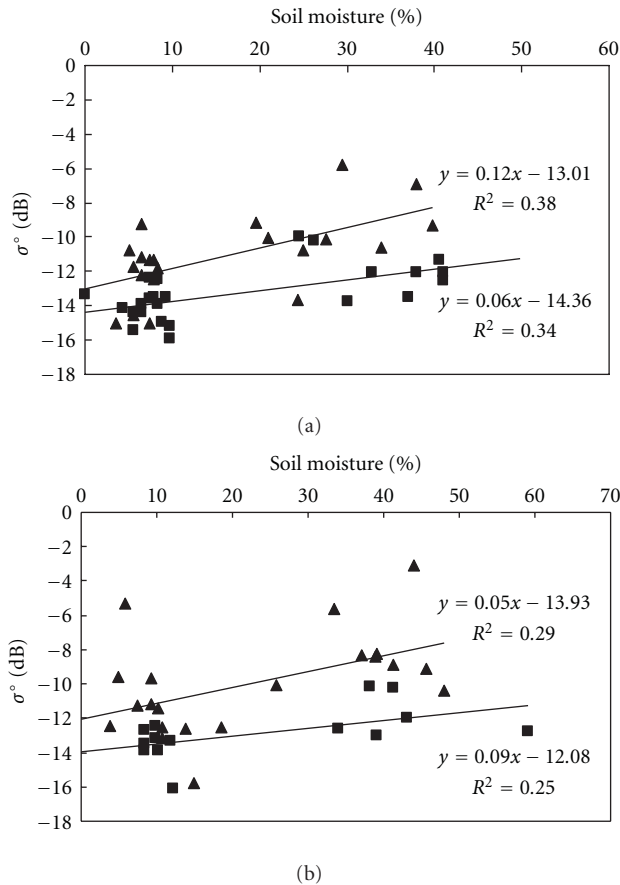


FIGURE 5: Linear regression models between backscattering coefficient, σ° , with ground measured soil moisture (0–5 cm depth) for soil drainage types: (a) moderate to good drainage and (b) poor drainage. Symbols for each field class; tilled (triangle), untilled (square).

be significantly affected by field surface conditions (tilled or untilled). This explains the increase in the backscattering coefficient for the tilled fields.

As presented in Figure 5, a regression analysis was also performed between σ° and soil moisture, separately for two drainage groups (good; moderately to well-drained soils; poor; poorly drained soils), according to each land use class (tilled versus untilled fields). The coefficient of determination (R^2) between σ° and surface soil moisture was 0.38 for tilled and 0.34 for untilled fields with good soil drainage. For the poorly drained soils, the R^2 value was 0.29 for tilled and 0.25 for untilled fields (Figure 5). These correlation coefficients were lower than those previously reported [57, 58]. Empirical relationships between σ° and near-surface water content show considerable scatter, and the relationships vary with land use (tilled/untilled). One probable reason for the absence of a good relationship between σ° and near-surface water content is that soils show different relationships between soil dielectric properties and soil water content. This is due to differences in particle-size distribution affecting the partitioning between bound and free water [59]. Another reason behind the observed discrepancy is the

directional effects of the rows on the SAR return signal which increases when the row direction is almost perpendicular to the SAR antenna, as for fields 1, 2, and 12 (Figure 1). This effect makes the return signal stronger compared with other fields. The accuracy of the proposed relationship for estimating soil moisture is considered satisfactory, because cartographic and measurement errors are common in this type of analysis. In spite of the large variation in radar and volumetric moisture content data, the positive correlation between σ° and volumetric soil water content shows that the backscattered radar signals are related to soil moisture. Generally, the backscattering coefficient was found to vary from -8 to -16 dB for volumetric soil moisture content that ranged from 42% to 12%. For tilled fields, the average of σ° is relatively high (-10 dB) compared with untilled fields (-12 dB) with a R^2 of 0.37.

At first, a decrease of σ° (3 dB) was noted between December 2, 2003, and January 19, 2004, for all fields (data not shown) when the soil was frozen (air temperature = -11°C). The backscattering coefficient decreased by 3 dB for the Mawcook, sandy loam soils in the untilled field 1. For the tilled field 2 (same soil type), the backscattering coefficient decreased by 2 dB where the frost depth increased from 8 to 50 cm. The decreased backscattering coefficient over the Bras d'Henri watershed was associated with a decreased surface soil temperature below 0°C , and depended on soil type. On November 2, 2004, a strong backscattering coefficient, of about -5 dB, was recorded; this increase may be explained by increased soil moisture content (about 40%) and amplification as a result of surface roughness. The portion of the transmitted energy from the soil surface to the sensor was larger when the soil was wet because of the strong dielectric differential between water and air. The same phenomenon occurred again on February 6, 2005, when an increased backscattering coefficient was also noted (i.e., $\sigma^\circ = -5$ dB) in most fields except for fields 1, 2, 9, and 14 (results not shown). In this case, the air temperature was recorded at 2°C for the satellite pass; the snow cover was between 0 and 9 cm, while the frost depth was about 50 cm. This increase in the backscattered signal was not associated with the thaw but rather with an increase in moisture on the soil surface.

3.3. Frozen Soil Mapping Algorithm. The linear regression in this study was used to identify different values of backscattering coefficients (σ°) that can be used to distinguish between frozen and unfrozen fields for different soil conditions. Three categories were considered for each soil series, as follows: tilled frozen soils, untilled frozen soils, and frost-free soils. The threshold for determining whether a field was frozen or not was predicted by the σ° value corresponding to the zero temperature from the regression model for each soil group (i.e., soil series having similar parent material, family particlesize, and drainage conditions). Thus, the soil condition (frozen or not) was identified by applying the predicted σ° thresholds for each delineation on the soil map.

In this temporal study, we assumed that soil surface roughness was constant over time for each land use type

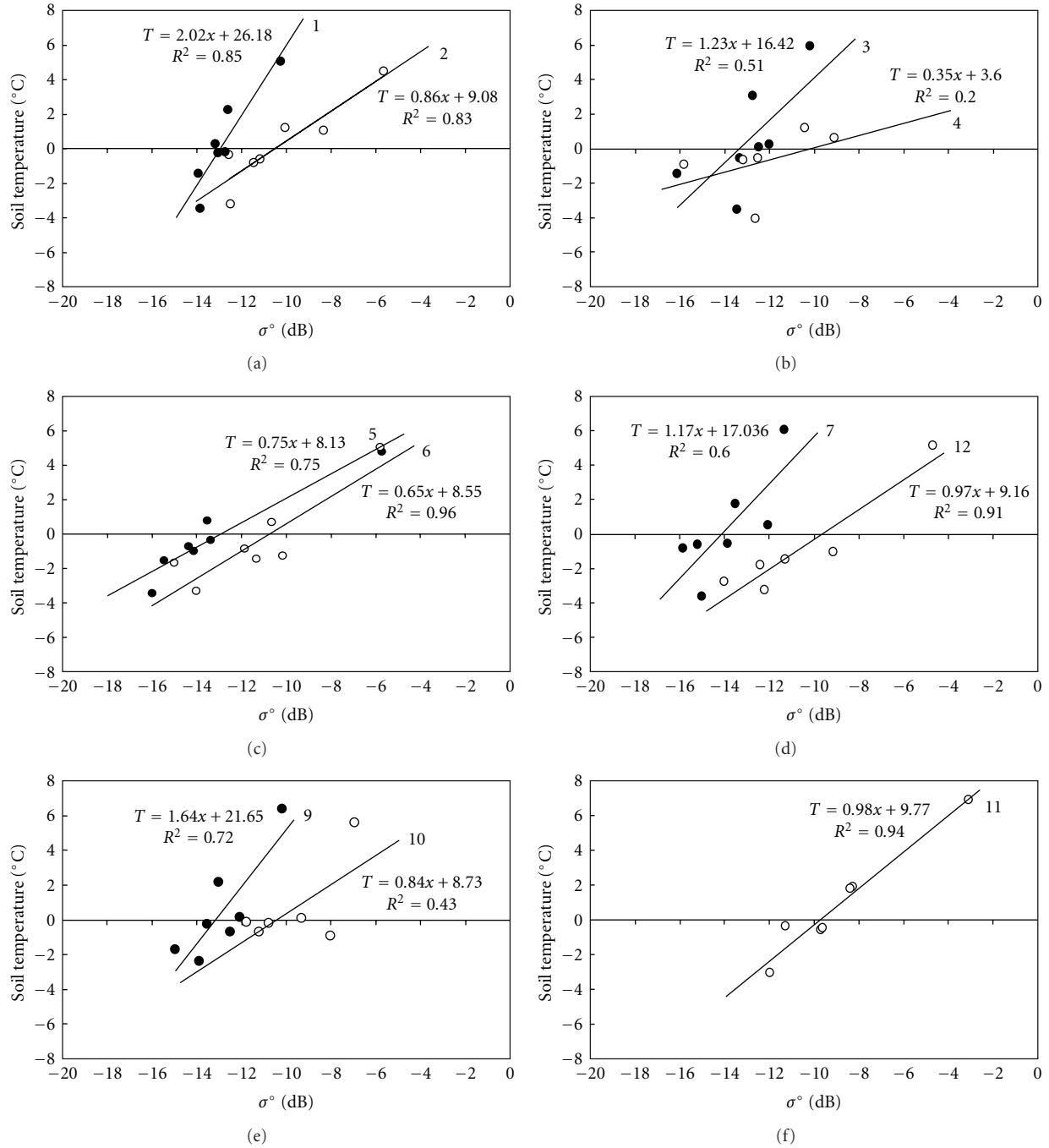


FIGURE 6: Linear regression models describing the variation of soil temperature measured at 5 cm in relation to the backscattering coefficient, σ° , according to soil type: (a) Mawcook, sandy loam, (b) Le Bras, loam, (c) Neubois, loam, (d) Beaurivage, sandy loam, (e) Woodbridge, loam, (f) organic soil, and land use type: tilled fields (\circ) and untilled fields (\bullet).

(untilled versus tilled fields) during the same winter season, because the soil surface would not be ploughed nor naturally modified before spring snowmelt [60]. Under this assumption, it is possible to consider that for each field, the backscattering coefficient (σ°) was related to soil surface moisture status [31]. In this section, the regression analysis was performed between the soil temperature at 5 cm and σ° , taking the soil series into account.

For the 12 fields under study, the average σ° was extracted and plotted versus the in situ measured soil temperature (Figure 6). Different simple linear regression models were performed for different soil types as well as for tilled and untilled soils. Figure 6 show that σ° increased as soil temperature increased, indicating a positive correlation between σ° and soil temperature. The soil types under study gave different R^2 values: 0.80 for Mawcook, sandy loam

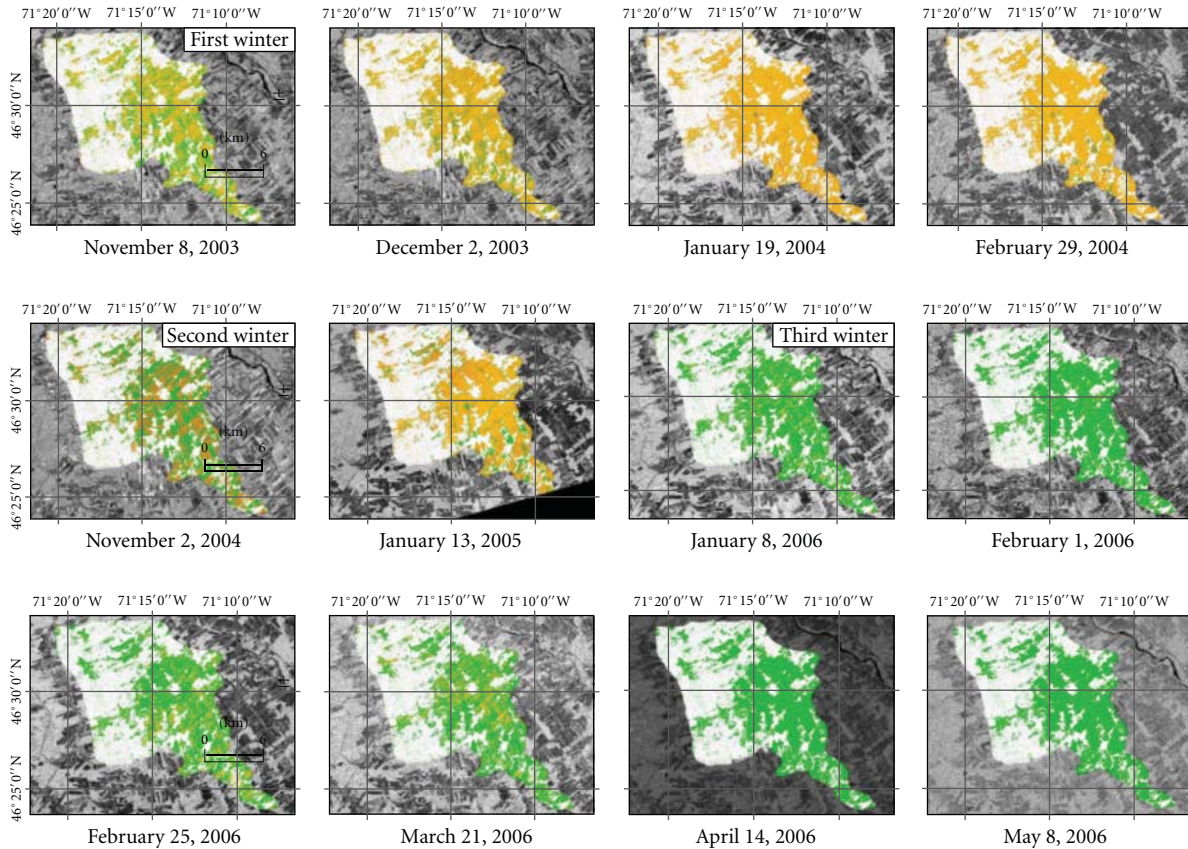


FIGURE 7: Maps of the frozen/unfrozen soil conditions in the Bras d'Henri watershed (2003–2006) using 12 RADARSAT-1 SAR images. Green: unfrozen soils, orange: tilled frozen soils, yellow: untilled frozen soils, and white: mask applied for forest area.

(fields 1 and 2), 0.74 for Beaurivage, sandy loam (fields 7 and 12), 0.85 for Neubois, loam (fields 5 and 6), 0.55 for Woodbridge, loam (fields 9 and 10), 0.35 for Le Bras, loam (fields 3 and 4), and 0.94 for the organic soil (field 11). A low coefficient of determination ($R^2 = 0.20$) was determined for Le Bras, loam, especially in the corn field after harvest (fields 4). This result can be explained by the interaction between the radar signal and dried corn residue and stalks remaining in the field after harvest. The moisture content of these stalks and residue may have varied throughout the field and during the fall season, which would increase the uncertainty of the estimated backscatter values. As the soil surface temperature decreased below 0°C , the σ° decreased by 3 to 5 dB depending on soil type. Also, the reader should note that for each soil type class, σ° for the tilled fields (fields 2, 4, 6, 10, 11, and 12) were always greater, by at least 2 dB, than σ° for the untilled fields. When the soil is frozen, it has a dielectric constant similar to dry soil. In this case, the signal penetrates the soil and is less sensitive to soil surface roughness. However, when the soil is unfrozen under the snow pack, soil water content increases, and the signal becomes more sensitive to soil surface roughness.

The regression equations given in Figure 6 identify the radar backscattering coefficient thresholds, which are used to differentiate frozen and unfrozen soils. These thresholds represent the backscattering values that correspond to soil

temperatures below 0°C (Table 7). Several maps of near-surface frozen soil conditions (frozen versus unfrozen soils) for the Bras d'Henri watershed were created for the winter seasons 2003–2004, 2004–2005, and 2005–2006 (Figure 7).

It should be emphasized that although the models developed in this study were applied to Bras d'Henri using available data to demonstrate models usefulness, however, more data should be acquired to update the developed models.

3.4. Frozen Soil Maps Derived from the Classification Algorithm. The classification algorithm developed in this paper was applied to the Bras d'Henri watershed (167 km^2) to identify frozen and unfrozen soils for all agricultural fields distributed over the entire watershed. To visualize the results, a color scale was used to display the near-surface frozen/unfrozen soils. Untilled frozen soils are in yellow, tilled frozen soils in orange, and unfrozen soils in green. A white mask was applied to cover the forest area that was excluded from the study (Figure 7). There are notable inter-annual variations in frozen soil distribution between each winter season over the Bras d'Henri watershed. Frozen soils covered a large area in 2004 (85%) and 2005 (74%) but covered only 35% of the area in 2006 (Table 8).

The minimum soil temperature at 5 cm was recorded as -7°C for the untilled Beaurivage soils on February 6, 2005; the maximum was 13°C at 1 cm for the tilled organic soils

TABLE 4: Classification results of six selected RADARSAT-1 SAR images compared with soil temperature at the 12 training/validation study fields.

Total		Classification results				
		Frozen	Unfrozen	Total	Success (%)	Omission (%)
Ground observations	Frozen	33	5	38	86.8	13.2
	Unfrozen	2	32	34	94.1	5.9
	Total	35	37	72	90.3	
	Commission (%)	5.7	13.5		Kappa = 0.81	

TABLE 5: Classification results of six selected RADARSAT-1 SAR images compared with soil temperature measurements at the 12 training/validation study fields, by land use.

				Classification results		
		Frozen	Unfrozen	Total	Success (%)	Omission (%)
Tilled fields						
Ground observations	Frozen	17	3	20	85	15
	Unfrozen	1	15	16	94	6
	Total	18	18	36	89	
Commission (%)		6	17	Kappa = 0.78		
Untilled fields						
Ground observations	Frozen	16	2	18	89	11
	Unfrozen	1	17	18	94	6
	Total	17	19	36	92	
Commission (%)		6	11	Kappa = 0.83		

on April 21, 2004. Soil temperatures showed strong variation near the surface (following changes in air temperature) but varied less at greater depths. The unfrozen moisture content increased in frozen soils with increasing soil temperatures at all depths and, more markedly, after the onset of snowmelt when soil temperatures increased rapidly (Figure 3).

In general, freezing starts in November and moves gradually toward the watershed depending on soil type, snow cover, and air temperature. The soil temperature decreased gradually as the frozen front progressed. When air temperature decreased in November, soil temperatures decreased quite uniformly throughout the unfrozen soil profile, and freezing set in abruptly after the 0°C isotherm was encountered. The progress of freezing apparently reflected the heterogeneity of the soil. At a given negative temperature, the quantity of unfrozen water varied considerably with soil type and was greater for soils with a finer texture. Furthermore, the greater organic matter content of organic soils (field 11) reduced both their soil heat capacity and soil thermal conductivity [61]. Also, they retained more water and the latent heat conductivity of water is greater than air.

This result may be understood as a complex interaction between thermal and hydraulic conductivities, both of which decrease with decreasing unfrozen water content. It is also related to the larger amount of latent heat that is released from soils with high water content. Soils with low water content (Beaurivage, loamy sand (field 14)) may be expected to initially freeze earlier because the release of latent heat is less. The maps show that the distribution of the frozen areas over

the watershed correlate well with soil type distribution and the interannual variation of air temperature and snow cover. The detectability of the freezing onset seems to be sensitive to land use (i.e., tilled versus untilled fields). On November 2, 2004, freezing had already occurred, particularly in the tilled fields, because the surface was directly exposed to low air temperatures, due to the low snow accumulation and because tillage promoted good drainage, which consequently accelerated the heat transfer through the porous soil.

When the near-surface frozen extension over the Bras d'Henri watershed is compared over the three winter seasons (2003-2004 to 2005-2006), the main difference between them is snow cover depth; it was substantial during the third winter season (~45 cm) but was 30 cm for the first winter and only 17 cm for the second winter. These results show that the presence of seasonal snow cover during the cold season has a significant influence on the ground thermal regime. In seasonally frozen ground regions, snow cover can substantially reduce the seasonal freezing depth. In fact, snow cover plays an insulating role by maintaining surface soil near the freezing point [62, 63]. Therefore, a frozen soil under a seasonal snow cover could eventually thaw during winter even though it may have been frozen before the snow cover occurred.

3.5. Validation of the Classification Algorithm. The empirical algorithm validation is based on the soil temperature data of the top 5 cm soil layer for the six RADARSAT-1 images acquired between January and May 2006. Using the 12 training/validation fields of the third winter season, confusion

TABLE 6: Classification results of six selected RADARSAT-1 SAR images compared with soil temperature at the 12 training/validation study fields, by acquisition date.

		Classification results			
		Frozen	Unfrozen	Total	Omission (%)
		January 8, 2006			
Ground observations	Frozen	11	1	12	92
	Unfrozen	0	0	0	100
	Total	11	1	12	92
Commission (%)		0	100	8	Kappa = NA ^(a)
		February 1, 2006			
Ground observations	Frozen	7	1	8	88
	Unfrozen	1	3	4	75
	Total	8	4	12	83
Commission (%)		13	25	17%	Kappa = 0.63
		February 26, 2006			
Ground observations	Frozen	11	1	12	92
	Unfrozen	0	0	0	100
	Total	11	1	12	92
Commission (%)		0	100	8	Kappa = NA ^(a)
		March 21, 2006			
Ground observations	Frozen	4	2	6	67
	Unfrozen	1	5	6	83
	Total	5	7	12	75
Commission (%)		20	29	25	Kappa = 0.50
		April 14, 2006			
Ground observations	Frozen	0	0	0	100
	Unfrozen	0	12	12	100
	Total	0	12	12	100
Commission (%)		0	0	0	Kappa = NA ^(a)
		May 8, 2006			
Ground observations	Frozen	0	0	0	100
	Unfrozen	0	12	12	100
	Total	0	12	12	100
Commission (%)		0	0	0	Kappa = NA ^(a)

^(a) Because only one class is represented, the Kappa coefficient cannot be calculated (division by zero).

matrices were computed to compare results from the proposed algorithm that classified soils as being frozen with the in situ soil temperatures. The analysis consisted of examining and displaying errors of commission and omission and the overall classification accuracy. From these percentages, a performance measure known as Kappa was calculated. The Kappa coefficient (κ) was used to represent the overall classification agreement [64]. Kappa values range from -1 to 1 ; a value of zero indicates that the effect of the classifier equals chance agreement, and a value of 1 indicates a perfectly effective classification without a contribution from chance agreement. Any negative value indicates a poor classification in which chance agreement is more important than the classification effect. Therefore, a Kappa value of 0.75 or greater indicates a very good to excellent classification performance [65].

Table 4 contains the full contingency table as evidence of classification results for all the six SAR images. The overall classification accuracy was 90% ($\kappa = 0.81$) over the Bras

d'Henri watershed. According to classification results, frozen soils had an average classification accuracy of 87% . The highest classification accuracy of 94% was obtained for the unfrozen soils, with only two fields incorrectly classified, while five fields were incorrectly classified for frozen soils. It is apparent that the soil attributes measured in the field were better suited for discerning the near-surface frozen and unfrozen status. In the next step, classification results were compared with land use, that is, tilled versus untilled fields (Table 5). The lowest individual class accuracy of 89% ($\kappa = 0.78$) was obtained for the tilled fields. This result may be explained by the higher within-class variability resulting from a greater diversity of tillage practices and orientation settings where freezing occurred and which would have increased the backscattering signal.

Table 6 presents the classification results for each RADARSAT-1 image. The best classification accuracy (100%) was achieved when all fields were thawed (March 2005). On

TABLE 7: Radar backscattering coefficient thresholds (dB) used to differentiate frozen from unfrozen soils taking soil and land use type into account over the Bras d'Henri watershed.

Soil types (field number)	Field type	
	Tilled	Untilled
Mawcook, sandy loam (1, 2)	−10.5	−12.9
Le Bras, loam (3, 4)	−11.8	−13.1
Neubois, loam (5, 6)	−10.8	−13.2
Beaurivage, sandy loam to loamy sand (7, 12, 14)	−9.5	−13.0
Woodbridge, loam (9, 10)	−9.9	−12.8
Organic soils (11)	−9.8	— ^(a)

^(a) Because the untilled field is not represented.

TABLE 8: Distribution of frozen/unfrozen soils for the 12 radar images acquired during the three winter seasons (2003-2004 to 2005-2006) over the Bras d'Henri watershed, by land use.

Winter season	Date (dd/mm/yyyy)	Untilled frozen soils (%)	Tilled frozen soils (%)	Unfrozen soils (%)
First	08/11/2003	31	34	35
	02/12/2003	39	43	18
	19/01/2004	47	49	4
	29/02/2004	43	52	5
Second	02/11/2004	31	38	31
	13/01/2005	39	40	21
Third	08/01/2006	19	21	60
	01/02/2006	10	12	78
	25/02/2006	24	27	49
	21/03/2006	23	29	48
	14/04/2006	10	14	76
	08/05/2006	9	11	80

March 2006, two out of six frozen fields were classified as unfrozen. The resulting classification accuracy is equal to 75%.

It is important to note some limitations in applying the proposed approach. First, the mapping of frozen soil is mainly realised during winter under the presence of a snow cover. When the snow is wet, the backscattered signal cannot penetrate the snow cover, and therefore, we cannot have reliable information about the soil surface status. Thus, SAR radar images should be acquired under dry or refrozen snow cover. Second, the proposed methodology assumes that roughness parameters will be time invariant. Although this may be a reasonable assumption within the same season, it is known that roughness in agricultural fields tends to decrease over time as a result of weathering and rainfall erosion. Then, it would be necessary to have an annual map of land use. Finally, agricultural fields have a periodic row structure that affects the surface backscattering values.

4. Conclusions and Future Perspectives

In this study, a classification algorithm was developed to classify the near-surface agricultural soil under snow cover as being frozen or unfrozen using RADARSAT-1 images. The developed algorithm is based on linear regression

analysis. Regression models were performed for different soil types and land uses to identify a soil-freezing threshold. This threshold was identified by establishing a relationship between the backscattering coefficient and the soil temperature measured at 5 cm below the soil surface. The coefficient of determination obtained for the regression models varies between 0.2 and 0.96.

The developed algorithm was validated by field measurements using the Kappa index. Results indicate that there is good association between image-derived surface soil status (frozen/unfrozen) and measured field soil temperature. Results of the Kappa index show that accuracy varies between 75% and 100%. Excellent accuracy values were obtained for untitled agricultural fields. The main discrepancies are associated with later stages of snowmelt, especially in March, when the frozen and unfrozen fringe is not stable.

The studied fields were stratified into two land use classes (tilled and untitled fields). It was found that the backscattering coefficient from tilled fields was greater than that from the untitled fields. These results may indicate that surface roughness, mainly caused by soil ploughing, plays an important role. Radar signals are probably responsive to multiple bounces by the near-surface rock fragments when they penetrate a few centimetres below ground surface, in addition to the scattering due to surface roughness.

Important observations were made in the monitoring of the interannual variations of soil temperature according to the atmospheric conditions and pedological attributes, and also in the monitoring of surface status.

The conditions under which the model was developed, applied, and validated are best suited to its application in agricultural areas where the vegetation is sparse, snow cover is dry, and the surface roughness does not change during the winter. In this study, we consider that soil surface roughness is constant or slightly altered during the winter season, since no agricultural activity is undertaken. However, soil surface roughness can change from year to year due to land use changes. This does not really affect the algorithm developed here, because a land use stratification is realised before applying the classification algorithm.

Of note, for higher soil temperatures than those observed in this study, soil moisture content may decrease (the soil may be considered dry), which allows the penetration of the backscatter signal into the soil; this will decrease the backscatter coefficient. However, classification between frozen and unfrozen soils is mainly based on a small range of soil temperatures around 0°C.

The new approach developed in this study may be considered a first step for classifying soil surface frozen/unfrozen status. Clearly, additional validations should be done for other similar watersheds. Another problem concerns the status of the soil surface under wet snow. This weakness is a limiting factor, because the radar return cannot necessarily be attributed to effects from the liquid soil water content. Additional research should concentrate on the retrieval of soil frozen/unfrozen status which may include the effects of temporal surface modification. To broaden the applicability of the model to other watersheds, additional validation work is needed. In particular, future research should investigate the application of the model to a broader range of soil types and moisture conditions. Further, the method developed in this study is applied for monopolarization C-band radar image and its applicability for multipolarizations and others radar frequencies needs to be determined. Multipolarisations SAR sensors such as RADARSAT-2 (operational since May 2008) can provide input for classification schemes from different scattering mechanisms. When data is acquired in polarimetric mode, both the amplitude and phase information of the SAR signal are retained; the use of this information provides input for classification algorithms. Hence, it will be possible to extract information on land use directly from images, which may make it possible to systematically update land cover maps and monitor land conditions.

Acknowledgments

This study is cofinanced by Agriculture and Agri-Food Canada and the Canadian Space Agency through the Government Related Initiative Program (GRIP). The authors gratefully acknowledge Dr. Karem Chokmani, Yves Gauthier, Stéphane Savary, Veronique Beaulieu, and Lisa-Marie Pâquet from INRS-ETE, Nadia Goussard, Mario Deschênes, and André Martin from AAFC, and the agri-environmental

counsellors of the *Club de fertilisation de la Beauce* for their expertise and technical assistance.

References

- [1] N. C. Hansen, S. C. Gupta, and J. F. Moncrief, "Snowmelt runoff, sediment, and phosphorus losses under three different tillage systems," *Soil and Tillage Research*, vol. 57, no. 1-2, pp. 93–100, 2000.
- [2] G. Y. Niu and Z. L. Yang, "Effects of frozen soil on snowmelt runoff and soil water storage at a continental scale," *Journal of Hydrometeorology*, vol. 7, no. 5, pp. 937–952, 2006.
- [3] G. Bélanger, Y. Castonguay, A. Bertrand et al., "Winter damage to perennial forage crops in eastern Canada: causes, mitigation, and prediction," *Canadian Journal of Plant Science*, vol. 86, no. 1, pp. 33–47, 2006.
- [4] B. Ulén, "Concentrations and transport of different forms of phosphorus during snowmelt runoff from an illite clay soil," *Hydrological Processes*, vol. 17, no. 4, pp. 747–758, 2003.
- [5] D. C. Garen and D. S. Moore, "Curve number hydrology in water quality modeling: uses, abuses, and future directions," *Journal of the American Water Resources Association*, vol. 41, no. 2, pp. 377–388, 2005.
- [6] E. Van Bochove, G. Thériault, P. Rochette, H. G. Jones, and J. W. Pomeroy, "Thick ice layers in snow and frozen soil affecting gas emissions from agricultural soils during winter," *Journal of Geophysical Research*, vol. 106, no. 19, pp. 23061–23071, 2001.
- [7] K. M. Hinkel, R. F. Paetzold, F. E. Nelson, and J. G. Bockheim, "Patterns of soil temperature and moisture in the active layer and upper permafrost at Barrow, Alaska: 1993–1999," *Global and Planetary Change*, vol. 29, no. 3-4, pp. 293–309, 2001.
- [8] U. Hillard, V. Sridhar, D. P. Lettenmaier, and K. C. McDonald, "Assessing snow melt dynamics with NASA scatterometer (NSCAT) data and a hydrologic process model," *Remote Sensing of Environment*, vol. 86, no. 1, pp. 52–69, 2003.
- [9] H. G. Jones, J. W. Pomeroy, D. A. Walker, and R. W. Hoham, *Snow Ecology: An Interdisciplinary Examination of Snow-Covered Ecosystems*, Cambridge University Press, Cambridge, Mass, USA, 2001.
- [10] J. Khaldoune, M. Bernier, E. Van Bochove, and M. C. Nolin, "Détection du gel et non-gel du sol en utilisant le radar polarimétrique à synthèse d'ouverture," *Canadian Journal of Remote Sensing*, vol. 34, no. 4, pp. 418–429, 2008.
- [11] T. Zhang and R. L. Armstrong, "Soil freeze/thaw cycles over snow-free land detected by passive microwave remote sensing," *Geophysical Research Letters*, vol. 28, no. 5, pp. 763–766, 2001.
- [12] B. Zuerndorfer and A. W. England, "Radiobrightness decision criteria for freeze/thaw boundaries," *IEEE Transactions on Geoscience and Remote Sensing*, vol. 30, no. 1, pp. 89–102, 1992.
- [13] F. Bonn and G. Rochon, *Précis de Télédétection: Principes et Méthodes. Vol. 1*, Presse de l'Université du Québec/AUPELF, Ste-Foy, Québec, Canada, 1992.
- [14] C. François, C. Ottlé, and L. Prévot, "Analytical parameterization of canopy directional emissivity and directional radiance in the thermal infrared. Application on the retrieval of soil and foliage temperatures using two directional measurements," *International Journal of Remote Sensing*, vol. 18, no. 12, pp. 2587–2621, 1997.

- [15] B. Coudert, C. Ottlé, and X. Briottet, "Monitoring land surface processes with thermal infrared data: calibration of SVAT parameters based on the optimisation of diurnal surface temperature cycling features," *Remote Sensing of Environment*, vol. 112, no. 3, pp. 872–887, 2008.
- [16] J. L. Davis and A. P. Annan, "Ground-penetrating radar for high-resolution mapping of soil and rock stratigraphy," *Geophysical Prospecting*, vol. 37, no. 5, pp. 531–551, 1989.
- [17] A. Pietroniro and R. Leconte, "A review of Canadian remote sensing applications in hydrology, 1995–1999," *Hydrological Processes*, vol. 14, no. 9, pp. 1641–1666, 2000.
- [18] M. Bernier and J. P. Fortin, "The potential of times series of C-band SAR data to monitor dry and shallow snow cover," *IEEE Transactions on Geoscience and Remote Sensing*, vol. 36, no. 1, pp. 226–243, 1998.
- [19] Y. Crevier, T. J. Pultz, T. I. Lukowski, and T. Toutin, "Temporal analysis of ERS-1 SAR backscatter for hydrology applications," *Canadian Journal of Remote Sensing*, vol. 22, no. 1, pp. 65–76, 1996.
- [20] D. W. Leverington and C. R. Duguay, "A neural network method to determine the presence or absence of permafrost near Mayo, Yukon Territory, Canada," *Permafrost and Periglacial Processes*, vol. 8, no. 2, pp. 205–215, 1997.
- [21] C. Lagacé and M. Bernier, "Développement d'une approche pour faire le suivi du gel saisonnier du sol sur le bassin de la rivière La Grande à partir de l'utilisation conjointe d'images SSM/I et RADARSAT," in *Proceedings of the 57th Eastern Snow Conference*, Syracuse, NY, USA, 2000.
- [22] M. T. Hallikainen, F. T. Ulaby, M. C. Dobson, M. A. El-Rayes, and L. K. Wu, "Microwave dielectric behavior of wet soil—part I: empirical models and experimental observations," *IEEE Transactions on Geoscience and Remote Sensing*, vol. 23, no. 1, pp. 25–34, 1985.
- [23] F. T. Ulaby, R. K. Moore, and A. K. Fung, *Microwave Remote Sensing: Active and Passive: Volume III*, Artech House, Dedham, Mass, USA, 1986.
- [24] C. Elachi, *Introduction to the Physics and Techniques of Remote Sensing*, John Wiley & Sons, New York, NY, USA, 1987.
- [25] E. J. M. Rignot, J. B. Way, C. Williams, and L. Viereck, "Radar estimates of aboveground biomass in boreal forests of interior Alaska," *IEEE Transactions on Geoscience and Remote Sensing*, vol. 32, no. 5, pp. 1117–1124, 1994.
- [26] C. Doussan, L. Jouniaux, and J. L. Thony, "Variations of self-potential and unsaturated water flow with time in sandy loam and clay loam soils," *Journal of Hydrology*, vol. 267, no. 3–4, pp. 173–185, 2002.
- [27] E. T. Engman and N. Chauhan, "Status of microwave soil moisture measurements with remote sensing," *Remote Sensing of Environment*, vol. 51, no. 1, pp. 189–198, 1995.
- [28] Y. Gauthier, "Détection par radar des zones à risque de gel pour les luzernières," in *Actes du Colloque, Nouvelles Technologies en Agriculture*, pp. 135–139, St-Jean-sur-Richelieu, Centre de Télédétection en Agro-Environnement, 1997.
- [29] J. B. Way, R. Zimmermann, E. Rignot, K. McDonald, and R. Oren, "Winter and spring thaw as observed with imaging radar at BOREAS," *Journal of Geophysical Research*, vol. 102, no. 24, pp. 29673–29684, 1997.
- [30] C. Lagacé, M. Bernier, and Y. Gauthier, "Cartographie du gel saisonnier du sol de taïga à partir d'images RSO de RADARSAT-1 et SSM/I de DMSP F-8," *Télédétection*, vol. 2, no. 3, pp. 161–175, 2001.
- [31] F. T. Ulaby, R. K. Moore, and A. K. Fung, *Microwave Remote Sensing: Active and Passive: Vol. 1. Fundamentals and Radiometry*, Artech House, Dedham, Mass, USA, 1982.
- [32] K. Boehnke and V. Wismann, "ERS scatterometer land applications: detecting soil thawing in Siberia," *Earth Observation Quarterly*, vol. 52, pp. 4–7, 1996.
- [33] V. Wismann, "Monitoring of seasonal snowmelt on Greenland with ERS scatterometer data," *IEEE Transactions on Geoscience and Remote Sensing*, vol. 38, no. 4, pp. 1821–1826, 2000.
- [34] J. S. Kimball, K. C. McDonald, A. R. Keyser, S. Froking, and S. W. Running, "Application of the NASA scatterometer (NSCAT) for determining the daily frozen and nonfrozen landscape of Alaska," *Remote Sensing of Environment*, vol. 75, no. 1, pp. 113–126, 2001.
- [35] L. -C. Lundin, "Hydraulic properties in an operational model of frozen soil," *Journal of Hydrology*, vol. 118, no. 1–4, pp. 289–310, 1990.
- [36] A. Musy and M. Soutter, *Physique du Sol*, Presses polytechniques et universitaires Romandes, Lausanne, Switzerland, 1991.
- [37] L. Nyberg, M. Stähli, P. E. Mellander, and K. Bishop, "Soil frost effects on soil water and runoff dynamics along a boreal forest transect: field investigations," *Hydrological Processes*, vol. 15, no. 6, pp. 909–926, 2001.
- [38] J. F. Villaseñor, D. R. Fatland, and L. D. Hinzman, "Change detection on Alaska's north slope using repeat-pass ERS-1 SAR images," *IEEE Transactions on Geoscience and Remote Sensing*, vol. 31, no. 1, pp. 227–236, 1993.
- [39] T. J. Pultz, Y. Crevier, R. J. Brown, and J. Boisvert, "Monitoring local environment conditions with SIR-C/X-SAR," *Remote Sensing of Environment*, vol. 59, no. 2, pp. 248–255, 1997.
- [40] J. B. Boisvert, Q. H. J. Gwyn, A. Chanzy, D. J. Major, B. Brisco, and R. J. Brown, "Effect of surface soil moisture gradients on modelling radar backscattering from bare fields," *International Journal of Remote Sensing*, vol. 18, no. 1, pp. 153–170, 1997.
- [41] N. Baghdadi, P. Paillou, G. Grandjean, P. Dubois, and M. Davidson, "Relationship between profile length and roughness variables for natural surfaces," *International Journal of Remote Sensing*, vol. 21, no. 17, pp. 3375–3381, 2000.
- [42] M. Zribi and M. Dechambre, "A new empirical model to retrieve soil moisture and roughness from C-band radar data," *Remote Sensing of Environment*, vol. 84, no. 1, pp. 42–52, 2003.
- [43] M. M. Rahman, M. S. Moran, D. P. Thoma et al., "A derivation of roughness correlation length for parameterizing radar backscatter models," *International Journal of Remote Sensing*, vol. 28, no. 18, pp. 3995–4012, 2007.
- [44] Q. P. Xu, J. B. Boisvert, N. Tremblay, F. Bonn, and R. J. Brown, "Évaluation des hyperfréquences pour le suivi de la teneur en eau et des cultures dans les histosols," *Canadian Journal of Remote Sensing*, vol. 24, no. 1, pp. 43–53, 1998.
- [45] H. Geng, Q. H. J. Gwyn, B. Brisco, J. B. Boisvert, and R. J. Brown, "Mapping of soil moisture from C-band radar images," *Canadian Journal of Remote Sensing*, vol. 22, no. 1, pp. 117–126, 1996.
- [46] L. Lamontagne, A. Martin, and M. C. Nolin, "Étude pédologique du bassin versant du Bras d'Henri (Québec)," Laboratoires de pédologie et d'agriculture de précision, Centre de recherche et de développement sur les sols et les grandes cultures, Service national d'information sur les terres et les eaux. Direction générale de la recherche. Agriculture et Agroalimentaire Canada, Québec, Canada, 2009.
- [47] L. Lamontagne and M. C. Nolin, *Cadre Pédologique de Référence pour la Corrélation des Sols*, Bulletin d'extension numéro 7, Équipe pédologique du Québec, Centre de recherches et de développement sur les sols et les grandes cultures, Agriculture et Agroalimentaire Canada, Sainte-Foy, Canada, 1997.

- [48] G. C. Topp, "Soil water content," in *Soil Sampling and Methods of Analysis*, M. R. Carter, Ed., pp. 541–557, Canadian Society of Soil Science, Lewis Publishers, Boca Raton, Fla, USA, 1993.
- [49] Soil Classification Working Group, *The Canadian System of Soil Classification*, Agriculture and Agri-Food Canada, Ottawa, Canada, 3rd edition, 1998, Publication 1646 (Revised).
- [50] A. K. Fung and K. S. Chen, "Dependence of the surface backscattering coefficients on roughness, frequency and polarization states," *International Journal of Remote Sensing*, vol. 13, no. 9, pp. 1663–1680, 1992.
- [51] N. Baghdadi, C. King, A. Bourguignon, and A. Remond, "Potential of ERS and Radarsat data for surface roughness monitoring over bare agricultural fields: application to catchments in Northern France," *International Journal of Remote Sensing*, vol. 23, no. 17, pp. 3427–3442, 2002.
- [52] N. Holah, N. Baghdadi, M. Zribi, A. Bruand, and C. King, "Potential of ASAR/ENVISAT for the characterization of soil surface parameters over bare agricultural fields," *Remote Sensing of Environment*, vol. 96, no. 1, pp. 78–86, 2005.
- [53] T. Toutin, "La correction géométrique rigoureuse : un mal nécessaire pour la santé de vos résultats," *Canadian Journal of Remote Sensing*, vol. 22, no. 2, pp. 184–189, 1996.
- [54] H. Rott and G. Domik, "The SAR-580 experiment on snow and glaciers at the Austrian test site," Final Report, European SAR-580 Campaign, JRC, Ispra, Italy, 1984.
- [55] N. Baghdadi, C. E. Livingstone, and M. Bernier, "Airborne C-band SAR measurements of wet snow-covered areas," *IEEE Transactions on Geoscience and Remote Sensing*, vol. 36, no. 6, pp. 1977–1981, 1998.
- [56] V. S. Frost, J. A. Stiles, K. S. Shanmugan, and J. C. Holtzman, "A model for radar images and its application to adaptive digital filtering of multiplicative noise," *IEEE Transactions on Pattern Analysis and Machine Intelligence*, vol. 4, no. 2, pp. 157–165, 1982.
- [57] F. T. Ulaby, P. P. Batlivala, and M. C. Dobson, "Microwave backscatter dependence on surface roughness, soil moisture and soil texture—part I. Bare soil," *IEEE Transaction on Geoscience Electronics*, vol. 16, pp. 286–295, 1978.
- [58] R. D. Martin Jr., A. Ghansem, and E. T. Kanemasu, "C-band scatterometer measurements of a tall grass prairie," *Remote Sensing of Environment*, vol. 29, no. 3, pp. 281–292, 1989.
- [59] L. P. Simmonds and E. J. Burke, "Estimating near-surface soil water content from passive microwave remote sensing—an application of MICRO-SWEAT," *Hydrological Sciences Journal*, vol. 43, no. 4, pp. 521–534, 1998.
- [60] M. Bernier, J. P. Fortin, Y. Gautier, R. Gautier, R. Royand, and P. Vincent, "Determination of snow water equivalent using radarsat data in eastern Canada," *Hydrological Processes*, vol. 13, no. 18, pp. 3041–3051, 1999.
- [61] K. M. Hinkel and S. I. Outcalt, "Identification of heat-transfer processes during soil cooling, freezing, and thawing in central Alaska," *Permafrost and Periglacial Processes*, vol. 5, no. 4, pp. 217–235, 1994.
- [62] R. Paquin, "Survie à l'hiver des plantes fourragères et des céréales sous les climats nordiques, en particulier au Québec: progrès et perspectives," *Phytoprotection*, vol. 66, pp. 105–139, 1985.
- [63] T. Zhang, T. E. Osterkamp, and K. Stamnes, "Influence of the depth hoar layer of the seasonal snow cover on the ground thermal regime," *Water Resources Research*, vol. 32, no. 7, pp. 2075–2086, 1996.
- [64] Y. M. M. Bishop, S. E. Fienberg, and P. W. Holland, *Discrete Multivariate Analysis: Theory and Practice*, MIT Press, Cambridge, UK, 1975.
- [65] R. A. Montserud and R. Leamans, "Comparing global vegetation maps with the Kappa statistic," *Ecological Modelling*, vol. 62, no. 4, pp. 275–293, 1992.

Research Article

Comparisons of Brightness Temperatures of Landsat-7/ETM+ and Terra/MODIS around Hotien Oasis in the Taklimakan Desert

Yoshinari Oguro,¹ Seiji Ito,¹ and Kiyoshi Tsuchiya²

¹ Department of Global Environment Studies, Hiroshima Institute of Technology, 2-1-1, Miyake, Saeki-ku, Hiroshima 731-5193, Japan

² Japan Meteorological Consultant Association, 6-32-10, Hirai, Edogawa-ku, Tokyo 132-0035, Japan

Correspondence should be addressed to Yoshinari Oguro, y.oguro.yx@it-hiroshima.ac.jp

Received 15 December 2010; Revised 22 February 2011; Accepted 20 March 2011

Academic Editor: Michel C. Nolin

Copyright © 2011 Yoshinari Oguro et al. This is an open access article distributed under the Creative Commons Attribution License, which permits unrestricted use, distribution, and reproduction in any medium, provided the original work is properly cited.

The brightness temperature (BT) of Taklimakan Desert retrieved from the data of Landsat-7/ETM+ band 6 and Terra/MODIS band 31 and 32 indicates the following features: (1) good linear relationship between the BT of ETM+ and that of MODIS, (2) the observation time adjusted BT of ETM+ is almost equal to that of MODIS, (3) the BT of Terra/MODIS band 31 is slightly higher than that of band 32 over a reservoir while opposite feature is recognized over desert area, (4) the statistical analysis of 225 sample data of ETM+ in one pixel of MODIS for different landcovers indicates that the standard deviation and range of BT of ETM+ corresponding to one pixel of MODIS are 0.45°C, 2.25°C for a flat area of desert, while respective values of the oasis farmland and shading side of rocky hill amount to 2.88°C, 14.04°C, and 2.80°C, 16.04°C.

1. Introduction

The brightness temperatures (BTs) retrieved from the data of thermal infrared (TIR) bands of the sensors onboard Terra, Aqua, and meteorological satellites are widely used in the study of global warming including energy flux between land surface and the atmosphere, while there are not a few demands for the BT retrieved from the TIR band of Landsat-7/ETM+ (Enhanced Thematic Mapper Plus). The spatial resolution of the data of the TIR band of Landsat-7/ETM+ is approximately 60 m which is a great advantage for the study of meso and small scale phenomena however it is extremely difficult to get satisfactory data due to long repeat cycle of 16 days [1, 2]. On the other hand, in case of Terra/MODIS (MODerate resolution Imaging Spectroradiometer) and Aqua/MODIS the TIR band data can be acquired almost in daily basis although the spatial resolution is approximately 1000 m [3, 4].

For the reflective solar bands, the data of the surface reflectance of Terra/MODIS were analyzed together with the data of Landsat-7/ETM+ and confirmed that the absolute

error of the land surface products was less than 5% [5]. In addition, the intercalibration between the reflected bands of Landsat-7/ETM+ and those of Terra/MODIS was performed for the vegetation analysis [6]. Based on these analyses, it was concluded that the reflectance bands of Landsat-7/ETM+ and Terra/MODIS have good linear relationship.

For TIR bands the level-2 MODIS land surface temperature (LST) product of 1 km spatial resolution (MOD11_L2) obtained from the TIR bands 31 and 32 of Terra/MODIS it was confirmed that the error of LST products ranging from 263 K (−10°C) to 322 K (49°C) is less than 1 K for the atmospheric column water vapor ranging from 0.4 to 3.0 cm [3]. Furthermore it was also confirmed that the error of the daily level-3 MODIS LST product of 1 km spatial resolution (MOD11A1 Version 5 for Terra and MYD11A1 Version 5 for Aqua) obtained from the same bands of both Terra and Aqua/MODIS was less than 1 K in the range from 263 K (−10°C) to 331 K (58°C) for the atmospheric column water vapor ranging from 0.4 to 3.5 cm [7].

The objective of this paper is to compare the BT of selected targets of Taklimakan Desert in China observed with

TABLE 1: Satellite specification of Landsat-7 and Terra.

Satellite	Sensor	Launch date	Altitude (km)	Inclination (degrees)	Swath (km)	Repeat cycle (days)	Crossing time (UTC)
Landsat-7	ETM+	April 15, 1999	705	98.2	185	16	10:00–10:15 (Descending node)
Terra	MODIS	December 18, 1999	705	98.2	2330	1-2	10:30 (Descending node)

TABLE 2: Band specification of the TIR bands of Landsat-7/ETM+ and Terra/MODIS.

Satellite	Sensor	Band	Center wavelength				
			Spectral range (μm)	For spectral range (μm)	For cumulative histogram at 50% of RSR (μm)	Spectral radiance ($\text{W}/(\text{m}^2 \cdot \text{sr} \cdot \mu\text{m})$)	Spatial resolution (m)
Landsat-7	ETM+	6	10.31–12.36	11.335	11.217	8.20 (LG) 6.09 (HG)	60
Terra	MODIS	31	10.78–11.28	11.030	11.011	9.55 (300 K)	1000
		32	11.77–12.27	12.020	12.027	8.94 (300 K)	

Note that LG and HG for Landsat-7/ETM+ indicate the low gain and the high gain, respectively.

the TIR bands of Landsat-7/ETM+ and Terra/MODIS and to clarify the relationship between the BT obtained from both sensors.

2. Analysis Data and Study Area

2.1. Data Analysis. The specification of Landsat-7 [2] and Terra [4] is shown in Table 1, which indicates that the orbits of two satellites are almost same and the observation time difference is within 30 minutes. The specification of TIR band of Landsat-7/ETM+ and Terra/MODIS is shown in Table 2. The relative spectral response (RSR) of band 6 (TIR band) of ETM+ [1, 2, 5] and bands 31 and 32 of MODIS [4, 8] is shown in Figure 1. The separation of RSR of MODIS band 31 and 32 is good which suggests the effectiveness of split-window (SW) method [9] to retrieve BT of the land surface. The major difference of two sensors is spatial and spectral resolution, swath width, and repeating cycle.

The instrument malfunction occurred on the Scan Line Corrector (SLC) of Landsat-7/ETM+ on May 31, 2003 subsequently SLC was turned off, and now only SLC-off mode data are acquired [2, 10]. In this study, we decided to analyze SLC-on mode data of ETM+ acquired before May 31, 2003. To reduce the shading effects on the BT of the land surface of vegetated area the data of higher sun elevation were selected.

2.2. Study Area. The study area is around Hotien Oasis of the southwestern part of Taklimakan Desert in Xinjiang, China. Covering the area between 74°E and 96°E, 36°N and 43°N Taklimakan Desert is the largest sandy desert in Asia with the area of about 270,000 km² [11, 12]. The main reasons of having chosen the area are

- (1) During a fairly large-scale research project “Japan-China Joint Study on Desertification (1989–1994)”, using a hand-held radiometer we have collected abundantly the land surface and underground temperature data of this area together with near surface meteorological data and also radio sounding data.
- (2) Surrounded by high mountain ranges with average height of 1200 meter above sea level the area is characterized with extremely dry atmospheric condition resulting in very little effect of water vapor.
- (3) Locating between two rivers, the Karakax River and the Yurungkax River, Hotien Oasis is the largest oasis in the southern part of the desert [13, 14]. There is a good weather station equipped with radio sounding facilities, land surface, and underground temperature observing facilities. This area was one of the major target areas of concentrated observation during the joint study.

The analyzed satellite data of Landsat-7/ETM+ and Terra/MODIS over and around Hotien Oasis are shown in Table 3, while the false color images of Landsat-7/ETM+ (R, B, G: bands 4, 3, and 2) and Terra/MODIS (R, G, B: bands 7, 2, and 1) over the Hotien Oasis in Taklimakan Desert observed on June 8, 2002 are shown in Figure 2. In addition, the observation areas of Landsat-7/ETM+ and Terra/MODIS are shown in Figure 3. The range of sensor nadir angles of Landsat-7/ETM+ is approximately ranging from 7.28° (west) to 7.28° (east) and that of Terra/MODIS is approximately ranging from 9.51° (west) to 8.09° (east). Furthermore, the data of meteorological observation of Hotien station is shown in Table 4.

TABLE 3: Analyzed data of Landsat-7/ETM+ and Terra/MODIS over the Hotien Oasis in Taklimakan Desert.

Satellite	Sensor	Product type	Acquisition date	Scene ID	Scan time (UTC)	Sun azimuth (degrees)	Sun elevation (degrees)
Landsat-7	ETM+	Level 1T	June 8, 2002	146-034 (Path-Row)	05:05:01 (Scene center)	119.65	65.23
Terra	MODIS	MOD021KM	June 8, 2002	13148 (Orbit number)	05:35–05:40	130.56–135.53	69.51–70.61

TABLE 4: The metrological observation on June 8, 2002 at the Hotien station (ID: ZWTN).

Time	Pressure (hPa)	Air temperature (°C)	Relative humidity (%)	Perceptible water (mm)	Visibility (km)	Wind speed (km/h)
00Z	858	21.2	28	15.28	—	—
12Z	851	35.2	28	6.76	—	—
—	854.3 (Mean)	27.9 (Mean) 20.1 (Min.) 35.8 (Max.)	21 (Mean)	0 (Precipitation amount)	15 (Mean)	10.7 (Mean) 14.4 (Max.)

Note that international station number 51828, 37.13°N, 79.93°E, and 1375 m (above sea level).

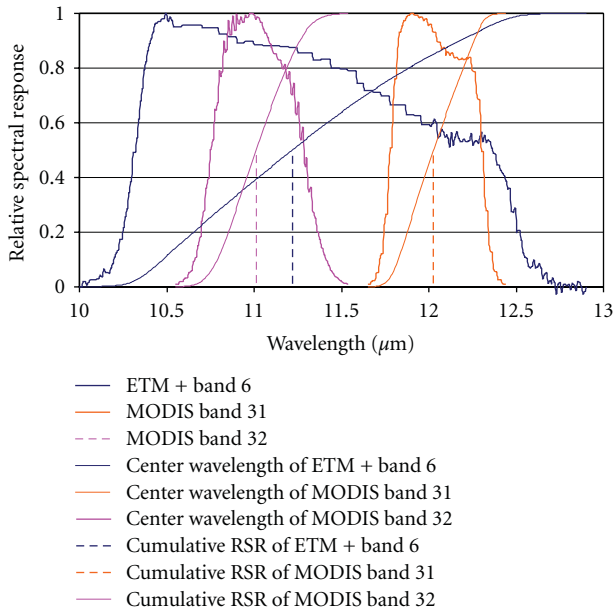


FIGURE 1: Characteristics of band 6 of ETM+, Terra MODIS bands 31 and 32.

3. Data Processing

3.1. Conversion of Landsat-7/ETM+ Band 6 Data to BT. Conversion of calibrated digital numbers (Q_{cal}) of Landsat-7/ETM+ Level-one Terrain-corrected (L1T) products back to observed spectral radiance (L_{λ}) requires the minimum and maximum limit of the original rescaling factors $L_{min\lambda}$ and $L_{max\lambda}$. The pre-launch calibration constants of the TIR band 6 of Landsat-7/ETM+ for converting Q_{cal} to observed

spectral radiance are shown in Table 5. The conversion equation [2, 15] is

$$\begin{aligned}
 L_{\lambda} &= \left(\frac{L_{max\lambda} - L_{min\lambda}}{Q_{calmax} - Q_{calmin}} \right) (Q_{cal} - Q_{calmin}) + L_{min\lambda} \\
 &= G_{rescale} \times Q_{cal} + B_{rescale}, \\
 G_{rescale} &= \left(\frac{L_{max\lambda} - L_{min\lambda}}{Q_{calmax} - Q_{calmin}} \right), \\
 B_{rescale} &= L_{min\lambda} - \left(\frac{L_{max\lambda} - L_{min\lambda}}{Q_{calmax} - Q_{calmin}} \right) Q_{calmin},
 \end{aligned} \tag{1}$$

where L_{λ} is observed spectral radiance in $W/(m^2 \cdot sr \cdot \mu m)$, Q_{cal} is quantized calibrated pixel value in digital numbers of 8 bits unsigned integer data, Q_{calmin} is minimum quantized calibrated pixel value corresponding to $L_{min\lambda}$, Q_{calmax} is maximum quantized calibrated pixel value corresponding to $L_{max\lambda}$, $L_{min\lambda}$ is observed spectral radiance scaled to Q_{calmin} in $W/(m^2 \cdot sr \cdot \mu m)$, $L_{max\lambda}$ is observed spectral radiance scaled to Q_{calmax} in $W/(m^2 \cdot sr \cdot \mu m)$, $G_{rescale}$ is band-specific rescaling gain factor in $W/(m^2 \cdot sr \cdot \mu m)$, and $B_{rescale}$ is band-specific rescaling bias factor in $W/(m^2 \cdot sr \cdot \mu m)$.

The data of the TIR band 6 of Landsat-7/ETM+ can be converted from observed spectral radiance (L_{λ}) to observed BT. The conversion equation [2, 15] is

$$T_6 = \frac{K_2}{\ln((K_1/L_{\lambda}) + 1)}, \tag{2}$$

where T_6 is observed BT in Kelvin, K_1 is calibration constant 1 (666.09 $W/(m^2 \cdot sr \cdot \mu m)$), K_2 is calibration constant 2 (1282.71 K) and L_{λ} is observed spectral radiance in $W/(m^2 \cdot sr \cdot \mu m)$.

TABLE 5: Calibration constants of the TIR band of Landsat-7/ETM+ for converting calibrated digital numbers to observed spectral radiance.

Band	$L_{\max\lambda}$ ($W/(m^2 \cdot sr \cdot \mu m)$)	$L_{\min\lambda}$ ($W/(m^2 \cdot sr \cdot \mu m)$)	G_{rescale} ($W/(m^2 \cdot sr \cdot \mu m)/Q_{\text{cal}}$)	B_{rescale} ($W/(m^2 \cdot sr \cdot \mu m)$)
6 (Low gain)	0.0	17.04	0.067087	-0.07
6 (High gain)	3.2	12.65	0.037205	3.16

Note that Q_{cal} is calibrated digital numbers.

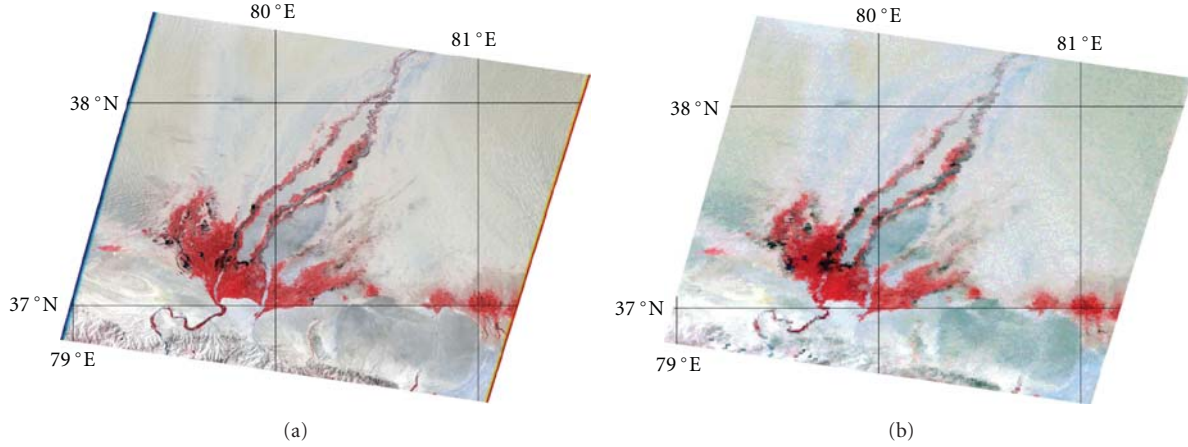


FIGURE 2: False color images of Landsat-7/ETM+ (R, B, G: bands 4, 3, and 2) (a) and Terra/MODIS (R, G, B: bands 7, 2, and 1) (b) over the Hotien Oasis in Taklimakan Desert observed on June 8, 2002. The geographic locations of the four corners (clockwise starting at the top left) of the image are UL (38.45°N, 78.87°E), UR (38.47°N, 81.70°E), LR (36.49°N, 78.92°E), and LL (36.50°N, 81.68°E). In the false color images, yellow is sandy desert and sand dunes, gray is desert of stones and pebbles, white is rocks, red is farmlands and grasslands, and black is water of river and reservoir.

TABLE 6: Calibration constants of the TIR bands of Terra/MODIS data (MOD021KM, Collection 5) for converting SI to observed spectral radiance.

Band	$R_{\text{scale}\lambda}$ ($W/(m^2 \cdot sr \cdot \mu m)$)	$R_{\text{offset}\lambda}$
31	0.00084002200	1577.3397
32	0.00072969760	1658.2212

Note that: SI is scaled integer.

3.2. Conversion of Terra/MODIS Bands 31 and 32 Data to BT. Conversion of the scaled integer (SI) values of the Scientific Data Sets (SDSs) of Terra/MODIS Level 1B Version 5.0 products back to observed spectral radiance (L_λ) requires the lower and upper limit of the original rescaling factors R_{scale} and R_{offset} written as attributes of SDSs. The pre-launch calibration constants of the TIR bands of Terra/MODIS 1 km spatial resolution data (MOD021KM, Collection 5) for converting SI to observed spectral radiance are shown in Table 6. The conversion equation [4] is

$$\begin{aligned}
 L_\lambda &= R_{\text{scale}\lambda}(SI_\lambda - R_{\text{offset}\lambda}), \\
 R_{\text{scale}\lambda} &= \frac{L_{\max\lambda} - L_{\min\lambda}}{32767}, \\
 R_{\text{offset}\lambda} &= -\frac{32767 \times L_{\min\lambda}}{L_{\max\lambda} - L_{\min\lambda}},
 \end{aligned} \quad (3)$$

where L_λ is observed spectral radiance in $W/(m^2 \cdot sr \cdot \mu m)$, SI_λ is scaled integer value of 16 bits unsigned integer data in

Dimensionless, $L_{\min\lambda}$ is observed spectral radiance scaled to 0 in $W/(m^2 \cdot sr \cdot \mu m)$, $L_{\max\lambda}$ is observed spectral radiance scaled to 32767 in $W/(m^2 \cdot sr \cdot \mu m)$, $R_{\text{scale}\lambda}$ is radiance rescaling gain factor in $W/(m^2 \cdot sr \cdot \mu m)$, and $R_{\text{offset}\lambda}$ is radiance rescaling offset factor in Dimensionless.

The data of the TIR bands 31 and 32 of Terra/MODIS can be converted from observed spectral radiance (L_λ) to observed BT applying the Planck's law of blackbody radiation. The conversion equation [4] is

$$T = \frac{hc/k\lambda}{\ln(2hc^2/(L_\lambda\lambda^5 \times 10^{-6}) + 1)}, \quad (4)$$

where T is observed BT in Kelvin, h is Planck constant ($6.62606896 \times 10^{-34}$ J·s), c is speed of light (2.99792458×10^8 m/s), k is Boltzmann constant ($1.3806504 \times 10^{-23}$ J/K), λ is center wavelength in meter, and L_λ is observed spectral radiance in $W/(m^2 \cdot sr \cdot \mu m)$.

From (2) and (4), the center wavelengths of the TIR band 6 of Landsat-7/ETM+ can be estimated as follows:

$$\begin{aligned}
 K_1 &= \frac{2hc^2}{\lambda_1^5 \times 10^{-6}} \Leftrightarrow \lambda_1 = 11.2167 \mu m, \\
 K_2 &= \frac{hc}{k\lambda_2} \Leftrightarrow \lambda_2 = 11.2326 \mu m, \\
 \bar{\lambda} &= \frac{(\lambda_1 + \lambda_2)}{2} = 11.2247 \mu m.
 \end{aligned} \quad (5)$$

The estimated center wavelength of the TIR band 6 of Landsat-7/ETM+ is nearly equal to the center wavelength

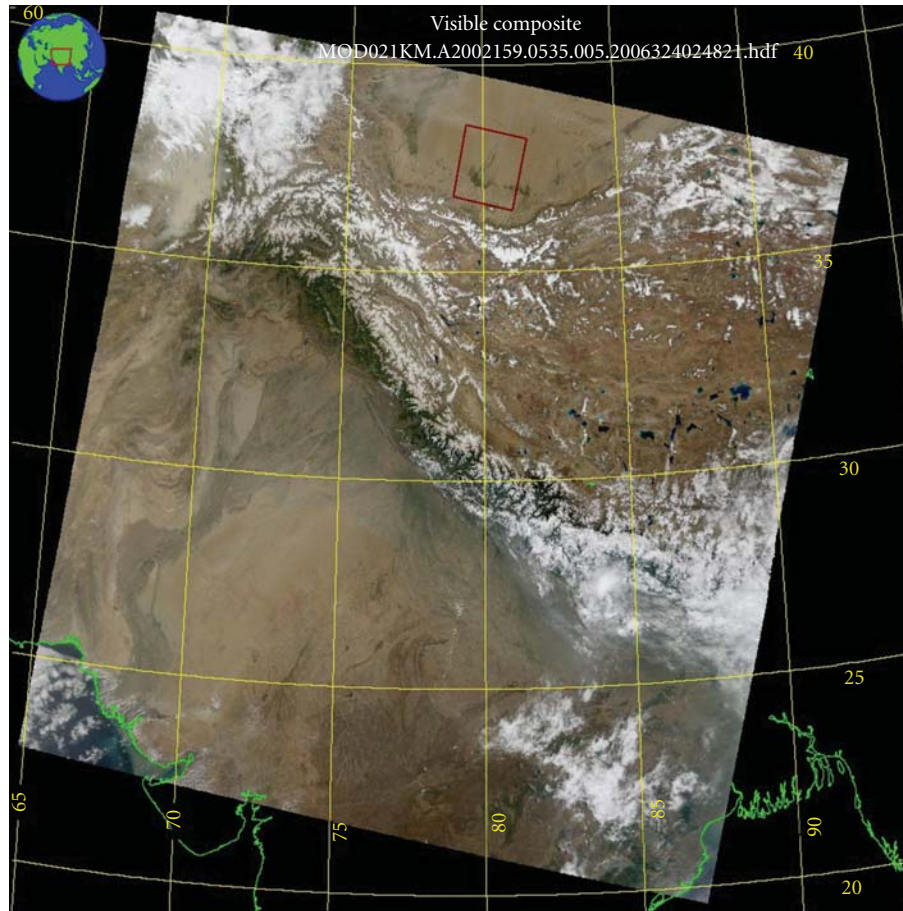


FIGURE 3: True color image of Terra/MODIS (R, G, B: bands 1, 4, and 3) observed at UTC 05:35 on June 8, 2002. The red rectangle indicates the observation area of Landsat-7/ETM+ on June 8, 2002 (Path-Row: 146-034).

obtained from the cumulative histogram at 50% of RSR as shown in Table 2.

4. Results and Discussion

4.1. Rough Analysis of the Entire BT of the Images. BT of Landsat-7/ETM+ band 6 and that of Terra/MODIS bands 31 and 32 were computed by (2) and (4), respectively. BT images over Hotien Oasis acquired on June 8, 2002 of Landsat-7/ETM+ band 6, Terra/MODIS bands 31 and 32 are shown in Figure 4. The geographic locations of the four corners are same as those in Figure 2. From Figure 4 it is found that the range of BT is approximately 20–60°C. In addition, BT of desert of Terra/MODIS band 32 image seems a little higher than the other images. An example of the surface temperature observed with a hand-held radiometer in the desert around the Hotien Oasis at 10:30–11:00 (local time) on September 26, 1992 is shown in Figure 5. The retrieved value seems to be reasonable in referring to these LSTs although the observation year and day are different.

4.2. Detailed Analysis of BT's Retrieved from the Data of Band 6 of ETM+ and MODIS Bands 31 and 32. For accurate

comparison of BT's retrieved from the data of band 6 of ETM+ and MODIS bands 31 and 32, following data processing was performed:

(1) correction of geometric distortions of the data in reference to the ground control points which had been accumulated during the Japan-China Joint Study of Desertification; (2) resampling of MODIS data of 1 km × 1 km size to make 900 m × 900 m pixels so that each MODIS pixel contains exactly 225 ETM+ (60 m × 60 m) pixels; since the difference of the sizes of the original and resampled pixels is small the Nearest Neighborhood Method was adopted for resampling; (3) five clear pixels of MODIS were selected from each category of landcover within the area of ETM+ image; (4) for each of 20 landcover categories, statistical values such as mean, standard deviation, maximum and minimum values, ranges, and ratios of the number of samples belonging to m (mean) ± 1 and 2σ (standard deviation) of 20 categories were computed for each of 5 ETM+ images corresponding to 5 selected pixels of MODIS image; (5) the average values of the items listed above were computed from the above stated 5 ETM+ image samples and shown in Table 7. The means of MODIS Bands 31 and 32 were computed from 5 pixels of each landcover category.

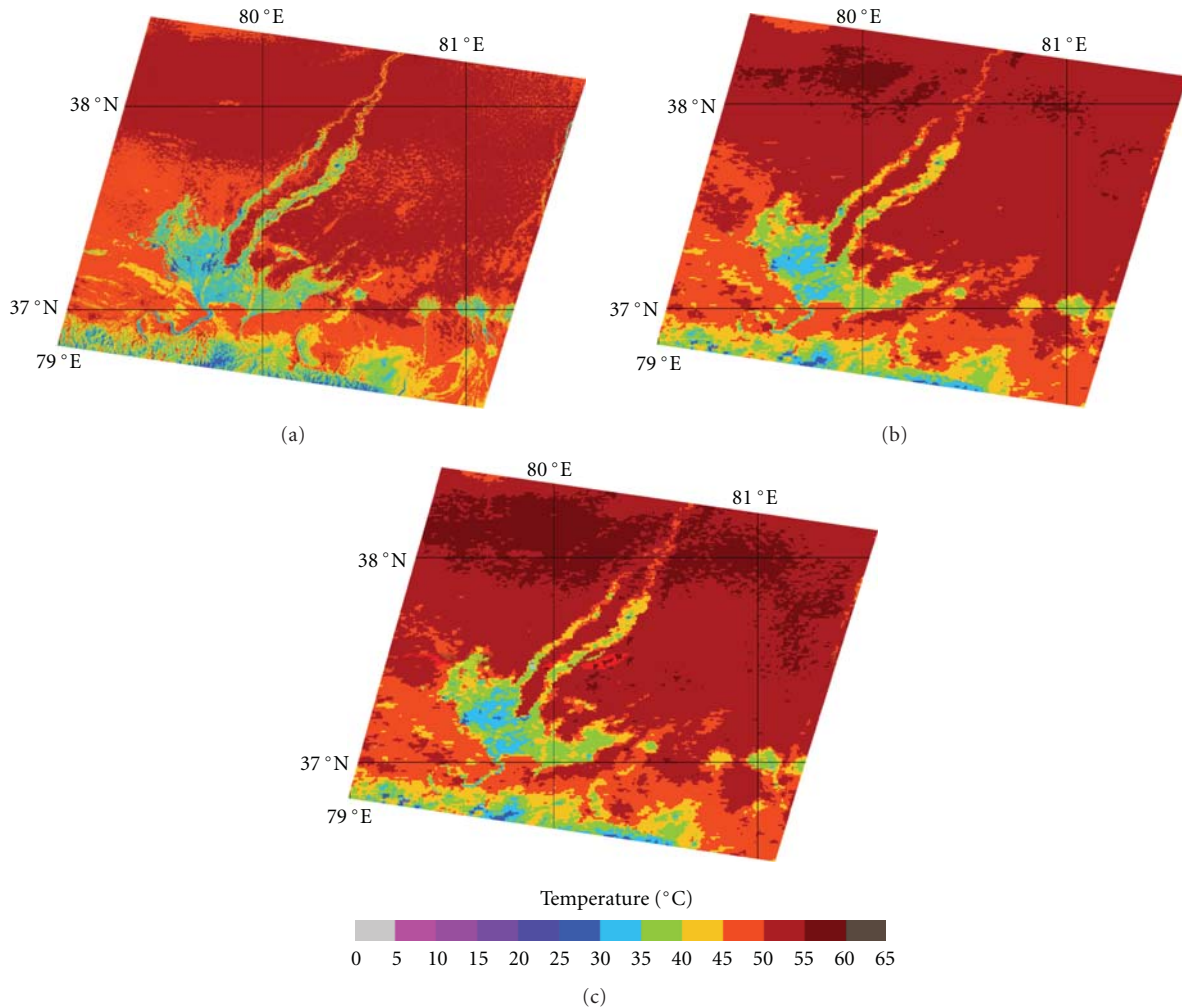


FIGURE 4: Brightness temperature images of Landsat-7/ETM+ band 6 (a), Terra/MODIS bands 31 (b), and 32 (c) over the Hotien Oasis in Taklimakan Desert observed on June 8, 2002. The geographic locations of the four corners are the same as in Figure 2.

Although it is clear from the table some noteworthy features of the BTs of ETM+ will be pointed out.

- (A) Surprisingly large range for specific targets: 16.04°C for shading side of rocky hill and 14.04°C for the oasis farmland, while comparatively small range for a flat desert with the value of 2.25°C . The reason of large range of the oasis farmland is due to the fact that subdivided farmlands are surrounded with tall wind and sand break forests. The low temperatures of the tree leaves and shadows of the forests contribute to the large range.
- (B) Reflecting the large values of ranges, the shading side of rocky hill and the oasis farmland show large standard deviation. The oasis farmland shows the largest value of 2.88°C while the flat desert shows the smallest value of 0.45°C . Since number of sample of MODIS is only 5 the standard deviation of MODIS data was not computed.
- (C) As to BT the observation time of MODIS is nearer to the local noon than that of ETM+ by about 30 min-

utes therefore the BTs of MODIS is generally higher than those of ETM+ except sunny side of rocky hills and the beach of the upper reach of the large river which have slightly higher BTs than MODIS. The reason is that the slope of the sunny side of these places with a favorable orientation for the sun received more sun radiation and was warmed up than other places.

- (D) Among the BTs of ETM+ for different landcover categories the top 3 ranking BTs of the target in the descending order is (1) sandy desert and sand dunes, (2) grassland and river beach of the lower reach of the large river, and (3) desert of stone and pebble, and rocky hill (sunny side) while the top 3 bottom ranking in the ascending order is (1) reservoir, (2) oasis farmland with scattered bare land, and (3) rocky hill with dry vegetation (shading side).
- (E) As to the distribution of the samples of ETM+ the distribution for the following categories shows semi-normal distribution: sunny side rocky hills, oasis farmland with scattered bright bare land and grass land near the upper reach of the large river.

TABLE 7: Summary of statistical analysis of the brightness temperature samples of ETM+ corresponding to one pixel of MODIS. In the table #1 σ and #2 σ are the ratio (%) of the numbers of samples of ETM+ in ($m \pm 1\sigma$) and ($m \pm 2\sigma$), respectively, in the area of one pixel of MODIS.

Name	ETM+							MODIS	
				Band 6				Band 31	Band 32
	Mean	Std.D.	Min.	Max.	Range	#1σ%	#2σ%	Mean	Mean
Desert (flat)	51.55	0.45	50.37	52.62	2.25	64.11	97.04	53.73	54.63
Area of small sand dune	50.21	0.58	48.76	51.79	3.03	61.22	95.89	52.22	53.28
Area of large sand dune	50.63	0.50	48.60	52.79	4.19	64.78	96.91	53.79	54.62
Desert of stone and pebble (bright)	45.70	0.54	44.01	46.96	2.95	77.53	96.80	47.20	47.82
Desert of stone and pebble (dark)	45.47	0.67	43.92	47.14	3.22	61.13	96.33	46.24	46.71
Rocky hill (sunny side)	45.11	1.67	39.92	49.60	9.68	67.66	96.42	44.61	45.14
Rocky hill (shading side)	35.28	2.80	29.66	45.70	16.04	71.64	95.13	39.19	39.25
Rocky hill with dry vegetation (sunny side)	40.83	1.90	34.54	45.36	10.82	69.78	95.62	40.01	40.25
Rocky hill with dry vegetation (shading side)	33.59	1.65	29.32	39.03	9.71	63.89	97.07	36.29	36.21
Oasis farmland	37.00	2.88	30.59	44.63	14.04	66.42	96.18	38.73	38.43
Oasis farmland with scattered bright bare land	32.65	2.31	29.04	41.08	12.04	70.49	95.33	34.41	34.17
Oasis farmland withscattered dark bare land	32.52	2.20	28.64	38.65	10.01	63.02	97.42	33.59	33.45
Oasis farmland with paved roads	40.30	2.09	33.63	45.07	11.44	67.18	96.11	41.30	41.48
Urban area with paved roads	42.05	1.39	37.75	45.59	7.84	67.62	96.36	43.08	43.11
Grassland near lower reach of large river	48.59	2.20	42.67	51.96	9.29	64.56	97.47	50.98	50.98
Grassland near upper reach of large river	40.70	2.08	35.78	45.66	9.88	68.44	96.07	40.98	41.16
River beach of lower reach of large river	48.63	1.64	41.53	51.38	9.85	70.09	96.67	49.82	50.36
River beach of upper reach of large river	41.92	1.07	37.71	45.24	7.53	76.96	94.98	41.22	41.84
Reservoir	23.84	0.98	22.50	30.71	8.21	77.91	96.40	26.89	26.17
Total (Mean)	41.40	1.56	37.31	45.84	8.53	68.11	96.33	42.86	43.11

m: mean, σ : standard deviation, unit of BT: °C, #1 σ = $m \pm 1\sigma$, #2 σ = $m \pm 2\sigma$, samples of ETM+: 225.

4.3. *Linearity between BT of Landsat-7/ETM+ and Terra/MODIS.* The relations between BT of Landsat-7/ETM+ band 6 and Terra/MODIS bands 31 and 32 are shown in Figures 6 and 7, respectively. In these figures, it can be seen that BT of Landsat-7/ETM+ and that of Terra/MODIS bands 31 and 32 indicate high correlations, and the correlation coefficients are approximately 0.97. The regression equations between Landsat-7/ETM+ band 6 and Terra/MODIS band 31 and 32 are

$$\begin{aligned} T_{31} &= 0.9625 \times T_6 + 3.0097 \quad (\text{for Terra/MODIS band 31}), \\ T_{32} &= 1.0140 \times T_6 + 1.1312 \quad (\text{for Terra/MODIS band 32}). \end{aligned} \quad (6)$$

4.4. *Effects of the Emissivity of the Targets and the Atmosphere to the BTs of MODIS Bands 31 and 32.* An attempt is made to estimate the effects of emissivity of the targets and the atmosphere to the BTs by introducing two adjustment parameters α and β into (2) and (4) as are shown in (7) and (8), respectively.

$$T_6 = \frac{K_2}{\ln((\alpha\beta K_1/L_\lambda) + 1)}, \quad (7)$$

$$T = \frac{hc/k\lambda}{\ln(\alpha\beta 2hc^2/(L_\lambda\lambda^5 \times 10^{-6}) + 1)} \quad (8)$$

where α is adjustment parameter to atmospheric effect, β is adjustment parameter to emissivity effect.

The land cover classification image over the study area is shown in Figure 8. The emissivity and pixel number of each category of the TIR bands of Terra/MODIS is shown in Table 8. The values of emissivity are taken from the paper by Wan [7]. The large part of the study area is occupied with bare land and rock, and the overall emissivity of the study area to Terra/MODIS bands 31 and 32 are 0.967 and 0.973, respectively.

The estimation result of overall BT of the study area is shown in Table 9. The value of α is function of the extinction coefficient of the atmosphere which is influenced by the amount of water vapor, dust, and minute sands blown up by the dust devil which frequently occurs in the area. Under such condition, it is difficult to obtain exact value of the extinction coefficient therefore two values of 1.000 and 1.032 for α are adopted in the computation. As to the value of β of ETM+ band 6, the average value of those of MODIS band 31 and 32 is adopted.

From Table 9, it can be concluded that the difference of BT between Landsat-7/ETM+ and Terra/MODIS is the observation time difference. On the other hand, it is concluded that in the difference of BT of Terra/MODIS bands 31 and 32, the atmospheric effect is approximately 0.21°C and the emissivity effect is approximately 0.35°C.

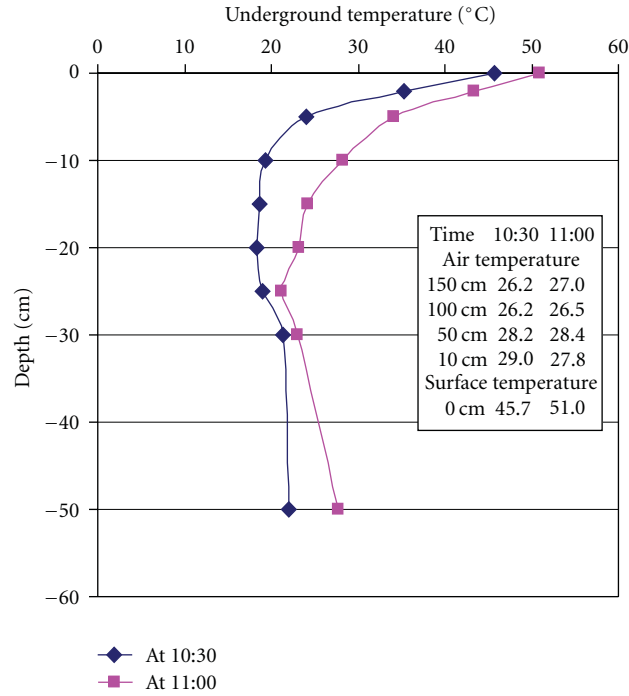


FIGURE 5: Examples of the surface and underground temperature together with the near surface air temperature distribution at 10:30 and 11:00 local time. The data at 10:30 were acquired at a flat area with sparsely grown short tamalix and reed while those of 11:00 were acquired at the top of a small sand dune of several meters height with scarcely grown short reed in Taklimakan Desert. The height of both places is 1200 m above sea level.

TABLE 8: The values of referred emissivity of the TIR bands of Terra/MODIS.

Legend	ϵ_{31}	ϵ_{32}	Pixels	Ratio%	$\Delta \epsilon_{31}$	$\Delta \epsilon_{32}$
Water	0.992	0.988	7200	0.02	0.00015	0.00015
Evergreen needleleaf forest	0.987	0.989	0	0.00	0.00000	0.00000
Evergreen broadleaf forest	0.981	0.984	0	0.00	0.00000	0.00000
Deciduous needleleaf forest	0.987	0.989	0	0.00	0.00000	0.00000
Deciduous broadleaf forest	0.981	0.984	0	0.00	0.00000	0.00000
Mixed forest	0.981	0.984	0	0.00	0.00000	0.00000
Woody savannas	0.982	0.985	0	0.00	0.00000	0.00000
Savannas	0.983	0.987	2700	0.01	0.00006	0.00006
Closed shrubland	0.983	0.980	284400	0.61	0.00603	0.00601
Open shrubland	0.972	0.976	3760082	8.11	0.07884	0.07916
Grassland	0.983	0.987	1763562	3.80	0.03739	0.03755
Cropland	0.983	0.987	524245	1.13	0.01112	0.01116
Bare soil and rocks	0.965	0.972	40008359	86.30	0.83281	0.83885
Urban and built-up	0.970	0.976	8100	0.02	0.00017	0.00017
Total	—	—	46358648	100.00	0.96657	0.97312

Note: $\Delta \epsilon = \epsilon \times \text{ratio}$.

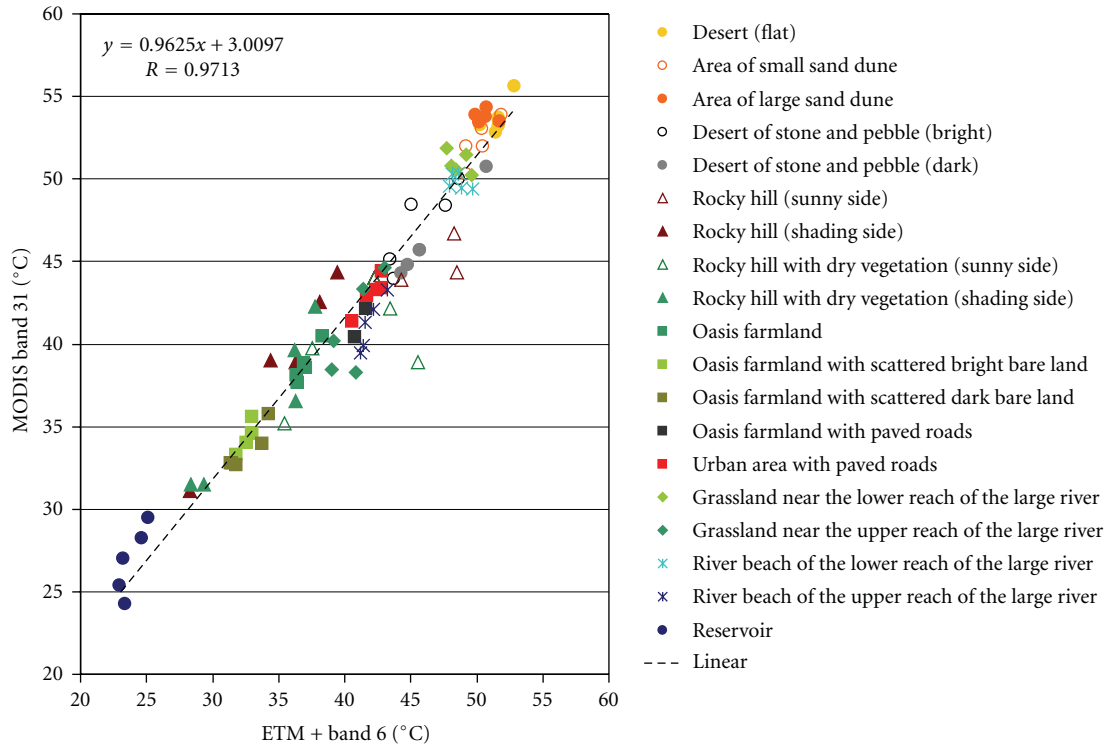


FIGURE 6: Comparison between the brightness temperatures obtained from band 6 of Landsat-7/ETM+ and Terra/MODIS band 31.

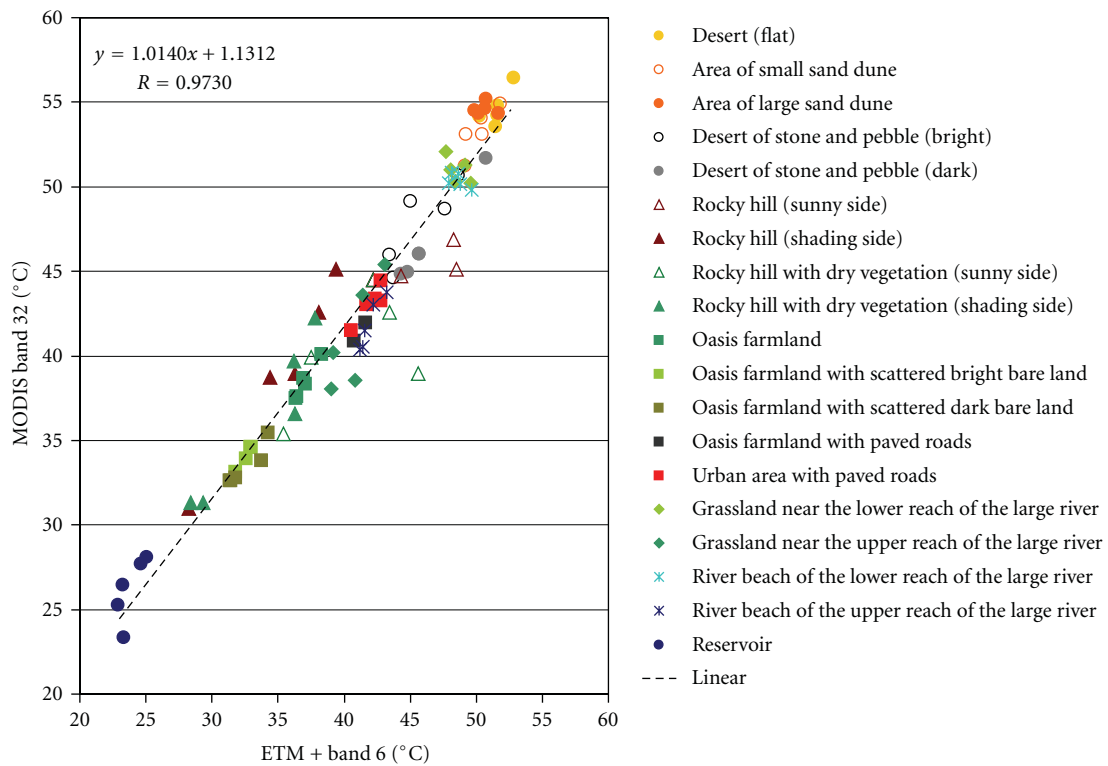


FIGURE 7: Comparison between the brightness temperatures obtained from band 6 of Landsat-7/ETM+ and Terra/MODIS band 32.

TABLE 9: The values of various factors adopted in the evaluation of the effects of emissivity and atmosphere to the value of brightness temperatures.

Adjustment parameters α and β	L_6 (W/(m ² ·sr· μ m))	L_{31} (W/(m ² ·sr· μ m))	L_{32} (W/(m ² ·sr· μ m))	BT ₆ °C	BT ₃₁ °C	BT ₃₂ °C	BT ₃₁ – BT ₃₂ °C
$\alpha = 1.000$ $\beta = 1.000$	12.35	12.95	11.92	47.02	49.01	49.57	–0.56
$\alpha = 1.000$ $\beta_6 = 0.970$ $\beta_{31} = 0.967$ $\beta_{32} = 0.973$	12.73	13.40	12.25	49.44	51.69	51.90	–0.21
$\alpha = 1.032$ $\beta_6 = 1.000$ $\beta_{31} = 1.000$ $\beta_{32} = 1.000$	11.96	12.55	11.55	44.56	46.57	46.91	–0.35
$\alpha = 1.032$ $\beta_6 = 0.970$ $\beta_{31} = 0.967$ $\beta_{32} = 0.973$	12.34	12.98	11.87	46.94	49.21	49.21	0.00

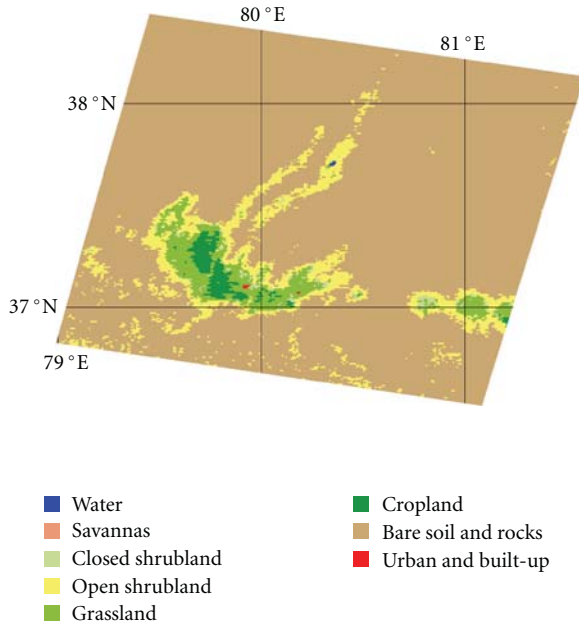


FIGURE 8: Land cover classification image [16]. The geographic locations of the four corners are the same as in Figure 2.

5. Conclusion

The result of the analysis lead to the following conclusions

- (1) good linear relationship between the retrieved BT from the data of Landsat-7/ETM+ band 6 and those of Terra/MODIS bands 31 and 32;
- (2) BT retrieved from the data of Terra/MODIS is slightly higher than that of Landsat-7/ETM+, however considering the observation time of Terra/MODIS is approximately 30 minutes nearer to the noon, it can be concluded that the value of BT of Terra/MODIS

will be equal to that of Landsat-7/ETM+ if adjustment for the observation time difference is made;

- (3) comparing of the retrieved BT of the targets from the observed data of Terra/MODIS band 31 and 32, the values of band 31 are slightly higher than that of band 32 over the water while with opposite trend over the desert and vegetated area;
- (4) the standard deviation and range of BT of ETM+ corresponding to one pixel of MODIS are 0.45°C, 2.25°C for a flat area of desert while respective values of the oasis farmland and shading side of rocky hill amount to 2.88°C, 14.04°C, and 2.80°C, 16.04°C.

Acknowledgments

Authors' sincere gratitude is due to three anonymous reviewers for their very precise comments and valuable suggestions. They are also very grateful to NASA for allowing them to use MODIS data freely.

References

- [1] G. Chander, D. J. Meyer, and D. L. Helder, "Cross calibration of the landsat-7 ETM+ and EO-1 ALI sensor," *IEEE Transactions on Geoscience and Remote Sensing*, vol. 42, no. 12, pp. 2821–2831, 2004.
- [2] NASA's Goddard Space Flight Center, "Landsat 7 Science Data Users Handbook-Data Products," http://landsathandbook.gsfc.nasa.gov/pdfs/Landsat7_Handbook.pdf.
- [3] Z. Wan, Y. Zhang, Q. Zhang, and Z. L. Li, "Validation of the land-surface temperature products retrieved from terra moderate resolution imaging spectroradiometer data," *Remote Sensing of Environment*, vol. 83, no. 1–2, pp. 163–180, 2002.
- [4] Members of the MODIS Characterization Support Team, *MODIS Level 1B Product User's Guide*, NASA/Goddard Space Flight Center, Greenbelt, Md, USA, December 2003, <http://mcst.gsfc.nasa.gov/l1b>.

- [5] S. Liang, H. Fang, M. Chen et al., "Validating MODIS land surface reflectance and albedo products: methods and preliminary results," *Remote Sensing of Environment*, vol. 83, no. 1–2, pp. 149–162, 2002.
- [6] N. Rochdi and R. Fernandes, "Intercalibration of vegetation indices from landsat etm+ and modis 500m data for lai mapping," Technical Note 3, pp. 1–11, Geomatics, Canada, 2008.
- [7] Z. Wan, "New refinements and validation of the MODIS land-surface temperature/emissivity products," *Remote Sensing of Environment*, vol. 112, no. 1, pp. 59–74, 2008.
- [8] Z. Wan, Y. Zhang, Q. Zhang, and Z. L. Li, "Quality assessment and validation of the MODIS global land surface temperature," *International Journal of Remote Sensing*, vol. 25, no. 1, pp. 261–274, 2004.
- [9] J. M. Galve, C. Coll, V. Caselles, and E. Valor, "An atmospheric radiosounding database for generating land surface temperature algorithms," *IEEE Transactions on Geoscience and Remote Sensing*, vol. 46, no. 5, pp. 1547–1557, 2008.
- [10] J. Storey, P. Scaramuzza, G. Schmidt, and J. Barsi, "Landsat 7 scan line corrector-off gap-filled product development," in *Proceedings of Pecora 16th Global Priorities in Land Remote Sensing*, American Society for Photogrammetry and Remote Sensing, Sioux Falls, SD, USA, 2005.
- [11] T. Ishiyama, N. Saito, S. Fujikawa, K. Ohkawa, and S. Tanaka, "Ground surface conditions of oases around the Taklimakan Desert," *Advances in Space Research*, vol. 39, no. 1, pp. 46–51, 2007.
- [12] A. Buhe, K. Tsuchiya, M. Kaneko, N. Ohtaishi, and M. Halik, "Land conver of oases and forest in XinJiang, China retrieved from ASTER data," *Advances in Space Research*, vol. 39, no. 1, pp. 39–45, 2007.
- [13] Y. Oguro, S. Takeuchi, and K. Tsuchiya, "Development of environmental dataset of Taklamakan Desert by TERRA/AQUA MODIS data," in *Proceedings of the 26th Asian Conference on Remote Sensing (ACRS '05)*, p. 22, Hanoi, Vietnam, November 2005.
- [14] K. Tsuchiya and Y. Oguro, "Observation of large fixed sand dunes of Taklimakan Desert using satellite imagery," *Advances in Space Research*, vol. 39, no. 1, pp. 60–64, 2007.
- [15] G. Chander, B. L. Markham, and D. L. Helder, "Summary of current radiometric calibration coefficients for landsat MSS, TM, ETM+, and EO-1 ALI sensors," *Remote Sensing of Environment*, vol. 113, no. 5, pp. 893–903, 2009.
- [16] M. C. Hansen, R. S. Defries, J. R. G. Townshend, and R. Sohlberg, "Global land cover classification at 1 km spatial resolution using a classification tree approach," *International Journal of Remote Sensing*, vol. 21, no. 6-7, pp. 1331–1364, 2000.

Research Article

Use of Imaging Spectroscopy for Mapping and Quantifying the Weathering Degree of Tropical Soils in Central Brazil

Gustavo M. M. Baptista,¹ Rodrigo S. Corrêa,^{2,3} Perseu F. dos Santos,^{3,4} José S. Madeira Netto,⁵ and Paulo R. Meneses¹

¹Geosciences Institute, University of Brasília, 70910-900 Brasília, DF, Brazil

²Department of Ecology, University of Brasília, 70910-900 Brasília, DF, Brazil

³Environmental Planning and Management Program, Catholic University of Brasília, 72030-170 Brasília, DF, Brazil

⁴College of Arts and Science, New Mexico State University, Las Cruces, NM 88003, USA

⁵Brazilian Agricultural Research Corporation, Embrapa 70770-901 Brasília, DF, Brazil

Correspondence should be addressed to Gustavo M. M. Baptista, gmbaptista@unb.br

Received 13 November 2010; Revised 15 February 2011; Accepted 3 March 2011

Academic Editor: Michel C. Nolin

Copyright © 2011 Gustavo M. M. Baptista et al. This is an open access article distributed under the Creative Commons Attribution License, which permits unrestricted use, distribution, and reproduction in any medium, provided the original work is properly cited.

The purpose of this study was to test the feasibility of applying AVIRIS sensor (Airborne Visible/InfraRed Imaging Spectrometer) for mapping and quantifying mineralogical components of three Brazilian soils, a reddish Oxisol in São João D'Aliança area (SJA) and a dark reddish brown Oxisol and Ultisol in Niquelândia (NIQ) counties, Goiás State. The study applied the spectral index RCGb [kaolinite/(kaolinite + gibbsite) ratio] and was based on spectral absorption features of these two minerals. The RCGb index was developed for the evaluation of weathering degrees of various Brazilian soils and was validated by the analysis of soil samples spectra imaged by AVIRIS and checked against laboratory mineralogical quantification (TGA: Thermal Gravimetric Analysis). Results showed to be possible mapping and quantifying the weathering degree of the studied soils and that the two selected areas presented different weathering degrees of their soils even for a same soil type.

1. Introduction

Soil is a product of forming factors such as parent material, climate, time, organisms, and topography. The great variability in soils results from interactions of these factors and their influence on the formation of different soil profiles. Mineral types and their proportions in soils are also dependable on soil-forming factors and have strong influence on agriculture, forestry, soil engineering, among others [1].

Tropical soil contain mineralogical variations that cannot be perceived in field works. The determination of soil mineral composition depends on laboratory analysis of soil samples collected in field, and an extrapolation of the representativeness of the results to a broader area depends on landscape morphological characteristics and accuracy of the field work [2]. For cartographic purposes, the spatial distribution of values from point-sampled minerals is done by using morphological criteria in correlation with topography, parent material, and other parameters.

Reliable criteria to discriminate soils with varied amounts of kaolinite and gibbsite do not exist, and the quantification of these two minerals in soils demands systematic samplings with high-density points. Because this procedure greatly increases costs of soil surveys, new techniques and resources that can ease pedological surveys are strongly desirable. Recent advances in remote sensing with the image spectroscopy appear to be a promising alternative in soil science. However, most of the optical remote sensing means cannot detect the entire soil body ("pedon") that extends from the surface to the parent material, and the thin, upper soil layer that is eventually sensed by optical sensors may be affected by many factors such as dust, rust, plowing, particle size distribution, vegetation coverage, litter, and physical and biogenic crusts. Thus, optical remote sensing of soils from far distances is a challenge [1].

Laboratory spectral analysis and multispectral data analysis have been utilized to detect the occurrence of some soil main components [2–18]. It is well known that a wide range

of soil constituents such as the total iron, water content, mechanical compositions, carbonate, and organic carbon can be derived through reflectance spectroscopy under laboratory conditions [1]. Many studies have pointed out the possibility of using hyperspectral images to display the occurrence and variation in concentrations of minerals in some pedological sequences in tropical environments, expanding the contribution of these new remote sensing products to soil research studies [1, 19–32]. In this sense, one of the most important factors for mapping pedological environments is to spatialized and map different degrees of soil weathering. A spatial differentiation in mineralogy is important for elucidating soil genesis processes, determining the most appropriate management systems, and classifying soils.

Soil formation in the tropics (i.e. Oxisols) is characterized by the remotion of SiO_2 , followed by the increase in Al_2O_3 concentration. The weathering degree of a soil is usually depicted by the Ki index, which is the molecular ratio of SiO_2 to Al_2O_3 . In the RCGb index kaolinite/(kaolinite + gibbsite), kaolinite $[\text{Al}_2\text{Si}_2\text{O}_5(\text{OH})_4]$ represents the SiO_2 leftover and gibbsite $[\text{Al}(\text{OH})_3]$ represents the Al_2O_3 concentration in soils [27].

Therefore, the purpose of this study was to evaluate the feasibility of applying a hyperspectral sensor (AVIRIS) for mapping and quantifying the weathering degree of some Brazilian soils.

2. Material and Methods

2.1. AVIRIS Sensor. AVIRIS (*Airborne Visible/InfraRed Imaging Spectrometer*) is one of the hyperspectral sensors that currently operate. It is an aerotransported system consisting of four spectrometers that continuously image at 0.4 to $2.5\ \mu\text{m}$ range of the optical reflected spectrum, on 224 bands, with approximate width of 10 nm, owned by the *Jet Propulsion Laboratory* (JPL/NASA). It was the first hyperspectral sensor to image Brazilian soils, and it has been used for rock, soil, vegetation, water, and snow mapping in many countries.

2.2. RCGb Spectral Index. Many hyperspectral sensors can detect kaolinite and gibbsite in soils but the presence of Al_2O_3 in both of the minerals spoils the use of Ki index (molecular ratio of $[\text{SiO}_2]/[\text{Al}_2\text{O}_3]$) in remote sensing. Therefore, indexes derived from Ki have been proposed to make possible the use of remote sensing for soil mapping [2]. The spectral index RCGb(kaolinite/kaolinite + gibbsite) used in this work was proposed by Baptista [33, Equation 1]. It is based on the spectral features of kaolinite and gibbsite and the values obtained with RCGb index have been showed to be proportional to Ki values. One can use the RCGb with either radiance (R) or reflectance (R) spectra because the spectral features of kaolinite and gibbsite are present in both spectra (1).

$$\text{RCGb} = \frac{((R_{2,127} + R_{2,226})/2 - (R_{2,176} + R_{2,196})/2)}{((R_{2,127} + R_{2,226})/2 - (R_{2,176} + R_{2,196})/2) + ((R_{2,226} + R_{2,286})/2 - R_{2,266})}, \quad (1)$$

where R is the radiance ($\text{W} \cdot \text{m}^{-2} \cdot \text{sr}^{-1}$) or reflectance value (%) in various wavelengths adapted to the AVIRIS' bands.

Validation of the RCGb spectral index adopted the same reflectance spectra analyzed by Madeira Netto [2] for 56 soil samples that correspond to the surface and deeper layers of 27 soil profiles [27]. Out of the 56 spectra, four samples with opaque minerals were removed, although these minerals have an influence on the determination of the RCGb spectral index. However, they are not a factor that impedes applicability, although they do slightly reduce the RCGb index efficiency [33]. The correlation factor between the RCGb index and Ki values for the 52 samples was $r = 0.93$, $P < .01$.

2.3. Study Areas. The study imaged areas considered a red-dish Oxisol transect in São João D'Aliança (SJA), a dark reddish brown Oxisol, and an Ultisol in Niquelândia (NIQ) counties, Goiás State, central part of Brazil (Figure 1). Most of the differences measured between hyperspectral images and their targets are rather explained by spectral calibration uncertainties, like relative radiometric calibration and errors in atmospheric correction, particularly when regarding water vapor, which has significant absorption features in the spectral domains (2143–2269 nm) used for clay content estimations [34]. In this regard, Baptista [33] found no significant differences between radiance images

and reflectance data corrected by the Green's method [35] or by Atmospheric Removal Program (ATREM) [36, 37] for Brazilian soil minerals. Therefore, the radiance raw data were neither corrected for atmospheric effects nor reduced to scaled surface reflectance of in this study.

The RCGb spectral index was applied to the concatenated AVIRIS data (Figure 2), as they were obtained on the same day with less than 1/2 hour between acquisitions—the flight over São João D'Aliança (SJA) and Niquelândia (NIQ) counties, Goiás State, Brazil. As neither image presented clouds, and the official website of the SCAR-B mission (<http://asd-www.larc.nasa.gov/scar/scarb.html> in June 8th 2000) considered the atmospheric conditions of the entire flight on that day to be “slight mist, no clouds, small fires, one large fire,” it was assumed that the atmospheric conditions did not significantly vary from one image to the other. Working scale was based on AVIRIS spatial dimension of 20 m and which correspond to 1:50,000.

A topological sequence was chosen in SJA (13 imaged plots, 1–13) and another in NIQ area (17 imaged plots, 1–17; Figure 2). The distance between surveying plots was of 100 m (Figure 2), covering 1.2 km in SJA and 1.6 km in NIQ. Soil samples were collected between 0–20 cm soil depth from the same sequence with an auger for mineralogical analyses in laboratory (Thermal Gravimetric Analysis, TGA).

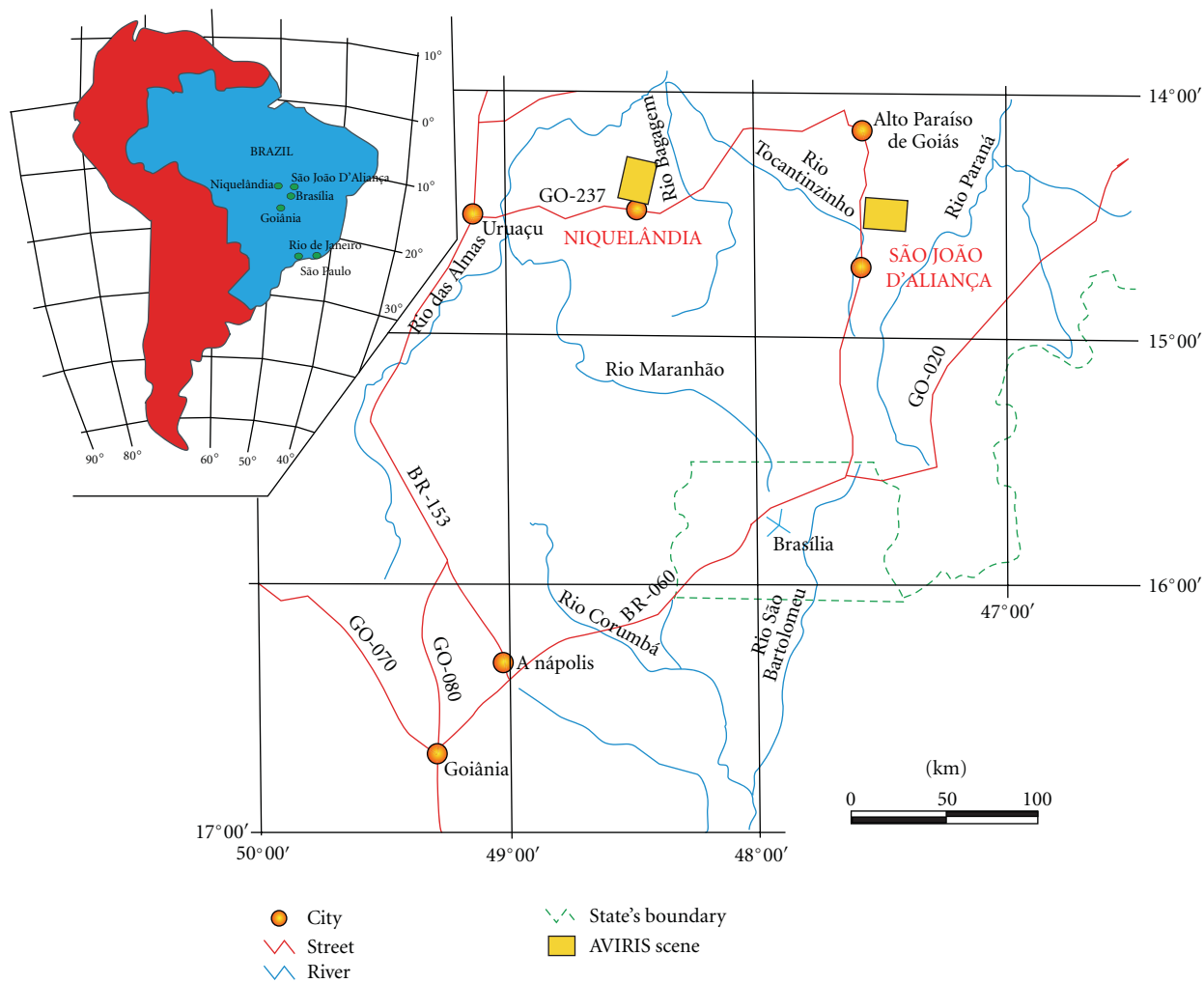


FIGURE 1: Study areas in central Brazil.

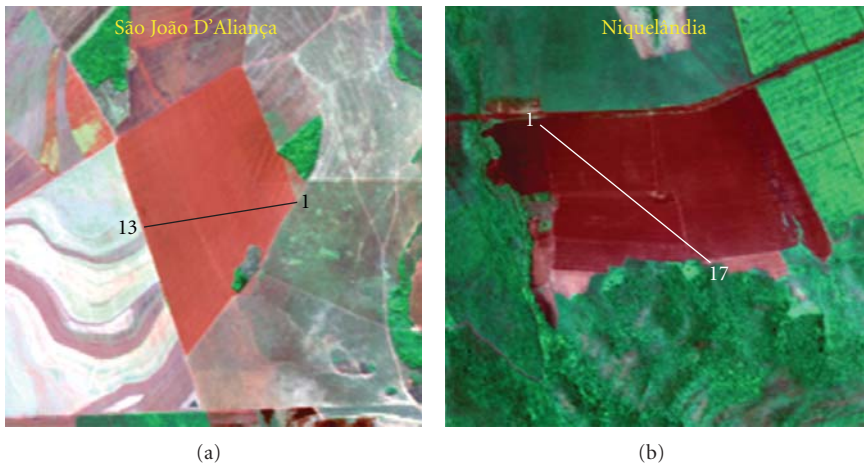


FIGURE 2: AVIRIS images of the areas, showing differences in soil grey scale due to either the absence (SJA) or the presence (NIQ) of opaque minerals (1:50,000).

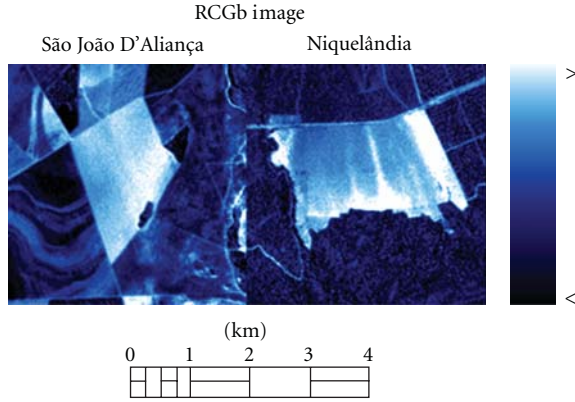


FIGURE 3: Spatial distribution of RCGb values in SJA and NIQ.

Comparisons between AVIRIS and TGA data were done by statistical methods, and AVIRIS data were then scaled for correction purposes for quantifying the weathering degree of the soils.

Response units of the two procedures (AVIRIS and TGA) to determine the RCGb refer to index, and the use of parametric tests is not appropriated. Thus, the Mann-Whitney test was used to compare the two sets of data [38].

3. Results and Discussion

The greater the value of RCGb, the greater the presence of silica in soils (represented by the kaolinite). On the other hand, lower values of RCGb show a tendency for greater amounts of alumina (gibbsite) to be present in soils. There was not an apparent variation in soil color that suggests no different weathering degrees of soils in the areas (Figure 2). But the application of RCGb index showed that the soils of São João D'Aliança (SJA) and Niquelândia (NIQ) have different weathering degrees (Figure 3). AVIRIS data processing allowed for a better division of the areas according to the weathering degree of their soils, because the result is not based only on soil color or the morphology of the terrain, but on the relation of the minerals by means of spectral analysis.

SJA area presented soils with smaller variation in weathering degree, depicted by a less intense tonal variation than the region of NIQ (Figure 3). The lighter portion of the terrain in SJA area (Figure 3) presents a gentle and long slope that may be a result of either new soil formation or a less eroded area. The darker portion of the soil spot in SJA (Figure 3) represents a small deep depression, which was eroded and currently accumulates more water. Higher amounts of water make soils and parent materials more subject to alterations, and less silica and more aluminum remain in these soils. In the lighter parts of NIQ (Figure 3) may occur deposition of silica as this area is at the foot hill of the Ultramafic unit. The terrain inclination results in water accumulation, silica removal, and the consequent relative concentration of aluminum in these soils. The RCGb shows such soils in darker color (Figure 3).

TABLE 1: RCGb obtained by means of TGA and AVIRIS data for samples collected in São João D'Aliança (SJA) and in Niquelândia (NIQ).

Soil samples	Minerals (%)		RCGb	
	Gibbsite	Kaolinite	TGA	AVIRIS
SJA 1	11.68	32.81	0.74	0.73
SJA 2	13.84	34.53	0.71	0.76
SJA 3	14.10	52.95	0.79	0.76
SJA 4	11.71	57.99	0.83	0.76
SJA 5	13.18	60.79	0.82	0.76
SJA 6	14.16	60.14	0.81	0.75
SJA 7	14.22	55.61	0.80	0.73
SJA 8	16.30	54.75	0.77	0.72
SJA 9	18.64	55.47	0.75	0.70
SJA 10	19.02	53.17	0.74	0.69
SJA 11	22.86	52.59	0.70	0.66
SJA 12	23.27	54.53	0.70	0.64
SJA 13	25.66	55.04	0.68	0.64
NIQ 1	30.66	19.71	0.39	0.52
NIQ 2	26.38	35.13	0.57	0.56
NIQ 3	23.08	39.69	0.63	0.58
NIQ 4	26.35	33.70	0.56	0.58
NIQ 5	27.09	54.85	0.67	0.60
NIQ 6	27.17	53.56	0.66	0.61
NIQ 7	24.98	47.61	0.66	0.62
NIQ 8	13.84	52.87	0.79	0.65
NIQ 9	20.71	52.28	0.72	0.68
NIQ 10	20.73	52.34	0.72	0.68
NIQ 11	21.34	47.67	0.69	0.69
NIQ 12	16.16	61.72	0.79	0.69
NIQ 13	19.06	50.27	0.73	0.70
NIQ 14	14.55	56.65	0.80	0.81
NIQ 15	7.61	57.25	0.88	0.81
NIQ 16	6.51	58.81	0.90	0.82
NIQ 17	11.49	60.97	0.84	0.68

AVIRIS data have been showed to be appropriate for quantifying the weathering degrees of the imaged soils. The reddish Oxisol in SJA had 11.7–25.7% of gibbsite and 32.8–60.8% of kaolinite. NIQ soils presented 23.1–30.6% of gibbsite, 19.7–54.8% of kaolinite (dark reddish brown Oxisol, NIQ 1–NIQ 5), and 6.5–19.0% of gibbsite, 50.2–61.7% of kaolinite (Ultisol; NIQ 12–NIQ 17, Table 1). A soil transitional area occurred between the two last soils types that correspond to plots NIQ 6–NIQ 11 on Table 1. This area showed a gradual variation in mineral amounts between the dark reddish brown Oxisol and the Ultisol (Table 1). Except for the plot named NIQ 1 (Table 1), soils in SJA and NIQ areas are kaolinitic, according to the Brazilian soil classification system [39]. NIQ 1 topographic position, where water accumulates, may explain such a difference of gibbsite and kaolinite concentrations. From the agricultural point of view, kaolinitic and gibbsitic soils demand different

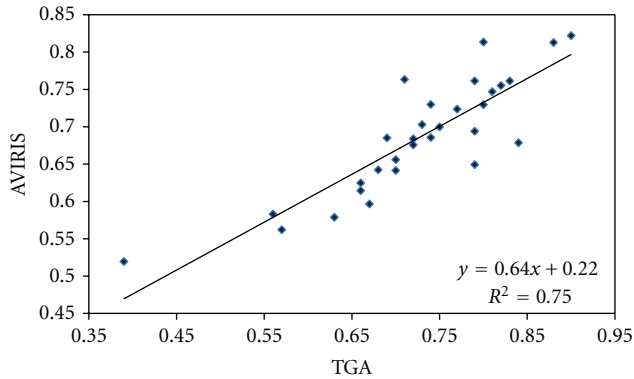


FIGURE 4: Regression of AVIRIS data on TGA values obtained in laboratory.

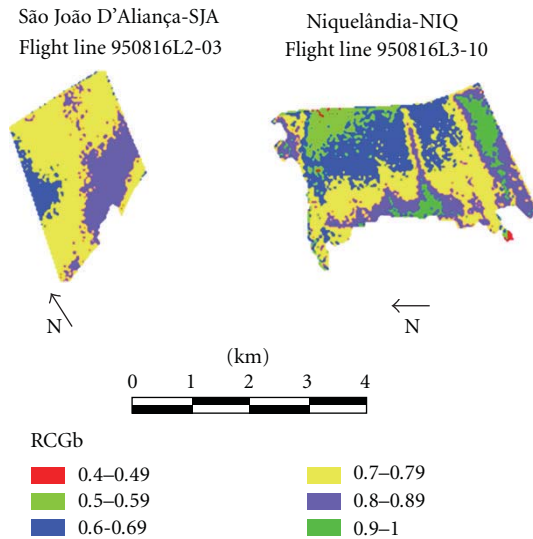


FIGURE 5: Quantitative mapping of the ratio kaolinite/(kaolinite + gibbsite).

chemical treatments. The use of RCGb identified differences in kaolinite and gibbsite contents within a same soil type as well (Figure 3) that can potentially optimize fertilizer applications if this characteristic is taken into account.

RCGb values were calculated from the proportions of kaolinite and gibbsite in the soils samples (TGA) presented and good fit ($R^2 = 0.75$; $P < .01$) on RCGb calculated from AVIRIS data (Table 1; Figure 4). The Mann-Whitney or U test showed no differences of RCGb values between the two AVIRIS and TGA. For SJA, n_1 and $n_2 = 13$ $e U_{\text{calc}} = 50$ and $U'_{\text{calc}} = 118$; if $U'_{\text{calc}} \geq U_{\text{tab}}$ or if $U_{\text{calc}} < U_{\text{tab}}$, reject H_0 , if not do not reject H_0 . For the greater $U_{\text{tab}} = 121$ and the lesser $U_{\text{tab}} = 45$, for n_1 and $n_2 = 13$ and $\alpha = 0.05$, therefore do not reject H_0 and the two populations are the same. For NIQ, n_1 and $n_2 = 17$ and $U_{\text{calc}} = 105.5$ $e U'_{\text{calc}} = 183.5$. For the greater $U_{\text{tab}} = 202$ and the lesser $U_{\text{tab}} = 87$, for n_1 and $n_2 = 17$ $e \alpha = 0.05$, do not reject H_0 and the two sample populations are also the same. Therefore, TGA and AVIRIS are independent, H_0 is true, and $\text{TGA} \approx \text{AVIRIS}$.

Dark reddish brown Oxisol in NIQ has a significant amount of opaque minerals such as magnetite (Fe_3O_4), which may reduce the efficiency of the spectral index. However, there was a good relationship between AVIRIS data and TGA values and this made it possible to spread out the quantitative mapping through the terrain (Figure 5). SJA presented three weathering degrees of kaolinitic soils, and NIQ had two plots of gibbsitic soils and five variations in the weathering degree of kaolinitic soils at 1:50,000 scale.

4. Conclusions

Conjoint treatment of images of bare soils from two different geological contexts showed that the AVIRIS sensor is able of capturing features to demonstrate that soils with different amounts of kaolinite and gibbsite can be investigated by means of the RCGb spectral index.

RCGb index could capture differences in amounts of kaolinite and gibbsite for a same soil type over a continuous area and depict its weathering degree.

The method can be utilized on a large scale due to the fact that this remote hyperspectral sensor is available on an orbital platform, favoring multitemporal analyses.

Further research should be carried out to better comprehend the factors that influence spectral features and to discover new mineral ratios, to improve spectroscopy as a method for mineralogical identification and quantification of tropical soils.

Acknowledgments

The authors would like to thank CNPq and Embrapa for funding this paper, and they also extend their thanks to NASA's *Jet Propulsion Laboratory*, in the person of Robert O. Green who furnished the AVIRIS data, which were fundamental to carrying out this study. Finally, the authors thank Professor Cynthia Ann Bell-Santos, of NMSU, for review and translation to English.

References

- [1] E. Ben-Dor, S. Chabrilat, J. A. M. Demattê et al., "Using Imaging Spectroscopy to study soil properties," *Remote Sensing of Environment*, vol. 113, no. 1, pp. S38–S55, 2009.
- [2] J. S. Madeira Netto, *Étude Quantitative des Relations Constituants Minéralogiques—Réflectance Diffuse des Latosols Brésiliens*, Application à l'Utilisation Pédologique des Données Satellitaires TM (Région de Brasília), l'ORSTOM, Paris, France, 1993.
- [3] S. A. Bowers and R. J. Hanks, "Reflectance of radiant energy from soils," *Soil Science*, vol. 100, pp. 130–138, 1965.
- [4] D. S. Orlov, "Quantitative patterns of light reflection by soils. I. Influence of particles (aggregate) size on reflectivity," *Science Papers of High School Biology*, vol. 4, pp. 206–210, 1966.
- [5] I. I. Karmanov, "Genesis and geography of soils: application of spectrophotometric coefficients to the study of soil-forming processes," *Soviet Soil Science*, vol. 2, pp. 152–165, 1968.

- [6] W. Flaig, H. Beutelspacher, and E. Rietz, "Chemical composition and physical properties of humic substances," in *Soil Components*, J. E. Gieseking, Ed., vol. 1 of *Organic Components*, Springer, New York, NY, USA, 1975.
- [7] J. Hlavay, K. Jonas, S. Elek, and J. Inczedy, "Characterization of the particle size and the crystallinity of certain minerals by infrared spectrophotometry and other instrumental methods—I. Investigations on clay minerals," *Clays and Clay Minerals*, vol. 25, no. 6, pp. 451–456, 1977.
- [8] A. Bedidi, B. Cervele, J. Madeira, and M. Pouget, "Moisture effects on visible spectral characteristics of lateritic soils," *Soil Science*, vol. 153, no. 2, pp. 129–141, 1992.
- [9] J. Madeira Netto, "Spectral reflectance properties of soils," *Photo Interpretation: Images Aeriennes et Spatiales*, vol. 34, no. 2, pp. 59–76, 1996.
- [10] J. Madeira, A. Bedidi, M. Pouget, B. Cervele, and N. Flay, "Spectral (MIR) determination of kaolinite and gibbsite contents in lateritic soils," *Comptes Rendus—Academie des Sciences*, vol. 321, no. 2, pp. 119–128, 1995.
- [11] J. Madeira, A. Bédidi, B. Cervele, M. Pouget, and N. Flay, "Visible spectrometric indices of hematite (Hm) and goethite (Gt) content in lateritic soils: the application of a Thematic Mapper (TM) image for soil-mapping in Brasilia, Brazil," *International Journal of Remote Sensing*, vol. 18, no. 13, pp. 2835–2852, 1997.
- [12] M. M. Valeriano, J. C. N. Epiphany, A. R. Formaggio, and J. B. Oliveira, "Bi-directional reflectance factor of 14 soil classes from Brazil," *International Journal of Remote Sensing*, vol. 16, no. 1, pp. 113–128, 1995.
- [13] L. S. Galvão and I. Vitorello, "Role of organic matter in obliterating the effects of iron on spectral reflectance and colour of Brazilian tropical soils," *International Journal of Remote Sensing*, vol. 19, no. 10, pp. 1969–1979, 1998.
- [14] J. A. M. Demattê and G. J. Garcia, "Alteration of soil properties through a weathering sequence as evaluated by spectral reflectance," *Soil Science Society of America Journal*, vol. 63, no. 2, pp. 327–342, 1999.
- [15] J. A. M. Demattê, R. C. Campos, and M. C. Alves, "Avaliação espectral de solos desenvolvidos em uma topossequência de diabásio e folhelho da região de Piracicaba, SP," *Pesquisa Agropecuaria Brasileira*, vol. 35, no. 12, pp. 2447–2460, 2000.
- [16] J. A. M. Demattê, A. R. Huete, L. G. Ferreira Jr., M. C. Alves, M. Nanni, and C. E. Cerri, "Evaluation of tropical soils through ground and orbital sensors," in *Proceedings of the 2nd International Conference on Geospatial Information in Agriculture and Forestry*, 2000.
- [17] D. J. Brown, K. D. Shepherd, M. G. Walsh, M. Dewayne Mays, and T. G. Reinsch, "Global soil characterization with VNIR diffuse reflectance spectroscopy," *Geoderma*, vol. 132, no. 3–4, pp. 273–290, 2006.
- [18] D. Summers, M. Lewis, B. Ostendorf, and D. Chittleborough, "Visible near-infrared reflectance spectroscopy as a predictive indicator of soil properties," *Ecological Indicators*, vol. 11, pp. 123–131, 2001.
- [19] V. Carrere and M. J. Abrams, "An assessment of AVIRIS data for hydrothermal alteration mapping in the Goldfield mining district, Nevada," in *Proceedings of the Airborne Visible/Infrared Imaging Spectro*, pp. 134–154, JPL Publication, Pasadena, Calif, USA, 1988.
- [20] G. M. M. Baptista, E. S. Martins, J. S. Madeira Netto, O. A. Carvalho Jr., and P. R. Meneses, "Use of AVIRIS data for mineralogical mapping in tropical soils, in the district of São João D'Alanca," in *Proceedings of the AVIRIS Earth Science and Applications Workshop*, pp. 33–42, JPL Publications, Goiás, Brazil, 1998.
- [21] G. M. M. Baptista, J. S. Madeira Netto, O. A. Carvalho Jr., and P. R. Meneses, "Mapping kaolinite and gibbsite of Brazilian tropical soils using imaging spectrometry data (AVIRIS)," in *Proceedings of the AVIRIS Earth Science and Applications Workshop*, pp. 267–274, JPL Publications, 1999.
- [22] V. Carrere and O. Chadwick, "An AVIRIS survey of Quaternary surfaces formed on carbonate provenance alluvium, Mojave Desert, southern Nevada," in *Proceedings of the 2nd Airborne Visible/Infrared Imaging Spectrometer (AVIRIS) Workshop*, 1990.
- [23] R. N. Clark, A. Gallagher, and G. A. Swayze, "Material absorption band depth mapping of imaging spectrometer data using a complete band shape least-squares fit with library reference spectra," in *Proceedings of the 2nd Airborne Visible/Infrared Imaging Spectrometer (AVIRIS) Workshop*, pp. 176–186, JPL Publications, 1990.
- [24] R. N. Clark, G. A. Swayze, A. Gallagher, N. Gorelick, and F. A. Kruse, "Mapping with imaging spectrometer data using the complete band shape least-squares algorithm simultaneously fit to multiple spectral features from multiple materials," in *Proceedings of the 3rd Airborne Visible/Infrared Imaging Spectrometer (AVIRIS) Workshop*, pp. 2–3, JPL Publication, 1991.
- [25] R. N. Clark, G. A. Swayze, and A. Gallagher, "Mapping the mineralogy and lithology of Canyonlands, Utah with imaging spectrometer data and the multiple spectral feature mapping algorithm," in *Proceedings of the 3rd Annual JPL Airborne Geoscience Workshop*, pp. 11–13, JPL Publication, 1992.
- [26] R. N. Clark, "Spectroscopy of rocks and minerals, and principles of spectroscopy," in *Manual of Remote Sensing*, A. N. Rencz, Ed., vol. 3 of *Remote Sensing for the Earth Science*, John Wiley & Sons, New York, NY, USA, 1999.
- [27] G. M. M. Baptista and J. S. Madeira Netto, "RCGb Index: a tool for mapping the weathering degree of the tropical soils in Brazil," in *Proceedings of the AVIRIS Earth Science and Applications Workshop*, Jet Propulsion Laboratory (JPL) NASA, Pasadena, Calif, USA, 2001.
- [28] A. P. Crôsta, C. Sabine, and J. V. Taranik, "A comparison of image processing methods for alteration mapping at Bodie, California, using 1992 AVIRIS data," in *Proceedings of the 6th Annual JPL Airborne Earth Sciences Workshop*, vol. 1, pp. 57–62, JPL Publication, 1996.
- [29] E. Ben-Dor, N. Levina, A. Singer, A. Karnieli, O. Braund, and G. J. Kidrona, "Quantitative mapping of the soil rubification process on sand dunes using an airborne hyperspectral sensor," *Geoderma*, vol. 131, pp. 1–21, 2006.
- [30] E. Ben-Dor, R. G. Taylor, J. Hill et al., "Imaging spectrometry for soil applications," *Advances in Agronomy*, vol. 97, pp. 321–392, 2001.
- [31] L. S. Galvão, A. R. Formaggio, E. G. Couto, and D. A. Roberts, "Relationships between the mineralogical and chemical composition of tropical soils and topography from hyperspectral remote sensing data," *ISPRS Journal of Photogrammetry and Remote Sensing*, vol. 63, no. 2, pp. 259–271, 2008.
- [32] G. Serbin, C. S. T. Daughtry, E. R. Hunt, J. B. Reeves, and D. J. Brown, "Effects of soil composition and mineralogy on remote sensing of crop residue cover," *Remote Sensing of Environment*, vol. 113, no. 1, pp. 224–238, 2009.
- [33] G. M. M. Baptista, Mapeamento e Quantificação da Relação Mineralógica Caulinita/(Caulinita+Gibbsita) de Solos Tropicais, por meio dos Dados do Sensor Hiperspectral AVIRIS

- (JPL/NASA), Tese (Doutorado), Universidade de Brasília, Brasília, Brazil, 2001.
- [34] P. Lagacherie, F. Baret, J. B. Feret, J. Madeira Netto, and J. M. Robbez-Masson, "Estimation of soil clay and calcium carbonate using laboratory, field and airborne hyperspectral measurements," *Remote Sensing of Environment*, vol. 112, no. 3, pp. 825–835, 2008.
- [35] R. O. Green, J. E. Conel, J. S. Margolis, C. J. Brugge, and G. L. Hoover, "An inversion algorithm for retrieval of atmospheric and leaf water absorption from AVIRIS radiance with compensation for atmospheric scattering," in *Proceedings of the 3rd Airborne Visible/Infrared Imaging Spectrometer (AVIRIS) Workshop*, pp. 51–61, JPL Publications, 1991.
- [36] B. C. Gao, K. B. Heidebrecht, and A. F. H. Goetz, "Derivation of scaled surface reflectances from AVIRIS data," *Remote Sensing of Environment*, vol. 44, no. 2-3, pp. 165–178, 1993.
- [37] B. C. Gao, K. B. Heidebrecht, and A. F. H. Goetz, "Atmosphere REMoval Program (ATREM) user's guide," Version 3.1. CSES/CIRES/University of Colorado. Boulder, Colo, USA, 1999.
- [38] J. H. Zar, *Biostatistical Analysis*, Prentice Hall, New York, NY, USA, 1989.
- [39] Embrapa, *Sistema Brasileiro de Classificação de Solos*, Serviço de Produção de Informação, Brasília, Brazil, 1st edition, 1999.

Research Article

Digital Soil Mapping in the Absence of Field Training Data: A Case Study Using Terrain Attributes and Semiautomated Soil Signature Derivation to Distinguish Ecological Potential

Dawn M. Browning and Michael C. Duniway

Jornada Experimental Range, Agriculture Research Service, U.S. Department of Agriculture, P.O. Box 30003, MSC 3JER, NMSU, Las Cruces, NM 88003-8003, USA

Correspondence should be addressed to Dawn M. Browning, dbrownin@nmsu.edu

Received 15 November 2010; Revised 10 February 2011; Accepted 26 February 2011

Academic Editor: Nicolas Baghdadi

Copyright © 2011 D. M. Browning and M. C. Duniway. This is an open access article distributed under the Creative Commons Attribution License, which permits unrestricted use, distribution, and reproduction in any medium, provided the original work is properly cited.

Spatially explicit data for soil properties governing plant water availability are needed to understand mechanisms influencing plant species distributions and predict plant responses to changing climate. This is especially important for arid and semiarid regions. Spatial data representing surrogates for soil forming factors are becoming widely available (e.g., spectral and terrain layers). However, field-based training data remain a limiting factor, particularly across remote and extensive drylands. We present a method to map soils with Landsat ETM+ imagery and high-resolution (5 m) terrain (IFSAR) data based on statistical properties of the input data layers that do not rely on field training data. We then characterize soil classes mapped using this semiautomated technique. The method distinguished spectrally distinct soil classes that differed in subsurface rather than surface properties. Field evaluations of the soil classification in conjunction with analysis of long-term vegetation dynamics indicate the approach was successful in mapping areas with similar soil properties and ecological potential.

1. Introduction

Soil properties are critical for understanding patterns of vegetation community composition and primary productivity in arid and semiarid ecosystems globally [1, 2]. The relationship between incoming precipitation and water availability for plant growth in these water-limited systems is modified by vegetation, topography, and soil properties that affect surface redistribution, infiltration, and water retention [3–5]. Therefore, spatially explicit information for relevant soil properties is needed to understand the mechanisms governing plant species distributions and vegetation dynamics, particularly in efforts to forecast responses to changing climate. High-resolution imagery and terrain data sets are increasingly available globally, enhancing opportunities for digital soil mapping opportunities to yield accurate spatially explicit soil maps that capture many of these important hydrologic properties with reduced effort.

Although soil mapping is a long-standing science, broad scale mapping efforts often lack sufficient detail for

understanding mechanisms regulating vegetation patterns and dynamics. This is particularly relevant for spatially extensive arid and semiarid regions (i.e., drylands). For example, in the United States, soil mapping efforts were initially focused on lands suitable for cultivated agriculture and fewer resources were allocated to mapping other areas, including drylands. Map units outside of valuable agricultural lands typically contain several different soils that can function quite differently from an ecological perspective. Therefore, in many drylands, updated soil maps with greater resolution and accuracy are needed to understand plant community patterns and dynamics. Digital, raster-based maps of soil properties are ideally suited for such analyses.

Enhanced availability of satellite imagery with increasing spectral, spatial, and temporal resolutions provide ample opportunities for predictive soil mapping at different levels of detail across a range of spatial extents [6–8]. McBratney et al. [9] proposed a framework for predictive digital soil mapping (DSM) that generalized Jenny's [10] five soil forming factors (climate, organisms, relief, parent material, and time) to also

consider spatial position and allow for interactions between soil forming factors to predict either spatially-explicit soil classes or discrete soil properties. The McBratney et al. [9] approach capitalizes on the availability of computing power and the ever-increasing wealth of remotely sensed data sources that serve as environmental covariates. The choice of satellite imagery for soil mapping should be based on cost and logistical (e.g., storage/computing) constraints in conjunction with the requisite detail of mapped result.

Land management and planning for spatially extensive drylands require prudent evaluation of the costs and benefits of available resources to meet the ever-increasing need for digital soil map layers. For example, in the USA, while detailed soil survey data are available in places, mapped soil units are often grouped together into general types based on the type and amount of potential vegetation and the site's ability to respond to management activities based on soil-vegetation feedbacks and properties (i.e., NRCS Ecological Site, see [11]). For such applications, a lower spatial resolution product that can be easily obtained over large areas, such as with Landsat imagery, serves a broader purpose more effectively than more detailed, labor-intensive soil map products. Furthermore, archive and contemporary Landsat imagery provides an easily assessable source of data commensurate with landscape features that coincide with the rangeland monitoring and land-cover mapping [12, 13].

Spectral information regarding soil surface conditions and vegetation indices as surrogates for vegetation cover have been combined with high-resolution terrain models to improve DSM efforts [7, 14]. Boettinger et al. [6] effectively demonstrate the utility of remotely sensed imagery (i.e., Landsat) for characterizing soil surface features in drylands with modest vegetation cover. In another study focused on automated soil mapping with Landsat imagery and terrain layers, Saunders and Boettinger [15] combine unsupervised classification techniques with classification trees to evaluate utility of this combined approach to classify soils compared to a classification approach based on expert knowledge and field survey data.

Physical properties of the land surface relevant to soil forming factors are provided by satellite imagery and topographic features derived from digital elevation data [6, 16]. The availability of environmental covariates in digital format along with computing power and integration with local knowledge of change and degradation are key components to a worldwide effort to map soils for land management and carbon storage planning [17]. Despite advances in the availability of digital data and modeling algorithms (e.g., [14]), predictive digital mapping of soil properties at broad spatial scales is commonly hampered by a lack of supporting ancillary or training data [18]. This is especially so in spatially extensive and often remote dryland ecosystems. We present a statistically-based approach to derive spectral signatures for classifying soils without prior extensive field sampling and then characterize the soil types and properties of the mapped soil classes to facilitate interpretation.

We set out to isolate the effects of soil properties on dynamic changes in shrub and grass vegetation over 71 years in an arid grassland in southern New Mexico, USA.

We assume soil properties delineated in our contemporary mapping effort represent those over the 71 year period. Requisite digital soils map data commensurate with patch-level dynamics were not readily available. The objectives of this study were to (1) delineate distinct soil classes within the study area using spatially explicit data layers for topographic and spectral features and (2) characterize derived soil classes to facilitate interpretation of observed vegetation dynamics.

2. Materials and Methods

2.1. Study Area. The study was conducted across a 150 ha landscape within the Chihuahuan Desert Rangeland Research Center in the northern Chihuahuan Desert of southern New Mexico, USA (Figure 1). The soil mapping endeavor was conducted as part of a larger study to discern the influence of soils in an analysis of long-term vegetation dynamics. The climate is characterized by a warm dry spring, hot wet summer, and cold dry winter. Long-term (1930 to 2008) average annual rainfall is 232.0 mm. Annual pan evaporation rates far exceed rainfall, with a measured annual average of 2,204.1 mm (1953 to 1979) [19]. The soil temperature regime for the area is Thermic, and the soil moisture regime is Ustic to Typic Aridic. The study area, with a long history of livestock grazing [20], occurs at 1,324 m elevation.

The area is dominated by sandy soils that are part of the broad alluvial plain of the ancestral Rio Grande River. Deposition of sediments by the Rio Grande on the alluvial plain ended approximately 1.6 million years ago [21], providing time for substantial pedogenic development including formation of argillic horizons and thick petrocalcic horizons. However, the area is now a mosaic of primarily sandy soil types due to postdepositional geologic and geomorphic processes, mainly tectonic uplift and reworking of the sediments by wind [22]. In areas receiving recent eolian deposition, surface textures are typically very coarse (>90% sand) and there is little clay or carbonate accumulation within the top meter. In eroded areas, the depth to the petrocalcic horizon can be relatively shallow (<50 cm) and the surface textures finer due to loss of surface soils.

The area was historically dominated by grasses but has transitioned to a shrub-dominated ecosystem [23, 24]. Shrub cover, dominated by honey mesquite (*Prosopis glandulosa* Torr.), increased from 1% in 1937 to ca.16% in 2008 [25]; this shift in mesquite dominance occurred amidst declines in grass cover, constituting black grama (*Bouteloua eriopoda*), tobosa (*Pleuraphis mutica*), and dropseed species (*Sporobolus* spp.) from ca. 19% in 1937 to 1% in 2008. Proliferation of shrubs and the decline in grasses were highly heterogeneous across space and time; interactions between soils and climate (i.e., drought) are expected to explain some of the observed heterogeneity.

2.2. Mapping Soils. A combination of unsupervised and supervised classification techniques were used to delineate distinct soil classes using spectral and topographic variables across the 150 ha study area. We chose to use Landsat 7

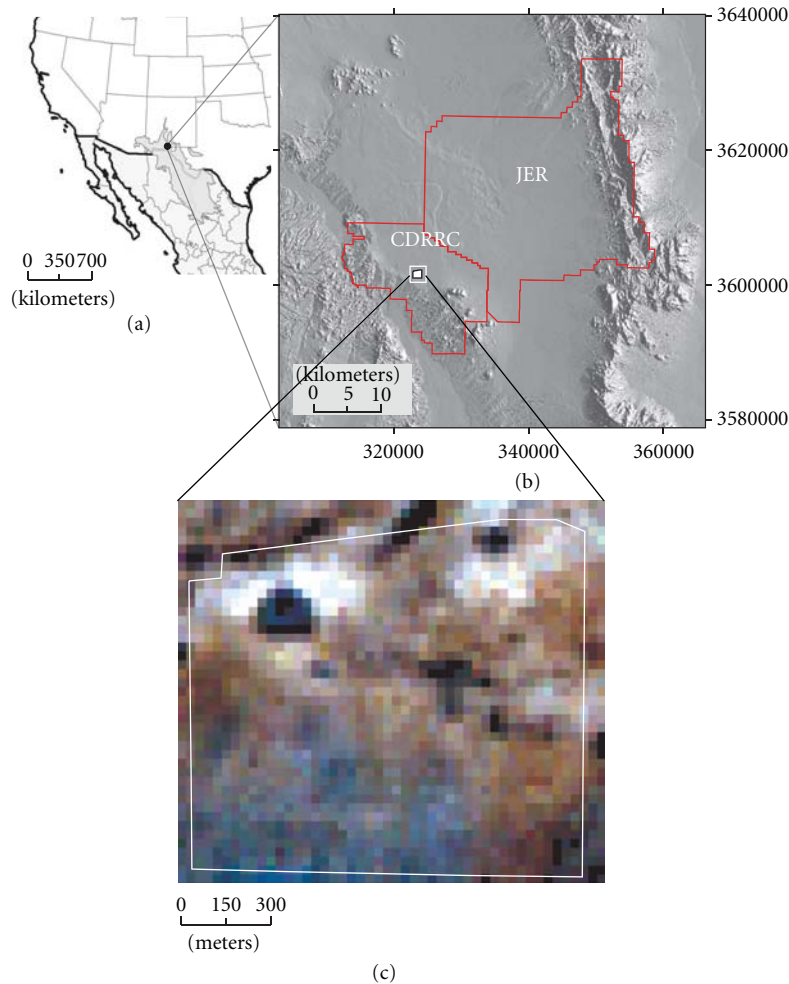


FIGURE 1: Location of the Jornada Basin LTER (JRN) in southern New Mexico at the northern extent of the Chihuahuan Desert (depicted in gray in Panel (a)). The 150 ha study site (white on inset map in Panel (b)) occurs on the Chihuahuan Desert Rangeland Research Center (CDRRC), which together with the Jornada Experimental Range (JER) constitutes the JRN. Topographic complexity of the JRN is illustrated with a shaded relief map from a 10 m digital elevation model. Panel c is a natural color composite Landsat 7 ETM+ image of the study site (in white outline). Color bands display as Landsat 7 band 3 (red), band 2 (green), and band 1 (blue) with no histogram stretch applied.

Enhanced Thematic Mapper (ETM+) imagery over that from other sensors for its accessibility (i.e., freely available) to land managers and soil scientists through the GLOVIS portal administered by the USA Geological Survey [26]. Spectral information was derived from a 24 February 2002 Landsat 7 ETM+ Level 1T image product that was precision and terrain corrected [27]. The winter image was selected from the Landsat archive to maximize the reflected radiant energy from the soil surface in winter, when vegetation cover is low and during a period of below-average rainfall. We assume that spectral properties reflected exposed soil surfaces based on a preponderance of evidence from long-term ecological research (LTER) site data sources collected at nearby study sites. Field-estimates of vegetation biomass collected 12–18 February 2002 indicate that production of annual and perennial grasses, forbs, and shrubs was near zero [28]. In addition, monthly observations of plant phenology corroborate the supposition that perennial grasses and shrubs were dormant when the image was acquired.

2.2.1. Input Layers. Topographic variables were derived from a digital terrain model (DTM) acquired with an airborne interferometric synthetic aperture radar (IFSAR) sensor in 2006 (Intermap Technologies Inc., Englewood, Colo. USA). The native spatial resolution of the DTM was 5 m. Topographic derivatives evaluated were slope, slope shape (planar and profile curvature), and the Topographic Wetness Index (TWI). TWI provides a relative index of whether a point is in a landscape position likely to receive run-in water by taking the natural log of the specific catchment area divided by the local slope [29, 30]. Higher TWI values indicate a point with greater contributing area and/or lower slopes; lower values indicate points with less contributing area and/or higher slopes. Slope, slope shape, and TWI were calculated using Model Builder and Spatial Analyst in ArcGIS (Environmental Science Research Institute, Redlands, Calif, USA, v 9.3).

The pixel-based parametric classification scheme requires all input layers share a common spatial resolution. We chose to summarize the fine-scale terrain data within a

neighborhood coinciding with the larger footprint of Landsat image pixels rather than to increase the redundancy in the spectral data by resampling to a smaller pixel size. This decision was based on the need to avoid limitations related to collinearity in the signature derivation process (see Section 2.2.2). We summarized topographic derivatives (using mean, standard deviation, minimum, and maximum values) within a focal 6×6 pixel window corresponding to the $30 \text{ m} \times 30 \text{ m}$ pixel size of the ETM+ image.

The ETM+ image was radiometrically calibrated, and spectral reflectance values were adjusted to remove the effects of attenuation and scattering of photons due to atmospheric interference using the COST model [31]. The atmospherically corrected reflectance values for the six multispectral bands ranged in value from 0 to 1; spectral index calculations were based on atmospherically corrected reflectance values. Short-wave infrared ETM+ bands (5 and 7) are sensitive to surface soil moisture [32] and are commonly used in digital soils mapping [6]. Normalized difference ratios were calculated for established band combinations (e.g., gypsic soil index [16] using ETM+ short wave infrared bands 5 and 7 and iron oxide index [33] using bands ETM+ bands 3 (red) and 1 (blue)). Our combination of spectral bands and topographic derivatives as inputs for the classification process represents environmental covariates commonly used for digital soil mapping (e.g., [7]).

2.2.2. Assessment of Spectral and Topographic Input Layers. Reflectance values for image bands representing distinct, yet overlapping, portions of the electromagnetic spectrum are correlated. Collinearity in image band values can prohibit the derivation of spectrally distinct signatures [34]. Our initial attempts to employ a statistically driven assessment of signature separability with the entire set of 20 spectral and topographic image layers were unsuccessful because redundancy in the dataset prevented the creation of invertible covariance matrices in ERDAS Imagine. Therefore, we implemented a combination of methods to reduce the number of image bands to drive the unsupervised classification. In an effort to facilitate data interpretation, we did not use principle components analysis to reduce dimensionality of the dataset. Instead, we evaluated correlation matrices for image bands to identify redundant bands, quantified the optimal index factor (OIF) [35] to identify the subset ($n = 3$) of spectral bands that maximize the variance within the Landsat ETM+ scene while minimizing duplication, and examined input image bands with the coregistered digital landform data layer. OIF is calculated for each 3-band combination as the sum of the standard deviations for the six Landsat image bands divided by the sum of the two pairwise correlations between the three candidate image bands [22].

2.2.3. Unsupervised Classification and Signature Derivation. The first step in the image classification process was to perform an unsupervised classification of the entire study area. Unsupervised classification is a computer-driven process that applies user-specified input parameters (such as convergence threshold and number of output classes) to

initialize thematic classes and to identify clusters of pixels with similar spectral characteristics. The unsupervised classification algorithm supported by ERDAS Imagine (v.9.3, ERDAS, Inc., Norcross, Ga, USA) is the Iterative Self-Organizing Data Analysis Technique (ISODATA). Because the initial clusters in the algorithm are based, in part, by the number of output classes specified by the user, it is important to double the number of classes you expect to retrieve (based on available data).

Existing soils maps were used to determine the number of output classes to specify for the ISODATA algorithm. In our case, the existing 3rd-order soil survey conducted in 1980 (mapped at 1:48,000 scale, largely mapped as associations or complexes) delineated two soil map units across the study area: Berino-Bucklebar association (25% Typic Haploargid and 60% Typic Calciargid) and Wink-Harrisburg association (35% Typic Haplocalcid and 25% Typic Petrocalcid) [36]. A spatially distinct, ephemerally flooded 2.8 ha playa occurs within the study area; the playa is characterized by heavy clay soils and was delineated previously [22]. In the classification process, we manually assigned image pixels associated with the playa to a separate soil class. Combining information from the 1980 soil survey with a recent landform map of the area that included four landforms (Alluvial Plain Uplifted, Alluvial Plain Eroded, Alluvial Plain Wind Worked, and Playa; [22]), we estimated a maximum of five distinct soil types in the study area. Doubling the number of potential soil classes to allow for good separation in unsupervised classification process, we specified 10 output classes from the unsupervised classification of the entire study area.

The ISODATA algorithm was implemented with the following parameters. We specified 10 output thematic classes, selected a default convergence threshold of 0.950, initialized clusters using statistics encompassing 95% of the data along the principal axis, and allowed a maximum of 10 iterations. The ISODATA algorithm assigns pixels to clusters based on the minimum spectral distance from the cluster centroid. The centroid is recalculated after each class assignment with the convergence threshold serving as a measure of "classification completion." This threshold represents the proportion of pixels that do not change classes from iteration to iteration. The ISODATA algorithm runs iteratively until either 95% of the pixels do not change clusters or the maximum number of iterations is completed. The 10 spectral signatures representing distinct soil classes of spectrally similar data were output for subsequent analysis and evaluation.

Transformed Divergence (TD) is a commonly used measure of signature separability in image classification [35]. The TD metric represents the spectral distance between two signatures based on the covariances between the signatures for a specific combination of spectral bands. Transformed Divergence is computed as follows:

$$D_{ij} = \frac{1}{2} \text{tr}((C_i - C_j)(C_i^{-1} - C_j^{-1})) + \frac{1}{2} \text{tr}((C_i^{-1} - C_j^{-1})(\mu_i - \mu_j)(\mu_i - \mu_j)^T), \quad (1)$$

$$TD_{ij} = 2000 \left(1 - \exp\left(\frac{-D_{ij}}{8}\right) \right),$$

where i and j = the two signature classes being compared, C_i is the covariance matrix of signature i , μ_i is the mean vector of signature i , tr is the trace function, and T is the transpose function [36, 37]. Mausel et al. [38] found that TD outperformed other statistical measures of separability in selecting the optimum subset of multispectral bands to distinguish between crop types in Hildago County, TX, USA. We used the TD measure to achieve two primary objectives: (1) determine the number statistically and spectrally separable soil classes occurring within the study area and (2) identify the subset of data layers that best discriminates between the distinct soil classes. The TD measure of signature separability ranges from 0 to 2,000 for a given class pair. We used a minimum value of 1,900 for all class pairs as the threshold to indicate spectrally distinct classes [35].

We used the TD measure in the ERDAS Signature Editor to determine the number of distinct soil classes based on spectral and topographic properties. We invoked the TD utility to calculate divergence values for all possible pairwise comparisons of 10 classes ($n = 45$ class-class comparisons). The TD utility outputs two matrices; the first matrix contains the class pairs and the second matrix contains the TD measure of separability for each associated class pair in the first matrix. For each iteration, we identified the class pair with the lowest TD value, merged the two specified classes in the ERDAS Signature Editor, deleted the original two signatures, and recomputed the TD metric. This process was performed iteratively until all class pairs had a TD value of 1,900 or higher, indicating spectrally distinct soil classes.

2.2.4. Supervised Classification. The second step in the classification process was to apply soil signatures derived from spectral and topographic input layers in the previous exercise back to atmospherically corrected ETM+ image (containing relevant spectral and topographic image bands) to perform the supervised classification. Supervised classification with parametric spectral signatures uses the statistical properties of the signatures to drive the class membership decision rule. We used the Maximum Likelihood decision rule, which does not employ a separate rule for overlap. This signifies that each pixel in the image will be applied to one of the spectral classes in the signature file. It is worth noting that supervised classification is traditionally used to classify multispectral imagery using field-collected or otherwise derived known vegetation or land surface data. In the absence of field-sampled training data for soils, we derived spectral signatures based solely on the Transformed Divergence metric to map distinct soils classes across the study area.

Small pixel clusters in the classified images may result from misclassification or aberrant reflectance data [39]. Further, while small patches of 1- and 2-pixel clumps could possibly represent soil inclusions, the number of small patches was low and would have complicated stratification of the site for field assessment. Therefore, we generalized the classified images slightly by removing 1- and 2-pixel clumps. These values were replaced with values of surrounding pixels.

2.3. Field Assessment of Mapped Soil Classes. To characterize soil classes mapped with this semiautomated classification procedure, we formulated a stratified random sampling strategy based on within-soil class topography. Depth to petrocalcic horizon is one of the key distinguishing soil properties in the study area. Much of the variability in the depth to petrocalcic in this area is due to reworking of the overlying sandy horizons by wind and water. To ensure our samples captured the representative range in deposition (likely deep) and erosional (likely shallow) areas we used stratified-random approach based on mean planar curvature within a $25\text{ m} \times 25\text{ m}$ moving window. We selected eight locations for field sampling within each of the three spectrally distinct soil classes (see Section 3.1, *Digital Soil Mapping*) for a total of 24 field samples.

For each sample location, we recorded horizon morphology and collected surface and subsurface samples for textural analysis. Soil was excavated using a hand auger to a depth of 100 cm or until a petrocalcic horizon was encountered. Horizon morphology information included descriptions of clay and carbonate accumulation in the top 100 cm. Each sample was classified to soil taxonomic Suborder following Soil Taxonomy [40]. At locations where a petrocalcic horizon occurred within 100 cm of the soil surface, we classified the soil to Great Group (e.g., Petrocalcicid). Soil samples were collected from the surface (0–5 cm) and the horizon encountered with the maximum clay content (as estimated in the field by hand) for later particle size analysis in the lab [41]. For each soil class, average soil surface and subsurface texture and frequency of each taxonomic class were calculated using the probability of inclusion from the stratified sampling (PROC MEANS; SAS version 9.2, Cary, NC, USA). Analysis of variance was conducted on surface and subsurface texture to test if classes differed in surface or subsurface sand, silt, and clay (PROC GLM; SAS version 9.2).

3. Results

3.1. Digital Soil Mapping

3.1.1. Assessment of Spectral and Topographic Variables/Input Layers. The three-step process to assess input bands for the unsupervised classification led to the selection of four spectral and two topographic input bands. The first step was to calculate the optimal index factor (OIF) on the six spectral bands to identify the three-band combination that maximized within-ETM+ scene variance with the least redundancy. The 1, 5, 7 band combination yielded an OIF value of 0.701. The second step was to evaluate the correlation between spectral data (bands and indices; Table 1) and topographic derivatives (Table 2). The correlation matrix for the spectral data revealed that the gypsic index exhibited the least correlation with other spectral bands when compared with the other two normalized indices and that band 1 was not strongly correlated with bands 5 and 7 (Table 1). The short-wave infrared bands (5 and 7) were highly correlated ($r = 0.959$); the TD metric was used to determine which of

the two short-wave infrared bands were more informative to characterizing the spectral signatures (i.e., Band 7, see Section 3.1.2). In general, topographic derivatives were less correlated with one another than the spectral bands (Table 2). In this case, visual inspection of candidate image bands (step 3) was most effective for identifying topographic derivatives for classifying soils. We evaluated maps for the 10 topographic derivatives with the existing (albeit general) 3rd-order soil survey [42] to determine that mean slope and maximum planar curvature most effectively represented relevant topographic features (i.e., relief and curvature). Selecting candidate image bands for an array of options to drive the image classification, while subjective, is a common procedure best accomplished in conjunction with available ancillary data sources [6, 15].

3.1.2. Spectral Signature Derivation. Starting with 10 signatures associated with classes from the unsupervised classification, we computed the Transformed Divergence (TD) metric eight times using all seven input bands (Band 1, Band 5, Band 7, $B5-B7/B5+B7$, $B3-B1/B3+B1$, mean slope, and maximum planar curvature) to achieve a minimum TD value of at least 1,900 for each class pair (Table 3). The minimum TD value ranged from 1,511 when evaluating 45 class pairs between 10 clusters to 1,940 when evaluating three class pairs between three clusters. There was a clear break in minimum TD values between the six pairwise comparisons for four (1,715) and the three pairwise comparisons for three clusters (1,940) (Table 3). Using the three spectrally distinct signatures, we then calculated the TD metric using the best six (of seven) input bands to determine that ETM+ Band 5 was the least informative of the seven image bands. The subsequent supervised classification was then performed using six input bands (i.e., Band 1, Band 7, gypsic index ($B5-B7/B5+B7$), iron oxide index ($B3-B1/B3+B1$), mean slope, and maximum planar curvature).

Spectral response curves for the three spectrally distinct signatures revealed a low dynamic range in values for the spectral bands and the normalized ratios; in contrast, mean slope (summarized within $30\text{ m} \times 30\text{ m}$ windows) demonstrated the largest difference between the three classes (Figure 2(a)). Relativized topographic derivatives were used in the image classification; absolute values are presented (Figures 2(b) and 2(c)) to illustrate that mean percent slope for soil class 1 was 3.4 and was considerably higher than mean percent slope of 2.1 for soil class 2 (Figure 2(b)). There were no distinguishable differences in mean maximum planar curvature for the three soil classes (Figure 2(c)).

3.1.3. Supervised Classification. Pixels that coincided with the ephemerally flooded playa were manually assigned to a separate soil class 4, constituting 1.6% of study area. This resulted in 41.2% of the study area classified as soil class 1, 50.1% mapped as soil class 2, and 7.1% mapped as soil class 6; soil class 6 was interspersed between class 1 and class 2 pixels (Figure 3(a); Table 4). Field assessment of the mapped soil classes was based on 24 field sites.

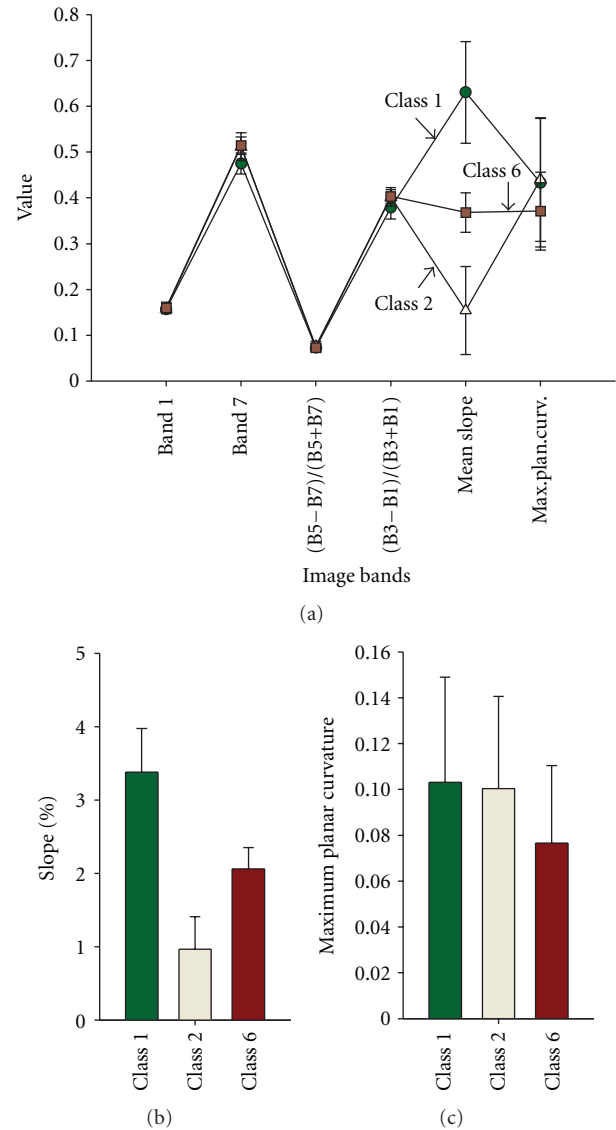


FIGURE 2: Class signatures for three spectrally distinct classes as determined using a minimum Transformed Divergence value of 1,900 (a). Six image bands were used in the maximum likelihood supervised classification; four bands were derived from a 24 Feb 2002 Landsat ETM+ image, and two were derived from a digital terrain model based on 5 m resolution IFSAR data. Band values represent atmospherically corrected reflectance (e.g., Bands 1 and 7), normalized difference ratios, or topographic derivatives standardized to range between zero and one. Average (standard deviation) absolute values for slope (b) and maximum planar curvature (c).

3.2. Field Assessment of Soil Classes. Field diagnostics and lab analyses indicated that soil classes 1 and 2 exhibited different subsurface properties and that soil class 6 is a transitional soil more similar to class 2 than 1 (Table 4, Figure 3(a)). Of the eight sites surveyed in soil class 1, none exhibited a petrocalcic layer within the top 100 cm. Five of the sites (68.5% of the area), with very little clay or carbonate accumulation in the top 100 cm, were classified as Cambids;

TABLE 1: Correlation matrix for six spectral bands and four normalized indices calculated from a 24 Feb 2002 Landsat ETM+ image. Normalized indices were calculated using ETM+ spectral bands: gypsic index $[(B5-B7)/(B5+B7)]$ from [16] and iron oxide index $[(B3-B1)/(B3+B1)]$ from ERDAS Imagine (v.9.3, ERDAS, Inc., Norcross, Ga, USA) software.

	B1 Blue	B2 Green	B3 Red	B4 NIR	B5 SWIR	B7 SWIR	B5-B7/ B5+B7	B3-B7/ B3+B7	B3-B2/ B3+B2	B3-B1/ B3+B1
Band 1	1.000	0.838	0.667	0.610	0.440	0.438	-0.128	0.555	-0.052	-0.021
Band 2		1.000	0.908	0.868	0.739	0.742	-0.232	0.450	0.205	0.449
Band 3			1.000	0.964	0.893	0.895	-0.269	0.334	0.596	0.729
Band 4				1.000	0.929	0.904	-0.177	0.237	0.586	0.731
Band 5					1.000	0.959	-0.144	-0.042	0.669	0.791
Band 7						1.000	-0.416	-0.121	0.672	0.802
B5-B7/ B5+B7							1.000	0.272	-0.203	-0.267
B3-B7/ B3+B7								1.000	-0.091	-0.066
B3-B2/ B3+B2									1.000	0.849
B3-B1/ B3+B1										1.000

TABLE 2: Correlation matrix for ten topographic indices derived from 5 m IFSAR digital terrain model. Variables were transformed to range between zero and one. Values are summarized from 36 pixels that occurred within a 30 m \times 30 m Landsat image pixel.

	Mean plan [†]	SD plan	Max plan	Mean pro	SD pro	Max pro	Mean slope	Mean TWI	SD TWI	Max TWI
Mean plan	1.000	-0.017	0.630	-0.431	-0.034	-0.313	0.028	-0.491	0.003	-0.430
SD plan		1.000	0.611	0.047	0.250	0.229	0.114	-0.052	0.183	0.099
Max plan			1.000	-0.261	0.152	-0.052	0.069	-0.387	0.105	-0.245
Mean pro				1.000	-0.016	0.588	0.047	0.397	0.093	0.376
SD pro					1.000	0.660	-0.135	-0.130	0.146	0.067
Max pro						1.000	-0.090	0.135	0.151	0.289
Mean slope							1.000	0.324	-0.427	-0.212
Mean TWI								1.000	-0.135	0.555
SD TWI									1.000	0.570
Max TWI										1.000

[†] plan: planar curvature; SD: standard deviation; pro: profile curvature; max: maximum; TWI: topographic wetness index.

TABLE 3: Transformed Divergence (TD) values for iterative assessment of spectral signatures to distinguish soil classes over a 150 ha study area on the Chihuahuan Desert Rangeland Research Center in southern New Mexico. Minimum (Min) and mean TD values were tabulated within the Signature Editor in ERDAS Imagine software (v.9.3, ERDAS, Inc., Norcross, Ga, USA).

No. clusters	Pairs per combination	Min TD value	Average TD value
10	45	1,511	1,887
9	36	1,365	1,882
8	28	1,595	1,882
7	21	1,614	1,870
6	15	1,481	1,867
5	10	1,658	1,859
4	6	1,715	1,856
3	3	1,940	1,957

the remaining three sites had illuvated clays and were classified as Argids. Carbonate accumulation in the three Argid locations was very slight, with only a few carbonate filaments occurring at depth in most locations. In contrast, all eight field sites in soil class 2 had a petrocalcic horizon

within the top 100 cm, distinguishing them as Petrocalcids. Average depth to a petrocalcic horizon in soil class 2 was fairly shallow (51.5 cm). All eight sites in soil class 6 exhibited some carbonate or clay accumulation; the majority of sites were Petrocalcids (63.6%) with the remaining sites classified as Argids (36.4%). Argids in soil class 2 had more visible carbonate accumulation with depth than did soil class 1; most soil class 1 sites had common carbonate filaments and nodules. No significant differences were detected in surface (0-5 cm) textures, although soil class 1 was slightly coarser (with more sand and less silt and clay) than soil classes 2 and 6 (Table 4). Subsurface textures of soil classes 1 and 2 were significantly different with class 2 having more clay (13.5 versus 9.2%) and silt (15.5 versus 11.7%) and less sand (71.0 versus 79.1%) than class 1. Soil class 6 had significantly less sand and more silt than 1 but did not differ in percent clay.

4. Discussion

4.1. Implications for Digital Soils Mapping. We demonstrate that combined use of unsupervised and supervised image classification methods with a semiautomated approach using the Transformed-Divergence metric to derive distinct signatures based on spectral and topographic features successfully

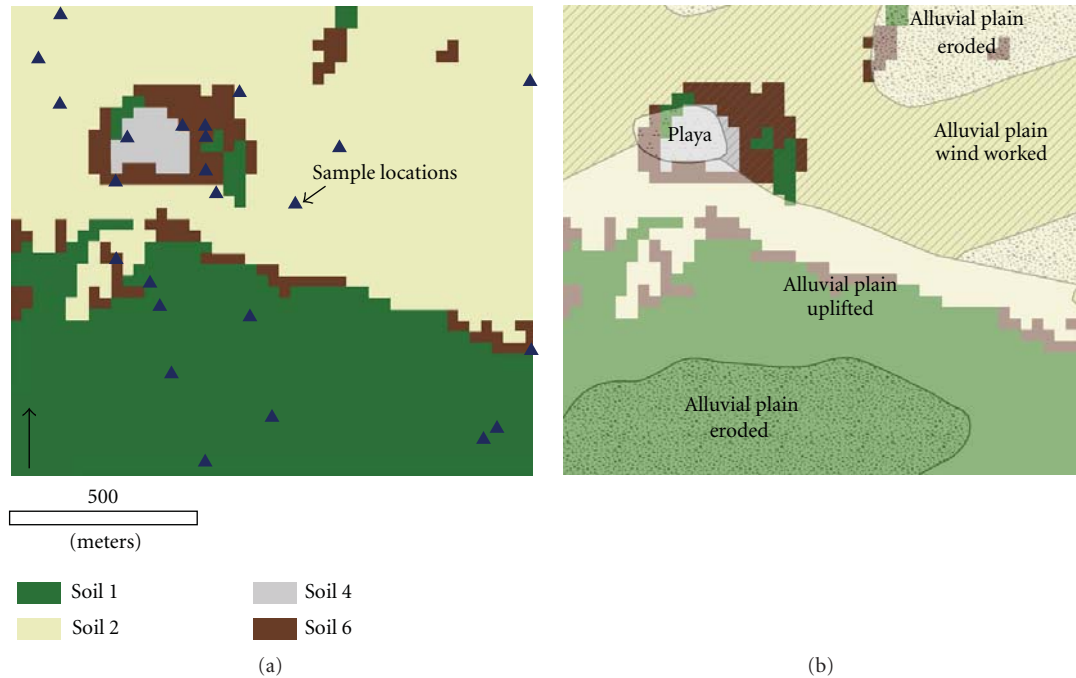


FIGURE 3: Supervised classification representing soil classes for the 150 ha study area on the Chihuahuan Desert Rangeland Research Center in southern New Mexico. Spectral classes were derived in an automated fashion using the Transformed Divergence feature in ERDAS Imagine. A field assessment of 24 points (blue triangles) was conducted by generating a stratified random sample to characterize soils within mapped classes (a); labels correspond to mapped soil classes. Mapped soil classes are depicted in the context of mapped landforms of the Jornada Basin (b); labels coincide with landforms described by Monger et al. [22].

TABLE 4: Field attributes associated with mapped soil classes that include percent of study area for each soil class, distribution of soil taxonomic orders and suborders (where possible) within each soil class, and average soil class properties. Soil classes were mapped by supervised classification of Landsat ETM+ imagery and topographic indices. Data were derived from field surveys of 24 sites ($n = 8$ for each soil class) where soils were augered to depth of 1 m.

Soil	Area [†]	Argid [‡]	Cambid [‡]	Petro-calcid [‡]	Soil Depth [§]	Surface [¶]			Subsurface [¶]		
						Sand	Silt	Clay	Sand	Silt	Clay
			%		cm		%			%	
1	41.2	31.5	68.5	0.0	>100.0	87.3 (1.7)a [#]	9.0 (1.2)a	3.8 (0.5)a	79.1 (1.7)a	11.7 (0.7)a	9.2 (1.0)b
2	50.1	0.0	0.0	100.0	51.1 (19.2)	83.3 (1.8)a	11.5 (1.0)a	5.1 (0.8)a	71.0 (2.4)b	15.5 (0.7)b	13.5 (2.1)a
6	7.1	36.4	0.0	63.6	36.3 (27.1)	82.6 (1.7)a	11.8 (1.0)a	5.6 (0.7)a	71.0 (2.1)b	17.5 (1.5)b	11.5 (0.9)ab

[†] Percent of study area corresponding to three mapped soil classes that were evaluated in the field.

[‡] Percent soil class.

[§] Average in soil class where petrocalcic occurred within 100 cm of the soil surface (Petrocalcids).

[¶] Average in soil class; surface is 0 to 5 cm; subsurface is horizon with maximum clay in the top meter.

[#] Standard deviation in parenthesis, numbers in columns followed by the same letter are not significantly different from Fisher's least significant difference ($P > .05$).

delineated two soils classes with distinct subsurface soil properties (soils 1 and 2) and one transitional class (soil 6). We explore reasons why subsurface (rather than surface) soil properties were distinguishable with our mapping approach in subsequent sections.

4.1.1. Mapping in the Absence of Field Data. Derivation of spectrally distinct signatures for supervised classification using the Transformed Divergence metric circumvented the need for guesswork in the soil mapping process. Yet, only

with a field sampling effort to characterize the mapped soil classes across the study area were we able to interpret the final product. This approach not only yielded an interpretable map of soil classes, but the delineated unique classes also provide an effective means to stratify the landscape for other types of interpolation (e.g., kriging). Such a stratification approach has some advantages over other sampling approaches designed to mimic the natural distribution of soils (e.g., [43]) in that it is effective in capturing rare but complex soil units (e.g., soil class 6), where a higher number of samples was needed for optimal characterization.

The combined use of unsupervised and supervised classifications in digital soil mapping is not necessarily novel. Saunders and Boettinger [15] combine unsupervised classification techniques with classification trees to compare a semiautomated image classification approach based on expert knowledge and field survey data. The novelty of our approach was in using a statistical metric to delineate distinct soil classes in the absence of field data or expert knowledge to train the supervised classification and characterizing the mapped soil classes as a means to assess the performance of this approach.

Field evaluation of mapped soil classes in this study indicates this approach can accurately map the distribution of soil types within a landscape without field samples to drive the image classification. We were surprised by the relatively small contribution of image bands in the visible spectrum and the TWI to distinguishing soil classes. We expected that shallow calcic and petrocalcic horizons would display different levels of brightness near the soil surface. In addition, selecting a Landsat image acquired in winter during a period of below-average rainfall to maximize reflected soil properties may have dampened the benefit of short-wave infrared bands (Band 7 and the normalized ratio of Bands 5 and 7) which are generally sensitive to near surface soil moisture. Although Mean TWI (calculated within $30\text{ m} \times 30\text{ m}$ window) did reflect a higher mean index value for the ephemerally flooded playa (Figure 4), it did not relate well to ancillary soil layers in the data screening process. It is possible that the ideal catchment area size for TWI calculations in this system is larger (or smaller). Future work will examine TWI at a range of spatial scales (i.e., window sizes). In contrast, the slope layer was an effective covariate in distinguishing soil classes. This is due to the improved accuracy and detail (5 m) afforded by the IFSAR sensor and the prominence of landform in soil formation at this site (see Section 4.1.2).

The increased resolution of terrain derivatives contributed to the effectiveness of this mapping effort. We contend that the enhanced accuracy of the IFSAR digital terrain model effectively captured slope and slope shape and that these properties were maintained in the summarized $30\text{ m} \times 30\text{ m}$ depiction of the derived layers. If our analysis had been based on a 30 m resolution slope layer derived from a widely available digital elevation model, we feel that subtleties of slope shape contributing to overland water flow would have been missed. Previous attempts to incorporate slope derived from the previous standard 30 m elevation product to map vegetation were unsuccessful [34]. This was particularly important for distinguishing soil class 6 which was juxtaposed between soil classes 1 and 2 (Figure 3) and may not have been particularly discernable using a native 30 m DEM product.

Spectral response of bare soils has been shown to demonstrate a linear relationship between reflectance in red and near-infrared image bands [44], where soil moisture and surface roughness are the primary factors which determine where upon the line individual soils occur [45]. Vegetation within a given image pixel will contaminate the pure soil response, and this principle has been applied to depict vegetation contributions to reflectance [46, 47]. We demonstrate

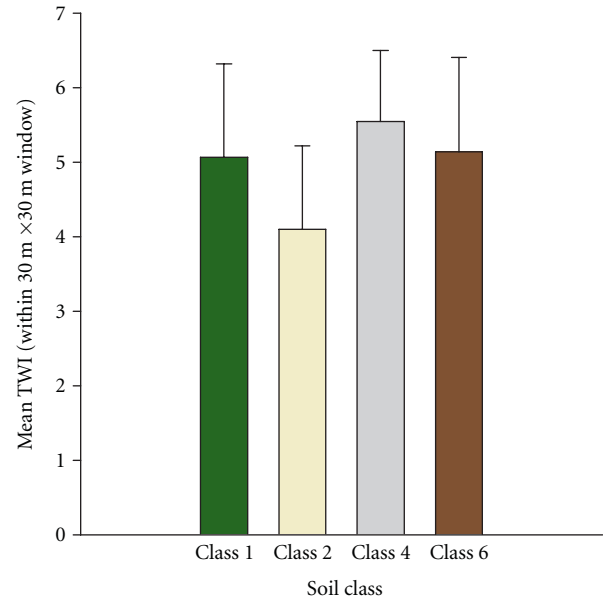


FIGURE 4: Mean Topographic Wetness Index (TWI) values summarized within 6×6 (5 m) pixel windows for each of four soil classes across the 150 ha study area. Three classes were mapped using a combination of unsupervised and supervised classification methods, and the fourth class (soil class 4) was identified as an ephemerally flooded playa by Monger et al. [22]. Mean values are plotted with error bars representing one standard deviation.

that reflectance values in the 23 Feb 2002 ETM+ image in this analysis were not detectably influenced by vegetation due to general conformity of all pixel values to the soil line (Figure 5). As noted earlier, soil moisture was very low for all soils during this time period, thereby circumventing its utility in distinguishing between soil types.

4.1.2. Mapped Soils in the Context of Landform. The success in mapping these subsurface properties was likely due to the correlation between slope, slope shape, and geomorphic processes that affect soil formation. Soil class 1 partially corresponds with the Alluvial Plain Uplift geomorphic area mapped by Monger et al. [22] (Figure 3(b)). The study area slopes gently to the north and is just below the ridgeline of this gentle uplift. The predominant wind direction in the study area is from the southwest to northeast [19]. Hence, soil class 1 is immediately on the leeward side of this ridge and likely has been accumulating eolian sediments since the uplift occurred, resulting in the younger soils with less clay and carbonate accumulation in the soil class. In contrast, soil class 2 is on a flatter, more stable portion of the landscape, where deposition of eolian sands is less pronounced and the petrocalcic horizon is within 100 cm of the soil surface.

Slope shape (maximum planar curvature), which in this system is likely an indicator of reworking of sediments by wind, was similar for soil classes 1 and 2. Although broad-scale deposition was not likely occurring across soil class 2, reworking of surface sediments by wind is common in this geomorphic surface [22, 48]. Soil class 6 is intermediate

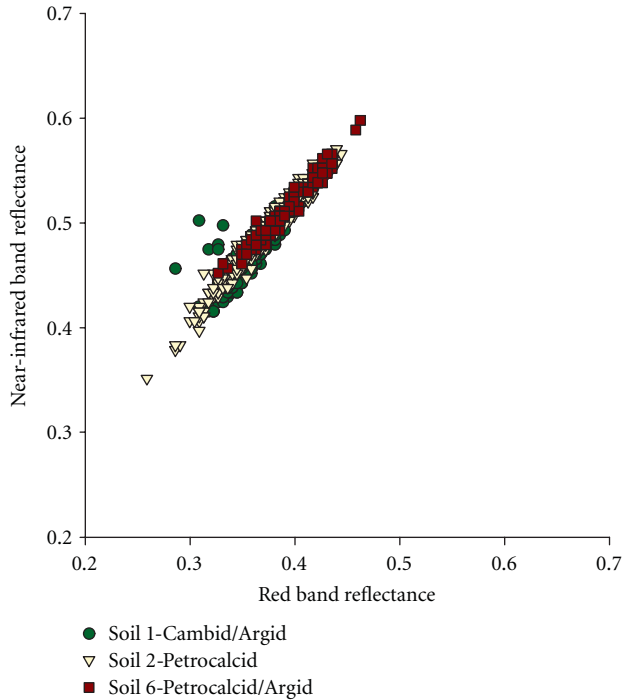


FIGURE 5: Soil line representing three mapped soil classes based on Landsat 7 ETM+ reflectance values corrected for atmospheric effects. Values are plotted for all pixels and support ancillary evidence to demonstrate that vegetation cover was very low and did not contribute substantially to the reflected spectral signal. See Table 4 for soil classification of field samples.

to classes 1 and 2 both in terms of soil properties and topography (Table 4, Figures 2(b) and 2(c)). Soil class 6 slope is intermediate to the flat class 2 and sloping class 1 and slope shape of class 6 was smoother (i.e., fewer undulations) than that of classes 1 and 2. This class primarily occurs at the toe-slope of soil class 1, and in the transition from soil class 2 to the playa (soil class 4). The shallow depth to petrocalcic and commonly observed surface carbonate fragments in the field indicate that soil class 6 represents areas dominated by erosion of surface horizons, due either to wind or water.

4.2. Enhanced Interpretation of Long-Term Vegetation Dynamics. We set out to generate a spatially explicit depiction of ecologically relevant soil properties to evaluate the influence of the topoedaphic template on our long-term analysis of vegetation dynamics. An understanding of the interactions between soils, vegetation, and landscape treatments is strongly desired by land managers and decision makers. The digital soil map produced by this effort captured important differences in soil properties that help to explain the divergent shrub and grass vegetation dynamics over the study area. Our analysis of changes in shrub and grass cover from 1937 to 2008 revealed that grasses were distributed over both dominant sandy soils in 1937, but grass loss and shrub proliferation diverged following the 1950s drought [49]. Soil class 1 was characterized by low water holding capacity in the top 100 cm with little clay or carbonate accumulation

with depth. Soils with these properties have been correlated with low grass resilience to drought due to inability to retain water during dry periods [3, 50]. Such low near-surface water holding capacity is expected to benefit mesquite (*Prosopis glandulosa*, the dominant woody invader in this system) since this species develops extensive, deep rooting systems soon after plants are established [51, 52]. In contrast, soil class 2 captured soils with slightly higher clay amounts and much greater near-surface carbonate accumulation (in the form of petrocalcic horizons) than soil class 1. Such shallow petrocalcic soils are known to promote resilience of grasses during drought due to their ability to retain water at plant available tensions for nearly a year following rain events [3, 40]. This high near-surface water holding capacity would likely lessen the competitive advantage of deep-rooted mesquite plants relative to shallow-rooted grasses by retaining a larger proportion of infiltrated water where it is available to both shallow- and deep-rooted species. Soil class 1 does also have a slightly steeper average slope (3.4%) and soil class 1 (0.9%, Figure 2). Soils with steeper slopes are likely to have a greater fraction of precipitation be lost to runoff than soils with shallower slopes. However, coarse surface textures (Table 4), modest differences in slope, and the importance of petrocalcic horizons for water dynamics [3] and grass persistence during drought [50] indicate that the subsurface soil properties were likely more important factor than the topography governing vegetation dynamics.

We demonstrate that it is possible to extract ecologically meaningful information about soil properties from a remotely sensed perspective. Extensive field sampling and knowledge of ground conditions is not required a priori, but the method does require post-hoc allocation of effort to characterize soil class maps generated. This study used established image processing techniques with a semiautomated method to derive soil class signatures to ultimately distinguish differences in site potential (i.e., shrub dominated versus shrub-invaded grassland; [49]). Field evaluations of the resulting soil classification and analysis of long-term vegetation dynamics among soil classes indicate the approach was successful in mapping areas with similar soil properties and ecological potential. As such, the method provides a basis for mapping soil classes across landscapes or for effectively stratifying sites to make the most efficient use of human resources.

Acknowledgments

This research was funded by the USA Department of Agriculture, Agriculture Research Service, and the National Science Foundation Long-Term Ecological Research Program, Jornada Basin LTER V: Landscape Linkages in Arid and Semiarid Ecosystems. M. Mattocks made substantial contributions to the field assessments and lab analyses to characterize soil properties. Derek Bailey facilitated access to the Chihuahuan Desert Rangeland Research Center for field analysis and sampling.

References

- [1] J. R. McAuliffe, "Landscape evolution, soil formation, and ecological patterns and processes in Sonoran Desert bajadas," *Ecological Monographs*, vol. 64, no. 2, pp. 111–148, 1994.
- [2] I. Noy-Meir, "Desert ecosystems: environment and producers," *Annual Review Ecology and Systematics*, vol. 4, pp. 25–51, 1973.
- [3] M. C. Duniway, J. E. Herrick, and H. C. Monger, "Spatial and temporal variability of plant-available water in calcium carbonate-cemented soils and consequences for arid ecosystem resilience," *Oecologia*, vol. 163, no. 1, pp. 215–226, 2010.
- [4] D. J. Tongway, C. Valentin, and J. Seghier, Eds., *Banded Vegetation Patterning in Arid and Semiarid Environments: Ecological Processes and Consequences for Management*, Springer, New York, NY, USA, 2001.
- [5] J. A. Ludwig, D. J. Tongway, R. W. Eager, R. J. Williams, and G. D. Cook, "Fine-scale vegetation patches decline in size and cover with increasing rainfall in Australian savannas," *Landscape Ecology*, vol. 14, no. 6, pp. 557–566, 1999.
- [6] J. L. Boettinger et al., "Landsat spectral data for digital soil mapping," in *Digital Soil Mapping with Limited Data*, A. E. Hartemink, A. McBratney, and M. d. L. Mendonça-Santos, Eds., pp. 193–202, Springer, Berlin, Germany, 2008.
- [7] D. Howell, Y. G. Kim, and C. A. Haydu-Houdeshll, "Development and application of digital soil mapping within traditional soil survey: what will it grow into?" in *Digital Soil Mapping with Limited Data*, A. E. Hartemink, A. McBratney, and M. d. L. Mendonça-Santos, Eds., pp. 43–51, Springer, Berlin, Germany, 2008.
- [8] K. Anderson and H. Croft, "Remote sensing of soil surface properties," *Progress in Physical Geography*, vol. 33, no. 4, pp. 457–473, 2009.
- [9] A. B. McBratney, M. L. Mendonça Santos, and B. Minasny, "On digital soil mapping," *Geoderma*, vol. 117, no. 1–2, pp. 3–52, 2003.
- [10] H. Jenny, *Factors of Soil Formation, A System of Quantitative Pedology*, McGraw-Hill, New York, NY, USA, 1941.
- [11] M. C. Duniway, B. T. Bestelmeyer, and A. Tugel, "Soil processing and properties that distinguish ecological sites and states," *Rangelands*, vol. 32, no. 6, pp. 9–15, 2010.
- [12] R. A. Washington-Allen, N. E. West, R. D. Ramsey, and R. A. Efroymson, "A protocol for retrospective remote sensing-based ecological monitoring of rangelands," *Rangeland Ecology and Management*, vol. 59, no. 1, pp. 19–29, 2006.
- [13] J. Lowry, R. D. Ramsey, K. Thomas et al., "Mapping moderate-scale land-cover over very large geographic areas within a collaborative framework: a case study of the Southwest Regional Gap Analysis Project (SWReGAP)," *Remote Sensing of Environment*, vol. 108, no. 1, pp. 59–73, 2007.
- [14] J. L. Boettinger et al., "Digital soil mapping—bridging research, environmental application, and operation," in *Progress in Soil Science*, A. E. Hartemink and A. B. McBratney, Eds., Springer, Dordrecht, The Netherlands, 2010.
- [15] A. M. Saunders and J. L. Boettinger, "Incorporating classification trees into a pedogenic understanding raster classification methodology, Green River Basin, Wyoming, USA," in *Digital Soil Mapping: An Introductory Perspective*, P. Lagacherie, A. B. McBratney, and M. Voltz, Eds., pp. 389–399, Elsevier, Amsterdam, The Netherlands, 2007.
- [16] S. J. Nield, J. L. Boettinger, and R. D. Ramsey, "Digitally mapping gypsic and natric soil areas using Landsat ETM data," *Soil Science Society of America Journal*, vol. 71, no. 1, pp. 245–252, 2007.
- [17] P. A. Sanchez, S. Ahamed, F. Carré et al., "Digital soil map of the world," *Science*, vol. 325, no. 5941, pp. 680–681, 2009.
- [18] A. E. Hartemink, A. McBratney, and M. d. L. Mendonça-Santos, Eds., *Digital Soil Mapping with Limited Data*, Springer, Berlin, Germany, 2008.
- [19] J. Wainwright, "Climate and climatological variations in the Jornada Basin," in *Structure and Function of a Chihuahuan Desert Ecosystem. The Jornada Basin Long-Term Ecological Research Site*, K. M. Havstad, L. F. Huenneke, and W. H. Schlesinger, Eds., pp. 44–80, Oxford University Press, Oxford, UK, 2006.
- [20] K. M. Havstad, E. L. Fredrickson, and L. F. Huenneke, "Grazing livestock management in an arid ecosystem," in *Structure and Function of a Chihuahuan Desert Ecosystem. The Jornada Basin Long-Term Ecological Research Site*, K. M. Havstad, L. F. Huenneke, and W. H. Schlesinger, Eds., pp. 266–277, Oxford University Press, Oxford, UK, 2006.
- [21] G. H. Mack, W. C. McIntosh, M. R. Leeder, and H. C. Monger, "Plio-Pleistocene pumice floods in the ancestral Rio Grande, southern Rio Grande rift, USA," *Sedimentary Geology*, vol. 103, no. 1–2, pp. 1–8, 1996.
- [22] H. C. Monger et al., "Regional setting of the Jornada Basin," in *Structure and Function of a Chihuahuan Desert Ecosystem. The Jornada Basin Long-Term Ecological Research Site*, K. M. Havstad, L. F. Huenneke, and W. H. Schlesinger, Eds., pp. 15–43, Oxford University Press, Oxford, UK, 2006.
- [23] R. P. Gibbens, R. P. McNeely, K. M. Havstad, R. F. Beck, and B. Nolen, "Vegetation changes in the Jornada Basin from 1858 to 1998," *Journal of Arid Environments*, vol. 61, no. 4, pp. 651–668, 2005.
- [24] L. C. Buffington and C. H. Herbel, "Vegetational changes on a semidesert grassland range from 1858 to 1963," *Ecological Monographs*, vol. 35, pp. 139–164, 1965.
- [25] D. M. Browning, A. S. Laliberte, and A. Rango, "Temporal dynamics of shrub proliferation: linking patches to landscapes," *International Journal of Geographical Information Science*.
- [26] C. E. Woodcock, R. Allen, M. Anderson et al., "Free access to landsat imagery," *Science*, vol. 320, no. 5879, p. 1011, 2008.
- [27] Goddard Space Flight Center, "Landsat 7 Science Data User's Handbook-Data Products," http://landsathandbook.gsfc.nasa.gov/pdfs/Landsat7_Handbook.pdf.
- [28] D. C. Peters, "Jornada Basin Long-Term Ecological Research site. Long-term datasets: Seasonal aboveground net primary production," <http://jornada-www.nmsu.edu/datacat.php>.
- [29] K. J. Beven and M. J. Kirkby, "A physically based variable contributing area model of basin hydrology," *Hydrological Sciences Journal*, vol. 24, no. 1, pp. 43–69, 1979.
- [30] E. M. O'Loughlin, "Saturation regions in catchments and their relations to soil and topographic properties," *Journal of Hydrology*, vol. 53, no. 3–4, pp. 229–246, 1981.
- [31] P. S. Chavez Jr., "Image-based atmospheric corrections—revisited and improved," *Photogrammetric Engineering and Remote Sensing*, vol. 62, no. 9, pp. 1025–1036, 1996.
- [32] F. F. Sabins, *Remote Sensing Principles and Interpretation*, W.H. Freeman and Company, New York, NY, USA, 3rd edition, 1997.
- [33] ERDAS Inc., *ERDAS Field Guide*, Leica Geosystems, Atlanta, Ga, USA, 2002.
- [34] K. E. Young et al., *Characterizing and predicting suitable aplomado falcon habitat for conservation planning in the northern Chihuahuan Desert*, New Mexico Cooperative Fish and Wildlife Research Unit, Las Cruces, NM, USA, 2002.

- [35] J. R. Jensen, *Introductory Image Processing: A Remote Sensing Perspective*, Prentice-Hall, London, UK, 2nd edition, 1995.
- [36] P. H. Swain and S. M. Davis, *Remote Sensing: The Quantitative Approach*, McGraw Hill, New York, NY, USA, 1978.
- [37] ERDAS Inc., *ERDAS Imaging On-Line Documentation*, ERDAS, Inc., Norcross, Ga, USA, 2009.
- [38] P. W. Mausel, W. J. Kramber, and J. K. Lee, "Optimum band selection for supervised classification of multispectral data," *Photogrammetric Engineering & Remote Sensing*, vol. 56, no. 1, pp. 55–60, 1990.
- [39] T. M. Lillesand and R. W. Kiefer, *Remote Sensing and Image Interpretation*, John Wiley & Sons, New York, NY, USA, 4th edition, 2000.
- [40] Soil Survey Staff, Ed., *Soil Taxonomy: A Basic System of Soil Classification for Making and Interpreting Soil Surveys*, U.S. Government Printing Office, Washington, DC, USA, 2nd edition, 1999.
- [41] G. W. Gee and D. Or, "Particle-size analysis," in *Methods of Soil Analysis*, J. H. Dane and G. C. Topp, Eds., pp. 255–293, SSSA, Madison, Wis, USA, 2002.
- [42] H. E. J. Bulloch and R. E. Neher, *Soil survey of Dona Ana County Area, New Mexico*, USDA-SCS, Washington, DC, USA, 1980.
- [43] B. Minasny and A. B. McBratney, "A conditioned Latin hypercube method for sampling in the presence of ancillary information," *Computers and Geosciences*, vol. 32, no. 9, pp. 1378–1388, 2006.
- [44] A. J. Richardson and C. L. Wiegand, "Distinguishing vegetation from soil background information," *Photogrammetric Engineering and Remote Sensing*, vol. 43, no. 12, pp. 1541–1552, 1977.
- [45] F. Baret, S. Jacquemoud, and J. F. Hanocq, "About the soil line concept in remote sensing," *Advances in Space Research*, vol. 13, no. 5, pp. 281–284, 1993.
- [46] A. R. Huete, D. F. Post, and R. D. Jackson, "Soil spectral effects on 4-space vegetation discrimination," *Remote Sensing of Environment*, vol. 15, no. 2, pp. 155–165, 1984.
- [47] A. R. Huete, "A soil-adjusted vegetation index (SAVI)," *Remote Sensing of Environment*, vol. 25, no. 3, pp. 295–309, 1988.
- [48] G. Bergametti and D. A. Gillette, "Aeolian sediment fluxes measured over various plant/soil complexes in the Chihuahuan desert," *Journal of Geophysical Research F*, vol. 115, no. 3, Article ID F03044, 2010.
- [49] D. M. Browning et al., "Multi-scale analysis of soil depth influence on patch dynamics associated with shrub proliferation," *Ecological Applications*. In Review.
- [50] C. H. Herbel, F. N. Ares, and R. A. Wright, "Drought effects on a semidesert grassland range," *Ecology*, vol. 53, pp. 1084–1093, 1972.
- [51] R. P. Gibbens and J. M. Lenz, "Root systems of some Chihuahuan Desert plants," *Journal of Arid Environments*, vol. 49, no. 2, pp. 221–263, 2001.
- [52] J. R. Brown and S. Archer, "Shrub invasion of grassland: recruitment is continuous and not regulated by herbaceous biomass or density," *Ecology*, vol. 80, no. 7, pp. 2385–2396, 1999.

Research Article

Estimation of Soil Moisture in an Alpine Catchment with RADARSAT2 Images

L. Pasolli,^{1,2} C. Notarnicola,² L. Bruzzone,¹ G. Bertoldi,³ S. Della Chiesa,^{3,4} V. Hell,³ G. Niedrist,^{3,4} U. Tappeiner,^{3,4} M. Zebisch,² F. Del Frate,⁵ and G. Vaglio Laurin⁵

¹ Department of Information Engineering and Computer Science, University of Trento, Via Sommarive, 14, 38123 Trento, Italy

² EURAC-Institute for Applied Remote Sensing, Viale Druso, 1, 39100 Bolzano, Italy

³ EURAC-Institute for Alpine Environment, Viale Druso, 1, 39100 Bolzano, Italy

⁴ Institute of Ecology, University of Innsbruck, Sternwartestr. 15, 6020 Innsbruck, Austria

⁵ Department of Computer Science, Systems and Production Engineering, Tor Vergata University, Via del Politecnico, 1, 00133 Rome, Italy

Correspondence should be addressed to L. Pasolli, luca.pasolli@eurac.edu

Received 15 December 2010; Accepted 22 February 2011

Academic Editor: Mehrez Zribi

Copyright © 2011 L. Pasolli et al. This is an open access article distributed under the Creative Commons Attribution License, which permits unrestricted use, distribution, and reproduction in any medium, provided the original work is properly cited.

Soil moisture retrieval is one of the most challenging problems in the context of biophysical parameter estimation from remotely sensed data. Typically, microwave signals are used thanks to their sensitivity to variations in the water content of soil. However, especially in the Alps, the presence of vegetation and the heterogeneity of topography may significantly affect the microwave signal, thus increasing the complexity of the retrieval. In this paper, the effectiveness of RADARSAT2 SAR images for the estimation of soil moisture in an alpine catchment is investigated. We first carry out a sensitivity analysis of the SAR signal to the moisture content of soil and other target properties (e.g., topography and vegetation). Then we propose a technique for estimating soil moisture based on the Support Vector Regression algorithm and the integration of ancillary data. Preliminary results are discussed both in terms of accuracy over point measurements and effectiveness in handling spatially distributed data.

1. Introduction

Soil moisture content is a key parameter in many hydrological processes. It controls the infiltration rate during precipitation events, runoff production, and evapotranspiration [1]. Thus it influences both global water and energy balances. As a consequence, the information about the spatial distribution and concentration of soil moisture is of great importance in both hydrological applications, such as floods predictions in case of extreme rainfall events, watershed management during dry periods, irrigation scheduling, precision farming, and earth sciences, like climate change analysis and meteorology. When we move the attention to the mountainous environment, such as the Alps, the scale of the spatial and temporal variability reduces, due to the heterogeneity and the variability of the environment [2, 3]. This aspect makes the knowledge of accurate and reliable information on soil moisture status much more complex and at the same time

important and critical for all the applications cited above [4].

In the last few years, the increasing number of space-borne sensors, with complete and frequent coverage of the Earth's surface, has determined an increasing interest for the estimation of bio-geophysical surface parameters from remotely sensed data. In this field, one of the most challenging problems is related to the estimation of soil moisture content from microwave sensors, in particular Synthetic Aperture Radars (SARs).

The sensitivity of microwave signals to the soil moisture content depends on the influence of water on the dielectric constant and has been well established in several studies [5–7]. The challenge in the moisture content retrieval from microwave signals is represented by the complexity and non-linearity of the estimation process. Moreover, several studies pointed out the sensitivity of the microwave signal to other target properties, such as the roughness of the soil and

the presence of vegetation, which introduce additional ambiguities and nonlinearity in the retrieval process [8, 9]. In order to reduce these effects, several studies have been carried out on the use of microwave data acquired with multiple incidence angles, frequencies, and polarization configurations. In particular, the combined use of C and L band microwave signals has shown to be particularly suitable in order to disentangle the vegetation contribution from that of the soil [10]. However, most operative satellite systems (e.g., ERS-2, RADARSAT, and ENVISAT) have onboard a C-band SAR sensor only, thus limiting the possibility of applying multifrequency approaches in operative conditions. Another possible solution is the integration in the retrieval process of data acquired by optical sensors, which may provide useful information for reducing the ambiguity due to the presence of vegetation [11]. Concerning the polarization features, the use of both co- and cross-polarized backscattering coefficients has shown to be effective for the reduction of the ambiguity in the signal due to roughness [12]. However, even though the polarimetric approach has demonstrated to be very promising, it has not been fully exploited yet due to only recent availability of fully polarimetric satellite orbiting sensors. Some recent papers deal with the use of polarimetric RADARSAT2 images. Hendrickx et al., 2009, validate the RADARSAT2 retrieved soil moisture values against ground measurements and optical indices in semiarid areas providing promising results.

Topography is another important aspect (in addition to the effects of vegetation and surface roughness) to be taken into consideration when dealing with the estimation of soil parameters. Satellite systems, in particular SAR systems, are strongly affected by the topography of the area. Distortion effects (i.e., foreshortening, layover, and shadowing) may occur due to the side-looking acquisition geometry (specific of the SAR sensor) and the presence of topography on the ground. Even if these extreme distortion effects do not occur, the SAR signal is affected by the local incidence angle and the distance between the target area and the sensor antenna. These topographic effects are usually taken into consideration during the calibration of the data. However, when dealing with mountain areas, such as the Alps, it is fair to expect to have a nonnegligible residual contribution within the signal due to the extreme topographic conditions [13]. Also this contribution may significantly influence the sensitivity of the microwave signal acquired by the satellite sensor to the moisture content of the soil and consequently could further increase the complexity of the estimation problem. However, limited effort has been devoted to this challenging aspect in the assessment of soil moisture in Alpine areas. For example, Paloscia et al., 2010, investigate the effectiveness of ASAR remotely sensed data in combination with optical images for the estimation of soil moisture in the Cordevole area (Veneto region, Italy). The analysis points out the significant influence of the vegetation coverage on the backscattering signal. However, the area of interest does not present significant variability in terms of topography, thus limiting the applicability of the presented analysis on other mountain areas with different topographic conditions. Heitz et al., 2010, correlated RADARSAT2 backscattering coefficients to

ground measurements indicating that retrieved soil moisture values are able to recognize the topographic soil wetness gradient.

From the methodological viewpoint, the retrieval of soil moisture content can be considered as a mapping problem from the space of the measured signal (i.e., the backscattering signal) to the space of the desired biophysical parameter (i.e., the soil moisture content). This task is commonly addressed by means of the inference of the desired mapping from theoretical forward models, such as the Integral Equation Model (IEM), with the use of iterative methods or nonlinear machine learning techniques [12, 14]. Theoretical models can describe a great variety of experimental conditions in terms of acquisition parameters and target properties. They ensure a high degree of generality to the estimation process and the possibility to handle operative conditions in which no (or very few) field ground truth is available. However, the formulation of theoretical models is typically extremely complex and involves a certain number of input parameters, thus making the inversion process nonlinear, analytically nontractable, and ill posed. Another critical point is the fact that theoretical models may rely on simplifications and approximations of the physical phenomena which may not be completely verified in the field especially in presence of complex environmental conditions [15]. This could be the case of the Alpine environment, due to the presence and heterogeneity of the vegetation coverage together with the effect of topography. These issues could significantly affect the accuracy and reliability of the estimation.

All these aspects make the problem of the characterization of soil moisture in alpine areas from remotely sensed data extremely complex and challenging. With the prospective of the integration of soil moisture estimates in real applicative scenarios, like those cited above, it is important to have a clear comprehension of the possibilities, but also the limitations, of the new generation satellite SAR sensors in combination with advanced state-of-the-art methodologies for the retrieval of soil parameters in the Alpine environment. Although some works in this direction have started, further analysis is required. The SOFIA project (SOil and Forest Information retrieval with RADARSAT2 images) inserts in this context and aims at investigating the capability of new generation polarimetric RADARSAT2 satellite SAR sensors in combination with advanced state-of-the-art methods for the estimation of soil and forest biophysical parameters in the Alpine environment. This paper introduces the rationale behind the experimental analysis carried out in the context of the SOFIA project for the specific topic of soil moisture estimation. The main objectives of the proposed work are

- (i) to present the test area and the setup for the ground measurements,
- (ii) to analyze the sensitivity of the RADARSAT2 polarimetric data on the soil moisture content in an Alpine catchment and the necessity to integrate SAR images with ancillary data,
- (iii) to present the first results of soil moisture estimation derived from the inversion procedure based on the Support Vector Regression technique.

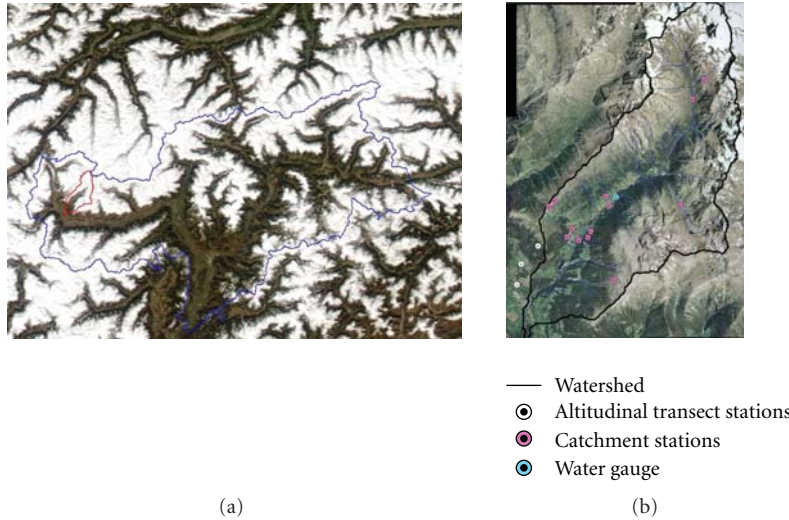


FIGURE 1: Study area of the SOFIA project: (a) Alto Adige Province and (b) Mazia Valley, with the localization of the fixed measurement stations. The stations called “Transect” are the most complete ones, including 4 soil water content sensors in each station at two depths (5 and 20 cm). The stations called “Catchment” include one soil water content sensor at two depths (5 and 20 cm).

The rest of the paper is organized as follows. Section 2 introduces the study area on which our analysis is focused and describes the dataset adopted. The analysis of the sensitivity of the RADARSAT2 data to the soil moisture content is presented in Section 3, while Section 4 is devoted to the proposed estimation algorithm and to the experimental setup for its validation. Section 5 shows the first experimental results achieved. Finally, Section 6 draws the conclusion of the work.

2. Study Area and Dataset Description

2.1. Study Area. The study area of the SOFIA project is the Alto Adige Province, located in Northern Italy (see Figure 1(a)). Alto Adige covers an area of about 7400 km² with a lowest altitude of 220 m and a highest one of 3900 m. Historical climate observations have proved that the climate in the Alps has changed significantly. In the future, the strongest climatic change in the Alps can be expected for the summer months with much drier and warmer conditions in all regions, particularly in the southern part [16]. In addition, climate models agree on a higher interannual variability [17]. This means on the one hand increasing drought periods (summer), while on the other hand higher probability of heavy rain (winter). These variations may have a strong impact on the water availability [18] for agricultural and human purposes and may be strongly related to natural hazards such as floods and landslides [19].

Thus, Alto Adige represents an interesting test site for the following reasons:

- (i) high vulnerability to climate change in fields highly connected to the projects objectives (drought, lack of water, natural hazards, yield),
- (ii) representativeness at least for the central and southern Alps,

- (iii) high diversity of land use with almost all types of land use of central European mountain areas,
- (iv) good data supply, good contact to partners and access to the results of several scientific projects.

Within the Alto Adige area, the Mazia valley (Figure 1(b)), and represented by the red contour in Figure 1(a), a small side valley into the Venosta valley, has been chosen for the first investigations on soil moisture content estimation. Mazia valley covers an area of ca. 100 km² with altitudes that vary from 920 meters a.s.l. (Sluderno) to 3738 meters a.s.l. (Palla Bianca). The area is almost dry, with mean annual precipitation of 525 mm (Mazia, 1580 meters a.s.l.). However, wet patterns with higher soil moisture can be observed mainly due to irrigation practice in highly intensively managed meadows (in the valley floor) and the presence of wet buffers along small rivers going down from the top of the mountains. The land use types present in the area are well representatives for the whole South Tyrol, thanks also to the high variability in altitude. Meadows and pastures present heterogeneous characteristics in terms of vegetation species and human usage, becoming less intensively managed moving from the lower to the higher altitudes.

The valley is equipped with 16 fixed stations for the measurement and monitoring in time of soil parameters (moisture content at 5 and 20 cm depth) and meteorological data (air temperature and humidity, precipitation, wind speed and direction, solar radiation) [20]. The stations are distributed along the valley in locations representative of different elevation, slope, aspect, soil type, and land cover conditions (see Figure 1). Meadows and pastures are a significant presence in the valley. All these conditions make this area particularly suitable for sampling the high spatial variability typical of the mountain environment.



FIGURE 2: RADARSAT2 image acquired on July 21st, false color RGB composition (R = HH, G = HV, B = VV).

2.2. Satellite Imagery. During the summer of 2010, two images were acquired by RADARSAT 2 over the Mazia valley on 3rd June and 21st July. The sensor acquisition mode was Standard Quad Polarization, with a mean incidence angle of 45° and an ascending orbit. The acquisition geometry has been selected such that the area of interest, characterized by a highly variable topography, was imaged minimizing the layover and shadowing effects on the east side of the valley, where a higher number of field measurement stations are present. Original images were provided in single look complex (SLC) format with pixel size of 4.93 m and 17.48 m in azimuth and ground range directions, respectively. Thus the data have been multilooked, calibrated, and geocoded with the help of a high-geometrical resolution (2.5 meters) digital elevation model and filtered with a Frost filter (window size 5×5) in order to reduce the effect of speckle noise. The final resolution of the processed images is 20 m. All the preprocessing has been carried out with the SARscape software (<http://www.sarmap.ch/>). Figure 2 shows the results of the preprocessing in the case of the 21st July image. Polarimetric features have been composed in this RGB image in order to enhance the different information content of each channel. On the west side of the valley, the effects of geometric distortions (i.e., foreshortening, layover, and shadowing) are particularly evident. These effects are minimized in the east side, thanks to the specific acquisition geometry selected.

2.3. Field Measurement Campaign. Contemporary to the satellite acquisitions, two field measurement campaigns have been carried out in the Mazia valley. The aim was to acquire information on the soil parameters (moisture content and roughness) and on the vegetation status (biomass and vegetation water content) of meadow and pasture areas. These measurements have been exploited during the project for different purposes: (1) the calibration of the fixed measurement stations located in the valley, in order to have consistent information at these locations also in correspondence to future satellite overpasses and acquisitions, (2)

TABLE 1: Ranges of variability of the dielectric constant (real part) values measured during the field campaigns.

	Meadow		Pasture	
	June 2010	July 2010	June 2010	July 2010
Min dielectric constant value	6.7	3.8	6.4	3.2
Max dielectric constant value	23.2	27	17.7	8.7
Average dielectric constant value	16.7	15.4	11.6	5.7

the analysis of the sensitivity of RADARSAT2 measurements to the properties of soils and vegetation in alpine areas, and (3) the development and validation of the algorithm for the estimation of the soil parameters from the satellite images.

Two different kinds of measurements have been performed: (1) destructive measurements of both vegetation and soil samples, by physically taking a sample of grass and soil. This kind of sampling was necessary to have accurate measurements of biomass, vegetation water content, soil gravimetric moisture, and bulk density. All the samples have been acquired, weighted, and then sealed in order to be dried in the laboratory according to standard measurement protocols [21]; (2) nondestructive measurements, which where possible thanks to the use of a mobile sensor (the Delta T WET 2 sensor, <http://www.delta-t.co.uk/>); these last measurements regarded only the soil dielectric constant, but had the advantage to be easier and faster with respect to the destructive measurements, so that it was possible to collect a higher number of samples. Sampling areas were selected in order to ensure a good representativeness in terms of local topographic and land use conditions. Moreover, repeated measurements (3 to 5) were collected in each sampling area and then averaged, in order to increase their spatial representativeness. More than 350 dielectric constant measurements were collected in more than 100 different sampling areas. Both destructive and nondestructive field measurements were concentrated on the west side of the valley, due to the better imaging properties of the selected acquisition geometry. Table 1 reports minimum, maximum, and average values of the dielectric constant measured on meadows and pastures during the two field campaigns. As can be observed, meadows present higher and much more variable dielectric constant values with respect to pastures, which are in general drier. This is probably due to the irrigation practice in some areas and to the differences in the soil type and vegetation coverage of meadows with respect to pastures. In fact, soil is quite heterogenous, ranging from Cambisols, Humic Leptosols, and Podzols to locally limited Planosols and Histosols in hydromorphic areas. Also organic content, grain size distribution, and bulk density are highly variable even within areas of the same land cover type. On meadows and pastures, the dominant soil type is brown soil. Above the tree line, combinations of brown soils and ranker appear. In the forest in contrary also semipodzols are common, partly also the overlapping transition in

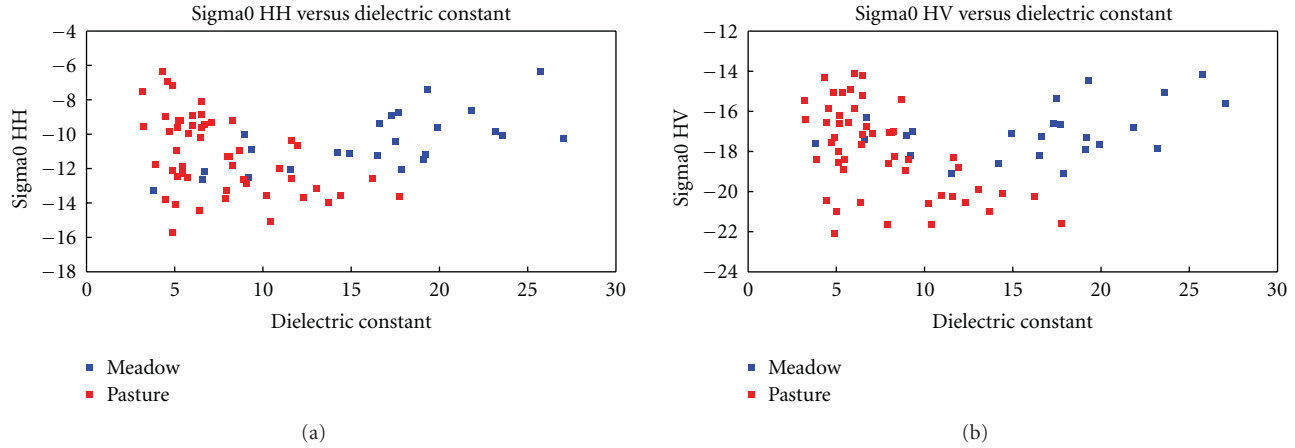


FIGURE 3: Scatter plots of backscattering coefficients extracted from the RADARSAT2 images versus dielectric constant measurements in the case of (a) HH polarization configuration and (b) HV polarization configuration.

semipodzolization of brown soils. Podzols are predominant for coniferous forests. In the vicinity of streamlets also gley may appear. Regarding the soil texture of fine earth, the fraction of sand is dominant (45–75%), the fraction of silt is quite variable (10–40%), and the fraction of clay is mostly low (5–15%). Therefore, soil moisture measurements might be an additional information to validate soil maps as well as to understand the effect of soil texture and organic matter.

In this paper, we address the real part of dielectric constant because it represents the dielectric properties to which the SAR e.m. waves are particularly sensitive. The imaginary part of dielectric constant is in general very low and in most cases can be considered negligible [5].

2.4. Ancillary Data. To carry out the analysis presented in this work, ancillary data already available or extracted from satellite optical sensors have been considered. In greater detail,

- (1) a digital elevation model (DEM) with high spatial resolution (2.5 m) obtained from the processing of airborne lidar acquisitions over the whole Alto Adige area during a measurement campaign in 2008,
- (2) two normalized difference vegetation index (NDVI) maps extracted from two images acquired by the NASA MODIS sensor onboard the Terra satellite as close as possible to the RADARSAT2 satellite overpasses (i.e., within ± 1 day from the RADARSAT2 acquisition). MODIS is a multispectral sensor with 36 spectral channels which acquires information in the visible and infrared portions of the spectrum with daily coverage of the whole Earth's surface. The high temporal resolution of this system allows extracting useful information of the area of interest maximizing the probability to have cloud-free acquisitions as close as possible to the date of interest. The spatial resolution of the sensor is 250 m in the red and near-infrared bands, the portions of the spectrum considered for the computation of the NDVI values,

- (3) a high-resolution (25 m) land-cover map of the Mazia valley derived from ortho-photos, ground surveys, and visual interpretation.

Ancillary data have been geocoded and resampled (bilinear convolution) in order to be completely superimposed with the RADARSAT2 images.

3. Sensitivity Analysis

In order to understand the sensitivity of the RADARSAT2 signal to the moisture content of the investigated area, scatter plots of the backscattering coefficients at different polarization configurations versus the dielectric constant values were generated. To this purpose, in the two satellite images a small 3×3 pixels region was considered in correspondence of each field measurement point. Then the backscattering values were averaged and the resulting mean value was associated to the corresponding field measurement. Samples associated to foreshortening and layover areas were discarded from the analysis. Finally, considering both the acquisition dates and both meadow and pasture land cover types, 75 samples were used in the analysis. Figure 3 shows the plots in the case of HH and HV backscattering coefficients (analogous results have been achieved for the VV and VH configurations).

From a first analysis, it is possible to observe that the points associated to meadows present an expected increasing trend versus the dielectric constant values (more evident in the case of the HH with respect to the HV polarization). On the contrary, no clear trend can be recognized in the samples associated to the pastures. In greater detail, these samples show a high level of ambiguity (i.e., samples with similar dielectric constant values present significant differences in terms of backscattering coefficients) especially for low dielectric constant values. As explained previously, different target properties and external factors may affect the microwave signal acquired by the satellite sensor. Taking into account the environmental conditions observed during the field measurement campaigns, two factors can be considered

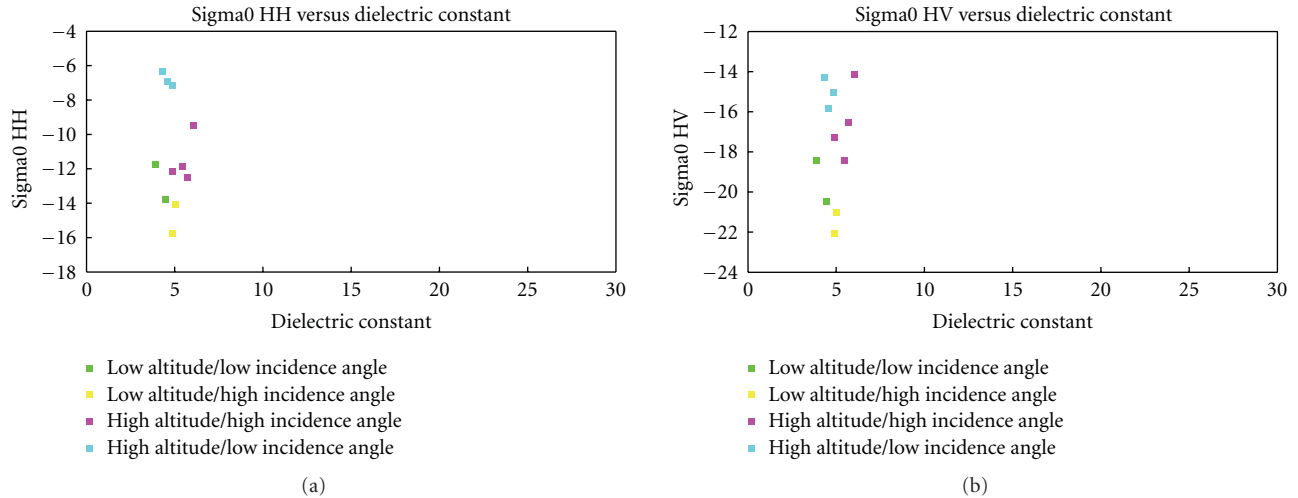


FIGURE 4: Scatter plots of backscattering coefficients extracted from the RADARSAT2 images versus dielectric constant measurements over pasture areas and with dielectric constant values between 4.5 and 5.5 in the case of (a) HH polarization configuration and (b) HV polarization configuration. The samples are grouped into 4 clusters according to the topographic features extracted from the DEM.

as mainly responsible for the variability and ambiguity observed in the pasture samples: (1) the topography and (2) the heterogeneity of the vegetation/land-cover. In the following, these two aspects are better investigated with the help of ancillary data, in order to understand if and to what extent they affect the RADARSAT2 measurements.

3.1. Effect of Topography. As explained previously, topography significantly affects the signal acquired by a satellite SAR system. In our case, although the calibration of the signal was carried out with the help of a detailed digital elevation model, residual topographic effects are expected to introduce significant ambiguity in the backscattering coefficients. This is expected especially for pastures, since they extend over large portions of the valley sides, with altitudes ranging from 1200 to 2400 meters. On the contrary, meadows are mainly located in the valley floor, thus they present similar topographic conditions.

In order to investigate the effect of topography on the backscattering signal, the digital elevation model has been exploited for the extraction of two topographic features: the local incidence angle of the SAR signal (i.e., the angle between the line of sight of the SAR sensor and the direction normal to the surface within the resolution cell, which takes into account the local topography of the area) and the local altitude. The samples associated to the pasture (which demonstrated the highest ambiguity in the SAR signal, as shown in Figure 3) were divided into different dielectric constant classes (e.g., below 4.5, between 4.5 and 5.5, between 5.5 and 6.5, and so on until 12.5; after this value the number of samples is reduced and the variability limited, as shown in Figure 3) in order to keep constant this variable in the analysis. Then, according to the topographic features, the samples of each class were grouped into four clusters: (1) low altitude/high incidence angle, (2) low altitude/low incidence angle, (3) high altitude/high incidence angle, and

(4) high altitude/low incidence angle. Intermediate conditions were excluded from the analysis. Figure 4 shows the resulting scatter plot for values of dielectric constant between 4.5 and 5.5 (which demonstrated the highest variability in the backscattering coefficients) and both HH and HV polarization configurations. Analogous results were obtained for the other dielectric constant ranges.

In the plots, it is possible to observe that samples with similar characteristics in terms of altitude and local incidence angle are quite close one to each other and located in specific portions of the feature space. In greater detail, samples acquired in areas with low altitude and high local incidence angles of the SAR signal present the lowest values of the backscattering coefficient. On the contrary, samples associated to areas with high altitude and low local incidence angles are characterized by the highest backscattering coefficients. The difference between these two extreme topographic conditions is particularly enhanced and can be quantified in 8–9 dB for both HH and HV polarization configurations. The samples with intermediate topographic characteristics, that is, low altitude and low incidence angle and high altitude and high incidence angle, are located between these two extremes. It emerges that both the local incidence angle of the SAR signal and the local altitude of the investigated area affect the backscattering coefficient, introducing attenuation or increase of its value. However, a certain level of variability still remains in the data, as can be observed for example, in the cluster of samples associated to high-altitude and high-local incidence angle. This suggests that topography is not the only factor that affects the SAR signal in these environmental conditions.

3.2. Effect of Vegetation/Land-Cover Heterogeneity. As it was observed in the Mazia valley during field campaigns, the Alpine landscape is characterized by a high variability and heterogeneity in terms of vegetation/land-cover. Meadows,

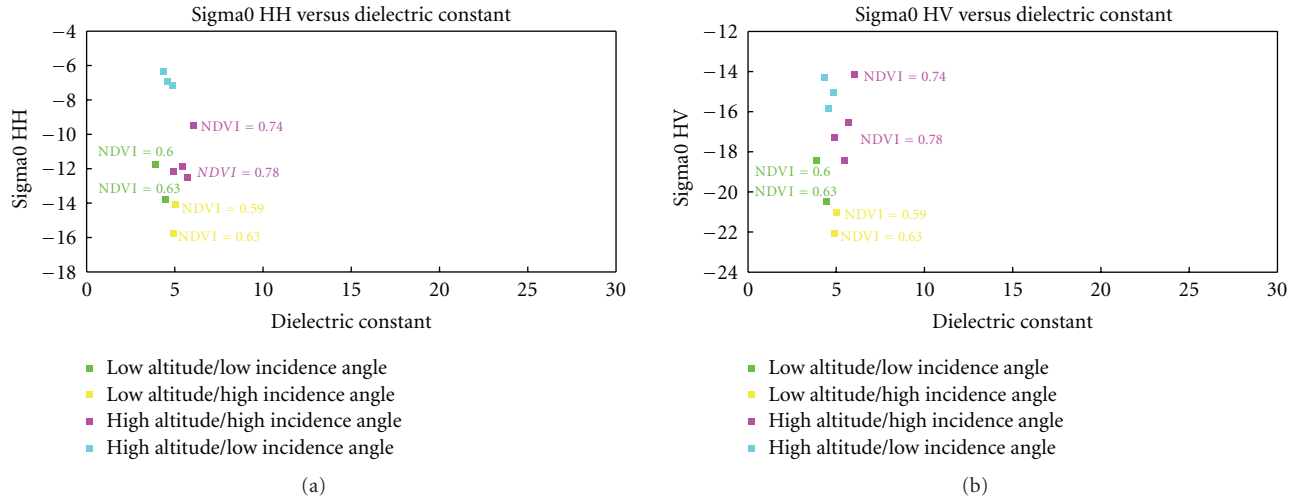


FIGURE 5: Scatter plots of backscattering coefficients extracted from the RADARSAT2 images versus dielectric constant measurements over pasture areas and with dielectric constant values between 4.5 and 5.5 in the case of (a) HH polarization configuration and (b) HV polarization configuration. NDVI values are shown for the samples which show strong residual variability in the backscattering coefficient value.

located in the valley floor, are intensively farmed and irrigated. The soil is typically homogeneous, flat in terms of roughness, and the grass is typically thick. Cut events during the summer period determine variations in the biomass of the vegetation coverage. Pastures have completely different characteristics. First of all, they are located on the sides of the valley where the terrain becomes steep and the altitude increases. The soil is heterogeneous, with the presence of stones and in some cases of large rock's areas when the altitude becomes higher. Also the vegetation coverage is irregular, presenting areas with a significant presence of grass and others less vegetated or quite bare.

Vegetation influences the microwave signal by introducing an attenuation effect with respect to bare soils, as indicated in several studies [22]. On the contrary, the presence of stones and rocks as well as the irregularity of the surface may increase the backscattering coefficient values, due to both multiple reflections and the high irregularity of the surface. Thus, these two factors may explain the residual ambiguity and variability observed in the SAR signal after taking into account the topographic effects. In order to verify this hypothesis, we exploited the normalized different vegetation index (NDVI) extracted from two MODIS Terra satellite images acquired as close as possible to the RADARSAT2 overpasses. This index is sensible to variations in the green leaf vegetation and thus in biomass. For the purposes of our analysis, it can be exploited as proxy to quantify the vegetation/land-cover heterogeneity of the alpine area. In particular, this index will have the highest values in presence of meadows with dense and tall vegetation, while the value will progressively decrease moving to cut meadows or pastures with lower vegetation coverage and an increasing presence of rocks. NDVI values were associated to the samples presenting similar characteristics in terms of dielectric constant value, topography, and land use class (meadow or pasture) but showing a residual variability in the backscattering values.

For the sake of brevity, in this paper, we will present the analysis just for the samples of Figure 4, but good agreement was found also for the other cases.

Plots shown in Figure 5 suggest that the NDVI can explain the residual variability within the samples of each topographic cluster. In particular, for each class of topographic conditions (e.g., high altitude/high incidence angle), it is possible to observe that lower NDVI values are associated to higher backscattering values and vice versa. This confirms the hypothesis that also the vegetation/land-cover heterogeneity affects the SAR signal in the investigated area. It is worth noting that the NDVI map considered for the analysis presented above is characterized by a quite coarse spatial resolution (250 meters) with respect to both the SAR images and the heterogeneity of the landscape. However, it provided useful indications (at least qualitative) for explaining the variability inside the SAR signal. Further and more detailed analysis will be carried out on this point, with the help of higher geometrical resolution images.

The sensitivity analysis presented in this sections suggests that the backscattering coefficients measured by the RADARSAT2 SAR sensor are sensitive to variations in the dielectric constant of soils, thus to variations in the moisture content. However, the microwave signal is also strongly affected by the topography of the area (also after standard topographic correction) and the heterogeneity of the vegetation/land-cover. These factors should be properly taken into consideration for the retrieval of the moisture content of soils in presence of these challenging environmental conditions.

4. Soil Moisture Estimation Technique

Due to the effect of topography and vegetation/land-cover heterogeneity on the SAR signal, the retrieval of soil moisture content in alpine areas becomes particularly challenging and complex. Estimation approaches based on the inversion of

theoretical models may be not effective. Due to the high complexity and heterogeneity of the physical phenomena that affect the microwave signal, it is fair to expect that theoretical models (which introduce in their formulation several approximations and simplifications) will be not reliable and accurate in the estimation. In order to deal with this issue, a possible solution is the direct exploitation of the information contained in the data acquired during the field campaigns by means of nonlinear machine learning techniques. In particular, in this work we propose to address the estimation problem with the ε -insensitive Support Vector Regression [23], which presents properties suitable for the challenges and constraints of the estimation problem of interest.

Thanks to its formulation, SVR is able to handle complex nonlinear estimation problems with good intrinsic generalization capability also in presence of a limited number of training samples [24, 25]. Moreover, it easily handles high-dimensional input spaces, also with features extracted from different sources. These properties allow us to effectively exploit the samples collected during the field campaigns to infer the mapping between the SAR images and the target variable and at the same time to integrate in the retrieval process the information extracted from ancillary data. The latter is required to properly take into account the effects of topography and vegetation/land-cover heterogeneity on the input SAR data.

4.1. ε -Insensitive Support Vector Regression. Let us consider a generic estimation problem. We would like to retrieve a continuous variable y (e.g., the soil moisture content), given a set $\mathbf{x} = (x^1, x^2, \dots, x^m)$ of m features extracted from the signals acquired using remote sensors. From an analytical viewpoint, the estimation problem can be expressed as

$$y = f(\mathbf{x}) + e, \quad (1)$$

where f denotes the desired and unknown input-output mapping and e is a Gaussian random variable with zero mean and unitary variance gathering all the noisy contributions affecting the considered estimation problem. The estimation of y corresponds to the problem of determining the function f' as close as possible to the true mapping f for the task considered.

Given a set of N reference samples $\{\mathbf{x}_i, y_i \mid i = 1, \dots, N\}$, the goal of the ε -insensitive SVR technique is to find a smooth function f' that approximates f while keeping at most a deviation ε from the targets y_i [23]. To this purpose, the original m -dimensional input domain is mapped into a higher dimensionality feature space, where the function underlying the data is supposed to have an increased flatness. Thus it is approximated in a linear way:

$$f'(\mathbf{x}) = \mathbf{w} \cdot \Phi(\mathbf{x}) + b, \quad (2)$$

where \mathbf{w} represents the vector of weights of the linear function, $\Phi(\cdot)$ is the mapping that projects the samples from the original into the higher-dimensional feature space, and b is the bias.

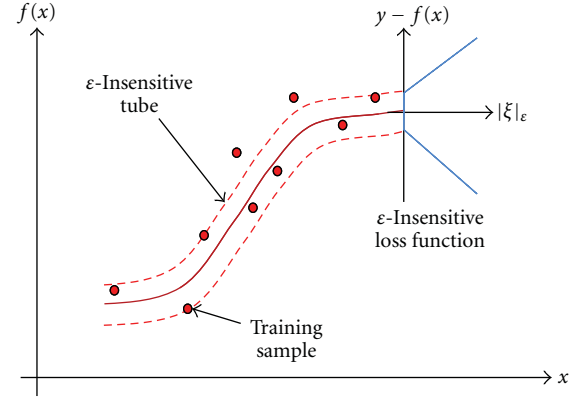


FIGURE 6: Example of a possible choice of the ε -insensitive loss function characterizing the SVR learning approach.

The optimal linear function in the transformed feature space is selected minimizing a cost function, which is the combination of the training error (empirical risk) and the model complexity (structural risk). The first term is calculated according to a ε -insensitive loss function, for example,

$$\lambda(\varepsilon) = \begin{cases} 0 & \Leftrightarrow |y - f'(\mathbf{x})| \leq \varepsilon, \\ |y - f'(\mathbf{x}) - \varepsilon| & \Leftrightarrow |y - f'(\mathbf{x})| > \varepsilon, \end{cases} \quad (3)$$

where ε is the tolerance to errors, that is, it allows one to define an insensitive tube surrounding the function f' (see Figure 6). Equation (3) means that losses smaller than this tolerance are neglected (thus increasing the robustness of the technique to the small errors and to the noise in the training set), whereas a penalty is assigned to estimates lying outside the tube. Equivalently, the penalty is expressed by means of nonnegative slack variables ξ, ξ^* , which measure the deviation of the training samples outside the ε -insensitive tube and are defined as follows:

$$\begin{aligned} \xi &= \lambda(\varepsilon) \Leftrightarrow \lambda(\varepsilon) > 0, \\ \xi^* &= \lambda(\varepsilon) \Leftrightarrow \lambda(\varepsilon) < 0. \end{aligned} \quad (4)$$

The second term is expressed through the Euclidean norm of the weight vector \mathbf{w} , which can be inversely related to the geometrical margin of the corresponding solution and thus (under a geometrical interpretation) to the complexity of the model. Thus, the cost function to minimize becomes

$$\Psi(\mathbf{w}, \xi) = \frac{1}{2} \|\mathbf{w}\|^2 + C \sum_{i=1}^N (\xi_i + \xi_i^*), \quad (5)$$

and it is subject to the following constraints:

$$\begin{aligned} y_i - [\mathbf{w} \cdot \Phi(\mathbf{x}_i) + b] &\leq \varepsilon + \xi_i, \\ [\mathbf{w} \cdot \Phi(\mathbf{x}_i) + b] - y_i &\leq \varepsilon + \xi_i^*, \quad i = 1, 2, \dots, N, \\ \xi_i, \xi_i^* &\geq 0. \end{aligned} \quad (6)$$

C is a regularization parameter that tunes the trade-off between the complexity (flatness) of the function f' and the tolerance to empirical errors.

The constrained optimization problem in (5) can be reformulated through a Lagrange functional, which leads in the dual formulation to a convex (easy to handle) quadratic problem (QP) and thus to a unique solution (global minimum of the cost function). Leaving out mathematical details (for those we refer the reader to [23]), the final result of the estimation problem, in the original input domain, becomes

$$\begin{aligned} f'(\mathbf{x}) &= \sum_{i \in N} (\alpha_i - \alpha_i^*) \Phi(\mathbf{x}_i) \cdot \Phi(\mathbf{x}) + b \\ &= \sum_{i \in N} (\alpha_i - \alpha_i^*) k(\mathbf{x}_i, \mathbf{x}) + b, \end{aligned} \quad (7)$$

where α_i and α_i^* represent the nonzero Lagrange multipliers of the QP and $k(\cdot, \cdot)$ is a kernel function. The latter must satisfy the Mercer's theorem, so that it can be associated to some type of inner product in the highly dimensional feature space (i.e., $k(\mathbf{x}_i, \mathbf{x}) = \phi(\mathbf{x}_i) \cdot \phi(\mathbf{x})$). Thus, the kernel function allows one to evaluate the similarity between a couple of samples in the transformed feature space as a function of the samples in the input space, that is, without the explicit definition of the mapping function $\phi(\cdot)$. This strongly reduces the analytical complexity related to the latter issue. Commonly adopted kernels are polynomial functions and Gaussian radial basis functions [24]. Lagrange multipliers weight each training sample according to its importance in determining the solution function f' . Samples associated to a nonzero Lagrange multiplier are called support vectors. The other samples have no weight in the definition of the result since they fall within the ε -tube (according to the definition of the ε -insensitive loss function). Consequently, to increase ε means to reduce the number of support vectors. This will increase the sparseness of the final representation of the data at the price of lower approximation accuracy on training samples. In this sense, ε quantifies the trade-off between data sparseness and approximation accuracy of the model.

4.2. Estimation Algorithm and Experimental Setup. The retrieval process is divided into two phases: (1) the training of the SVR algorithm and (2) the estimation phase.

During the training, the available training samples (i.e., the measurements acquired during the field campaign associated to the corresponding values of the microwave signal extracted from the RADARSAT2 images) are provided to the technique in order to learn the underlying relationship between the input features and the output target value. Typically, the samples are divided into two subsets: the first is used as training and the second is used as validation to assess the estimation performance of the technique (in terms of accuracy or other quality metrics) with different configurations of the free model parameters. In our analysis, in order to avoid problems related to the choice of the training and validation sets, we applied a k -fold cross validation procedure. Training samples are divided into k subsets. Iteratively, $k - 1$ subsets are used for the training of the regressor while the remaining subset is exploited for the validation.

At the end of the k iterations, the performance over the validation sets is averaged. In this way, all the samples are considered for both training and validation of the algorithm, thus ensuring a high robustness and good generalization of the training procedure. The selection of the best model among different possible configurations of the free model parameters (model selection issue) has been carried out by means of a multiobjective model selection strategy, which allows one to jointly optimize different and competing quality metrics. In this way the model selection process becomes more robust, since it relies on multiple criteria and not just one. Moreover, multiple optimal solutions are obtained according to the concept of Pareto optimality. Each one represents a different tradeoff among the considered quality metrics. The user has thus the possibility to choose the configurations which meets the requirement in terms of estimation quality related to the application considered. For further details we refer the Reader to [26].

After the regressor is trained, it is applied to the multi-dimensional image (which shall contain the same features considered during the training of the technique) in order to obtain the estimated moisture content map.

In our experiments, we considered a 5-fold for the cross validation procedure and the mean squared error (MSE) and the slope of the linear trend of estimated versus true target values as quality metrics to drive the multiobjective model selection. The optimal solution is selected on the basis of a visual inspection of the estimated Pareto front (i.e., the set of optimal solutions of the multiobjective model selection problem). Concerning the SVR technique, we selected an RBF Gaussian kernel and the following ranges for the model parameters: $[10^{-3}; 10^3]$ for γ , the kernel width, $[10^{-4}; 10^3]$ for C , and $[10^{-4}; 10]$ for ε .

As input features of the estimation system, we considered the four polarimetric configurations of the RADARSAT2 image: the altitude and the local incidence angle extracted from the DEM as topographic features and the NDVI and land-cover maps as features for the characterization of the vegetation/land-cover heterogeneity. Different experiments were carried out with different combinations of these features selected according to a sequential forward selection (SFS) strategy, in order to define the subset of them that provides the best results in terms of estimation accuracy.

From an operative viewpoint, for the implementation of the SVR algorithm, we considered the LibSVM software, freely available online [27]. The multiobjective model selection and the sequential forward feature selection strategies were implemented on our own using Matlab.

5. Experimental Results

5.1. Quantitative Assessment with Punctual Measurements. In order to evaluate the estimation performance of the SVR algorithm, different quality metrics were considered: the mean squared error (MSE) (or equivalently the Root MSE (RMSE)), which provides an information on the average error over the estimates; the slope and intercept of the linear regression line between estimated and true target values,

TABLE 2: Estimation accuracies achieved by the proposed algorithm with the best input feature configuration.

	Global	Meadow	Pasture
RMSE	2.68	4.05	1.68
R^2	0.79	0.58	0.75
Slope	0.78	0.58	0.7
Intercept	2.26	7.15	2.3

which indicate whether and to what extent the retrieval algorithm under- and overestimates the target variable with respect to the ideal case of a one-to-one line; the determination coefficient (R^2), which provides a measure about the spread of the estimates around the linear regression line (in the ideal case of a one-to-one line, this metric equals one). These metrics were evaluated over the available reference samples according to the 5-fold cross validation scheme described before. As previously explained, different input feature configurations were considered in the experiments according to the SFS strategy. Here, due to space constraints, we show and discuss the case with the input feature configuration that provided the best performances, that is, the configuration containing 2 polarimetric features (HH and HV), the 2 topographic features (Altitude and Local Incidence Angle), the NDVI, and the land-cover map. Table 2 presents the accuracies achieved by the proposed algorithm in this case, while Figure 7 shows the scatter plot of estimated versus measured dielectric constant values.

Globally, the achieved accuracies are promising, with an RMSE of 2.68 and a determination coefficients near to 0.8. Analyzing in more detail the results, it is possible to observe that the retrieval algorithm provides better performance over pastures with respect to meadows. In the latter case, the error is slightly higher and the algorithm tends to overestimate low values and underestimate high values of the dielectric constant. This effect is probably due to (1) the range of variability of the target variable, which is much larger in the case of meadows with respect to pastures and (2) the number of reference samples, which is lower in the case of meadows with respect to pastures (see Table 1). Both these factors may increase the complexity of the retrieval problem in the case of meadows. Further effort will be put on this issue, in order to better understand and, if possible, overcome the limitations of the estimation over meadows.

5.2. Soil Moisture Content Maps. After the training phase and the assessment over point measurements, the SVR algorithm was tested over the distributed dataset available, that is, the RADARSAT2 images acquired in June and July over the Mazia valley. The two images were provided in input to the trained SVR with in addition ancillary data according to the input features configuration considered for the training of the algorithm. The results of this processing step are two maps representing the estimated dielectric constant values over the area of interest and are shown in Figure 8. The masked values correspond mainly to forest, water bodies, rocks, and urban areas, according to the land use mask.

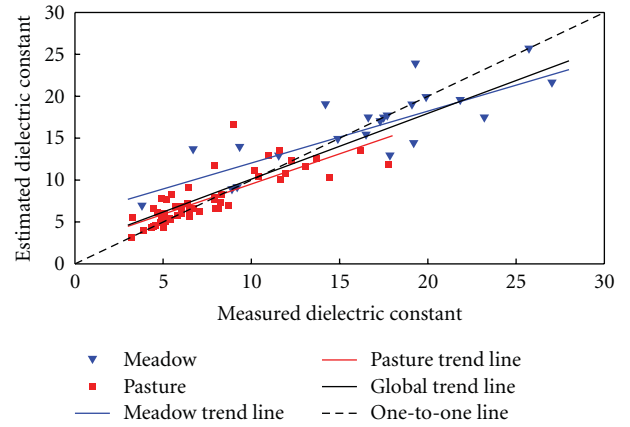


FIGURE 7: Scatter plot of estimated versus measured dielectric constant values obtained with the proposed algorithm with the best input features configuration.

From a qualitative viewpoint, the maps reproduce well the expected trend of soil moisture content, presenting high values near to the valley floor (where the irrigated meadows are located) and progressively decreasing values moving to the pastures at higher altitudes. At the same time, the humidity patterns are well recognized, as for example, in the case of the small rivers going down to the valley floor along the side shown in the details of the maps (Figures 8(a) and 8(b)).

A comparison between the map of June and that of July indicates that the soil in the second date presents a drier behavior, especially in the lower part of the valley side, as can be observed in the details shown in Figure 8. This trend is confirmed by the field measurements carried out in the areas during the two campaigns, as indicated in Section 2.3. In the upper part of the valley side, the maps indicate a slightly drier condition in the case of the June 2010 acquisition. This behavior will be better validated with the help of the soil and meteorological measurements provided by the stations located in the valley, as soon as the data will be available and properly calibrated.

6. Conclusion

In this paper, polarimetric RADARSAT2 SAR images are exploited for the estimation of soil moisture content in an alpine catchment. We first carried out a sensitivity analysis with the help of field measurements of the target parameter and ancillary data. This analysis pointed out that both topography and vegetation/land-cover heterogeneity strongly affect the backscattering signal acquired over alpine areas, introducing a significant variability and ambiguity in the data. The altitude, the local incidence angle, and the NDVI revealed to be useful features to explain the high level of variability intrinsic in the SAR data.

The following step was the development of a technique for the estimation of soil moisture content from the RADARSAT2 images. We opted for an algorithm based on the ϵ -insensitive Support Vector Regression technique.

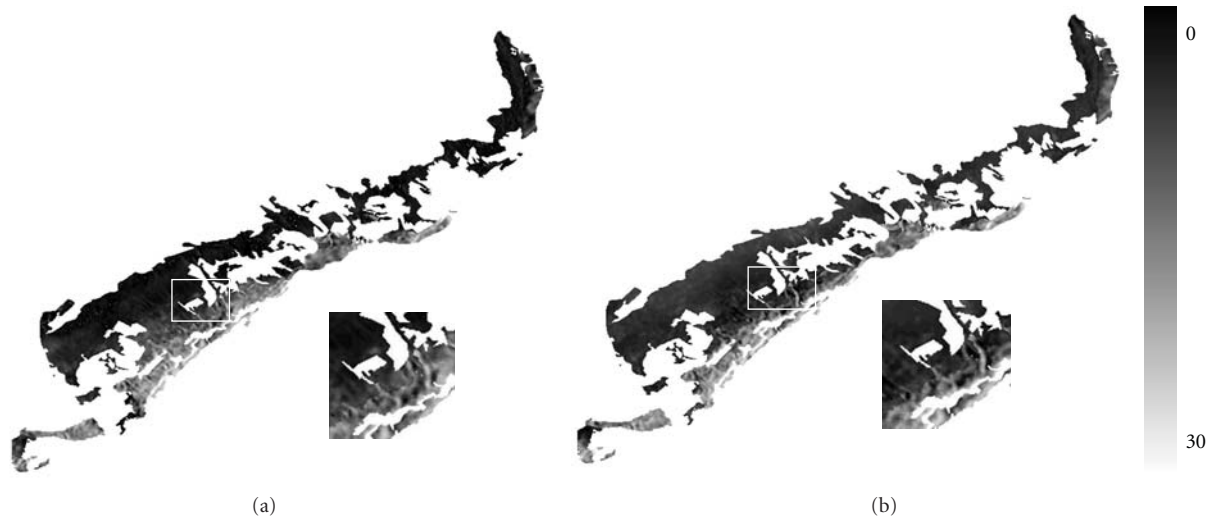


FIGURE 8: Maps of the dielectric constant of the east side of the Mazia valley: (a) 3rd June 2010 and (b) 21st July 2010. The small squares represent a zoom over particular areas extracted from the maps of June and July (indicated with the white square).

Thanks to its formulation, this method is able to handle complex nonlinear estimation problems with good generalization ability also when a limited number of reference samples is available. Moreover, it handles easily high dimensional input spaces, also containing heterogeneous features. The latter characteristic is important in order to integrate in the retrieval process the information extracted from ancillary data. Preliminary results achieved indicate that the proposed technique is promising in terms of (1) capability to exploit the information provided by the ancillary data to reduce the ambiguity intrinsic into the SAR signal and address the complex estimation problem in alpine areas, (2) estimation accuracy over punctual measurements, and (3) capability to reproduce the soil humidity patterns when applied on distributed data.

Future development of this work regards first of all a better characterization of the effect of vegetation/land-cover heterogeneity on the SAR signal. This will be carried out with the help of high geometrical resolution data. In particular, the effect of rocks and stones on the microwave signal in relationship to the retrieval of soil parameters will be analyzed. A second interesting development is the exploitation of the polarimetric capability of the RADARSAT2 sensor by means of polarimetric decompositions of the signal, in order to improve the feature extraction/selection process and thus the retrieval of soil parameters. Moreover, an extended validation of the algorithm, by exploiting the measurements provided by the field stations in the Mazia valley and further RADARSAT2 SAR acquisitions over the whole Alto Adige area will be considered. Finally, the availability of high resolution spatially distributed surface soil moisture maps coming from the RADARSAT2 sensor can represent a major improvement for the validation of distributed hydrological models.

References

- [1] I. Rodriguez-Iturbe, P. D'Odorico, A. Porporato, and L. Ridolfi, "On the spatial and temporal links between vegetation, climate, and soil moisture," *Water Resources Research*, vol. 35, no. 12, pp. 3709–3722, 1999.
- [2] I. Rodriguez-Iturbe, G. K. Vogel, R. Rigon, D. Entekhabi, F. Castelli, and A. Rinaldo, "On the spatial organization of soil moisture fields," *Geophysical Research Letters*, vol. 22, no. 20, pp. 2757–2760, 1995.
- [3] M. Gebremichael, R. Rigon, G. Bertoldi, and T. M. Over, "On the scaling characteristics of observed and simulated spatial soil moisture fields," *Nonlinear Processes in Geophysics*, vol. 16, no. 1, pp. 141–150, 2009.
- [4] R. B. Grayson, A. W. Western, F. H. S. Chiew, and G. Blöschl, "Preferred states in spatial soil moisture patterns: local and nonlocal controls," *Water Resources Research*, vol. 33, no. 12, pp. 2897–2908, 1997.
- [5] F. T. Ulaby, R. K. Moore, and A. K. Fung, *Microwave Remote Sensing: Active and Passive*, vol. 2, Artech House, Norwood, Mass, USA, 1986.
- [6] J. R. Wang, "The dielectric properties of soil-water mixtures at microwave frequencies," *Radio Science*, vol. 15, no. 5, pp. 977–985, 1980.
- [7] T. J. Jackson, "Soil moisture estimation using special satellite microwave/imager satellite data over a grassland region," *Water Resources Research*, vol. 33, no. 6, pp. 1475–1484, 1997.
- [8] F. T. Ulaby, P. P. Vatlivala, and M. C. Dobson, "Microwave backscatter dependence on surface roughness, soil moisture and soil texture, Part-I: bare soil," *Search Results IEEE Transactions on Geoscience Electronics*, vol. 16, no. 4, pp. 286–295, 1978.
- [9] F. T. Ulaby, G. A. Bradley, and M. C. Dobson, "Microwave backscatter dependence on surface roughness, soil moisture and soil texture, part-II: vegetation covered soil," *IEEE Transactions on Geoscience Electronics*, vol. 17, no. 2, pp. 33–40, 1979.

- [10] C. Notarnicola and F. Posa, "Combination of X, C and L band SAR images for retrieval of surface parameters," in *SAR Image Analysis, Modeling, and Techniques IX*, vol. 6746 of *Proceedings of SPIE*, Florence, Italy, September 2007.
- [11] C. Notarnicola, M. Angiulli, and F. Posa, "Use of radar and optical remotely sensed data for soil moisture retrieval over vegetated areas," *IEEE Transactions on Geoscience and Remote Sensing*, vol. 44, no. 4, pp. 925–934, 2006.
- [12] S. Paloscia, P. Pampaloni, S. Pettinato, and E. Santi, "A comparison of algorithms for retrieving soil moisture from ENVIS AT/AS AR images," *IEEE Transactions on Geoscience and Remote Sensing*, vol. 46, no. 10, Article ID 4637966, pp. 3274–3284, 2008.
- [13] A. J. Luckman, "The effects of topography on mechanisms of radar backscatter from coniferous forest and upland pasture," *IEEE Transactions on Geoscience and Remote Sensing*, vol. 36, no. 5, pp. 1830–1834, 1998.
- [14] C. Notarnicola, M. Angiulli, and F. Posa, "Soil moisture retrieval from remotely sensed data: neural network approach versus Bayesian method," *IEEE Transactions on Geoscience and Remote Sensing*, vol. 46, no. 2, pp. 547–557, 2008.
- [15] F. Mattia and T. Le Toan, "Backscattering properties of multi-scale rough surfaces," *Journal of Electromagnetic Waves and Applications*, vol. 13, no. 4, pp. 493–527, 1999.
- [16] M. Brunetti, M. Maugeri, and T. Nanni, "Changes in total precipitation, rainy days and extreme events in Northeastern Italy," *International Journal of Climatology*, vol. 21, no. 7, pp. 861–871, 2001.
- [17] L. P. Graham, S. Hagemann, S. Jaun, and M. Beniston, "On interpreting hydrological change from regional climate models," *Climatic Change*, vol. 81, no. 1, pp. 97–122, 2007.
- [18] T. P. Barnett, J. C. Adam, and D. P. Lettenmaier, "Potential impacts of a warming climate on water availability in snow-dominated regions," *Nature*, vol. 438, no. 7066, pp. 303–309, 2005.
- [19] P. Horton, B. Schaefer, A. Mezghani, B. Hingray, and A. Musy, "Assessment of climate-change impacts on alpine discharge regimes with climate model uncertainty," *Hydrological Processes*, vol. 20, no. 10, pp. 2091–2109, 2006.
- [20] G. Bertoldi, S. Della Chiesa, G. Niedrist, A. Rist, E. Tasser, and U. Tappeiner, "Space-time evolution of soil moisture, evapotranspiration and snow cover patterns in a dry alpine catchment: an interdisciplinary numerical and experimental approach," *Geophysical Research Abstracts*, vol. 12, 2010, EGU2010-12109, 2010, EGU General Assembly, Vienna, Austria.
- [21] J. Cihlar, M. C. Dobson, T. Schmugge et al., "Procedures for the description of agricultural crops and soils in optical and microwave remote sensing studies," *International Journal of Remote Sensing*, vol. 8, no. 3, pp. 427–439, 1987.
- [22] T. Lakhankar, H. Ghedira, M. Temimi, A. E. Azar, and R. Khanbilvardi, "Effect of land-cover heterogeneity on soil moisture retrieval using active microwave remote sensing data," *Remote Sensing*, vol. 1, pp. 80–91, 2009.
- [23] V. Vapnik, *The Nature of Statistical Learning Theory*, Springer, New York, NY, USA, 1995.
- [24] L. Bruzzone and F. Melgani, "Robust multiple estimator systems for the analysis of biophysical parameters from remotely sensed data," *IEEE Transactions on Geoscience and Remote Sensing*, vol. 43, no. 1, pp. 159–174, 2005.
- [25] L. Pasolli, C. Notarnicola, and L. Bruzzone, "Soil moisture estimation from microwave remote sensing data with non-linear machine learning techniques," in *Image and Signal Processing for Remote Sensing XV*, vol. 7477 of *Proceedings of SPIE*, Berlin, Germany, September 2009.
- [26] L. Pasolli, C. Notarnicola, and L. Bruzzone, "Multiobjective model selection for non-linear regression techniques," in *Proceedings of the IEEE International Geoscience and Remote Sensing Symposium (IGARSS '10)*, pp. 268–271, Honolulu, Hawaii, USA, July 2010.
- [27] C.-C. Chang and C. J. Lin, "LIBSVM-A library for Support Vector Machines," <http://www.csie.ntu.edu.tw/~cjlin/libsvm/>.